Label-Free Multiphoton Imaging by Binary Wavefront Manipulation, AO and Super Resolution

by

Adrian Ross Liversage

(Under the Direction of Luke J. Mortensen)

Abstract

Modern microscopy makes many modalities available to the biological investigator, but selecting the appropriate technique is important. Modalities range from light microscopies that can be used to observe translucent samples at resolution of approximately 500nm, to multi-photon techniques that enable imaging inside thicker tissue samples at resolutions down to 250nm. Phase and differential phase contrast microscopies are label-free techniques that enable imaging of individual and bulk cells such as MSCs, and how, as they differentiate, deposited mineral can be quantified and analyzed computationally. We present a robust, user friendly phase imaging system that can be operated by any lab user to investigate translucent samples without the need to understand how the imaging technique works. Multi-photon microscopy enables high resolution imaging within thick tissues using fluorescence or other physical phenomena such as second harmonic generation (SHG). These non-linear modalities are particularly susceptible to optical aberrations present within biological samples. We recover high resolution imaging by means of a high spatial frequency digital micromirror (DMD), and binary wavefront modulation. A genetic algorithm optimizes the pattern by evaluating the intensity of the intrinsic SHG point spread function in the living bone. We present a near eight-fold intensity and 62.5% spatial frequency improvement in vivo while recording mitochondrial dynamics within a bone cavity approximately 120μm below the surface of the skull. Further improvements to high-order aberrations are investigated by decreasing the correction time, analyzing the impact of sparsity of DMD elements and by combining low- and high-order aberration correction to further improve depth of penetration in living bone tissue. NIR illumination of biological tissue enables deeper penetration and further reduction of the

focal volume and by combining this 3-photon emission with image scanning microscopy (ISM) to image beyond the diffraction limit, we envision high resolution imaging within living skull to elucidate the underlying mitochondrial dynamics critical in elucidating osteogenic factors.

INDEX WORDS: [biomedical engineering, biomedical imaging, microscopy, multi-photon, phase imaging, SHG, adaptive optics, super-resolution]

Label-Free Multiphoton Imaging by Binary Wavefront Manipulation, AO and Super Resolution

by

Adrian Ross Liversage

B.Tech., Tshwane University of Technology, Republic of South Africa, 2004

A Dissertation Submitted to the Graduate Faculty of the University of Georgia in Partial Fulfillment of the Requirements for the Degree.

Doctor of Philosophy

Athens, Georgia

2024

Label-Free Multiphoton Imaging by Binary Wavefront Manipulation, AO and Super Resolution

by

Adrian Ross Liversage

Major Professor:	Luke J. Mortensen
Committee:	Paul J. Campagnola
	Cheryl T. Gomillion
	Peter Kner
	Ross A. Marklein

Electronic Version Approved:

Ron Walcott
Dean of the Graduate School
The University of Georgia
December 2024

Dedication

"The Road goes ever on and on, Down from the door where it began. Now far ahead the Road has gone, And I must follow, if I can, Pursuing it with eager feet, Until it joins some larger way Where many paths and errands meet. And whither then? I cannot say."

— Bilbo Baggins, JRR Tolkien,
The Lord of the Rings

Yvette, as Bilbo sings on his way, we have a long path yet to walk together, and almost every day is a moment where we've never been further from the Shire. Our expectations of life are being exceeded daily, and it is because I attached my carriage to your horse.

Also dedicated to those who supported me through many years, now decades, of education.

Acknowledgments

My parents who raised me so well, my father who passed during this fulfillment of this work.

Thank you Luke and the University of Georgia for supporting my work.

Contents

List of Figures

List of Tables

Chapter 1

Introduction

1.1 Elements of Modern Microscopy

Our understanding of the world around us begins with what we can see. From the initial development of tools, that required observation of problems and precise knowledge of materials appropriate for creation of the necessary tools to solve them, to the prediction of celestial events, we had to see in order to measure and predict. For most of our history, the naked eye was the primary tool for observation of the heavens and biological specimens, but scientists of the late 16th century developed the first glass lenses and quickly expanded to the development of telescopes and microscopes, basic cylinders with few lenses, manipulating light so that very small objects could more easily be seen. It wasn't until the late 17th century that Anton van Leeuwenhoek observed bacteria, ushering in a new era of investigation into the microscopic elements in the natural world. This revelation saw microscopy become more popular among scientists, and as discoveries compounded, the microscope as a tool became indispensable. As these microscopes became commonplace in laboratory settings, the desire to observe more detail lead to significant developments in microscopy technologies, and we now have many modalities that allow for investigation and precise measurement of various microscopic samples. Reduced to its fundamental components, any modern imaging system still bears a great resemblance to the first microscopes, most notably the objective lens which collects light for collection and viewing.

With the availability of so many options, considerations must be made to select the appropriate modalities for specific problems. The nature of the sample under investigation serves as the primary criterion for the selection, most importantly whether the light illuminating the sample will be transmitted through

the sample and collected, or if light emitted by the sample in the epi-direction will be collected.

The simplest transmitted light microscopy technique is called brightfield microscopy, which most people would be familiar with, as this technique is widely used in high schools and laboratories around the world as the first port of call in microscopy. Brightfield is useful for imaging thicker tissues stained with dyes such as haematoxylin and eosin (H&E), those used by pathologists. When an investigation requires imaging samples that are unstained, other transmission techniques are available, such as differential interference contrast (DIC), or differential phase contrast (DPC) both of which produce images with high contrast of sub-cellular organelles that are of interest to investigators.

Required spatial accuracy can be considered the second criterion for microscopy modality selection. How small are the features within the sample that are the subject of measurement? The metric by which the capability of a microscope to measure spatial information is measured is called resolution. The resolution (or resolving capability) of a microscope refers to the minimum separation of two features that can be identified as two separate structures. Any light passing through an aperture is affected by diffraction (Figure 1.1a), and when two light sources are close to each other, their respective diffraction patterns overlap (Figure 1.1b). When the diffraction patterns overlap excessively (Figure 1.1c), the point sources cannot be resolved. By increasing the resolution of an imaging system, shorter distances between objects can be resolved.

There is a physical limitation to how small this resolution can become, defined by Ernst Abbe as approximately $\frac{\lambda}{2NA}$, where NA is the numerical aperture of the imaging setup. [1] Whether light is collected after being transmitted through the sample, or emitted by the sample, it is important to note that not all of the light is collected. Objective lenses have a number of characteristics that are important to understand when setting up an imaging system. Most critically among them [2], the range of angles that an objective lens will collect photons from is described by the numerical aperture (NA), where $NA = n \cdot \sin(\alpha)$, α is half the full aperture angle, and n is the numerical aperture of the medium surrounding the objective lens (or immersion medium). [3].

For example, if we implement an imaging system with green excitation light of 500nm, as per Abbe's findings, the diffraction limit is approximately 250nm in a system with an NA of 1. For the purposes of most biological investigation, this is sufficiently small, as most cells range in size from 1μm to 100μm. It is too large to distinguish molecules and proteins, which range in size from 1nm to 100nm. To improve the resolution, as per the diffraction limit formula, reducing the wavelength will result in increased resolution, but delving into the

[1] The physical definition of λ is $\frac{1}{frequency}$, or the wavelength. In this case the wavelength of light.

[2] Others include the magnification, immersion medium, and back aperture diameter.

[3] This medium can be air, water, oil, or others.

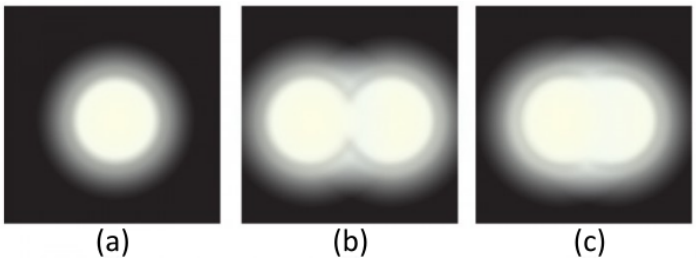

Figure 1.1: (a) The diffraction pattern of monochromatic light that has passed through a circular aperture. (b) This pattern is the result of two point sources similar to (a), that overlap due to diffraction, these can be resolved. (c) If two point sources are nearer to each other, they become indistinguishable.

ultra-violet (UV) range of excitation light becomes expensive, does not provide sufficient contrast and will damage the biological sample.

The resolution at which we can resolve separate objects within a field of view depends on the technology, each of which has limiting factors (Table 1.1) [1].

For instance, while scanning electron microscopy (SEM) offers the highest spatial resolution, it is necessary to prepare the sample by fixation, stabilization, drying and coating. As such, SEM is not appropriate for living samples, but can provide excellent measurements of very small, excised samples. Further, the information collected by SEM is purely spatial. For the purpose of imaging living tissue, many options are available to the investigator. For example, widefield single photon microscopy offers a robust, fast, and user-friendly technique that provides more specific results regarding cells, sub-cellular organelles and proteins. The natural extension of widefield single photon microscopy is confocal laser scanning microscopy (CLSM), which significantly improves the resolution of conventional single photon microscopy by scanning the sample point by point, and the addition of a pin-hole to reject out of focus light [2, 3].

Table 1.1: Microscopy techniques and approximate resolution

Technology	Wavelengths	Approximate Resolution
Video Microscopy	450-550nm	20μm
Micro Radiography	0.01-10nm	5μm
Micro-Computed Tomography	0.01-10nm	1μm
Light Microscopy	400-650nm	300nm
Confocal Laser Scanning Microscopy	400-650nm	200nm
Nano-Computed Tomography	0.01-10nm	50nm
Atomic Force Microscopy	-	50nm
Scanning Electron Microscopy	3.7pm (@100keV)	10nm
Transmission Electron Microscopy	2.5pm (@200keV)	1nm

Each of the techniques listed in table 1.1 have a dedicated field of research upon which they are based, but for the purposes of this work, the primary methods of interest are phase and confocal laser scanning microscopies. These two methods answer the first criterion (nature of the sample) differently and can be applied to both fixed and living biological samples. While an investigator would always seek to maximize the spatial resolution and select according to the second criterion, the resolution available in light and confocal microscopies is sufficient to measure the relevant features of biological samples.

Chemical specificity can be regarded as the third criterion, and in this respect, these selected techniques provide the ability to examine numerous cell types, organelles, and proteins. To this purpose, fluorescence microscopy leverages the development of fluorescent markers that have become a staple of biological investigations such tissue regeneration [4, 5] and drug discovery [6]. While these markers enable important discoveries, florescent markers or the application of markers may cause deviation from the normal function. As such, label free techniques which provide insight into the more representative state of samples have a wide range of use, while they carry limitations. Phase imaging is a label free technique but requires a semi-transparent sample and is limited in spatial resolution.

Other physical phenomena such as second and third harmonic generation imaging (SHG, THG) have become more accessible as longer wavelength light sources have become more affordable and reliable. SHG is particularly strict in requiring non-centrosymmetric samples[4], which makes the modality highly sensitive to filamentous proteins in biological samples, such as collagen type I [8]. This requirement limits SHG imaging to aa limited group of samples, but

[4] SHG dyes can also be applied to samples [7].

provides high specificity and high contrast [9]. THG is very useful in identifying the boundaries between regions of mismatched refractive index and can be used to identify cell boundaries [10], dendritic spines in neural imaging [11], and even to measure the speed of blood flow in living animals [12, 13]. While these modalities add another tool to our toolbox, there are practical difficulties that make them less common in literature. The excitation wavelengths necessary for emission in widely used spectra of collection is longer than what is available as continuous wave (CW) sources, requiring ultra-fast long wavelength sources. Once this change is implemented, power, transmissivity, and reflectance considerations are needed to integrate such sources into existing microscopes.

These selection criteria that have been presented are often at odds and selecting according to one criterion may mean that another cannot be met[5], so that balancing these factors to obtain the relevant information while avoiding photobleaching and phototoxic effects is the primary goal of an effective microscopist [14].

[5] Secondary considerations such as complexity of the technique of the cost of the technique add more to the decision-making process.

1.2 Phase Microscopy

The refractive index (n) of a medium is the ratio of the speed of light through a vacuum to the speed of light through that medium ($n = \frac{c}{v}$). The refractive index of a biological sample is spatially heterogeneous, and this causes the light transmitted through the sample to be impacted differently, so that the phase of the electromagnetic wave is changed according to the optical path length (OPL). Photographic equipment and the human eye are insensitive to these phase changes, but the information conveyed by these phase changes can be important. When the phase changes are converted to amplitude changes, phase contrast microscopy (PCM)[6] can be used to examine living cells without the requirement of fixation of staining, which is of great significance to biologists.

[6] Frits Zernike was awarded the Nobel prize in physics in 1953 for the invention of PCM.

As the light passes through the sample of thickness (t), the velocity of the light is altered according to the refractive index (n) and the OPL is given as: $OPL = n \times t$. The wavefront that emerges from the sample is then defined as the phase shift from the unperturbed wave: $\delta = \frac{2\pi\Delta}{\lambda}$ where the optical path difference Δ is given by: $\Delta = (n_2 - n_1) \times t$. Here we can see that in cases where the refractive index of the sample differs from the surrounding medium, the wavefront is either advanced or retarded according to the thickness of the sample as well as the difference in refractive index.

In an example of these differences, a monolayer of cells in culture would be between 5 and 7μm thick with a refractive index circa 1.36, while the refrac-

tive index of PBS (Phosphate-buffered saline) is 1.335. The resulting OPL of 125nm is in the order of one quarter of a wavelength of green light (500nm).

Superposition is the principle by which two waves interact with each other and form a new wave according to their amplitude. The result of two waves interacting could be constructive (amplitude of the resulting wave is increased) or destructive (amplitude of the resulting wave is decreased). When considering the superposition, it becomes clear that the maximum (minimum) phase deviation is $\frac{\lambda}{2}$ (-$\frac{\lambda}{2}$). Creating a contrast mechanism using these phase differences is accomplished by means of an annular aperture (phase ring or condenser annulus) and a conjugate phase plate which is placed carefully at the objective back focal plane (BFP). The phase of light that does not interact with the sample is advanced by $\frac{\lambda}{4}$ at the annular aperture whereas the light waves interacting with the sample are retarded by $\frac{\lambda}{4}$. This sum of interference is $\frac{\lambda}{2}$ which allows for destructive interference and the illumination can be dimmed to increase the contrast. By varying the phase shift of the phase plate, the phase contrast can be set to either positive or negative (example images in Figure 1.2).

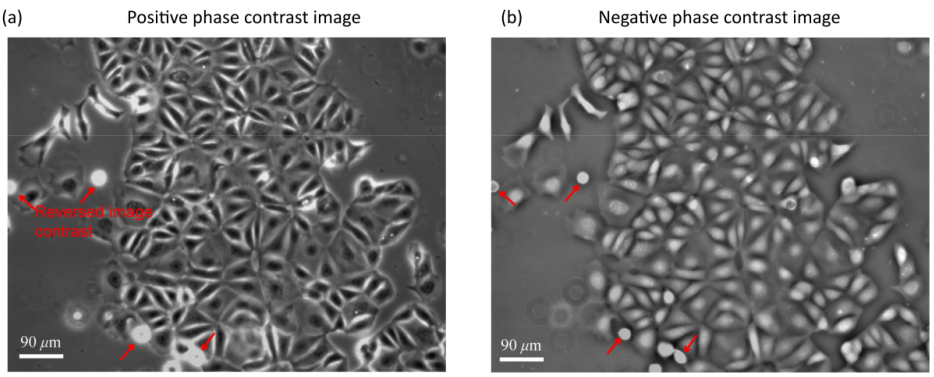

Figure 1.2: (a) An example of positive phase contrast image where the cell body has lower intensity than the background. (b) The negative contrast image shows all cells with intensity higher than the background. Cells marked with red arrows are mitotic [15].

Due to the label free and non-destructive nature of PCM it can be used to image living cells over long periods of time ($>$ 24 hours) and enables biologists to observe the proliferation of cells and allows for quantification of subcellular features. Unwrapping of the phase is however not possible as the intensity variations are confounded with numerous variations. While this results in useful images, the quantitative information (specifically the optical thickness) is lost. As digital image sensors have become ubiquitous within imaging, new methods in which the phase information can be recorded were developed, called quanti-

tative phase imaging (QPI) in which phase information is recorded separately from the brightfield image and can be used in image processing. QPI techniques include methods such as ptychography, digital holographic microscopy, and differential phase contrast (DPC). Generally, an image processing algorithm is applied to the collection of captured images in which interference patterns are recorded and the output is an intensity and phase image.

Within the brightfield illumination construct used for phase imaging, limitations remain. The nature of the sample must be considered. For physiologically relevant studies into the living tissue to which phase imaging is unsuited, alternative modalities must be reviewed. Penetration through opaque tissue with epi-detected[7] imaging capability is a requirement for in vivo imaging, requiring modalities that can provide optical sectioning and specificity.

[7] Transmitted light passes through the sample and is captured on the opposite side of the sample. In the epi-detected configuration, light excites the sample and newly generated, scattered or reflected light is captured on the same side of the sample as the illumination.

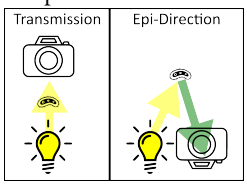

1.3 Fluorescence Microscopy

The term fluorescence was first used by George Stokes to describe the emission of light by a sample that has absorbed light [16]. Vibrational energy is then lost as the molecule returns from the excited state (S_1) to the relaxed, or ground state (S_0), most often described using Jablonski diagrams (Figure 1.3b). This loss of energy results in an emitted photon, shifted to a slightly longer wavelength (loss of energy), a phenomenon known as Stokes shift [17, 18]. For example, the nuclear stain DAPI (4',6-diamidino-2-phenylindole) is excited by a broad spectrum of light peaking at 360nm, but the peak of emitted light is 460nm (Figure 1.3c). As the Stokes shift increases, discernment of the emission from the excitation becomes easier, as a wider range of optical filters can be used to pick off appropriate wavelengths of light.

This single photon fluorescence provides investigators with ample methods to mark specific characteristics of cells and tissues, depending on the nature of the dyes and how they interact with cells. DAPI, which can pass through an intact cell membrane, can be used to stain both live and fixed cells, but less efficiently in live cells, and can thus be used to indicate membrane viability [8]. With so many markers available, fluorescence microscopy has become ubiquitous in biological studies, and commercial systems are readily available and affordable.

[8] This is not a common application of DAPI, but it is mentioned as an example.

Where phase imaging requires transmission of the source light through the sample, fluorescence is not generally used in this configuration. In brightfield illumination it is difficult to separate the excitation and emission light and as such, fluorescence diascopy (transmitted light fluorescence) is not commonly used. Ensuring that the excitation light is not directly transmitted into the collection path of the microscope optimizes the contrast provided by fluorescence.

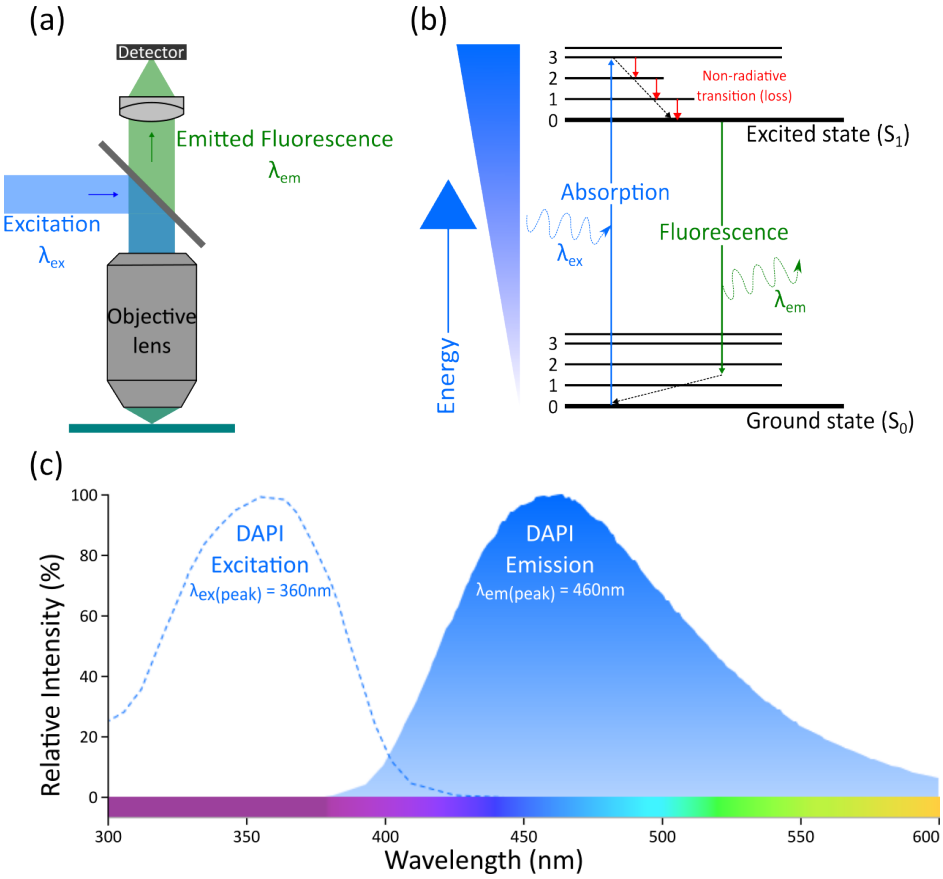

Figure 1.3: (a) The elementary components required for widefield fluorescence microscopy, with an excitation source and resulting fluorescence at a red-shifted wavelength. (b) An illustration of the underlying mechanisms of fluorescence by means of a Jablonski diagram. (c) An example of the Stokes shift in DAPI (from Thermo Fisher's Fluorescence SpectraViewer).

By carefully designing spectral overlap with specific dichroic mirrors and filters, the excitation light can be separated from the emission path and when it is absorbed by the sample, the light emitted by the fluorescent molecules is emitted spherically. This means that instead of collecting the emitted light transversally from the illumination, using a well selected dichroic mirror, this emitted light can be collected by the same objective lens that transmitted the excitation light. This is known as epi-direction detected imaging.

Specifically, widefield fluorescence microscopy is the illumination of the sample by a narrow, unfocused band light source, and the ensuing detection

of the light emitted by the sample. As a result of this wide excitation, the entire sample is illuminated simultaneously and contribution from in- and out-of focus light combines to generate the final image. This results in a low signal-to-noise ratio (SNR) as the out of focus light contributes much of the emitted light. To overcome this limitation, pioneers in fluorescence microscopy implemented pinholes in the emission path to reject out of focus light, in a technique known as confocal microscopy. [9] By placing a pinhole in the excitation path, a further improvement can be realized by exciting a small focal volume within the sample and further reduce emitted light that does not contribute to useful image information.

Further improvements of fluorescent techniques became accessible as modern excitation sources were developed, which were reliable and affordable. These laser sources could generate high power with narrow spectra at high repetition rates. Longer excitation wavelengths enable multi-photon microscopy which is a range of nonlinear modalities whereby a fluorophore absorbs multiple photons and emits only one. This nonlinearity occurs when two (two-photon excitation; 2PE) or three (three-photon excitation; 3PE)[10] photons arrive at the fluorophore simultaneously [19], but in order for the absorption of these photons to elicit an emission photon, the sum of the energy of the excitation photons must coincide with the energy gap of the fluorophore. The high photon fluxes in the range of 10^{20} to $10^{30}/\text{cm}^2$ required for this to occur without damaging the sample, are only feasible at the focus of an excitation source such as pulsed laser beams. These techniques provide optical sectioning, and significantly reduce photo-damage as the focal volume is so small as to only excite a very small region [20]. An ideal candidate for this high photon flux excitation comes in the form of near-infrared (NIR) or short-wave infrared (SWIR)[11]. Titanium Sapphire (Ti:Sapph) sources are capable of generating these wavelengths with beneficial characteristics, such as extremely short pulse duration (in the femtosecond range), low average power (with high peak power) excitation which maximizes the fluorescence of the desired observation volume but even further reduces photo-damage.

To create point scanned images of a wider field of view, the focal volume is scanned by means of high speed resonant and galvanometer scanners guiding the excitation to various points on the sample, with the emitted light collected by single point detectors such as photon multiplier tubes (PMTs). With full control of the scan position relative to the detected emission light intensity, an image can be constructed. In cases of bright emission, these images can be generated close to video rates, but in some cases, more integration time is required to collect enough photons, and imaging time increases.

[9] This diagram illustrates the principle of confocal microscopy where out of focus light is rejected.

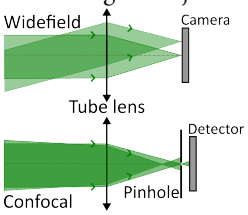

[10] Rough Jablonski diagram for one-, two- and three-photon excitation processes.

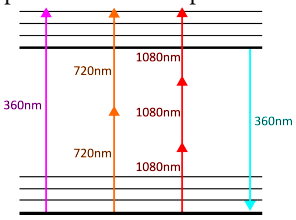

[11] Generally, the wavelength range from 750-1000nm is considered NIR, while 1001-2500nm is SWIR.

Table 1.2: Types of scattering according to wavelength

Rayleigh Scattering	**Mie Scattering**	**Optical Scattering**
$\text{Particle}_{(<50\text{nm})} < \frac{1}{10}\lambda$	$\frac{1}{10}\lambda < \text{Particle}_{(50-500\text{nm})} < \lambda$	$\text{Particle}_{(>1\mu\text{m})} > \lambda$

Additionally, the long wavelengths used in multi-photon microscopy carry the benefit of deeper penetration into tissue. However, where the incident particles are much smaller than the excitation wavelength, scattering of the light becomes impactful on the quality of the generated images, regardless of long wavelengths. Table 1.2 describes the various scattering effects and the size of the particles relative to the excitation and emission wavelengths.[12] When observing small particles, light of short wavelength is more scattered, and when particles are larger, longer wavelengths are more scattered. The intensity of Rayleigh scattered light varies according to the fourth power of the wavelength of the incident light so that $I \propto \frac{1}{(\lambda)^4}$, so that even longer wavelength excitation is subject to scattering [21]. This intensity loss varies according to table 1.2, describing intensity losses according to the wavelength and particle size in question. Many of the biological features of interest are much smaller than the excitation wavelength of 2PE, and as such are subject to Mie scattering, but the longer wavelengths are less scattered, increasing the depth of penetration. Because of these advantages, 2PE fluorescence microscopy is widespread in imaging of thin, thick and living tissue samples [22–24] in research.

[12] Remember that the emitted light is also subject to the scattering tissue in the emission path.

Scattering of the short wavelengths used in confocal imaging is high (Figure 1.4), whereas longer wavelengths reduce this impact [25]. Increasing the wavelength reduces the impact of scattering as photons of longer wavelength penetrate deeper into the tissue, up to the wavelength of approximately 1300nm where an ideal "biological window" exists. Further increases in the wavelength result in an increase in absorption of light by water, but a second window exists between approximately 1500nm and 1700nm, after which the water absorption becomes untenable and increasing the wavelength is ineffective. Progress in laser technology, especially fiber lasers, has made longer wavelength sources more reliable and affordable, and as such investigation leveraging these biological windows at 1300nm and 1550nm has become more widespread.

Autofluorescence, which is the natural emission of light within samples, can be useful in the case of biological samples such as mitochondria and lysosomes [26]. When autofluorescence imaging is the goal, illumination and emission

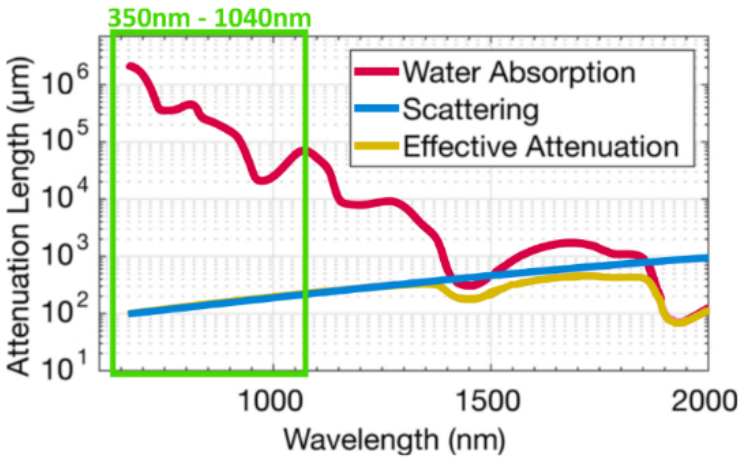

Figure 1.4: The theoretical effective attenuation lengths of Mie scattering and water absorption. The green box indicates the excitation capabilities of many commercially available multiphoton imaging systems.

schemes must be well designed to not overlap emission in cases where the label free autofluorescence is to be used in conjunction with stained fluorescent molecules. For example, in the case of metabolic coenzymes reduced nicotinamide adenine dinucleotide (NAD(P)H) and oxidized flavin adenine dinucleotide (FAD), the optical redox ratio of autofluorescence from NAD and FAD can be used to measure mitochondrial dynamics and creates many opportunities to investigate the study of these dynamics in metabolic-related diseases and cancer [27].

1.4 Second Harmonic Generation Microscopy

While the benefits of multiphoton microscopy provide justification for its use, one drawback is particularly noteworthy. Generally, fluorescence microscopy requires labeling of specific proteins so that excitation by narrow bands of light will result in the emission of light in spectral bands that can be arranged so that multiple fluorescent labels can be used simultaneously. These labels alter the target, and the behavior of the resulting cells or tissues may not be truly representative of regular system function. As discussed in section 1.3, autofluorescence allows label free investigation of some cells and tissues and section 1.2 introduced phase contrast microscopy which is a label free technique with significant limitation in term of chemical specificity.

Second Harmonic Generation (SHG) imaging is based on a nonlinear optical effect and has long been used as a microscopy technique by providing a contrast mechanism for the visualization of structure within biological samples. SHG light is produced when two photons of the same energy (wavelength) interact simultaneously with an appropriate molecule and a photon exactly one half of the excitation wavelength (twice the frequency) is emitted. This energy conservation contrasts with the losses incurred by multi-photon effects during the relaxation phase of the process where photons are emitted[13], and as such SHG does not cause photobleaching [9]. SHG requires the target material to be noncentrosymmetric, and fortunately some biological tissues are assembled into large noncentrosymmetric structures, particularly collagen types I and II [8, 28]. [14]

[13] Where the band gap in the low energy photons is released as vibration or heat.

[14] Other biological structures include microtubules and myosin [29, 30].

Briefly, the phenomenon can be described by considering the nonlinear polarization of a material as:

$$P(t) = \chi^{(1)} \cdot E^1(t) + \chi^{(2)} \cdot E^2(t) + \chi^{(3)} \cdot E^3(t) + \dots \tag{1.1}$$

Here, P represents the induced polarization, $\chi^{(n)}$ the n^{th} order susceptibility and E the electric field [31]. The previously discussed single photon absorption process is described by the first term, while the second term describes SHG. Both two- and three-photon fluorescence are described by the third term, which also describes another nonlinear process known as Third Harmonic Generation (THG).

Here we can also see why SHG has the noncentrosymmetric requirement. Within the electric dipole approximation, the induced polarization in a centrosymmetric sample from one direction would be equal and opposite to the other, and so they cancel each other. The SHG process is also described by means of the Jablonski diagram (Figure 1.5).

SHG is a coherent process, the result of high photon density that induces a nonlinear polarization and generates a coherent wave at exactly half the excitation wavelength. This coherence leads to a phase matching requirement, where some form of phase matching must occur between nonlinear scattering elements within the focal volume for there to be enough signal to detect. A comparison can be made to the linear processes of Mie scattering and Rayleigh scattering.[15] Smaller particles relative to the wavelength scatter equally in the forward and backward directions, but larger particles generate mostly forward scattering [32–34]. So where fluorescence microscopy is well suited to epi-directional microscopy as the emitted photons are generated equally in all directions, in SHG microscopy the thickness of the sample relative to the excitation has bearing on whether forward (F) or backward (B) will dominate. Measurement of this ratio

[15] Mie and Rayleigh scattering show how the particle size impacts the scattering direction.

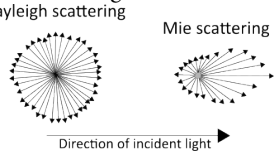

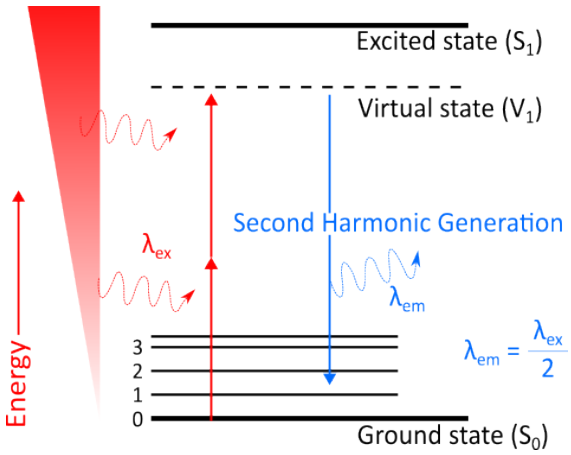

Figure 1.5: The Jablonski diagram of the Second Harmonic Generation phenomenon.

requires that the forward generated SHG is measured through the sample. The orientation of the specimen also plays a large role in the F/B ratio and it has been shown that mature collagen fibrils show a high F/B ratio when compared to immature fibrils [32]. This F/B ratio has been used as a secondary quantification metric for the classification of cancerous cells [35], and healing in tendons [36]. An example of the difference in backward SHG (Figure 1.6a) where only collagen is visible, and the forward SHG (Figure 1.6b) where the sarcomeres in the muscle fibers are visible [37].

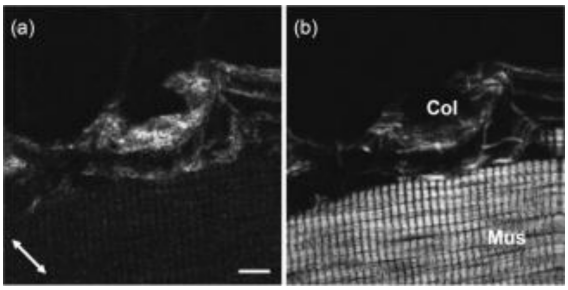

Figure 1.6: (a) Backward SHG and (b) Forward SHG images of a 4μm slice of where collagen matrix and muscle are clearly visible. Scale bar is 10μm. Arrow is the polarization of the excitation. From the manuscript [37]

For the purposes of in vivo studies using SHG imaging, the F/B ratio becomes less problematic as the epi-detected signal is the only signal used to compose the image. In this configuration with "very" thick samples, forward gen-

erated SHG is back-scattered by underlying tissue layers and both back-and forward generated SHG signal is collected. The effects of scattering are clear in the final images, but they remain useful for studying the SHG contrast that is generated in samples such as collagen within bone tissue. Other useful SHG characteristics result in numerous quantification methods that can be leveraged.

With the goal of identifying diseased tissue based solely on SHG images, quantification of SHG images includes some simple, first order statistics which examine the histogram, such as mean, standard deviation, kurtosis, skewness [38, 39]. While these have been used successfully, there are more complex, second and higher order quantification methods that we hope could help to identify diseases even earlier. Second order statistical evaluation of images are derived from newly generated matrices, such as those resulting from gray level co-occurrence matrices (GLCM), which lead to numerous metrics [16] such as angular second moment (ASM), contrast (also inertia), entropy, and correlation [40]. While some investigators have found that a combination of these features results in the best means of discerning tissues [41], others have had success with only energy or contrast [42]. Combinations of these first and higher order quantification metrics seem to have resulted in the optimal results, where classification of infarcted rat hearts was improved (Table 1.3) [38].

[16] In the original work, Haralick identified 14 textural features, but these four mentioned are independent.

Table 1.3: Classification of infarcted rat hearts using first and second order statistics

Classifier	Accuracy
GLCM	72%
First order statistics	86%
FOS + GLCM	95%

1.4.1 Third Harmonic Generation

Where the description of SHG references the second term of the nonlinear polarization equation (Equation 1.1), the third term described another nonlinear process called Third Harmonic Generation (THG). THG though, has a different requirement to generate contrast to the SHG requirement. All materials have a χ^3 susceptibility, but the Guoy phase will cancel out in most tight focusing conditions. In order for signal to be nonvanishing, there must be a change within the third order susceptibility or a change in the refractive index [43]. Interfaces like this are abundant in biological tissues, and as such THG, can be used to identify the boundaries between tissues and even between subcellular organelles, which is especially useful in transparent samples that provide

little intrinsic contrast. As can be seen from equation 1.1 and Figure 1.7, three photons interact simultaneously at the interface and a photon of one third the wavelength (3× energy) is emitted [44].

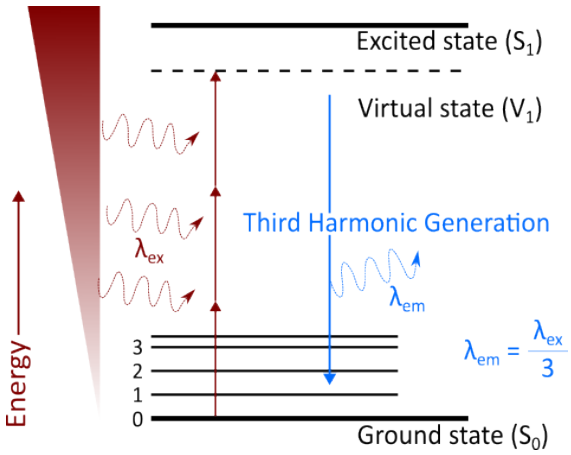

Figure 1.7: The Jablonski diagram of the Third Harmonic Generation phenomenon.

Higher photon density is implicit in the third order nonlinearity, but with the availability of modern light sources, the average power is well within reach of most researchers interested in using the modality for imaging. However, the parameters of the excitation source that impact the signal are pulse duration, energy and repetition rate, which show a large deviation from what we expect in two-photon fluorescence where the fluorescence signal scales linearly with pulse duration, THG scales quadratically [45]. Modern objective lenses are of high quality, NA and broadband, but with numerous layers of glass, they contribute significantly to pulse broadening. In their comparison of high NA objective lenses Guild et.al found that at lower wavelengths (relative to THG requirements; 700nm), NeoFluar 1.3NA 40× contributed approximately 2500fs^2 of group dispersion delay (GDD) [46] (Figure 1.8). This shows that even with a high-quality light source, the glass components used to condition the excitation can render the focal volume incapable of generating a suitable focal volume for THG.

By default, the wavelengths of interest when imaging with SHG or THG, the excitation wavelengths enter the NIR regime and gain the benefit of deeper penetration, although they do increase the point spread function (PSF) size and reduce the resolution[17]. An example image combining SHG and THG (Figure 1.9) shows how much contrast is generated by THG at the interfaces of the adipose tissue and by SHG in the collagen. Label free images such as

[17] PSF size = $0.61\frac{\lambda}{NA}$

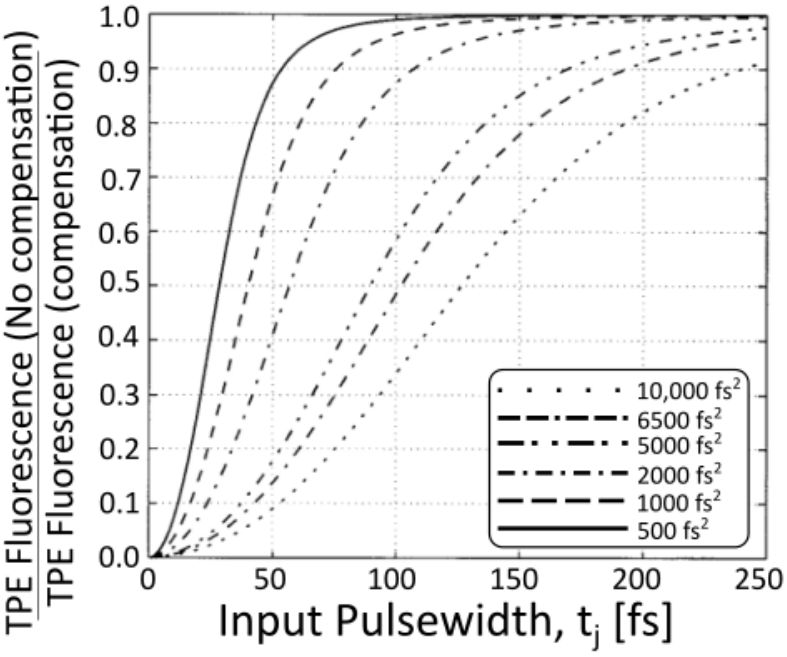

Figure 1.8: Relative fluorescence with and without pre-chirp at various levels of GDD. Directly from [46].

this provide investigators with more representative data regarding biological subsystem functions and how they respond to stimuli.

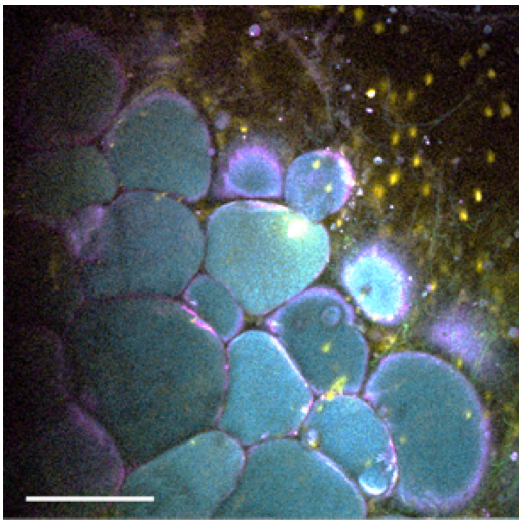

Figure 1.9: A label free image of chinchilla perirenal tissue at a depth of 30μm, where yellow and cyan are 2-photon and 3-photon autofluorescence respectively, green is SHG, and magenta is THG. Scale bar is 100μm. Directly from the manuscript [47].

1.5 Super-resolution Microscopy

While using either multi-photon, SHG or THG, the excitation wavelengths are in the high reds and can extend into NIR (750-1000nm), which according to the calculation of the diffraction limit, will reduce the resolution of such an imaging system. In terms of resolution, any benefits gained from the lower scattering of photons of these longer wavelengths is reduced by the larger PSF. To investigate the smallest fibrils (10-100nm [48]) and the narrowest canaliculi within bone (200-900nm in humans [49], 50-400nm in mice [50]), or extracellular vesicles (EVs) (30nm-10μm [51]), the wavelengths of interest in 2PE, 3PE, SHG, and THG require that we consider what techniques are available to improve the resolution of imaging systems.

Super-resolution imaging is a group of techniques that improve the resolution of imaging systems, beyond the diffraction limit as established by the wave theory of light [52]. To accomplish this paradox, packets of information that are outside of the limits can be multiplexed with information within the limits. Even averaging the signal of a regular imaging technique across multiples exposure cycles, where we exchange information within the sample with some noise can be considered increasing the resolution of an image. But generally, the clas-

sical examples of super-resolution microscopy are photoactivated localization microscopy (PALM), stochastic optical reconstruction microscopy (STORM), and structured illumination microscopy (SIM).

SIM was first proposed and implemented in 1995 [53], but the name SIM was first coined in 2000 by Gustafsson [54]. Famously, the technique leverages the Moiré effect where two patterns interfere with each other and in the case of SIM are multiplicatively superimposed causing the Moiré fringes to appear (Figure 1.10a). Each of these fringes is coarser than the original pattern, but the information of the high frequency patterns remains accessible, provided the illumination pattern is known [55]. As previously discussed, the diffraction limit is a physical limit placed on the spatial resolution of an imaging system, but when considering the Fourier (frequency) domain, this means that all of the frequencies captured within an image would appear inside a circle of a fixed radius (Figure 1.10b). [18] This "base" observable region, approximately $\frac{1}{d_0}$ (d_0 is the diffraction limit), defines the set of patterns that can be created in the illumination light. SIM does not change this region physically, rather moving the information into the region from outside with the knowledge that in the case of sinusoidal striped pattern, the Fourier transform is a delta function with 3 points in the frequency space (Figure 1.10c). By extending this sequence and changing the phase of the illumination patterns, the resolution can eventually be doubled (Figure 1.10d,e) after reconstruction.

[18] Remember that low frequency information is closer to the origin in the Fourier space and the further from the origin, the higher the spatial frequency.

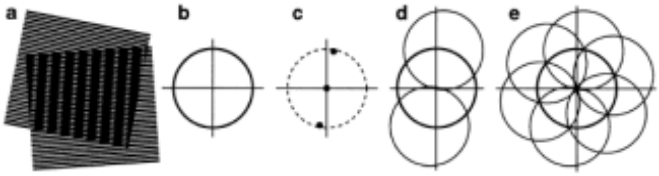

Figure 1.10: From Gustafsson's manuscript describing SIM in terms of Fourier optics [54]. (a) Moiré fringes generated by superimposing two line patterns. (b) The "base" observable region. (c) A sinusoidally striped pattern with three Fourier components which defines origins for two new "base" regions. (d) By extending the origins of a sequence, it is possible to acquire information from twice as much area in the frequency domain, resulting in a factor of two increase in resolution (e).

In their experimental presentation of the method, Gustaffson imaged HeLa cells and showed an enhancement larger than two (1.11a-d), down to a resolution of approximately 115nm. This illustrates another appealing feature of SIM, that no special treatment of the sample is necessary, and any sample prepared for fluorescent imaging can be imaged using SIM.

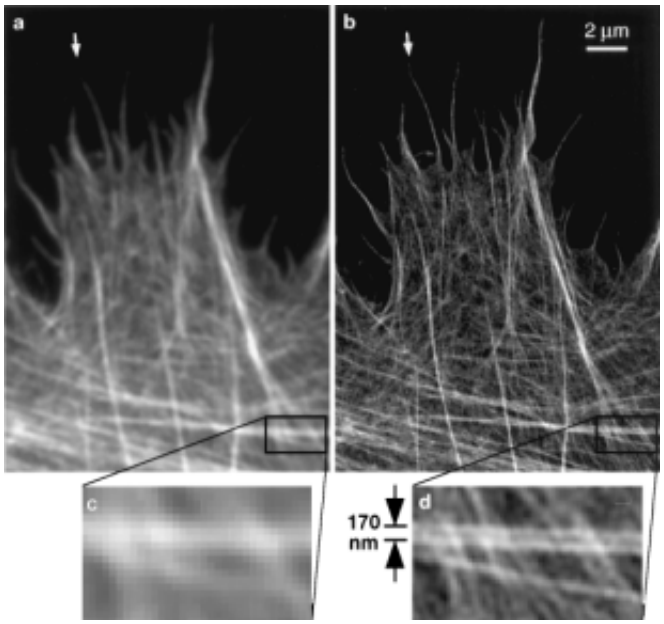

Figure 1.11: From Gustaffson's manuscript implementing SIM [54]. (a,c) Conventional microscopy and (b,d) SIM of HeLa cells. Fibers in (d) are separated by less than the resolution limit.

From this brief description of SIM, it can be seen that through clever manipulation of information theory and optical phenomena, super-resolution can lead to significant enhancement of the resolution of an imaging system. Where SIM leverages structured illumination, a similar technique, image scanning microscopy (ISM), expands the captured information by structuring the detection.

To fully understand how the structured detection of ISM expands the captured information, a more thorough understanding of confocal microscopy is necessary. In a confocal microscope, the two fundamental tools are the raster scanning of a diffraction limited laser focus of a sample, and the recording by confocal detection (through a pinhole) which rejects out of focus light. When appropriately adjusted, the size of the confocal pinhole should be large enough to pass all light from a point source in the focal plane, which ensures the highest sensitivity for photons originating in the center of the focus [56]. Once again, the diffraction limit restricts the lateral extension of the laser focus defining the resolution of the imaging system. Theoretically, by reducing the diameter of this pinhole to a fully closed aperture would result in a doubling of the resolution, but practically no photons would be collected. Even reducing the diameter of

the pinhole by moderate degrees causes significant losses of collected photons, and so the concept sees very little application. Colin Sheppard proposed a solution to the confocal pinhole size problem in 1988 [57], and Gregor & Enderlein fleshed out the description in 2019 [56].

The ISM concept simply proposes the replacement of a point detector by an array detector, [19] which captures a small image at each scan point (giving rise to the name Image Scanning Microscopy). The effective pixel size should be in the range of $50 - 80$nm and each pixel of the array records its own confocal scan image, each with a slightly different perspective. After completing one scan of the sample, there are as many scan images as there are pixels within the detector. The spatial resolution of these images corresponds to that of a confocal microscope with a zero-size pinhole because of the small pixel size, but in this instance all photons are collected somewhere on the detector, so the collection efficiency is much higher. [20]

[19] A point detector such as a PMT, in a configuration such as one described in section 1.3.

[20] This is provided that the detector effective region is close to 100%.

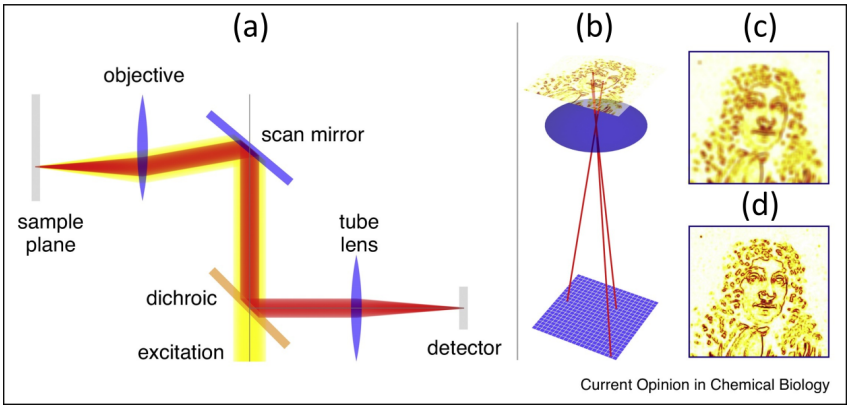

Figure 1.12: (a) The basic setup of an ISM system where light emitted from the sample is descanned and collected on an array detector. (b) Each pixel on the detector records a separate image at a slightly offset angle from the central pixel. (c) Simply summing the images results in a blurred image of the sample. (d) An optimized algorithm is required to obtain the high resolution image of the sample using the scanned images. [56]

In ISM microscopy, the emission light is descanned (Figure 1.12a) similarly to what we see in confocal scanning microscopy, and so the only difference between the methods is the introduction of an array detector to replace the single point detector in confocal microscopy. Similarly to SIM, the reconstruction of the various images is core to exceeding the diffraction limit, and by simply summing the individual scanned images results, each acquired at a different angle (Figure 1.12b) results in a blurred image of the sample (Figure 1.12c). Adjustment of each

of the sub-images is required to enhance the resolution to beyond the diffraction limit.

Initially, ISM implementation were devised using emCCDs [58], which require milliseconds of dwell times per image (sub-image for ISM), and it became obvious that much time was being wasted in collection, as a very small region of the camera was being use. York et al [59] presented a method using a digital micromirror device (DMD) to generate a multi-focus excitation, thereby increasing the speed and efficiency of the ISM method.

Over the last decade, photodiodes have become more readily available and with the advent of avalanche photo diodes (APDs), single photon counting resolution with high-speed digital outputs have been implemented and introduced to the market as individual detectors, or multiplexed as SPAD (Single Photon Avalanche Diode) arrays. This combination of high speed and high temporal resolution has led to the use of SPAD cameras in ISM and FLIM systems [60]. Further, ISM has been shown to work in multi-photon [61, 62], SHG [63] and reflectance light microscopy [64]. While photo-diode implementations work well, it is noted that at low signal strength, photodiodes have a lower signal-to-noise ratio (SNR) than PMT based detectors [65], which have been shown within the ISM framework to increase the SNR [66].

Due to the low barrier to upgrading an existing confocal laser scanning microscope to an ISM implementation, commercial implementations are readily available, such as the AiryScan microscope from Zeiss [67], Re-scan confocal microscope (RCM) from Confocal.nl [68], and Olympus's SpinSR10 [69]. The claims from these off-the-shelf systems is that the image resolution enhancement can range from $1.2\times$ to $1.4\times$.

1.6 Adaptive Optics

The PSF which measures the response of an optical system to an infinitely small light source can be modeled theoretically. Image formation in a light microscope is a linear process in which each imaged object is the effective summation of infinitely small point objects. By convolving the object and the imaging setup's PSF, the image is formed.[21] Now we know that the most basic building block of any imaging system is the PSF, which is negatively affected by optical aberrations, regardless of the technique or modality. Aberrations caused by the slight imperfections or misalignment of the optical components are called system aberrations. More critical aberrations are sample aberrations, which are caused by mismatched refractive indices, primarily between the lens medium (often water) and the embedding medium (dependent on the sample) [70, 71].

[21] An illustration of the convolution of and object with the PSF

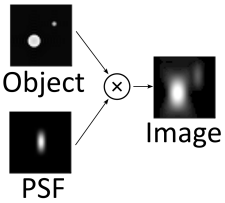

As the imaging depth increases, the PSF size increases and the imaging quality degrades. Biological tissue especially is comprised of myriad refractive indices from various cell types and heterogeneity in molecule sizes and so the composition of the sample affects the PSF differently depending on the sample tissue.

Contributions of low and high order aberrations combine to degrade the image quality significantly in brain tissue at 90μm [72], but scattering of photons is an additional component that degrades the PSF quality. Attenuation of signal emitted from a sample is caused by a combination of scattering and absorption given as: $\mu_e = \mu_s + \mu_a$ or $\frac{1}{l_e} = \frac{1}{l_s} + \frac{1}{la}$. The scattering length of a sample l_s (l_e is the effective attenuation length, and l_a is the absorption length constant) is the distance over which intensity is reduced e-fold. Multiple scattering events occur when light penetrates deep within the sample so that the confounding elements of low and high order aberrations, and scattering reduce the intensity, contrast and resolution of imaging at depth [73].

Characterization of the strength of aberrations is the root mean square (RMS) deviation of the optical path length (OPL) [22] and most often a compensation to correct these specified aberrations would be $\lambda/10$ or below. The information in the RMS of aberrations provides no information about the spatial characteristics, and as such, the more widespread form of aberration characterization is offered in the decomposition into the aberration modes based on Zernike polynomials. Commonly, the distorted wavefront is characterized as:

[22] The product of the physical distance that light travels through a medium and the refractive index of said medium.

$$W(\rho, \varphi) = \sum_{n=0}^{\infty} \sum_{m=-n}^{+n} a_n^m Z_n^m(\rho, \varphi) \tag{1.2}$$

Here, the $W(\rho, \varphi)$ is the deviation of the OPL as a function of ρ, the radial coordinate normalized to the pupil radius and φ, the azimuthal angle. The superposition of Zernike polynomials $Z_n^m(\rho, \varphi)$ with the amplitude coefficients a_n^m results in a more thorough characterization of the aberrations. Each of the resulting terms from this characterization is referred to as an optical Zernike mode and corresponds to specific types of aberration, for example:

- Z_0^0 : Piston, which is a direct, constant phase change. For the purposes of aberration correction, this mode is useless, but with enough poke distance, this can be useful for remote focusing.
- $Z_1^{\pm 1}$: Wavefront tilt, which can easily be introduced into an optical system by tilted mirrors.
- Z_2^0 : Defocus. At a system level, this is often caused by chromatic aberrations. [23]

[23] Chromatic aberrations are the result of dispersion where the refractive index of a medium varies by wavelength.

- $Z_{\pm 2}^{\pm 2}$: Astigmatism, which indicates that rays of light in perpendicular planes have different foci.

- $Z_3^{\pm 1}$: Coma, where off-axis point sources appear distorted dues to a variation in magnification over the entrance pupil of the system.

These are descriptions of the lower order Zernike modes, and they continue through higher order named modes such as trefoil, tetrafoil, spherical, and secondary and tertiary iterations of these already named. Each polynomial is orthogonal and changes in each mode do not impact other modes. Beyond the first 10 polynomials each of the higher order modes is related to prior, lower order polynomials, but with higher spatial frequency (Figure 1.13).

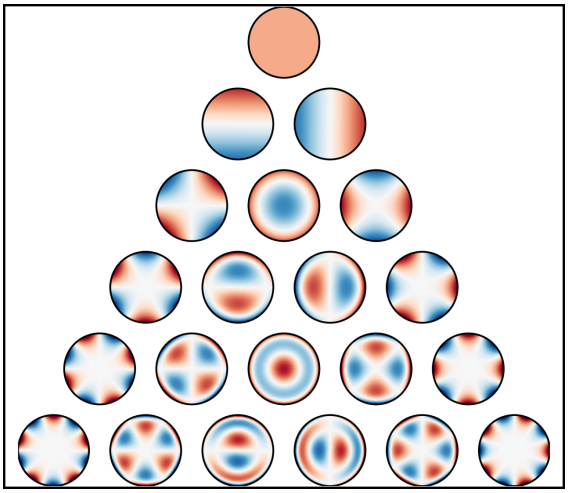

Figure 1.13: The widely used pyramid organizing the first 21 Zernike polynomials which orders them vertically by radial degree, and horizontally by azimuthal degree.

Adaptive optics (AO) is the concept of correcting for system and sample induced aberrations. Electro-optical components such as deformable mirrors (DMs) and spatial light modulators (SLMs) can manipulate the electromagnetic wave to correct for aberrations. Deformable mirrors are constructed by fixing a reflective material onto a number of actuators that act as pistons, poking the individual actuators and changing the shape of the reflective surface (which can be continuous of segmented), and can manipulate up to a maximum Zernike mode specified by the physical limitations of the device. Appropriate placement of a deformable mirror would correct the distorted wavefront and improve the PSF quality (Figure 1.14). In such a configuration, a wavelength of the emitted light that is not used in image generation is picked-off and directed towards a high-speed wavefront camera (along a non-common path).

A Shack-Hartmann configuration is used where the light from a single point source is imaged through a lenslet array and imaged on the wavefront camera. The distorted image will generate an array of spots that is not uniform, and an algorithm can be implemented to compute the appropriate compensatory shape which when applied would restore a flat wavefront.

Alternatively, sensorless approaches can be implemented in which no wavefront sensor is present. In such a case, the system and sample aberrations are inferred by acquiring image measurements taken with small changes applied to the deformable mirror or adaptive electro-optic component. The orthogonal modes of sensorless approaches require no specialized hardware other than the adaptive component, and do not introduce the non-common path, and fit perfectly into the Zernike polynomial approach, where each mode is independently evaluated by the effect on the PSF. The difficulty in the sensorless approach is the time required to acquire the images and calculate the compensatory mirror voltages. This leads to unnecessary time that the sample is exposed to light and leads to photobleaching in stained samples. As previously mentioned, this is exacerbated by the depth and turbidity of the tissue.

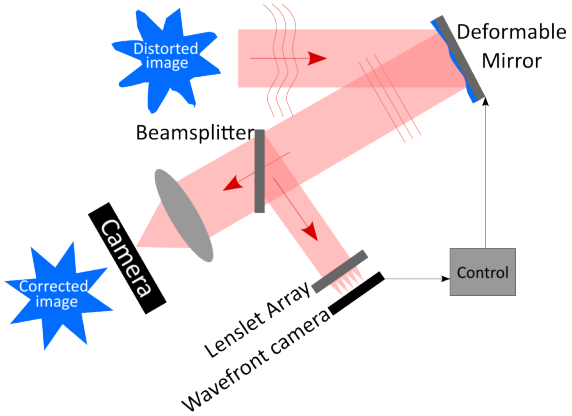

Figure 1.14: Adaptive optics integrated into a microscope system. The distorted wavefront is corrected by means of a deformable mirror after an unused wavelength is separated from the image path and imaged by a Shack-Hartmann wavefront sensor[74].

1.6.1 Aberration correction in super-resolution

Correcting low and high order aberrations increases the intensity of fluorescent signal as well as spatial resolution [75] and when combined with super resolution techniques such as SIM, very fine features of biological tissue can be studied.

As SIM is a super resolution technique well suited to in vivo imaging of cells with lateral resolution in the region of 120nm and can be run at high rates [76], making it an ideal candidate for enhancement by AO. In this combination the sample aberrations still play a significant role in the degree of improvement, but substantial improvements can be made [77]. Extending the super resolution technique to 2-photon applications has also seen remarkable improvement in resolution and up to 40-fold intensity [78].

In the case of ISM, the quality of the PSF plays a vital role in image formation and improving the quality will equally improve the contrast and resolution of these systems, but the combination remains untested in the field. It has been shown that due to the image formation technique in detector array configurations of ISM, information on the aberrations is being encoded into the image and from this information corrections can be conducted [79].

1.7 Scatter Correction

As imaging is extended to deeper tissue, the more scattering lengths exponentially reduce the number of photons that generate the excitation volume. Photons are scattered as they interact with the molecules within the sample, and those that are no longer reaching the focal volume can be divided into two categories, non-diffuse, and diffuse. Both contribute negatively to the loss of focal volume, as the photon density within the focal volume is reduced in both cases. The excitation and emission light are both subject to scattering, and in the case of emission, the non-diffuse photons that are collected have a negative impact on the signal-to-noise ratio (SNR). Where confocal microscopy rejects this out of focus light, other imaging modalities require more complex techniques to overcome scattering effects.

Manipulation of higher spatial frequency is necessary to compensate for these high order aberrations and scattering and with the advent of spatial light modulators (SLMs) and digital micromirrors (DMDs) scatter correction within tissue has become accessible to more researchers. The premise of scatter correction is that the position of specific rays within the excitation path can be manipulated in order to maximize the focal volume, and this can be achieved by means of phase [80], polarization[81] or binary modulation[82, 83]. Where SLMs manipulate the phase and amplitude of the wavefront, DMDs which can only switch individual segments on or off, are more often used in binary amplitude modulation. Although it is faster, binary amplitude modulation is less efficient than phase modulation [84]. We see this by expressing the emitted scalar field as:

$$u(r,t) = Re\{A(r)\exp[i(\varphi(r) - \omega t)]\} \tag{1.3}$$

where A specifies the amplitude and φ the spatially varying phase of the electric field. For any field $u(r,t)$ propagated from the focal spot through the scattering medium, some function $u' = (r,-t)$, the inverse function that retraces the scattering impact, exists. Because the constant phase within u must satisfy $\varphi(r) = \omega t$, then u' must satisfy $\varphi(r) = -\omega t$ so that we can reverse an arbitrary field u to the original focal spot [85]. Here we see how the amplitude and amplitude recovery impacts the field as a multiplicative component, whereas recovery of the phase impacts the field significantly.

Implementation of DMDs or other binary optical components to control the phase of wavefronts is achieved by means of Lee Holography [86] that can be setup to manipulate the phase in the range from 0 to 2π [87, 88], but comes at the cost of lower resolution (<1000 segments). In order to achieve this phase control using a DMD device that can only switch mirrors on or off, the amplitude signal must be filtered in the Fourier plane to obtain complex field modulation. The Lee method generates the amplitude pattern by:

$$f(x,y) = \frac{1}{2}[1 + cos(2\pi(x-y)v_0 - \varphi(x,y))] \tag{1.4}$$

which can also be written as:

$$f(x,y) = \frac{1}{2} + \frac{1}{4}e^{i2\pi(x-y)v_0}e^{-i\varphi(x,y)} + \frac{1}{4}e^{i2\pi(y-x)v_0}e^{i\varphi(x,y)} \tag{1.5}$$

Here there are three terms that have three center spatial frequencies $(v_x = 0, v_y = 0)$, $(x_x = v_0, v_0 = -v_0)$, and $(v_x = -v_0, v_y = v_0)$ [89]. Three orders of diffraction referred to as 0, $+1$, and -1 when v_0 i higher than the highest spatial frequency of $\varphi(x,y)$. Then the last component of the last term corresponds to the desired phase modulation tilted by an angle corresponding to the diffraction order. To select the specific term a 4-f system with an iris in the Fourier plane can be implemented.

With these conditions, the resulting field is $e^{i\varphi(x,y)}$. Because the DMDs are only capable of binary modulation, a binary amplitude hologram can be generated by thresholding as per:

$$g(x,y) = \begin{cases} 1 & \texttt{if} f(x,y) > \frac{1}{2} \\ 0 & otherwise \end{cases} \tag{1.6}$$

Ultimately, the phase of the desired field is encoded in $f(x, y)$. For a given spatial sampling, the approximation $g(x, y)$ for the binary amplitude modulation is less efficient, as the pattern is blurred by the square shape of the signal. To obtain an accurate approximation of the phase profile, sufficient oscillations inside a larger superpixel are required, which means a decrease in resolution [90].

Generally though, DMDs are used to correct scatter effects in binary modulation working on the principle of reducing the impact of segments contributing negatively to the electric field by switching those elements off. Sequential algorithms switch specific segments off and on while comparing the resulting electric field, which can be represented by E_m and where the vectorial sum of fields is maximized (Figure 1.15a,d), the state of the segment under test is maintained. The procedure continues through each of the segments in the active region of the device (Figure 1.15d,e and c,f) and ultimately each segment that contributes negatively to the total electric field is switched off [91].

Searches like the sequential algorithm can be optimized and numerous search options have been investigated, such as parallel searches [92] or genetic algorithm [87], but this type of search is well suited to machine learning methods such as particle swarm [83] or others.

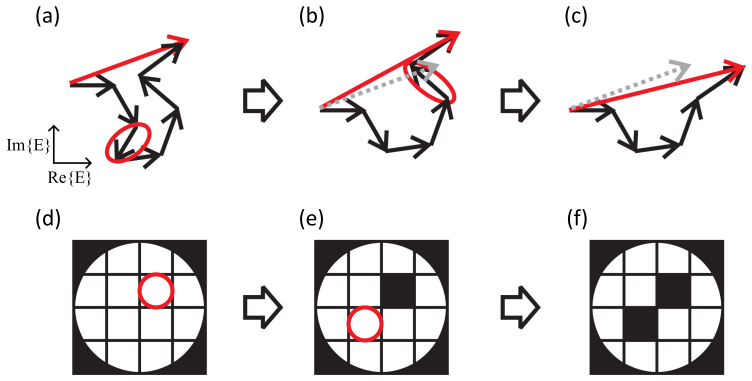

Figure 1.15: A graphical representation of the sequential algorithm for two segments. The black arrows represent the electric field of each input channel as they travel through the sample and the red arrow is the total electric field at the target output. In the first step, a segment which contributes negatively to the total amplitude is switched off (a,d) and the resulting red vector is increased (b). Another segment is identified to be switched off (b,d), and when the algorithm has completed, each of the segments that contributed negatively to the total field are switched off and the red vector is maximized (c,f). Directly from the manuscript [91]

Relevance of the ultimate optimized pattern projected onto the corrective device is highly dependent on the persistence time of the sample. For example, the persistence time of paint (TiO_2) is in the order of multiple hours, but the persistence time of living tissue ranges from minutes to milliseconds [93–95] due to blood flow and heartbeat [85]. In vivo studies that rely on scatter correction to achieve depths exceeding what is possible with conventional methods will then require rapid updates to compensate for the short persistence and relevance of the optimized manipulative pattern. Alternatively, the scattering components within the tissue that contribute most significantly to the distortion of the excitation light can be considered separately from those with the shortest persistence times.

1.8 Dissertation Overview

Now, armed with the basic understanding of microscopy modalities and where they are most appropriate, we can envision a path to imaging different types of biological samples. We also have the tools to evaluate and quantify images output by these systems to improve the quality of imaging in various aspects.

Our interests in examining the potency of mesenchymal stromal cells (MSCs) which are cultured in monolayers on transparent plastic containers, are well suited to DPC imaging. These samples are well suited to DPC as the technique can be used to image translucent cells without labeling, and provides sufficient resolution. In Chapter 2 a robust implementation of DPC was constructed and applied in differentiating MSCs.

Applications of 2-photon imaging were investigated in Chapter 3 where tissue slices of volumetric muscle loss were imaged to quantify fibrogenesis in cases where subcritical injuries result in large deposits of collagen. Imaging nanoparticles under various conditions was also conducted, where aberrations begin to play a role in degradation of image quality.

The primary aims of further work were to recover imaging quality within scatter tissues using a DMD to remove photons that contributed negatively to the intensity of the emitted light. As such aim 1A in Chapter 4 is scatter correction by binary wavefront correction using a genetic algorithm and intrinsic SHG deep within bone. Aim 1B in Chapter 4 is the combination of low order aberration correction and scatter correction to recover image quality deep within bone.

Finally, aim 2A is the reduction of scattering by implementing multi-photon, SHG, and THG imaging at longer wavelengths, and is discussed in Chapter 5

where aim 2B is the implementation of ISM super-resolution microscopy using an achromatic optical setup.

Chapter 2

Differential Phase Contrast

> "Most people have no concept of how an automatic transmission works, yet they know how to drive a car. You don't have to study physics to understand the laws of motion to drive a car. You don't have to understand any of this stuff to use Macintosh."
>
> — Steve Jobs

2.1 Introduction

Throughout the introduction (Chapter 1), the criteria for selection of microscopy techniques was discussed, based on the sample, the need to observe the sample without perturbation of function, and the requisite resolution. Each modality has its own set of advantages and disadvantages and weighing up these pros and cons will eventually lead to the elimination of some methods for specific use cases. Phase imaging microscopy aims to recover the optical path length (OPL) of a sample from amplitude (intensity) images. In most cases, this immediately eliminates opaque samples such as fixed tissues. Transparent samples such as cells are an ideal biological candidate for use with phase imaging, provided they are not excessively thick (hundreds of microns become untenable). Various phase imaging techniques have been used to image intra- and inter-cellular dynamics [96–98] with the first recorded imaging of cell division made using phase imaging.[24]

[24] Specific references for the recording by Dr. Kurt Michel are hard to come by, but reference is made to this recording on the Zeiss website.

Over the last decade, biomedical research has investigated the potential of mesenchymal stromal cells (MSCs) which are defined by the International Society for Cellular Therapy (ISCT) as cells having the capacity to differentiate to osteoblasts, adipocytes, and chondrocytes in vitro [99]. Additional properties of MSCs include their adherence to plastic under standard culture conditions, and specific phenotypes[25]. Use of MSCs in a variety of regenerative therapies has been proposed, and it is not always clear whether the cells differentiate into the targeted tissue or generate cell types that benefit the tissue [100]. However, MSCs from different tissue sources, donors, or expansion levels exhibit varying degrees of immunosuppressive response to IFN-γ. This heterogeneous functional response reduces therapeutic efficacy, thereby complicating their use in regenerative medicine and its causes are poorly understood [101, 102].

[25] ISCT specified phenotype of MSCs

Positive (≥ 95% +)	Negative (<2% +)
CD105	CD45
CD73	CD34
CD90	CD14 or CD11b
	CD79α or CD19
	HLA-DR

The current state of cell manufacturing processes at industrial scale requires improved efficiency in all aspects of the process. Of particular interest is insight into the potency of cell lines and the ability to apply interventions before investing time and resources into the culturing of MSCs. While chemical analysis of these cells can provide this insight, it is disruptive [103, 104]. One proposed method to reduce this disruption while retaining the ability to predict the potency of cells is by means of morphological analysis, whereby features such as the area, circumference or ellipticity of cells are input to algorithms to evaluate their potential against known superior performers.

These transparent cells, with the need for morphological feature analysis by computation form an intersection with the specific subset of phase imaging techniques known as quantitative phase imaging, which enables the computational analysis of phase images.

2.2 Differential Phase Contrast Microscopy

In general, quantitative phase imaging techniques require spatially coherent illumination such as interferometry [105], whereas phase contrast requires only an partially coherent illumination, which can be achieved through an asymmetric illumination pattern [106]. While reducing the complexity of the microscope setup, such techniques also provide twice the lateral resolution, improved optical sectioning, and the reduction of speckle noise [106]. In their novel approach to achieving quantitative phase using asymmetric illumination, Tian et al implement illumination side computational control [107], where homogenous intensity patterns are used to illuminate the sample at coded angles, all while considering the Fourier space, which they called differential phase contrast (DPC).

Phase information can be extracted from two intensity images when the sample has been illuminated at two opposite angles, call them I_L (left) and I_R (right). Computing the DPC image is then as simple as calculating the difference between the images:

$$I_{DPC} = \frac{(I_L - I_R)}{I_{tot}} \tag{2.1}$$

Here, $I_{tot} = I_L + I_R$ which is the brightfield image of the sample. When a thin amplitude object is in the focus of the imaging system, illuminating from the left or the right will not change the intensity, as a real object will have a symmetric Fourier transform. This means that the image calculated in I_{DPC} will contain no amplitude information, but when the OPL varies across the sample, features within the sample can cause slight changes in the propagation direction [108]. Then the difference between the differently illuminated images I_L and I_R contains some information regarding the phase gradient of the imaged object. The phase image is recovered by deconvolving the DPC image using the calculated transfer function.

In the initial application of their work, Tian et al used four simple components, (1) a 10× (0.25NA) objective lens, (2) a 100mm tube lens, (3) a CMOS camera, and (4) an LED array (with means to control the array) (Figure 2.1). With an existing upright microscopes, a few simple modifications can be implemented to apply this quantitative phase technique. As such, we looked to implement a similar setup, with the aim of furnishing the lab with a quantitative phase imaging tool that would allow for computational investigations of MSCs and their morphology.

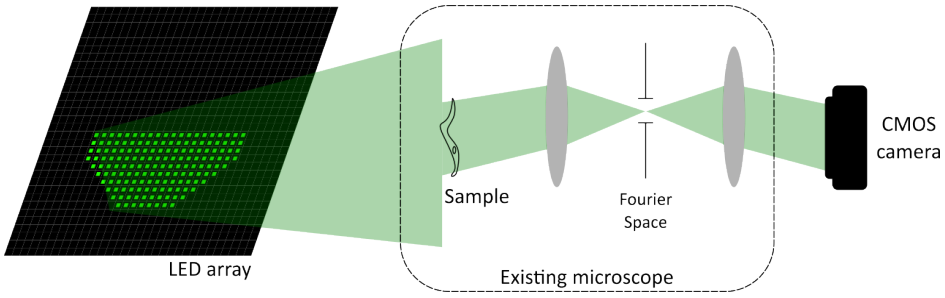

Figure 2.1: The basic setup of the DPC microscope integrated into an off the shelf upright microscope as per [106].

Once the physical setup is complete, control of the camera and LED array to capture the amplitude images at various angles is required. For rapid instrumentation of electrical devices and integration of numerous such devices, LabVIEW™ [26] is a visual programming language that is widely used for data

[26] LabVIEW stands for Laboratory Virtual Instrument Engineering Workbench.

acquisition, instrument control and industrial automation. Fortunately, most manufacturers of cameras and other such instruments provide LabVIEW drivers that can rapidly be integrated into larger setups, and the Andor Zyla 4.2 (ZYLA-4.2-2P-CL10) is no different. There are some difficulties in the installation of the camera drivers for the native Andor software, but with some struggling, the installation will be robust and useful within the LabVIEW environment.

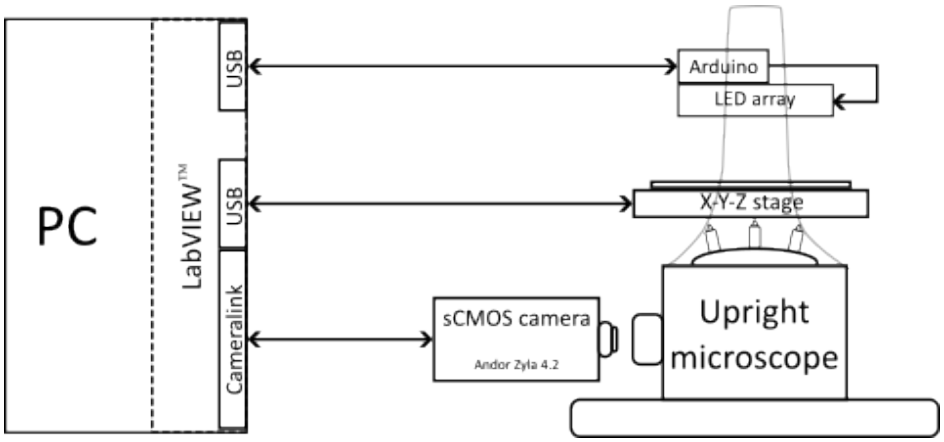

Figure 2.2: Block diagram of the electronic components integrated into the upright microscope.

LabVIEW provides the ability to communicate serially with devices properly equipped with RS232 or USB channels. The easiest method for integrating an Arduino® with a LabVIEW GUI is to write a complete communication protocol. Communications between each of the instruments is handled via the PC through LabVIEW, but an Arduino Uno is used to control the Adafruit LED array (Figure 2.2). Arduino's library requirements for easy communication with Adafruit devices are easily handled by the Arduino IDE app (installable through Microsoft® Windows app store), specifically for this setup, refer to appendix A for specifics regarding the Arduino libraries, A.1 for the inter-communications document (ICD), and the source code programmed onto the Arduino Uno A.2. No flow diagram is necessary for the communication between the Arduino and the LED array, as the Arduino simply responds to the LabVIEW instruction by setting the array according to the message received, for examples refer to table 2.1.

The wavelength of the illumination should be in the green range, centered at approximately 515nm [27]. The Adafruit array is set to illuminate at RGB value 0x000700 (R = 0x00, G = 0x07, B = 0x00). According to the datasheet of the LED array, one can set these values to 0x15, which adds an element of white light that increases the intensity while broadening the spectrum. According to

[27] Measured wavelength of the LED array

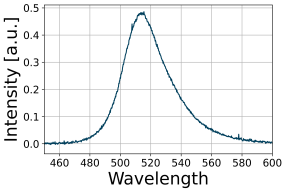

Table 2.1: Example serial message between LabVIEW and Arduino

Message to Arduino	Programmed behavior
`0x7C 01 08 00 07 07 07 15 15 15 66`	Turn on a circle of LEDs centered arou the pixel in the 7th row and 7th colum at full RGB, just the outline

www.academo.org this RGB value should result in a wavelength of 510nm, and 525nm corresponds to an RGB value of 0x4A0700, but the best results were achieved with RGB value 0x4A0700.

Tian et al. [106] also studied the importance of the coherence parameter σ which identifies all of the LEDs that generate illumination angles within the NA of the objective lens. In this context, $\sigma = \frac{NA_{illum}}{NA_{obj}}$, and selection of the radius of the half-circle is important, as images acquired with the most coherent illumination contain artifacts as a result of scattering of the out-of-plane objects. Higher σ values provide sufficient contrast for edge features, and the lower frequency spatial changes are also better captured. In our implementation, we use a 10× objective lens with an NA of 0.3, which allows us a theoretical resolution of approximately 430μm.

A graphical user interface (GUI) (Figure 2.3) was programmed to allow the user to change the destination of the saved images, setup automated features such as the movement of the stage to fixed positions covering a rectangular region, or observation of the brightfield image[28]. Resulting images are not phase images, but instead collections of the amplitude images from each of the four angles (top, bottom, left, right). The brightfield image is the summation of the various amplitude images (Figure 2.4), but reconstruction of the phase requires an algorithm, and we used the algorithm provided by the Waller lab in either Python® or Matlab®, and the edited Matlab code for this reconstruction can be found in appendix A.4.

[28] In the screenshots of the GUI, the fluorescence setup is also included and will be discussed later in this document.

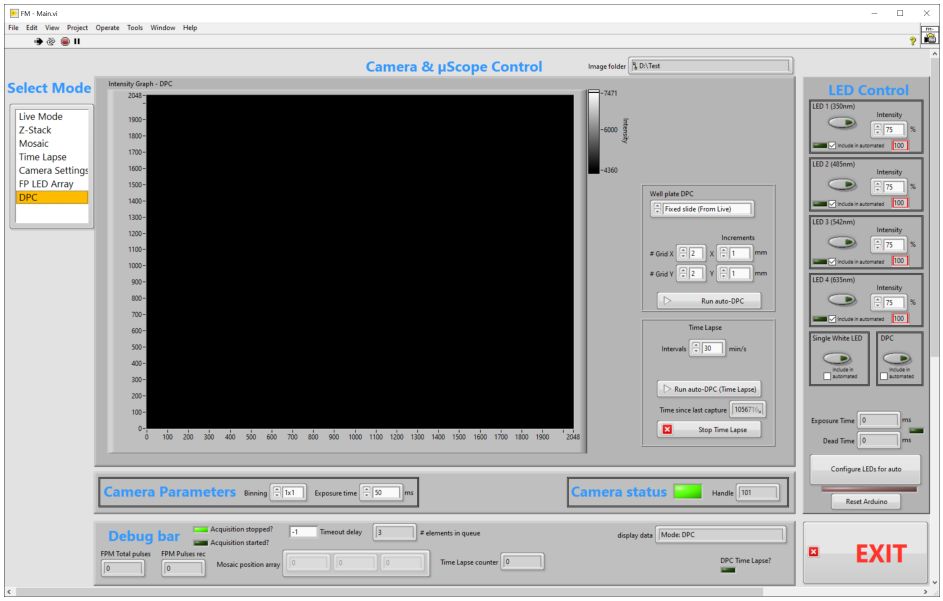

Figure 2.3: A screenshot of the user interface that enables DPC imaging. Options include exposure time setting and the ability to generate a grid of DPC images with definition of the grid dimensions as well as the step size between each DPC image capture.

A *tiff*[29] amplitude image file is recorded of each illumination angle as per 2.4, when summed, show that no phase information is recorded in the brightfield image. Once the reconstruction, using the Matlab [30], has been completed, the resulting DPC image is recorded in the folder on an equal level to the various angled images. The phase target (Quantitative Phase Target; $9911 - 2 - 1 - 4$, Benchmark Technologies) contains numerous features such as USAF target, focus star, "wedding cake", and fixed lines targets, ranging from 50nm to 350nm in height on a Corning eagle XG glass with a refractive index of 1.52. We found that while there were specks of dirt on the phase target the phase differences were measurable (Figure 2.4).

[29] TIFF files are generally used in scientific imaging, as the raw data is preserved. TIFF stands for Tag Image File Format and has a .tif or .tiff file extension.

[30] Matlab code for the reconstruction of image is recorded in appendix A.4

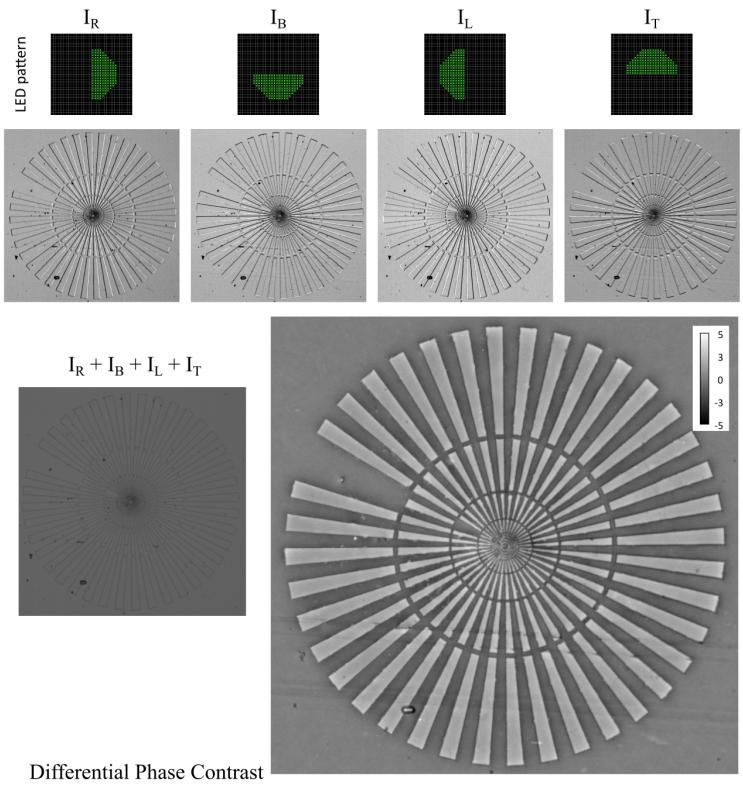

Figure 2.4: Resulting images from the four angles of illumination, the brightfield result of the summation, and the DPC result in pi radians. Star target component of the phase target at 350nm high features.

2.2.1 DPC artifact removal - Halo

Resulting DPC images closely resemble traditional phase images, especially in terms of one of the primary issues prevalent in phase imaging called the "halo" effect seen at the edges of sharp features. For the purposes of segmentation [109], this can be beneficial, but in truth, the negative phase that is shown is not real and obscures morphological features of the sample [110]. As per Kandel [111] the halo is caused by limitations in the spatial coherence of the illumination. In order to enable quantitative measurements of features within DPC images, they proposed a simple algorithm (Figure 2.5) to correct the low and high frequency data of the resulting images that restores the artifact-free DPC image.

Fast Fourier transforms (FFT) are a specific Hilbert transform that can be used on spatial images to express the image in terms of the spatial frequencies present therein. Low frequencies are at the origin and higher frequencies farther

away from the origin. By applying the filtering as specified by the algorithm, of $0°$, $45°$, and $90°$ the higher frequencies (fine details) are unaffected, while content impacted by the halo is subjected to a derivative combined with a signum function. The regions affected by the halo, and the angled filters, are defined by the variable $\frac{1}{L_c}$ which as per the original work can be configured for an imaging system (one value for L_c per objective lens). The value of L_c in our $10\times$ DPC system is set to 2μm.

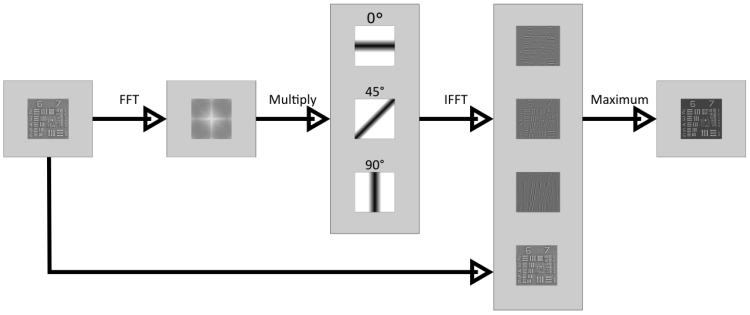

Figure 2.5: The direct algorithm to remove the halo artifacts from DPC images by filtering the k-space images at various angles and then selecting the maximum pixel values in image space between the filtered and original images. From the paper [111].

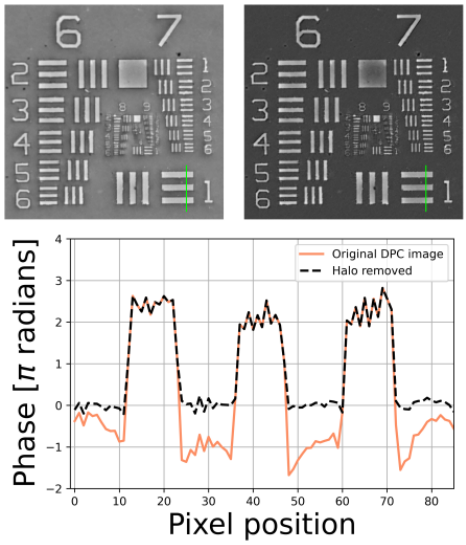

Figure 2.6: Cross sections of the original DPC image (top-left) and the halo-free DPC image (top-right) show that the maximum phase values are retained, while the extreme negative glow is removed. Cross sections taken from identical positions.

[31] Reconstruction times using the Matlab script require approximately 6 seconds with the PC hardware used at the time.

While the DPC image generation is not done in real-time with the current computational shortcomings [31], the filtering and removal of halo artifacts is not computationally intensive and would the DPC images be generated in real-time, the halo removal algorithm could be switched on or off and executed in real-time.

Imaging of a USAF target with halos removed shows how the negative phase is corrected, while the positive phase is retained (Figure 2.6). Once the images have been reconstructed the halo can be removed using a Python script (Appendix A.5).

2.2.2 DPC artifact removal - Banding

Another artifact that is apparent in the resulting DPC images is that certain bands of "grey" appear, especially when shorter exposure times are used for the sub-image capture (Figure 2.7a). In the original publication describing the use of an LED array to drive DPC imaging from the Waller lab [106], images with similar banding are presented but the causes are not discussed. For the sake of power efficiency LEDs are most often driven by pulse width modulation (PWM), where a square wave of electric power switches the LEDs on and off periodically at specific duty cycles. Higher duty cycles drive the LED to be brighter, and lower duty cycles less bright. Clearly this application of PWM can impact imaging at high frequency, but the PWM frequencies of these LEDs is much higher than the 50ms (20Hz) minimum exposure time implemented in the DPC imaging. Another feature of LEDs and LED arrays is the update/refresh rate. For the specific 32×32 LED array that we integrated into the system, a $\frac{1}{8}$ update rate or scan is implemented, where the array is divided into four sections ($\frac{32}{8} = 4$). The array updates one row at a time at a much lower frequency than the PWM, and that introduces the banding effect into our DPC images (Figure 2.7b). By extracting the low frequency sinusoidal pattern within the cross section of the DPC image, a Fourier filter can be applied to remove the banding and make the stitching of multiple images more consistent (Figure 2.7d).

Similarly to the scan generation of banding is the rolling shutter that is implemented by default in the Zyla 4.2 sCMOS camera. Here, the detector is divided into two halves, a top and a bottom. Exposures begin in the middle, where the detector is divided, and each row of pixels activated until each of the rows has begun collecting photons. Then the readout and deactivation of rows follows the same "rolling" pattern (Figure 2.7c). When both the illumination and collection are being scanned, any phase mismatch will result in banding artifacts. An alternative to this shutter mechanism is the global shutter sequence where

the whole detector is enabled and disabled simultaneously. Such a sequence removes the need for synchronization of the camera to the illumination source. For the purposes of our implementation, the rolling shutter is the default and not changed to the global shutter sequence, as timing between exposure start and end is less than 1ms, so when operating the system at hundreds of milliseconds of exposure time, the rolling shutter effect should not impact imaging.

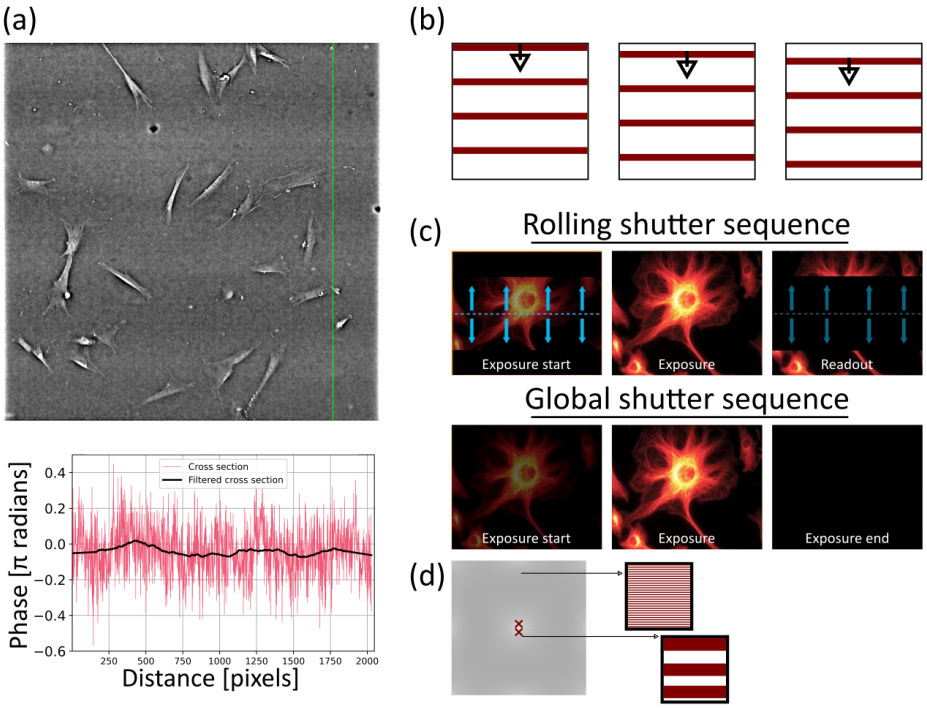

Figure 2.7: (a) A DPC image of MSCs acquired with exposure time of each sub-image being 400ms. The cross section of the green line below (in red), and the smoothed cross section (in black). (b) LED arrays employ a scan to update the LEDs as per the current settings at a rate of $\frac{1}{8}$. For the LED array in our system, that is dividing the array into four sections. (c) CMOS cameras can be set to use either a rolling or a global shutter. Our Andor camera presents these figures in the manual illustrating that in severe cases, using the rolling shutter can put something like a scan effect into images. (d) Higher frequencies create narrow bands and lower frequencies thicker bands within k-space of images that can be filtered out if identified (x's marked).

2.2.3 Quantification of DPC images

As previously discussed, the optical path length of the sample defines the degree to which the illumination light is retarded. This optical path length can then be used to calculate the height of the features within the image.

Using the phase values φ returned by the reconstruction algorithm in section 2.2, the calculation of the optical path length is:

$$OPL = \frac{\varphi\lambda}{2\pi} \tag{2.2}$$

where λ is the wavelength of the illumination. Once the OPL is known, the height of the feature can be calculated by:

$$Height = \frac{OPL}{RI} \tag{2.3}$$

where RI is the refractive index of the sample. In the case of our phase target, the refractive index is a known, as is the height of the feature, as they were measured using atomic force microscopy (AFM).

To confirm the quantification of DPC images, the USAF targets on the phase target were imaged and the OPL ground truth plotted against the measured phase and the derived feature height (Figure 2.8). Within the phase target, various feature heights are available, ranging from the lowest 50nm features to the highest 350nm features. Phase measurements and the calculated feature heights drift as the feature height increases, which we see when considering the lowest features, as the drift becomes less pronounced as the feature heights increase. Monolayers of plastic adherent cells are expected to be orders of magnitude thicker than the hundreds of nanometers of the phase target, ranging from 5μm to 50μm [112], and as such a calibration factor for the feature height calculations can be introduced in the case of thicker samples should known heights be available for micron scale features.

In the case of machine learning, the accuracy of feature height is not paramount, provided consistency of measurements across a monolayer of cells, meaning that the machine learning is applied to images acquired using an identical system. As such, even without a calibration factor, the DPC image acquired with this system can be used in a variety of algorithms to classify cells.

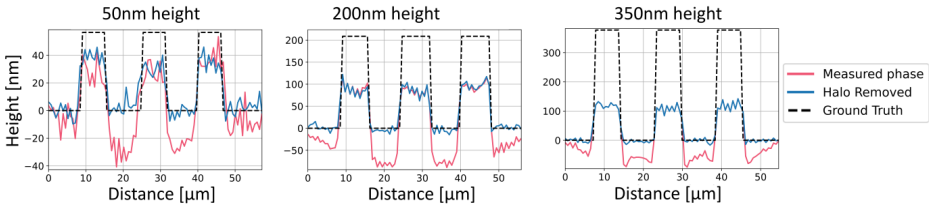

Figure 2.8: Comparing the measured optical path length of the phase target against the known feature heights.

2.3 Fluorescence Microscopy - Integrated into upright microscope

Within the same chassis used for the DPC imaging, a basic fluorescence microscope was also implemented. As per the original works describing the DPC using an LED array, the LED array illuminates samples from above in the upright microscope [107]. By making a few small changes to the illumination path of the chassis, new illumination can be input to the back port of the microscope. Each of the four LEDs specified have a BNC connector that enables intensity control via an analog voltage (Figure 2.9).

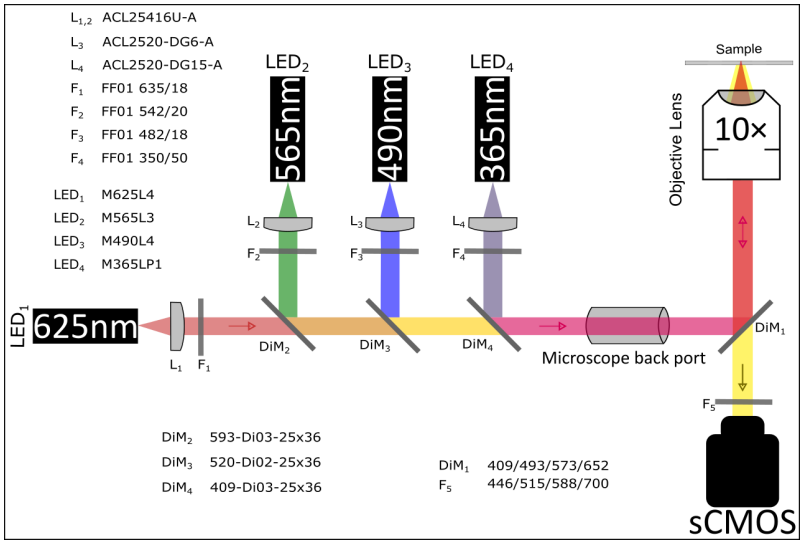

Figure 2.9: Optical schematic diagram of the fluorescence components used to construct the single-photon microscope including four high intensity LEDs, appropriate filters and dichroic mirrors.

Programmatic control of the electronic components is achieved through LabVIEW and an Arduino Uno, with wiring instructions presented (Figure B.1) in the appendix B.1. This Arduino is separate from the Arduino used to control the LED array illuminating the DPC images. Once again, LabVIEW communications are executed via the GUI and the analog voltages controlled by the Arduino and MCP4728 (Adafruit) set the intensity of the specific LEDs individually.[32] Intercommunication specification is described in appendix B.2, and the Arduino code used for this Arduino is listed in appendix B.3.

[32] Refer to Figure 2.3 where control elements of the individual LED intensities are visible on the right-hand side of the GUI.

It is important to note that for the GUI to operate properly, that both Arduinos need to be active, as the GUI enables fluorescence and DPC imaging simultaneously. Additionally, the Andor camera and stage need to be turned on and plugged in, else the GUI will return an error. The stage can be manually controlled via the joystick, or via the GUI, and once a position is found for either fluorescence or DPC imaging, mosaicing can be set up and the completion thereof automated.[33]

[33] Or in fact DPC and fluorescence serially, all automated to output fluorescence and DPC images into the same folder.

2.4 DPC Applications

Among the works that the DPC imaging has been used for, within our research, the primary application is label free imaging and characterization of cell morphology. It has been shown that the morphological features of MSCs can be used to predict their potency [113] and a label free technique would be especially useful in large scale manufacturing of cells. Traditional methods of characterizing MSC morphology requires staining of the cytoskeleton, and perhaps contextual assistance by means of nuclear stains, so that fixation of cells is required. This terminal sample preparation means that efficiency of cell culture is reduced. Further, it means that during cell culture in industrial settings, there will be a delay between measurement of cell potency and affecting appropriate change to recover expected culture in cases where the potency is deemed inferior. In future industrial implementations of cell manufacturing, DPC imaging could be continuously used to monitor incubation. This option to image these cells by means of a label free modality such as DPC in an environment that allows for live cell imaging will lead to more efficient cell manufacturing and the ability to react immediately to any culture issues that may arise.

Within our team, the DPC imaging has been used to investigate MSC morphology with respect to several cellular characteristics, such as the lipidomic profile associated with morphology and potency, the extra-cellular deposition of differentiated MSCs, and the interaction of MSCs with T-cells. To, this end T-cells were introduced to a monolayer culture of MSCs and imaged over a pe-

riod of 12-16 hours. The cells were maintained using a temperature controlled stage, appropriately mixed air supply, humidity, and media. DPC images were acquired at an interval of 30minutes and a video of these cells shows how the MSCs interact with T-cells (Figure 2.10). We found that over the 14 hours T cells often aggregated and then MSCs reached out to ingest the aggregated T cells (Figure 2.10a-d; yellow highlight). In other regions MSCs aggregated and over time removed T cells nearest them. Over numerous such investigations, the MSCs seem to stretch out to interact with T cells but retract within a short period (perhaps one hour).

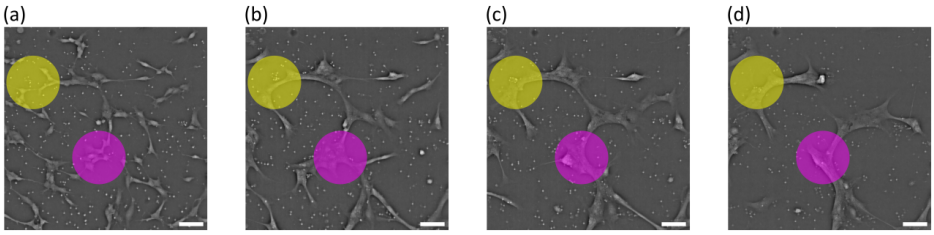

Figure 2.10: MSCs interact with T cells seemingly ingesting T cells over time the T cells aggregate (yellow highlight; a-b) and then MSCs reach out to interact with them (yellow highlight; c-d). In some cases that MSCs aggregate and eliminate T cells in their immediate vicinity (purple highlight, a-d). Scale bar is 25μm.

In another study within our lab using the DPC imaging, the phenotypic information extracted by the phase images was used to evaluate the differences in cells treated by known agents that affect the immune regulation of MSCs [114]. Here, certain phenotypic features were identified using DPC and correlated to the single cell lipidome obtained using MALDI-MSI. Whole-well DPC images were acquired, stitched together and co-registered with the MALDI acquired images to associate the datasets correctly (Figure 2.11).[34] Ultimately, cells stimulated by IFN-γ could be differentiated from unstimulated cells by a principal component analysis, confirming morphological changes previously found in similar investigations [113].

[34] Achieved using a combination of CellProfiler and ImageJ.

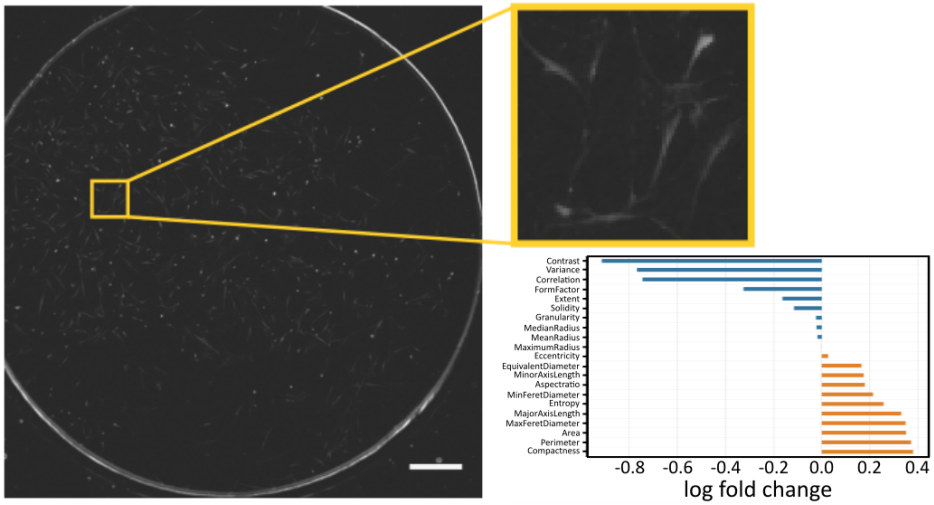

Figure 2.11: DPC image of an 8mm silicon well populated with IFN-γ stimulated MSCs collected by raster scanning of the motorized stage in steps of 1.6mm. Scale bar is 1mm. CellProfiler™ output of morphological features of the segmented DPC image of cells.

Similarly, DPC imaging was used to investigate the process by which MSCs differentiate into osteocytes, and the minerals that they deposit. Longitudinal investigations across four weeks were executed, with DPC imaging of whole-wells each week, comparing the mineralization of various cell-lines. Replicates of the cell-lines were also stained using alizarin red which is widely used to detect the presence of calcium deposits in tissue. These were imaged using a color microscope to evaluate the red and confirmed that older samples contained more red, corresponding to more calcium deposits.[35] DPC images for the various time points were examined by a gray-level co-occurrence matrix (GLCM) [40] to determine if any secondary features of the GLCM when input to a neural network would enable the accurate classification of the samples. Outputs of the GLCM show a trend of decreasing energy over the first two weeks, but oddly, the energy of weeks three and four see higher energy (Figure 2.12a). This can be explained by the the calcium deposits reaching confluence across the Petri dish and filling out gaps that may have been present in prior weeks. In the beginning, there is low, homogenous phase change across the regions of the dish where cells are not present. As the cells deposit calcium, gaps appear around the deposits and the phase changes more variably across the surface (Figure 2.12b). A point is reached where the calcium deposits fill in these gaps and the phase changes are

[35] Matlab was used to extract the RGB data and compare levels of red hue.

limited once again (Figure 2.12c). The GLCM simply measures features such as energy and does not differentiate between a low and high phase where changing features are not present.

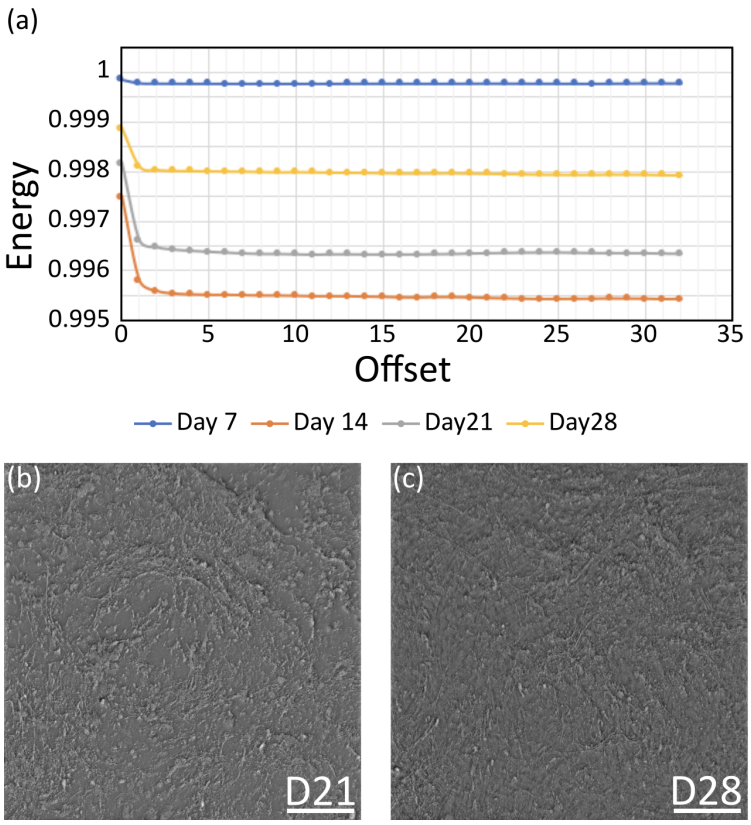

Figure 2.12: GLCM measured at numerous pixel offset values ($0 - 32$) and the measured energy at four time points. Day 7 shows the highest energy while day 14 shows the lowest (a). The reduction in energy after day 14 can be attributed to mineralization which produces strong features (b) but at day 28 the mineralization fills in the gaps and features are less pronounced (c). Scale bar is 250μm.

2.5 Discussion

Due to the ubiquity of digital image processing in modern microscopy, the quantitative nature and relatively low cost associated with DPC, we decided to implement DPC in an existing upright microscope. This allowed us to observe cells over longer periods of time and to analyze the images using computational methods.

For the sake of future work analyzing morphological features of cells, the DPC imaging built into our microscope is effective, and the adaptation of an existing upright microscope was cheap and relatively simple. Some imaging artifacts are introduced by the cheap LED array but can be removed by FFT filtering techniques. Other, more traditional artifacts, called halos, are also present, but modern hardware enables the real-time correction of these halos so that the DPC quantification can be used in classification techniques such as neural networks.

Additionally, single-photon fluorescence imaging is built into the upright microscope and the GUI. Four channels are available, but importantly the automation of the fluorescence imaging, such as time-lapses, Z-stacks or mosaicing (stitching) is available. The custom GUI allows users to set the exposure time of the camera to extract more signal in cases of low fluorescence, which is applied to each of the time-lapse, Z-stack or mosaicing modes. Users can set large regions to be scanned by the automated microscope stage by defining the step-size to move between each sub-image acquisition.

DPC imaging also allows the user to do time-lapse and mosaiced imaging, which is ideal for investigations of live cells over long periods of time, up to multiple days.

While all of these modes are available, the methodology and technicalities are obscured from the user, giving them a powerful, effective, yet simple tool to use in the lab.

Chapter 3

Multi-Photon Imaging

3.1 Introduction

As briefly discussed in the introduction chapter (Chapter 1), the benefits of multi-photon microscopy arising from the reduced focal volume include lower intensity from out-of-focus light, intrinsic optical sectioning, and deeper penetration into biological tissue. While the theoretical concepts of 2-photon excitation are relatively old, they only became practical reality as high power excitation sources were realized, so over the last 30+ years, a solid theoretical and experimental background exists.

When excited appropriately, the illuminated molecule will relax, returning to the electrical ground state, and in this process, release a photon of lower energy (longer wavelength) (Figure 3.1).

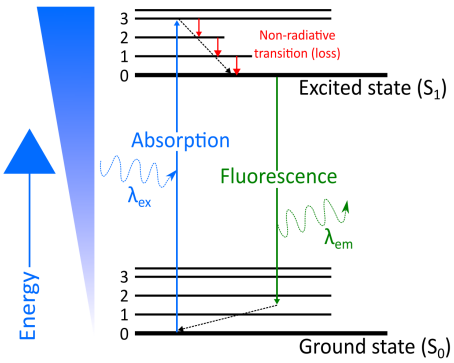

Figure 3.1: The Jablonski diagram of absorbance. The blue lines represent the two photons absorbed and the green line the relaxation from the singlet state S_1 to S_0.

The intensity and frequency of the excitation and emission light are dependent on the properties of the molecules in question as per [115]:

$$S_0 + hv_{ex} = S_1 \tag{3.1}$$

where h_v is the photon's energy, h is Planck's constant, v_{ex} is the frequency of the excitation light, S_0 is the ground state of the fluorophore, and S_1 is the excited state.

Efficiency of this process varies across molecules, and is defines as Φ, a value from $0-1$, with 1.0 being maximum efficiency (also known as quantum yield) and is simply:

$$\Phi = \frac{n_e}{n_a} \tag{3.2}$$

where n_e and n_a are the number of emitted and absorbed photons respectively. Another definition of quantum yield is defined by using the decay rates of the excited states as:

$$\Phi = \frac{k_f}{\sum_i k_i} \tag{3.3}$$

where k_f is the rate of spontaneous emission and is divided by the sum of all rates of the excited decay.

Considering the efficiency of fluorescence in these terms leads one to consider the fluorescence lifetime, which is the average time that molecules stay in their excited state before emitting a photon, which follows:

$$[S_1] = [S_0]_0 e^{-t/\tau} \tag{3.4}$$

where $[S_1]$ is the concentration of excited molecules at time t, $[S_0]$ is the initial concentration and τ is the decay rate, and instance of exponential decay.

With modern instruments, the lifetime of fluorescent samples can be measured, and used to create images of cells and tissues in a method known as fluorescence lifetime imaging (FLIM)[116]. With the emergence of more cost-effective single photon avalanche diode (SPAD) detectors, time-correlated single-photon counting (TCSPC) devices have made FLIM imaging popular. As the single photon counting requires a large statistical model on which to base FLIM values, imaging in this modality requires long measurement times [117], but for the purposes of intensity based fluorescence imaging, this fluorescence lifetime is not critical. Fluorescence intensity I_f is proportional to the amount of light absorbed, and the quantum yield Φ as per:

$$I_f = kI_0\Phi[1 - (10^{-\epsilon bc})] \tag{3.5}$$

here, k is a proportionality constant based on the specific instrument, I_0 is the intensity of the excitation light, ϵ is the molar absorptivity, b the path length, c is the concentration of the fluorescent substrate.

2-photon excitation is the result of absorption of two photons as they arrive simultaneously at a molecule, [36] with the requisite energy to excite the specific fluorescent molecule. Due to this requirement, fluorescence emission intensity varies with the square of the excitation intensity, but the number of photons required to elicit this phenomenon is in the range of one million times that required by single photon absorption. A benefit of this non-linear relationship is that multi-photon fluorescence offers implicit optical sectioning, generating much less out of focus emission.[37]

[36] In this context simultaneously means within an interval of approximately 10^{-18} seconds.

This intensity is the crux of image formation, and the instruments used to collect these emitted photons define the required methods of image construction. Once of the most common photon collection instruments is a photonmultiplier tube (PMT), which multiplies the current produced by incident light in multiple stages, and at gains of up to 160dB (100 million times) enable photon detection even in cases of extremely low emission flux. PMTs have a very high frequency response which enables high speed imaging, but when used in fluorescence imaging, their low noise and high gain characteristics are the primary reason to use them in low light environments.

[37] The famous image here shows the difference between single- and 2-photon emission, from [118].

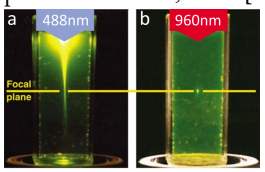

(a) is the single-photon, and (b) the 2-photon emission of Fluorescein by 488nm (a) and 960nm (b).

Creating whole images of specific regions of interest requires scanning the focal volume across a sample, and with reflectors attached to galvanometers this can be achieved at relatively high speeds, with synchronization of two scanning galvos, slow and fast axes, the single voltage (translated from the current output from the PMT) measured at each scan position can be used to form an image. Where in confocal (single photon) fluorescence microscopy, the emitted light follows the excitation path, striking the galvos, and passing through the pinhole. When using multi-photon, this "descanned" geometry is no longer required, and the PMT can be placed as close to the collecting objective lens as makes sense.[38] This configuration optimizes photon collection by reducing the path length, optical element count and enables the collection of more scattered photons, essential for maximum depth penetration.

[38] The emitted light could also be collected without passing through the objective, useful for thin samples.

3.2 Microscope Setup

Our home-built 2-photon system employs output from the Ti:Sapphire laser can be adjusted between 680 and 1080nm[39] (Figure 3.2). With a repetition rate of 80MHz, the 3W average power translates to 37.5nJ of pulse energy, which is significantly impacted by system losses so that power at the sample is reduced

[39] Maximum average power is output at 680nm and decreases as the wavelength is tuned upward.

to a maximum of approximately 600mW average power and approximately 7.5nJ of pulse energy. Cumulative losses arise from transmission of specific wavelengths through lenses where portions of the energy are absorbed by the materials, resulting in the need for dielectric anti-reflective coatings to be applied to glass lenses. These coatings are also necessary on reflective surfaces in optical setups, and with upwards of ten glass lenses in the beam path, the impact of 90% transmission compounds and eventually, the input 3W is reduced to approximately 600mW (Figure 3.3).

Power input to the optical path is controlled by means of a half-wave plate followed by a polarized beam splitter (PBS) before the beam is "cleaned" again by being passed through a 100μm pinhole.[40] Conjugate to the back-pupil plane (BPP) is a deformable mirror (DM), the merits of which will be discussed in subsequent chapters, but in short, corrects the wavefront to counteract aberrations caused by the system or the sample. Numerous optical relays act as $4f$ components to magnify the beam and overfill the back aperture of the objective lens to maximize the high NA.[41] The beam is then passed through a galvo/resonant scanner combination device, the scan and tube lenses, and finally through the objective lens to the sample.

[40] Profiling the output of the pinhole results in the spot below.

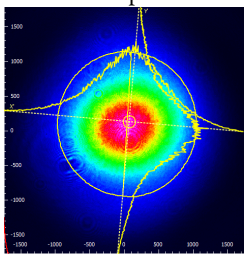

[41] Multiple $4f$ systems will certainly contribute to system aberrations and some correction of these aberrations is required.

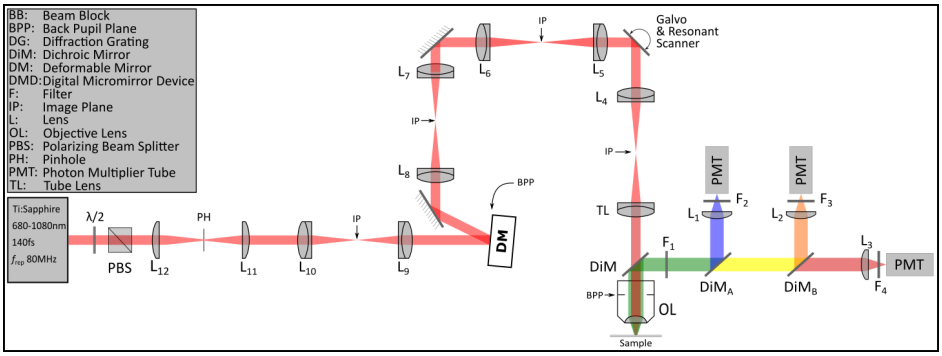

Figure 3.2: Optical schematic diagram of the home-built 2-Photon microscope.

In this epi-direction collection configuration, the emitted light is collected by the objective lens and emission wavelengths are picked off by a dichroic mirror right above the objective lens. Further dichroic mirrors pick-off shorter wavelengths and notch filters are used to accurately tune imaging to specific ranges. Photon multiplier tubes (PMT), single photon cameras, collect the emitted light and convert the photons to electrical current (Parts list of these components can be found in appendix C.1).

Photons collected by the PMTs cause a current to flow at the output of the PMT, which can be converted to a voltage through a transimpedance amplifier

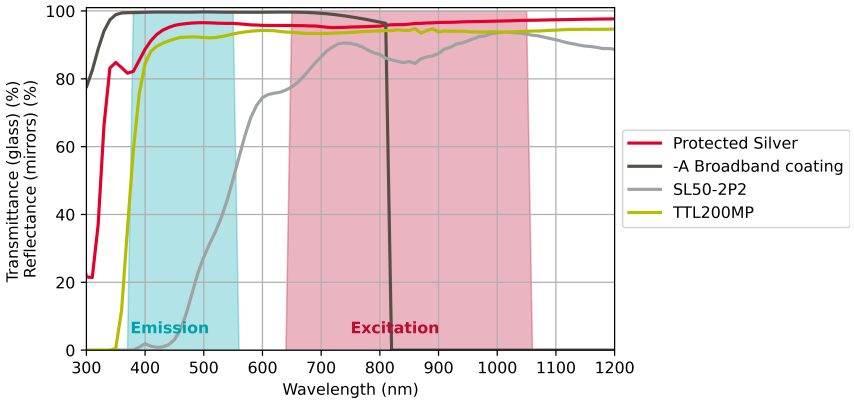

Figure 3.3: Transmission (glass lenses) and reflectance (mirrors) as a percentage specified by Thorlabs for the specific components utilized in the optical path. The scan lens accounts for the most loss in the excitation path, but the tube and scan lenses are not in the emission path.

(TIA). This voltage is then sampled by a high frequency DAQ (digital acquisition) device that samples at rates exceeding 100MHz. Electronic control of the microscope is configured and executed by scanimage [119], a commercially available Matlab based application which synchronizes the galvo and resonant scanners to the PMT signal, reconstructing the image accordingly.

3.3 Applications

By implementing this 2-photon modality and the support that it provides in labeled and label free contexts enabled the investigation of numerous studies where high specificity and resolution can extract information from samples that would not be possible in other more easily available imaging.

3.3.1 VML Imaging

In the field of regenerative medicine, investigations into the body's ability to recover from injuries and attempts to discover therapies that can aid recovery remain a challenge. Volumetric muscle loss (VML) results in non-recoverable loss of muscle fibers that leads to chronic functional impairment of soft tissue [120]. The mechanisms underlying the immune response to muscle damage are not fully understood, and understanding the processes requires a broad

approach. In a collaboration with investigators from the Georgia Institute of Technology, who had identified that these critical VMLs resulted in the long-term presence of M2-like macrophages and fibroadipogenic progenitors (FAP), we used our multi-photon microscope to image and quantify the ratio of these macrophages and FAPs to collagen [121].

Three groups of murine quadriceps muscle tissue sections (10μm thick) were examined to quantify the number of FAPs (stained with CD206) and M2-like macrophages (stained with PDGFRα) to relative collagen content (label-free SHG). Uninjured muscles were used as the control, while subcritical and critical VMLs were expected to exhibit fibrogenesis.[42]

[42] 2mm biopsy punches were used to generate subcritical injuries, while 3mm punches were used for critical injuries. This was based on previous work that identified 3mm as a critical injury incapable of myofiber regeneration in mice [122].

To quantify the collagen visible within the 80×80μm images, a normalization of each image within the dataset was undertaken, so that the images were directly comparable. Using the Otsu thresholding built into ImageJ, a binary mask of the SHG channel was acquired, and the mean value of the mask was used to attribute an SHG value to each image. Individual M2s and FAPs were counted within each image and the ratio of FAPs/collagen and M2s/collagen recorded.

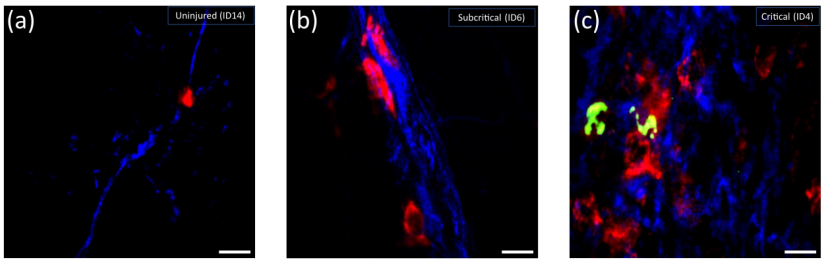

Figure 3.4: 2-Photon imaging of the FAPs (green), M2s (red) and collagen (SHG, blue). The uninjured muscle (a) presents very little collagen, whereas the subcritical (b) and critical (c) VMLs show much more collagen, as well as M2s and FAPs. Scale bar is 10μm.

Uninjured tissue did not result in many M2-like macrophages or FAPs near to collagen fibrils (Figure 3.4a), while in the case of critical VML, they do appear to co-localize in regions of collagen deposition (Figure 3.4c). Fewer FAPs and M2s were present in the subcritical injured samples than in the critical, which showed a significant difference compared to the uninjured muscle (Figure 3.5).

These means of quantification aided in elucidating key immune cellular factors that contribute to fibrosis within injured muscle, and lead to an inability to repair tissues and the cellular and molecular level.

Due to the nature of the thin tissue sections, the long excitation wavelengths used, sample aberrations do not critically impact imaging quality. System aber-

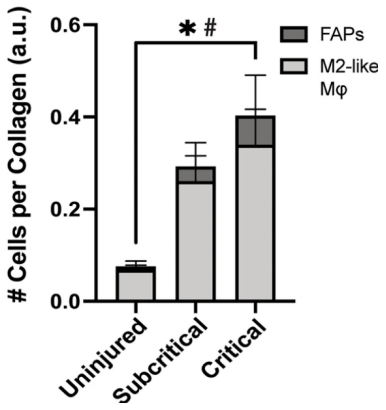

Figure 3.5: M2 (light gray) and FAP (dark gray) per detected collagen within the injury site imaged. One-way ANOVA with repeated measures two-way ANOVA with Fisher's LSD test. $^{*}p < 0.05$ for M2s per collagen and $\#p < 0.05$ for FAPs per collagen.

rations contribute more significantly to the degradation of the PSF and were corrected using the deformable mirror [123].

3.3.2 Imaging of Nanoparticles

Fluorescence imaging provides a means for visualization, identification and quantification within biological systems. As material science enabled higher power means of excitation, it also enables integration of synthetic methods with a reduction to nanoscale, and a class of optical reporters known as quantum dots. Quantum dot nanocrystals provide an alternative to conventional organic dyes and fluorescent proteins, but offer more stability against photobleaching [124]. These probes should be selective for the specific target, have low toxicity for the host organism and have excellent fluorescent properties that allow for visualization of the probe's localization and distribution at relevant tissue depths [125].

3.3.3 2-Photon imaging of nanoparticles

In a collaboration with members of the biophysics department at the University of Toledo, who synthesized perovskite nanocrystals, we characterized their nanoparticles to assess their potential as deep tissue fluorescent probes [126]. Characterization of the nanoparticles required an array of experiments, beginning with measuring the emission intensity based on the concentration of the diluted nanoparticles. A dried pellet of the nanoparticles was dispersed in 1mL of DMSO (dimethyl sulfoxide) and sonicated for even distribution. Various concentrations of the solution were then prepared and evaluated. For each concentration, a 75μL volume was placed into an 8mm reusable silicon gasket sandwiched between a coverslip and microscope slide. This sample was then imaged using an excitation power of 20mW average power. Intensity as measured by the PMTs showed very low emission at low concentrations ($180 - 250\mu$M), but steadily increased as the concentration was increased beyond 400μM, and the limit of detection was calculated as 163μM (Figure 3.6).

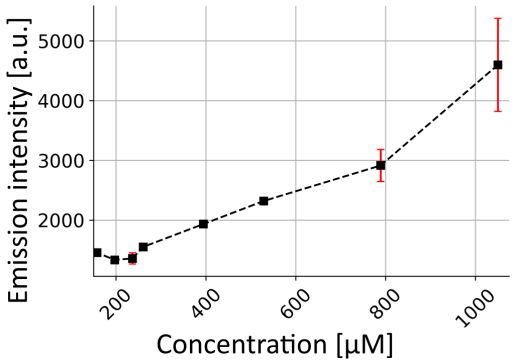

Figure 3.6: 2-photon emission of perovskite nanoparticles in solution at various concentrations. Error bars are standard error.

As the application of these nanoparticles is imaging within scattering tissue samples, some phantom diffusers were employed and the intensity of the emission compared across a range of scattering lengths from ℓ_s= 0.052μm^{-1} to ℓ_s= 0.156μm^{-1}. This was achieved my applying translucent adhesive tape across the various concentrations of nanoparticle solutions. As a final measure of the emission through a scattering medium in vitro, the samples were situated beneath a murine cranial plate. As expected, emission intensity was reduced as the scattering coefficient was increased, with the biological tissue showing the most significant reduction of intensity (Figure 3.7a). To present the measurements equally, each intensity was matched to the lowest emission intensity at 4mW excitation power. Here we can see that while the resulting emission is not related to the square of the excitation, it is not linear and cannot be single-photon emission. We also see that in an equalized representation, imaging through the cranial tissue sample follows the squared power law more closely than the other cases (Figure 3.7b). This could be due to any number of small differences that impact imaging done over the period of a few hours, such as photobleaching, sample movement, or even heterogenous scattering within the cranial tissue.

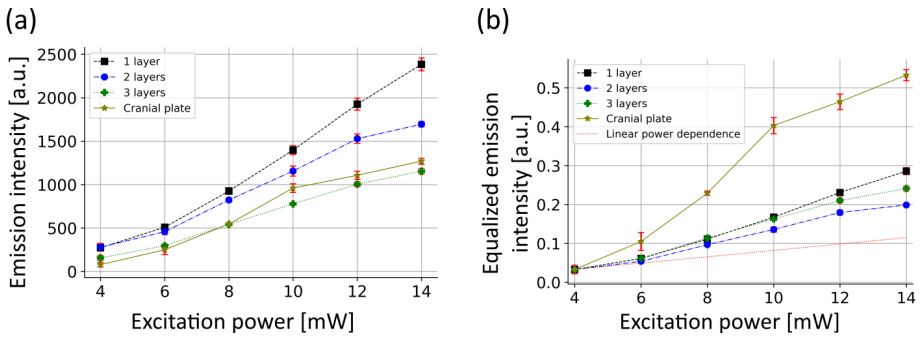

Figure 3.7: 2-photon emission of perovskite nanoparticles in solution at various concentrations. Error bars are standard error.

Progressing towards in vivo imaging of nanoparticles, imaging of perovskite nanoparticles in solution (a concentration of 780μm in DMSO) through brain tissue was conducted. Here, narrow capillary tubes (5μL) were used to pull up a small volume of the solution and then placed at approximately 20° inside a freshly excised murine brain (Figure 3.8c,d). A direct comparison between the silicon protected ($C_sPbBr_3@SiO_2$) and unprotected (C_sPbBr_3) nanoparticles dispersed in toluene showed that the protected nanoparticles remain stable over a relevant time period,[43] and fluoresced brightly at depths exceeding 200μm (Figure 3.8a), while the unprotected nanoparticles lost the ability to fluoresce effectively (Figure 3.8b).

[43] At least long enough to prepare the solution, draw it into the capillary tube, find the sample in the imaging program, and acquire the images. At least one hour.

With confirmation that the nanoparticles provide sufficient emission through scattering tissue, we conducted an experiment inside a living sample. MSCs were cultured and prepared beforehand, co-labeled with Hoechst 33342 to show cell nuclei, and then incubated for a period of one hour along with protected nanoparticles. Once the MSCs had taken up the nanoparticles, a concentration of 1.2 million cells per milli-liter was taken up into a 100μL volume of 0.9% saline solution and injected into the ear of an anesthetized mouse by means of an intra-dermal injection. The ear was shaved and lightly secured between a microscope and a coverslip. Glycerol was used to create a more homogenous refractive index within the sample and aided in keeping the ear flat. Such a high concentration of cells and nanoparticles meant that we expected to find emission throughout the area of the injection. Scanned images of MSCs reveal successful uptake of nanoparticles (green in Figure 3.9) surrounding nuclei (cyan in Figure 3.9).[44]

[44] The red arrow in Figure 3.9 shows likely Hoechst debris.

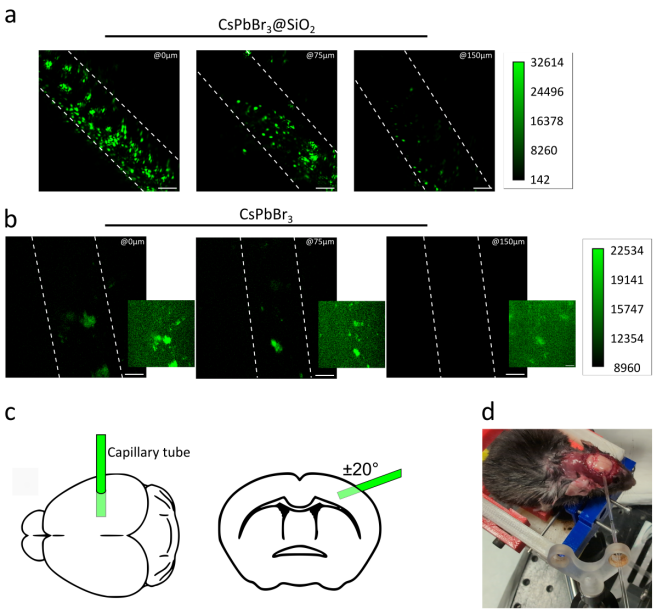

Figure 3.8: The silicon protected nanoparticles remain stable when in a solution of toluene and as the depth of penetration is increased, the emission intensity reduces (a). When the unprotected nanoparticles are a toluene solution, they quickly lose the ability to fluoresce, but low emission intensity can be collected at depths up to 200μm (b). (c) and (d) show how the experiment was conducted, placing the capillary tube into the ex vivo brain tissue.

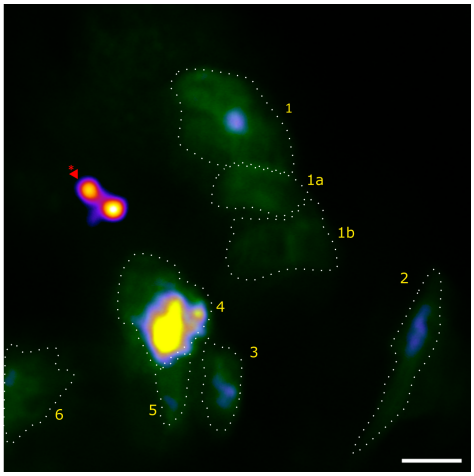

Figure 3.9: Silicon protected perovskite nanoparticles taken up by MSCs and intradermally injected into a mouse ear. Notions of cells outlines are indicated with dotted lines. Nanoparticles in the green channel, with Hoechst in cyan. Scale bar is 10μm.

Nanoparticles aid in the pursuit of deep tissue imaging, but in this case, we only attempted to image inside the ear of a living mouse at approximately 20μm within the skin. At this depth, sample aberrations and scattering do not significantly impact emission intensity or resolution, and show the potential of nanoparticles as bright markers that will enable tracking of cells applied as therapeutics, provided the nanoparticles are not triggering or interfering with the immune response of injuries that might be used to evaluated MSC therapies.

3.3.4 Organoid Imaging

Organoids are miniature models of organs that have revolutionized the fields of developmental biology and cancer research, and are particularly useful as they engineer and support the appropriate tissue microenvironment [127, 128]. In some of the previously presented images in this document, monolayers of cells were discussed, adherent to plastic (in the case of MSCs), that have been and continue to be indispensable to regenerative bioscience research. Cellular interactions can be observed by such cultures, but they do fail to recapitulate various physiologically relevant features, which is thought to lead to inefficient translation of research to clinical application of a number therapies [129]. Organoids promise to provide a three-dimensional model that truly represents the in vivo environment in vitro, enabling more efficient investigation of cellular interactions, tissue patterning and more.

In collaboration with the Georgia Institute of Technology, who engineered a number of organoids from MSCs, we imaged these 500μm diameter organoids to quantify the differentiation of MSCs into osteocytes. These organoids were engineered as spherical scaffolds with a base of matrigel [130], and MSCs were later added and cultured for 28 days. A comparison was made between organoids stimulated with osteogenic media and those without, and no staining was applied, so that label-free imaging would establish differences in collagen content.[45] Matrigel has been shown to autofluoresce in high concentration [131], and in the resulting images, red features show how matrigel scaffold supports the cells and mineral deposition. Similarly to how SHG was measured in section 3.3.1, collagen was quantified in the control (Figure 3.10a) and organoids cultured in osteogenic media (Figure 3.10b). Here we see a difference in the amount of collagen deposited by the cells over 28 days, and SHG collagen quantification across eight of each condition showed that the difference is significant (Figure 3.10c).

[45] A difference in the organoids can also be see by the naked eye, as per this photograph; left are undifferentiated, and right are more opaque differentiated organoids.

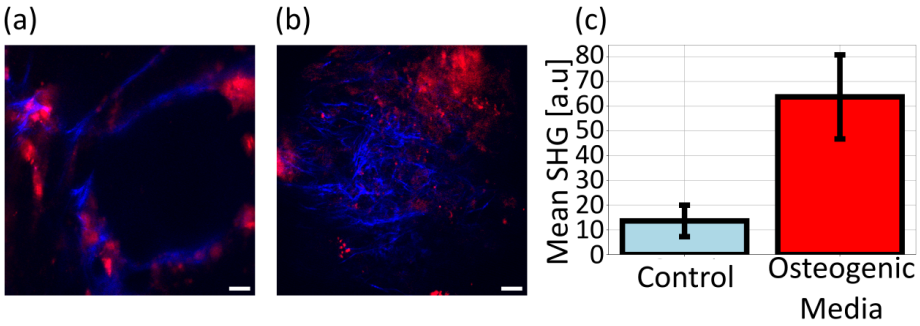

Figure 3.10: At a depth of approximately 30μm the autofluorescence (red) from the matrigel seems to hold up the collagen deposits revealed by SHG (blue; a,b) regardless of whether the MSCs were undifferentiated (a), or differentiated (b). Quantification of the collagen shows a significant difference in collagen deposition (c). Scale bar is 25μm.

Imaging at the surface, or relatively shallow depths (circa 30μm) required approximately 5mW of average power but to image through the entire organoid, the average excitation power was increased to approximately 150mW at depths exceeding 200μm. At these depths, the scattering medium becomes disruptive and the electromagnetic wavefront is distorted so that image quality is greatly reduced, but the visible effect is that lower autofluorescence and SHG is emitted (Figure 3.11 a,b)

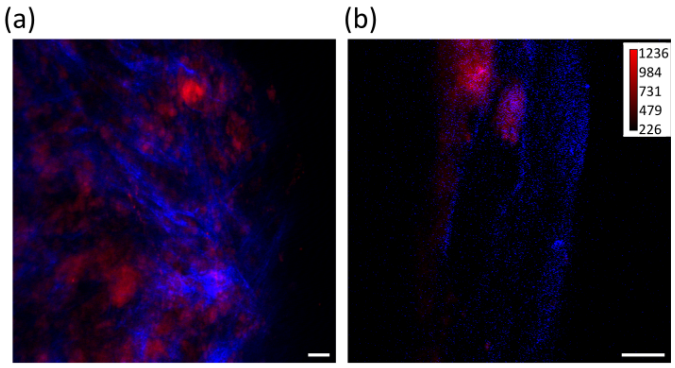

Figure 3.11: Imaging the matrigel and MSC organoids at the surface (a) shows high emitted autofluorescence (red) and SHG (blue), but as the depth increases to approximately 150μm, both imaging modalities become less effective as emitted light is reduced (b). Color calibration bar for the autofluorescence (red) channel applies to both images a and b. Scale bar is 10μm.

3.4 Discussion

Multiphoton imaging is a reliable modality that provides high specificity and intrinsic optical sectioning. When samples are thin, we are able to easily see specific markers such as those inside 10μm tissue sections where macrophages and FAPs have been labeled. SHG, is an energy preserving non-linear coherent process that enables label-free imaging of collagen, and provides a means of quantifying collagen and when combined with 2-photon imaging can be used to characterize tissues under various conditions.[46] As thicker samples are investigated, depending on the nature of the tissue, the turbid nature of the medium degrades the PSF so that the flux density and resulting emitted fluorescence is reduced. In the following chapter a method of recovering the imaging quality through turbid media is discussed.

[46] While longer wavelengths provide improved penetration, the SHG signal is reduced as the wavelength increases as the hyperpolarizability tensor decreases [9, 132]

Chapter 4

Scatter Correction

"A little concise is better than a lot scattered."

— Kamaran Ihsan Salih

4.1 Introduction

Imaging presented thus far has not shown much degradation as a result of aberrations, whether they are induced by the system (optical path) or by the sample. We did see in section 3.3.4 that through approximately 200μm of matrigel scaffold and mineral deposits by MSCs cultured in osteogenic media, the PSF quality at lower power is reduced, and impacts the resulting image quality. While multi-photon microscopy has been applied in biological tissue [133], osteogenic processes have not been fully investigated in thick living bone tissue. Investigation of these osteogenic processes in pathologies such as osteogenesis imperfecta (OI), and hypophosphatasia (HPP), could unlock treatments for those inflicted by these diseases. These processes have not been observed at depth within thick bone into the deep marrow, so an understanding of the aberrations within such an environment is necessary. While increasing the wavelength of the excitation light provides a degree of improvement in depth of penetration, they remain subject to scattering effects beyond the ballistic range.[47] The effect of scattering on the SHG PSF intensity through bone tissue can be seen in figure 4.1[48], where a peak in intensity is reached, but rapidly degrades as the scattering nature of the opaque tissue overwhelms the PSF. To overcome this degradation of the PSF by enlargement and poor formation, the instantaneous excitation power can be increased to a point [134], but aberration correction can be useful when power has been maximized.

[47] Ballistic photons are those that propagate through a medium without scattering. The range of these photons depends on the wavelength and the scattering medium.

[48] Depths described within this plot can be measured from various points, as the focal volume generates SHG signal as the surface enters the focal volume but is not completely within the focus.

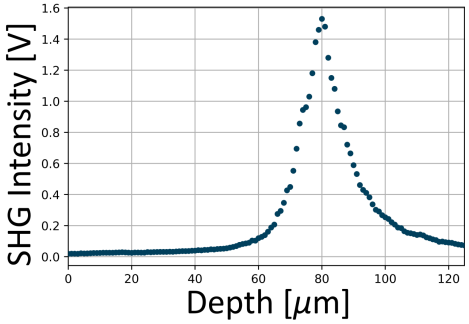

Figure 4.1: SHG signal measured by a PMT shows a peak followed by rapid decrease in signal collected.

Low order tissue aberrations, such as spherical aberrations have been well studied and can be effectively modeled and corrected [135], but sample-induced aberrations caused by the complex structure of tissue can vary dramatically even within similar tissue and require correction [70]. As discussed in section 1.6, lower order aberrations can be corrected by means of electro-optical devices such as deformable mirrors (DM), which feature relatively low spatial frequency, able to correct a number of Zernike modes limited by the device [136]. Following a sensorless approach, using the SHG PSF as a guide, the system presented in section 3.2 was modified to correct the sample aberrations [123]. Such approaches, using DMs have been shown to achieve good results in correcting aberrations in homogenous tissues, such as drosophila brain [137], zebrafish [78], and mouse brain [138], however, in highly scattering media such as bone, the number of scattered modes is much larger than the number of degrees of freedom of the DM and the correction becomes less effective [139]. Devices with a high number of degrees of freedom do exist, such as spatial light modulators (SLM), which are electro-optical devices capable of manipulating the intensity, phase, or polarization of light in a spatially varying manner. While the pseudo-continuous nature of SLMs enables efficient phase modulation, the drawback is the update or refresh rate, up to 1kHz in the latest devices. These devices have been shown to achieve reasonable convergence times [91, 140] when applied in continuous phase modulation [80], polarization modulation [81], and binary modulation [82, 83], but in the case of living biological samples, the persistence time of aberrations can be as low as milliseconds [94, 95]. This means that effective and up-to-date corrections of the higher order aberrations require rapid implementation. While SLMs have been used broadly in projectors, they have steadily been replaced by digital micromirror devices (DMD) which boast update rates

of up to 32kHz and hold potential for applications that have relied on SLMs in the past, but have been anticipating faster devices. While much faster, and comprising hundreds of thousands of micromirrors[49] (a high number of degrees of freedom), the drawback of DMDs is that without complex off-axis holography, they are suitable for amplitude modulation [80]. Therefore, DMDs are most often used to manipulate the wavefront by switching on only segments (pixels) that constructively contribute light to the focus, known as binary amplitude modulation [88]. Due to the high speed and degrees of freedom, it was decided to implement a binary amplitude high order aberration correction setup using a DMD in addition to the DM implemented to correct low order aberrations.

[49] Micromirrors in the device that we have integrated have a diameter of 16μm.

Binary amplitude search techniques are required to find the optimal pattern that maximizes the resulting PSF. Search heuristics are abundant, and methods such as sequential [80], parallel [92], machine learning [137, 141], genetic algorithm [87] have been demonstrated to yield effective enhancement in simulations [82], and so have potential for use in dynamic living biological tissues.

4.2 Genetic Algorithm

Genetic algorithms are inspired by nature, incorporating the principles of genetic evolution to explore a given search space for an optimal solution and are best suited to problems where the solution can be constructed by perceived genes. In the case of binary modulation using a DMD, each pixel represents a gene, with two mutation options, *on* or *off*. When the state of all DMD pixels is "flattened" to a single sequence of binary levels, for example 101000110110 and 011101000101, crossover between two sequences can be executed and the result, for example 101000000101,[50] evaluated. This evaluation of new generations is where the power of the algorithm lies, as some metric is utilized to decide which patterns among a group of individuals are the top performers and most suitable for subsequent breeding and evaluations.

[50] Here the two example values are split into two at the half and the front half of the first number concatenated with the back half of the second number.

Detail regarding the implementation of this genetic algorithm are based on those presented in [82, 87, 142] and illustrated in figure 4.2 and described here in full. As mentioned, a fixed number N of random binary sequences (patterns) represented by 1-dimensional arrays are introduced. Each of these individual patterns consists of S segments (pixels), each represented by p_j which is set to 1 (*on*) or 0 (*off*). Each pattern is then projected to the DMD, and the resulting PSF measured, and the list of individuals ranked according to a fitness metric, in our case, the measured intensity.

New generations are then created by selecting the top $\frac{N}{2}$ ranked patterns, propagated directly to the new generation, but also used to produce the remaining $\frac{N}{2}$ patterns bu means of mutation and crossover, the two halves forming the new generation G. Mutation is executed according to a predefined rate R, defined as: $R = (R_0 - R_{end}) \cdot exp(-\frac{n}{\lambda}) + R_{end}$ where R_0 is the initial mutation rate, R_{end}, the final mutation rate, n is the generation index, and λ is the decay factor [87]. Crossover is implemented by splitting genes and joining the components with appropriate components of other high performing patterns. This can be achieved using a random or fixed point for the split. To ensure that the algorithm does not simply act as an aperture, a limit is placed on the number of *on* pixels permitted for each individual, specified as 52.5%. This restriction acts as another layer of mutation, possibly disrupting well-established patterns and delaying convergence. These newly generated patterns are projected onto the DMD and the resulting PSFs measured once again, and the algorithm repeats these steps until a fixed number of generations have been generated and evaluated.

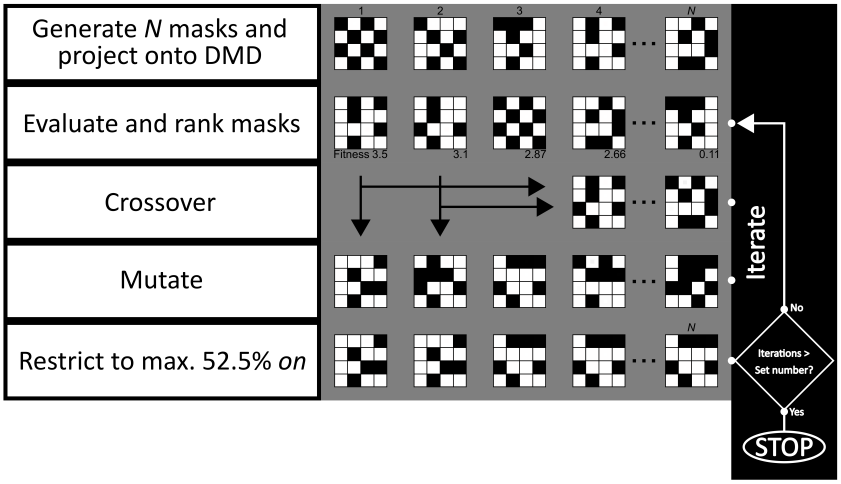

Figure 4.2: A description of the steps executed during the genetic algorithm, where a patterns are generated, evaluated, mutated and crossed-over, with new generations being evaluated until a number of iterations have been completed.

Optimization of the genetic algorithm's parameters is achieved by trial and error, as there are no existing ideal parameters for specific scenarios, but rather best practices to follow. This trial and error is necessary for specific scenarios where gene length or shape contributes to the evaluation metric differently. Our solution vectorizes the individual patterns, but when the pattern is arranged appropriately for projection onto the DMD, certain mutations and gene

crossovers might be overly impactful. Another factor that could cause variation among scenarios is the gain of the photon collection device, altering the SNR variability between measurements. As such, to evaluate the performance of the algorithm according to known array sizes (based on the number of pixels, or segments to be projected onto the DMD) simulations were run comparing pattern lengths (essentially the number of degrees of freedom), the mutation rates (including R_0 and R_{end} and non-exponential decay) and recording the results. Thousands of each scenario were simulated and the results are presented in figure 4.3.

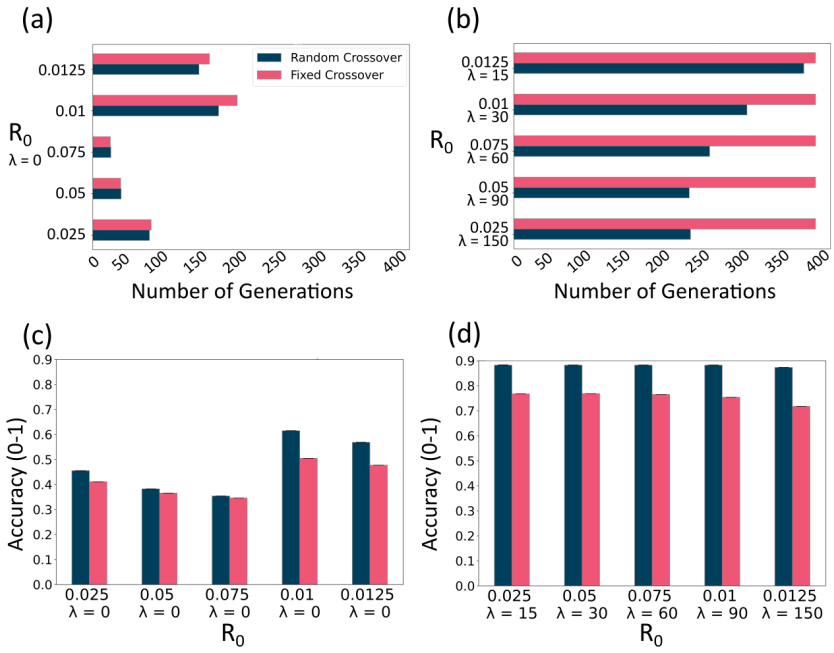

Figure 4.3: Results of genetic algorithm simulations show that when time to convergence is considered, no exponential mutation decay rate results in faster convergence (a,b), and that when no exponential decay is implemented, there is not a large difference between a fixed and random crossover. When the accuracy of the optimized solution is considered, the exponential decay rate is best, and in this case a random crossover outperforms the fixed crossover (c,d).

Simulations were run using a random binary array (with lengths 373, 1436, and 5785) as the target, and the evaluation metric the euclidean distance of the individual arrays to the target. Simulation results in figure 4.3a and b show the significant difference in applying an exponential decay rate λ to the search, where convergence[51] was reached more rapidly when no exponential decay is applied (figure 4.3a,b). When an exponential mutation decay rate is applied

[51] Convergence here was defined as the euclidean distance between the current generation and the target not changing positively for more than a specified number of generations.

(figure 4.3b), convergence requires many more generations, but ultimately the accuracy is much improved (figure 4.3d). Without an exponential decay, the mutation rate remains constant (for instance, in figure 4.3a, the mutation rate R_0 is 0.0125 and the end rate R_{end} is also 0.0125), and so optimization reaches a point where too many changes are being made in each generation (figure 4.3c) [143]. Deciding to run an optimization without an exponential decay would be to decide that the optimal solution is less important than a rapid convergence. Here, the options were a fixed position crossover (various positions were simulated) and a random crossover position. Without an exponential decay, the difference between a fixed position and a random position crossover did not show much difference in the number of generations to convergence (figure 4.3a), but when the exponential decay is included, the random crossover is quicker (figure 4.3b). Similarly, the accuracy in both cases of mutation decay rate is improved when the crossover position is randomized (figure 4.3c,d).

By considering these results, particularly in terms of the accuracy, an exponential decay rate is implemented in all subsequent results, along with a random crossover position. While the values of λ cannot be transposed to other implementations of genetic algorithm, the general shape of the exponential is maintained across subsequent experiments, with the number of generations, R_0, R_{end}, and λ contributing to the shape of the plot.[52]

[52] An example exponential decay is shown here, across 200 generations where $R_0 = 0.01$, $R_{end} = 0.0025$, and $\lambda = 25$.

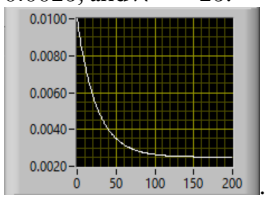

Evaluation of any optimization technique used in a scatter correction is important to be able to measure the quality of the correction. Vellekoop and Mosk [84] proposed an evaluation metric η (essentially given by $\frac{I_{\text{optimized}}}{I_{\text{reference}}}$), implemented by [82, 84], given in full as:

$$\eta = \frac{I_k^a}{\frac{1}{N}\sum_m I_m^b} \tag{4.1}$$

where the intensity of the m^{th} pixel is given by I_{m}, the k^{th} pixel is the spot intensity, and a and b refer to the image after (a) and before (b) correction. In the case of before, the initial pattern is set to 50% segments on, and in the after state, the number of on segments is limited to 52.5%. Subsequent experiments, with resulting optimized DMD patterns are quantified by means of this η value.

For experimental implementation of the GA in both transmission and epi-detection setups, each pattern is comprised of a number of DMD pixels arranged in a circle that is aligned with the incident elliptical excitation beam. The diameter of this active area remains constant (across 512 DMD micromirrors) while the degrees of freedom vary from low, set to a total of 373 segments each comprised of 24×24 DMD pixels, medium (1436; 12×12 super pixels), and high (5785; 6×6 super pixels). The strict limit on the number of segments

was set to 196 of 373 segments to limit the optimization from significantly exceeding 50% on segments.

4.3 Transmission Geometry

An initial evaluation of the Genetic Algorithm, applied using binary wavefront modulation and a DMD, was performed in a transmission geometry setup, which has been widely used in scatter correction implementations [80, 83, 144]. A transmission geometry propagates light through an objective lens, and then collects the light through a condenser lens opposite it. As such, transmission geometry is not suited for imaging thick samples, but for the purpose of verifying our optimization implementation with the DMD, transmission geometry is suitable.

Iterating through a fixed number of generations of the GA as described above, parameters set to $R_o = 0.01$, $R_{end} = 0.0025$, and a decay rate of $\lambda = 50$ were found to return enhancement that matched those found in the literature. It is important to note that calculations of the mutation ratio and decay depend on the number of generations, and should the number of generations be adjusted, the value of λ should be selected to match the slope given by these values across 350 generations,[53] similar to those presented in [82] and [145].

[53] The 350 mentioned here, is applicable to the results in this section which are presented across 350 generations.

Comparing three pattern sizes, each with a different number of controlled segments, shows results that match current literature, with the measured enhancement being proportional to S (number of segments). This enhancement is guided by the theoretical maximum achievable enhancement in binary wavefront modulation of $\eta = \frac{N}{2\pi}$ [82]. Source light was 780nm from the Coherent laser reflected off the DMD (ALP4.3; V3495, Vialux) and filtered by an iris in the Fourier plane, as per [88] and then passed through a 10× air objective lens (Plan Fluor 10×/0.30, Nikon). From here, the light is scattered by a ground glass diffuser ($DG10 - 120 - MD$, Thorlabs) and then collected by a 20× air objective lens (Plan Fluor 20×/0.45, Nikon) and captured on an sCMOS camera (Zyla 4.2, Andor, Oxford Instruments). The lenses, diffusor, and camera were all mounted on a cage rod set up to secure the alignment of the critical components.

The results of our work can be seen in Figure 4.4, and Table 4.1 summarizes the imaging conditions applicable to each case. Figure 4.4b shows the corrected spot when employing 5785 segments (each in turn grouping 36 (6×6) mirrors of the DMD), where 4.4a shows the initial speckle light where no clear PSF is visible. Figure 4.4c shows a horizontal profile through the spot from 4.4a and 4.4b showing the improvement in captured intensity. Repeating these results

for the remaining cases of 373 and 1436 segments Figure 4.4d confirms that the enhancement is dependent on the number of active segments. In the case of 5785 segments, the GA reaches convergence before 500 generations (not displayed in 4.4d), but the average resulting η is 197.

Table 4.1: Imaging conditions of each DMD pattern configuration

Segment count	**Configuration**		**Enhancement,** η
	Segment size	Exposure time (ms)	
373	24×24	20	21.1
1436	12×12	10	75.8
5785	6×6	4	197

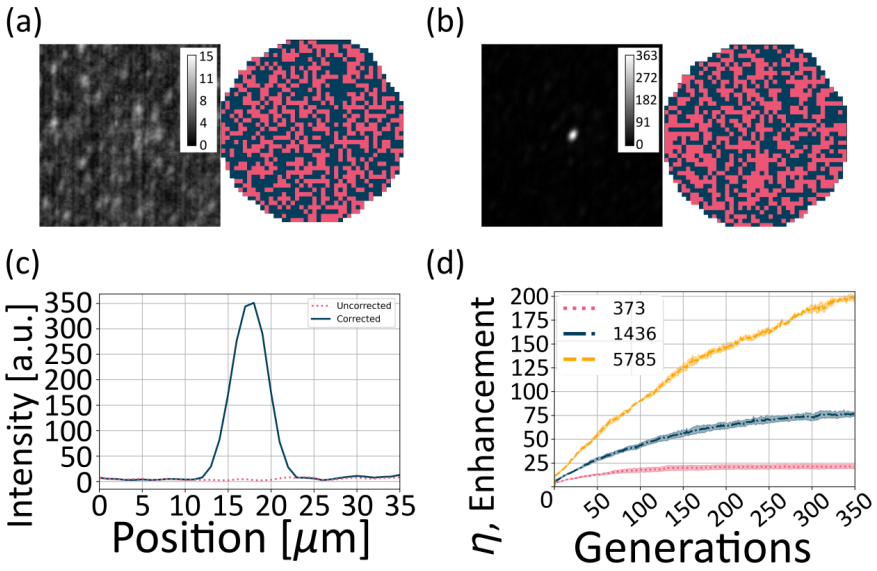

Figure 4.4: (a) The initial random DMD pattern and resulting image after the glass diffuser shows a highly distorted unclear PSF and (b) the corrected DMD pattern with the resulting PSF (note the different calibration). (c) A cross section of the image from (a) and (b) showing significant improvement, which is recorded as part of (d) revealing that more degrees of freedom leads to more enhancement.

These results show that the implementation of a genetic algorithm in conjunction with the optical placement of the DMD works as expected. When directly comparing the results of this configuration against those presented in literature (Figure 4.5) [82, 83, 146, 147], we find that our implementation is working and suitable for epidetection implementation.

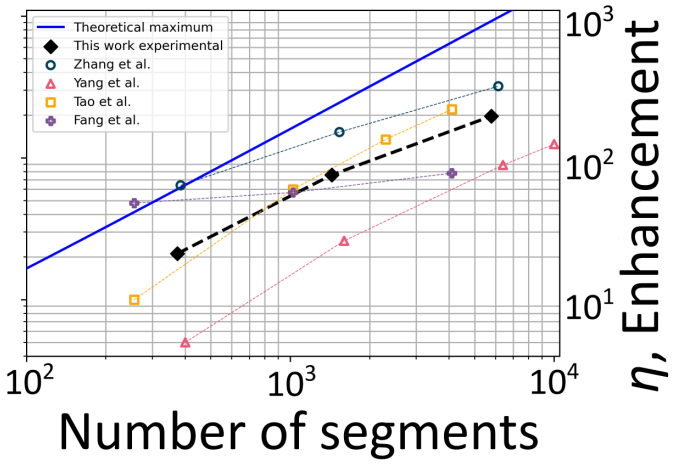

Figure 4.5: Enhancement metric presented on a log-log plot compares well to previously presented methods in [82, 83, 146, 147]. Experimental data resulted in $\eta = 21.1$ for 373 segments, $\eta = 75.8$ using 1436 segments, and $\eta = 197$ using 5785 segments.

4.4 Phantom Samples

As the goal is improvement of image quality at depth within bone tissue, the transmission geometry setup is not suitable and was replaced by an epi-detection configuration. This updated version of the custom microscope engages a Ti:Sapphire laser (Chameleon Ultra II, Coherent) for excitation in the wavelength range 680nm - 1080nm, and is illustrated in Figure 4.6. Output from the source laser is modulated using a Pockels cell ($350 - 105$, Conoptics) and immediately thereafter, a pinhole is used to improve the Gaussian properties of the beam. The beam is expanded to utilize approximately 30% of the DMD (ALP-4.3 (V4395), ViALUX) active array surface, within the 10.5mm height limit of the active array. A resonant-galvanometer scanner (MDR-R, Sutter Instrument) allows for scanned imaging, and finally, a 60× water immersion objective lens (LUMFLN60XW, Olympus) focuses the light onto the sample. To measure and optimize the DMD pattern, the sample-emitted light is captured by the sCMOS camera (Zyla 4.2, Andor, Oxford Instruments) through an appropriate filter for the SHG guidestar ($FF01 - 390 - 18$, Semrock) when excited at 780nm, by moving the dichroic mirror DiM_1 to its appropriate position. Capturing an image of the sample over a wider field of view, DiM_1 is moved to reflect emitted light to be collected by the photon multiplier tubes (PMTs) ($H10770 - 40$, Hamamatsu Photonics K.K.), using trans-impedance ampli-

fiers (59 − 179, Edmund Optics), and scanimage [119] controls the resonant scanner and FPGA (PXIe-7975R and NI5734, National Instruments). To capture images of GFP in the murine samples, an appropriate optical bandpass filter was used (FF01 − 457/50, Semrock). The sCMOS camera and DMD are controlled by a custom LabVIEW (National Instruments) program. All the epi-detection experiments conducted included lower-order adaptive optics, with the system correction turned on, as per previous adaptive optics work within the group [123].

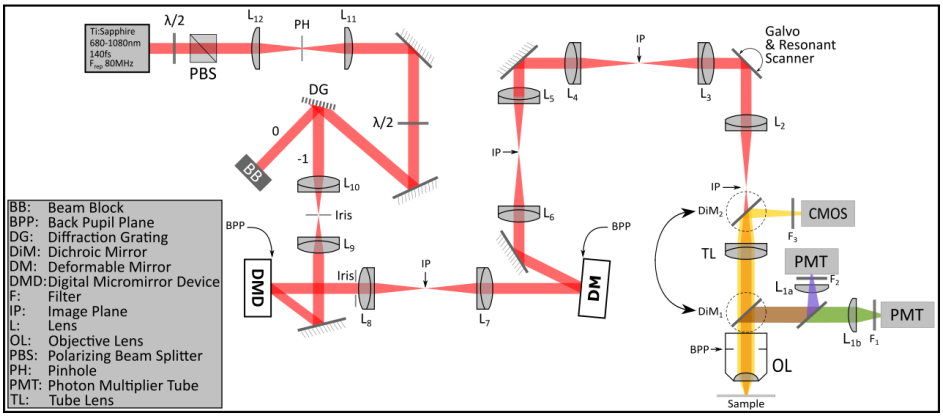

Figure 4.6: Schematic diagram of the microscope system. The DMD, imaged onto the back of the objective lens, is comprised of micromirrors (13.68μm diameter) tilting at +12° or -12°. A diffraction grating (DG) compensates for dispersion generated by the surface of the DMD. The distances and angles presented in this figure are not representative of those implemented in practice.

Phantom samples used in experiments to show the applicability of the epi-detection geometry and DMD correction are 3-fold. Firstly, extended fluorescent plastic slides (92001, Chroma Technology), measuring at 1.2mm thick, which provide bright 2-photon fluorescence emission[54] at 585nm. Second, thin fluorescent samples were prepared, which consisted of a microns thick layer of Fluorescein-5-Maleimide sandwiched between a microscope slide and a coverslip. Finally, Potassium Titanyl Phosphate (KTP, with formula $KTiOPO_4$) were procured (KTP-403H, EKSMA Optics) with the idea that the SHG generated by the KTP would be a reasonable phantom for SHG generated by the collagen in bone tissue. Throughout the evaluation of phantom samples, translucent tape (70005119527, 3M) was used as the diffuser, where the scattering length was measured to be ℓ_s= 0.64, with an approximate thickness of 30μm. Various

[54] Chroma Technology do not specify the spectrum of excitation of emission of this product.

layers were then applied to the phantom samples between the objective lens and the sample.

The thin fluorescent sample was evaluated under the conditions of one, and three layers of tape. Figure 4.7a shows the measured relative enhancement of each phantom sample when 373 segments were employed in the optimization of the DMD pattern. Enhancement of the thin fluorescent sample is slightly reduced when the additional two layers of tape are applied to the sample, in both cases converging on an optimized solution after approximately 100 generations. Comparing enhancement measured using the thin fluorescent sample to the extended fluorescent sample, through three layers of tape, we observed an increased enhancement that converges at an η value of approximately six after approximately 150 generations. This difference can be attributed to the increased photon flux emitted by the extended sample due to a combination of sample brightness and more of the sample being excited by the focal volume. The enhancement measured in the KTP sample in figure 4.7a shows a similar trend with additional improvement from generation $150 - 300$, before returning to an enhancement value similar to that of the extended fluorescent sample.

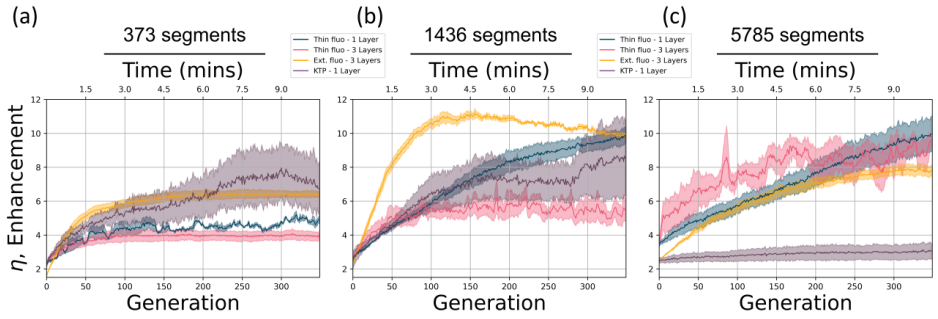

Figure 4.7: Experimental enhancement, η, for the three phantom samples, thin fluorescent, extended fluorescent, and extended KTP crystal under various diffusers, where 373 (a), 1436 (b), and (c) 5785 segments were used during optimization.

Resulting enhancements in figure 4.7(a-c) match the expectation set in Figure 4.5, with increased enhancement correlated to increased degrees of freedom. Similarly, the optimization convergence is delayed when more controllable degrees of freedom are available to the GA, which is best presented in Figure 4.7c, where the enhancement has not converged in any of the phantom samples. While the gradient of each enhancement remains positive after 350 generations, the time to run 350 generations with 20ms exposure time (and other overheads) exceeds ten minutes, which becomes a significant translational drawback.

We found that the role of initial intensity I_0 (in our case, the first generation average intensity) or the number of photons measured in the target region of interest, is a restrictive factor in achieving consistent enhancement. Total signal in a target region of interest consists of ballistic (unscattered) photons, sub-diffuse photons [148] that are subjected to fewer scattering lengths, and fully scattered photons. Sufficient ballistic and sub-diffuse photons are necessary as a basis for the initial correction of the GA. May et. al. [149] showed that in the specific case of a thin fluorescent sample, enhancement cannot be expected when I_0 is too low (< 10) but higher measurable enhancement is achieved when I_0 increases, and GA is most effective when I_0 reaches or exceeds 1000.

In this work, where the phantom samples are obscured by three layers of tape, photons experience approximately 4.5 scattering lengths, which we have classified as sub-diffuse. As more layers are applied, we reduce the number of ballistic photons, and thereby I_0. The dependence of enhancement on I_0 accounts for the results such as Figure 4.7c where I_0 is low and the segment count is higher. In this case the enhancement is unconverged after 350 generations, yet maintains a positive gradient. The effect of reduced I_0 can be corrected by setting it to be equal across each experimental case, or by increasing the excitation power.

When considering Figure 4.8c, f, i, and l, where 5785 segments were used in the optimization, it becomes clear why the GA converges later when using more segments. Each individual segment among the 5785 has a smaller impact on the intensity (or other evaluation metric) in the target spot than the equivalent individual segment among a total of 373. Where concentrated regions of *on* segments yield the optimal intensity (or other evaluation metric), lower segment counts reach the arrangement faster than in the case of more, smaller segment configurations.

In the case of KTP crystal-based phantom samples, which emit primarily forward SHG due to their phase matching properties [8] there are few backscattered photons to collect, so the initial photon count in the optimization is lower than the fluorescent case. Therefore with 5785 segments used, even with fewer layers of translucent tape applied a much lower enhancement was achieved than in fluorescent results, as per Figure 4.7c.

From results of each pattern presented in Figure 4.8, the correction patterns appear to concentrate *on* segments in a specific region of the DMD. This is indicative of a lower-order correction that may be the result of residual spherical aberration during the refractive index change that occurs as the excitation light enters the sample.

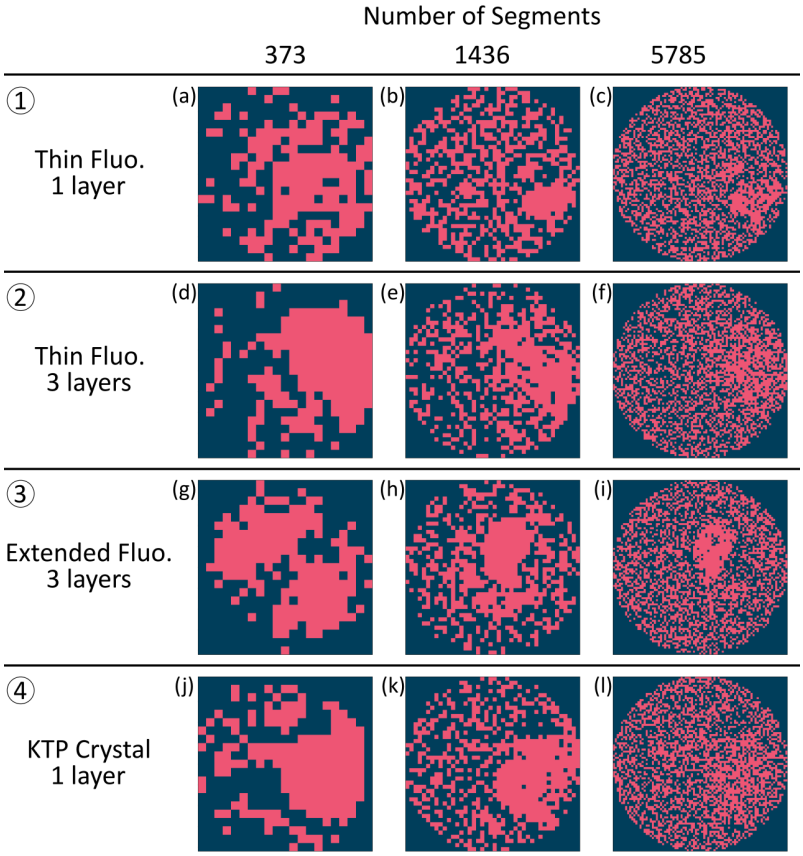

Figure 4.8: Optimized patterns according to segment counts for each of the various phantom samples evaluated. Optimized patterns for the thin fluorescent sample, with 1 layer of translucent tape as diffuser are shown in row 1, where 373 (a), 1436 (b), and 5785 (c) segments are used. Optimized patterns for the thin fluorescent sample, with 3 layers of translucent tape are shown in row 2, where 373 (d), 1436 (e), and 5785 (f) segments were used. Optimized patterns for the autofluorescent plastic slide (extended sample) with 3 layers of translucent tape are shown in row 3, where 373 (g), 1436 (h), and 5785 (i) segments were used. Optimized patterns for the mounted KTP crystal with 1 layer of translucent tape, where 373 (j), 1436 (k), and 5785 (l) segments were used.

4.5 High-frequency Wavefront Correction in Biological Samples

Using a label-free approach to imaging within the bone, we use the intrinsic SHG signal generated by the collagen in bone tissue. Légaré et al.[33] showed that the fraction of backscattered SHG light that reaches the surface of a thick tendon tissue is approximately 21%. The measured F/B (Forward/Backward) ratio of SHG in that thick sample was approximately 4, so it can be deduced that approximately half of the emitted SHG at the surface is backward generated, and the other half is back-scattered [33]. Similar ratios can be expected in bone samples which are comprised of similar collagen arrangements. During optimization, segments in the DMD mask that "switch on" photons that contribute to a stronger focus would be favored over segments that correct epi-directed photons. Latent lower-order corrections could be favored during optimization and although scattering is strong, the prevalence of lower-order aberrations, such as spherical aberration, would still require compensation.

For biological examination of the scatter correction, a freshly excised, fifteen-week-old PhAM floxed (photo-activatable mitochondria) skull sample (#018385, The Jackson Laboratory) was fixed in 4% paraformaldehyde (PFA) and 96% phosphate-buffered saline (PBS) for 48 hours and then mounted in a Petri dish using a PDMS elastomer (Sylgard 184, Dow Corning). IACUC was strictly adhered to in treatment of animal samples. A manual 3-axis stage was used to prevent spurious movement during the correction and point-scan imaging.

Illumination of the sample with 780nm at approximately 300mW and a depth of $\sim 140\mu$m (well past the mean free distance for adult mouse bone tissue of $\sim 45\mu$m [137]) provides sufficient photons for the optimization to improve. The result was a correction time of approximately 15 minutes for a population size of 100 across 50 generations, 120ms integration time, and overhead latency of approximately 2.5 minutes to record 373 segment individuals within the population for each generation. Figure 4.9d shows the low signal in the average image of the initial generation, with the uncorrected mask projected onto the DMD in 4.9b. The enhancement over 50 generations can be seen in figure 4.9a, with the average image of the SHG spot in the bone in 4.9e, and the corrected DMD mask in 4.9c. The optimized mask in 4.9c indicates lower-order aberration correction, which could be due to spherical aberration which is commonly present due to the shape of the skull. Low persistence times are associated with living tissue [149–151], and while correction in an excised skull would not suffer from such low persistence times, achieving apparent convergence within 50 generations is appealing for translation of the technique to living bone by

reducing the duration of optimization. The difference in the intensity profiles of 4.9d and 4.9e indicates a significant increase in the SHG spot in the bone after correction.

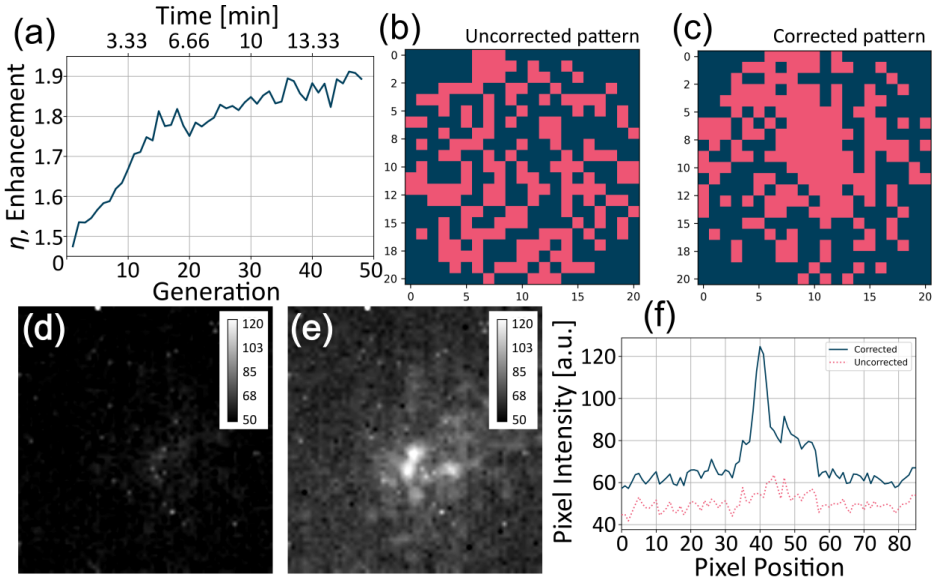

Figure 4.9: Scatter correction implemented at a depth of $\sim 50\mu$m with calculated enhancement in (a), the result of uncorrected DMD pattern, generation 1 (b) and corrected DMD pattern, generation 50 (c). The first generation results in an image shown in (d) and the corrected pattern in an image as per (e), population size = 100. The improvement in the corrected versus initial spot intensity is shown in (f) (cross section from top-left to bottom-left.

Resulting optimized DMD patterns were then projected to the DMD for use in the point-scanning implementation where both GFP and SHG channels are observed simultaneously.

Images collected at a depth of 140μm, through the whole skull bone, using both uncorrected and corrected DMD patterns illustrate the increased contrast in both GFP and SHG channels (figure 4.10) when using the optimized pattern. At this depth, imaging the bone marrow in a 15-week-old mouse, the collagen no longer resembles the condensed formation of bone with lacunae, but fibrillar features are more prevalent. The Green fluorescent protein (GFP) present in the mitochondria of the murine sample (figure 4.10b,d) are imaged separately from the SHG in bone and other collagen-based tissues (figure 4.10c,e).

Applying the uncorrected DMD pattern results in low intensity in the GFP (Figure 4.10b) channel and few visible spots of mitochondria, but application of the corrected DMD pattern returns increased intensity (Figure 4.10d). A

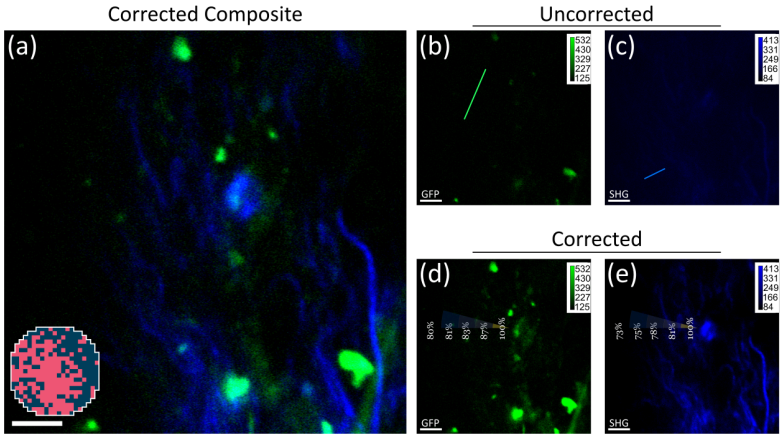

Figure 4.10: At a depth of $\sim 140\mu$m, the bone marrow is imaged, and clear punctate mitochondria are visible after correction (a). The corrected DMD pattern is inset in (a), 52.21% segments "on". Application of the uncorrected DMD pattern yields low signal in both the GFP (b) and SHG (c) channels. After correction, the GFP channel (d) shows mitochondria that were not visible using the uncorrected DMD pattern. The improvement in SHG when applying the corrected DMD pattern is clear in (e). Fourier Ring Correlation shows an increase in spatial resolution of 905nm in GFP (h), and 688nm in SHG (i). Scale bar is 10μm.

cross section of the identified line shows a 2-fold increase in intensity with new peaks indicating previously undiscerned mitochondria (Figure 4.11a). From the center of the correction, the effective mean contrast improvement is reduced to 80% outside a radius of 400 pixels.

The SHG visible when the uncorrected DMD pattern is applied presents few features of interest (Figure 4.10c), as opposed to the individual fibers revealed when applying the corrected DMD pattern (Figure 4.10e). The cross section at the blue line in figure 4.10c shows increased intensity by a factor exceeding 2, but clearly more individually discernible fibers (Figure 4.10b).

Measurement of image resolution was carried out using the Fourier Ring Correlation (FRC) BIOP Plugin for ImageJ [152] presented in [153] which requires two input images to calculate the FRC. The smoothed FRC outputs for each image were isolated and presented in figure 4.10c, d. We found that the spatial frequency in the image of the GFP increased by 905nm, while the increase in spatial frequency within the SHG images was 688nm.

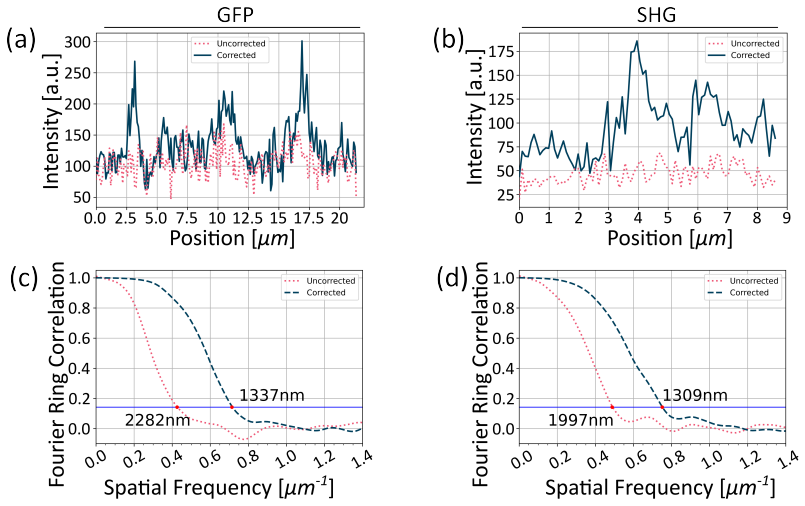

Figure 4.11: Cross sections from 4.10b,c show intensity improvements in GFP more than 2-fold (a) and within SHG more than 3-fold (b), with the improvement in FRC also showing improvements in GFP (58.5%)(c) and SHG (65.5%) (d).

Collagen contains fine fibrillar structures that interconnect, filling the spaces between osteocytes, while the punctate nature of the mitochondria within the cells leads to the expectation of improved spatial resolution for both channels. Scanned images using the corrected DMD mask allow us to more easily identify the mitochondria and other tissues, enabling more studies of mitochondrial metabolism in deep tissue, and tissue structural organization, as in our previous investigations [154, 155].

4.5.1 Normalized Power Confirmation

To confirm that initial DMD patterns are directly comparable to switching each of the DMD segments on, while halving the power, we provide raster scanned images of an ex vivo murine skull bone using various patterns projected onto the DMD at a depth of $\sim 90 \mu$m. When an uncorrected pattern is projected, the resulting image is very similar to the image captured when all of the DMD segments are on, but the power is matched to the case in which half of the segments are used (Figure 4.12a-b), in this case 140mW, and 70mW. When the optimized pattern is introduced, the resulting intensity is significantly increased (Figure 4.12c). In cross sectional analysis of the GFP (Figure 4.12d), we see how similar the intensity of the initial and "all on" cases are, which is also the case in

the SHG examination (Figure 4.12e). This confirms that comparing the DMD patter in this way is meaningful.

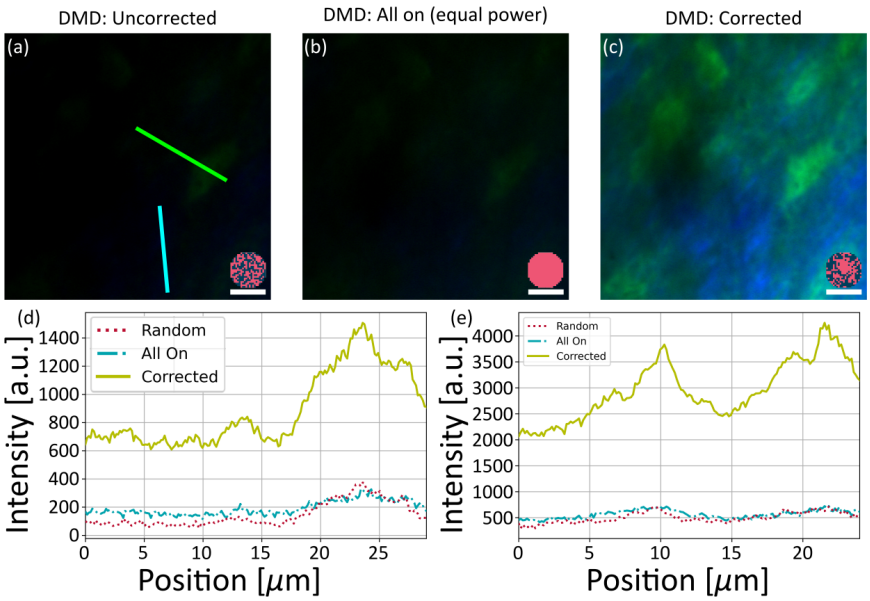

Figure 4.12: Comparing the scanned image when an uncorrected DMD pattern (a) and where all of the DMD segments are used, but the input power is halved (b) shows how reducing the power by half matches reducing the segment sparsity by half. When the optimized pattern is applied (c), the intensity is significantly increased. A cross section at the green line in the GFP channel shows that the initial and "all on" cases are very similar, but the corrected image shows a near 7-fold increase (d). Similarly, the SHG cross section at the blue line shows an intensity increase of nearly 7. Scale bar is 10μm.

4.6 In Vivo Scatter Correction Dynamic Imaging

To study the underlying mechanisms of bone pathologies, imaging within bone at depths relevant to osteogenesis is required. Locating bone marrow cavities within the murine skull requires excitation power exceeding 200mW to penetrate beyond 80μm where we empirically find such cavities more regularly. Such cavities are expected to reveal how osteocytes, osteoblasts and osteoclast interact with the bone front. By imaging within such bone marrow cavities inside

the bone of PhAm-floxed mice which express GFP in their mitochondria, we envision elucidation of these interactions in living tissue.

Following the procedures described in prior experimentation, including a living sample required additional support for the sample to avoid untenable movement by the sample. To this end, a head-bar which connects the stable automated stage to the mouse skull was introduced after the murine skull was exposed (Figure D.2). [55]

Imaging of a bone marrow cavity at a depth of approximately 115μm revealed some dim mitochondria (figure 4.13a) where an uncorrected DMD pattern was projected onto the DMD active area. After correction, numerous cells are visible due to the mitochondria within cell organelles (figure 4.13b) where larger cells can be distinguished from more punctate mitochondria within the marrow.

[55] As per IACUC procedures using 4% isoflurane to initially anesthetize the mouse and maintain anesthetization using approximately 1.5% isoflurane in air.

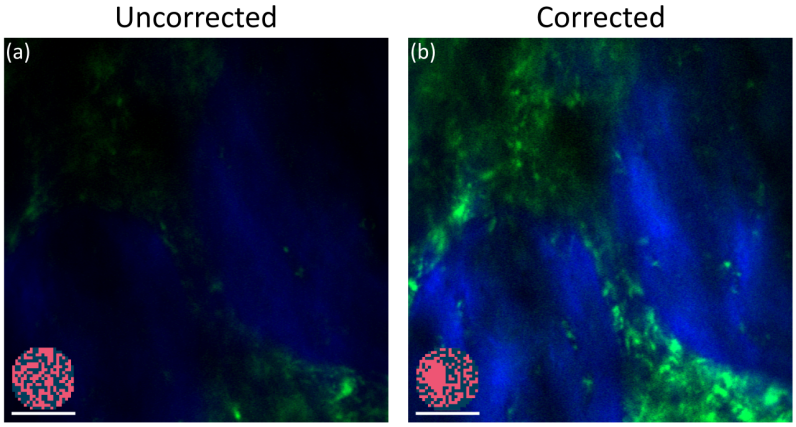

Figure 4.13: Ar a depth of approximately 115μm, some dim mitochondria are visible (a), and after correction numerous newly visible organelles are clearly visible along with brighter collagen (b). Scale bar is 50μm.

Intensity improvement in the GFP channel shows a significant improvement by a factor of 8 (figure 4.14a), and of 7 in the SHG (figure 4.14b). Frequency information within the image is improved by 62.5% (figure 4.14c) in GFP and 38.2% in SHG (figure 4.14d). Collagen visible in this region shows the separation of two cavities by a channel and is not expected to reveal much mitochondria except within the osteocytes fixed within the extra-cellular matrix forming the mineralized bone.

These improvements in intensity and spatial frequency allow for identification of individual cells associated with mitochondrial organelles, moving within the marrow cavity over time. We recorded a 34-minute time lapse of the region (Supplementary Video1; Registration using SIFT [156]) and several cells moving

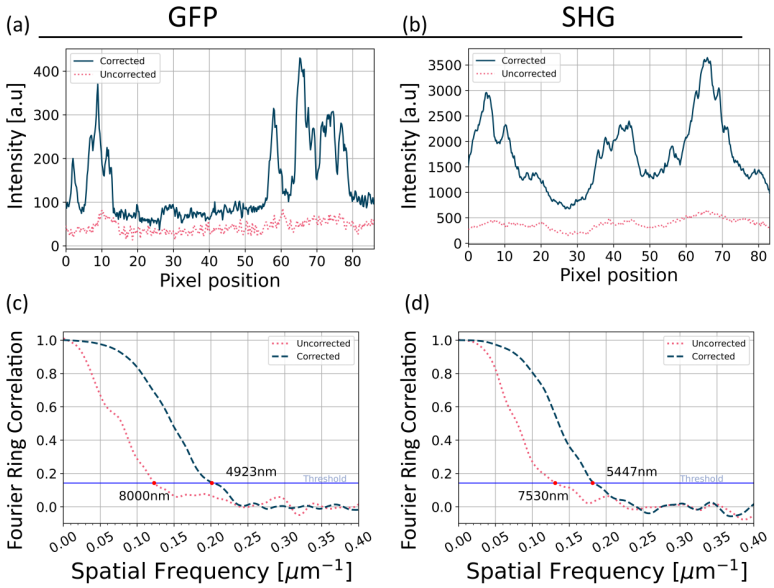

Figure 4.14: Cross sections of the images in 4.13 show an 8-fold increase in GFP intensity (a), and a 7-fold increase in SHG signal (b). Spatial frequency as measured by FRC reveal an improvement of 62.5% in GFP and of 38.2% in SHG.

through the channel between two cavities are identified and tracked. Within the cavity, some cells are visible throughout the recording (Figure 4.15a-f; cell 1), moving more rapidly across the cavity than other cells (e.g. Figure 4.15b; cell 2) which are visible for long periods of time, but movement is restricted to the passage between the cavities. A standard deviation projection identifies regions in the field of view where the most movement occurs (Figure 4.15g). In the bottom right (cell 4) is initially stationary but moves more quickly after 25 minutes. Over the 34 minutes, the fluorescence intensity appears consistent, and the entire imaging session of approximately four hours saw no discernible decrease in signal - suggesting minimal photobleaching and long-term validity of the scattering correction in living bone. As the bone tissue within the skull is relatively static and the correction duration is in the range of 12 minutes, the optimized pattern is well conditioned for long-term aberrations, averaging out the short-term aberrations, and providing an image enhancement for longer than in some other tissues. For example rapid decorrelation has been found in the brain to occur in under 100ms [151], and in lymph nodes longer than 10 minutes [94]. In the bone we do find that photobleaching does eventually

occur, which can be limited by properly tuning parameters of the illumination [157, 158].

Observation of this region over time (34 minutes) revealed a number of moving cells interacting with regions of the marrow, often slowing for a few minutes before again moving through the cavity (Figure 4.15a-f). Minimal movement over the 34 minutes is artificially removed by the linear stack alignment tool bundled with Image-J [156] after a low sigma (1.0 for each of X, Y, and Z) 3D Gaussian blur to increase the likelihood of automatic identification of cells.

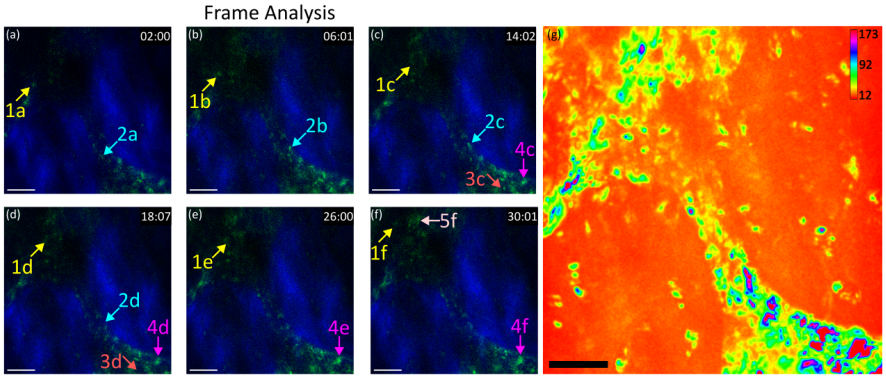

Figure 4.15: Cells identified by organelles containing visible mitochondria reveal movement over the half-hour period within the cavity, moving through (a)-(f). The standard deviation projection reveals that many cells churn without changing their position dramatically (g). Scale bar is 50μm.

With such improvement of GFP intensity using the intrinsically available SHG as guidestar, study of mitochondrial dynamics and their role in osteopathologies such as hypophosphatasia and osteogenesis imperfecta is enabled, but at the cost of correction durations exceeding ten minutes. Alternative approaches to reduce the correction times include methods such as F-SHARP [71], which effectively decouples the speed of the measurement from the speed of the modulating component (such as SLM or DMD), but the compensatory pattern cannot be applied until the measurement is completed, similar to IMPACT [94]. Increasing the speed by creating a common path interferometric version of F-SHARP with immediate updates, in a technique called DASH [149], results in even faster correction with excellent enhancement at depth. These state-of-the-art techniques have been shown to rapidly correct scattering in brain tissue, at depths of 600-900μm in 2-photon configurations. This is equivalent to imaging through 4-6 scattering lengths [159], which is approximately 1.33$\times$ deeper than what we achieved (most images presented were at a depth of 125μm inside bone which is approximately 3 scattering lengths). Direct comparison of scatter

correction inside bone tissue is not feasible, as these techniques are most used in neurological investigations where a clearing agent is used or a craniotomy performed to simplify imaging.

4.7 Single Pixel Collection

While the method outlined has shown excellent results in bone tissue, which is relatively static in the time span of hours, interest in correcting tissue with highly dynamic characteristics requires a shorter correction time. Implementing the genetic algorithm approach on the DMD, but simply replacing the high resolution sCMOS camera by a single pixel PMT should result in faster corrections, but perhaps at the cost of effective scatter correction. Usage of the sCMOS camera in sections 4.5 and 4.6 requires exposure times ranging from 90 to 150ms for evaluation of each individual within a population. This is necessary to collect sufficient photons and elevate the acquired signal beyond the noise floor so that a PSF becomes visible and scatter correction durations extend from 9 to 15 minutes for 50 generations (Figure 4.16a). Replacing the camera by a PMT and reducing the exposure time to 100 or 10ms (and potentially even 1ms) for evaluation of each individual reduces the scatter correction time to below 2 minutes. Similar approaches [160] use random DMD patterns and evaluate each one, building up an average optimized pattern based on the performance of each pixel across the evaluated sets of patterns. By using a PMT to evaluate each pattern within the GA, more control over the search is possible than by a random search. However, without the multi-pixel images for each evaluation when using the sCMOS camera, the η metric cannot be applied, and a simple factor of intensity (current generated by the PMT) improvement is used to measure the intensity of the image generated by the optimized pattern against the initial generation.

Where the correction within an ex vivo sample using the sCMOS camera took nearly 15 minutes (Figure 4.16a) and achieved an enhancement of 1.9 across 50 generations, using a PMT with an exposure time 100ms reduced the correction time to under 9 minutes [56] (Figure 4.16b) and increased the intensity by a factor close to 2.2. Further reducing the exposure time to 10ms resulted in noisier measurements, bu the average intensity of each generation shows an increase in intensity of 1.75× in less than 90 seconds for 50 generations (Figure 4.16c).

[56] Apparent convergence was reached after less than 4 minutes.

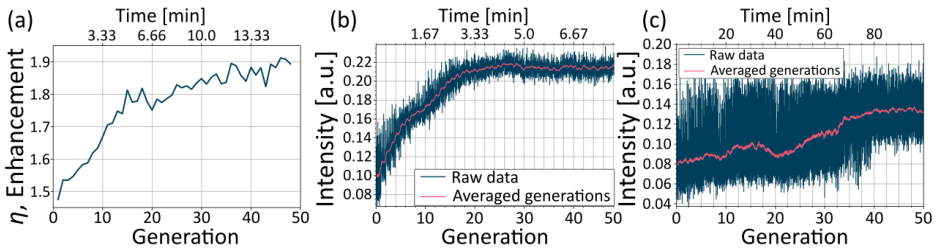

Figure 4.16: Raw and averaged intensities during the scatter correction within murine skull samples using SHG as the guidestar and a PMT as the detector. Long integration times of 100ms per individual result in smooth measurements (a), while shorter integration times of 10ms result in more stochastic intensity measurements (b).

As PMT gain is an important factor in the measurements of intensity, an investigation into the effect of gain on the resulting correction was conducted. Gain of a PMT also increases the noise floor, so that contribution of stray photons and dark current require longer exposure times to elevate the relevant signal beyond the background. A number of scatter corrections with exposure time set to 10ms were executed and the equalized intensity improvements plotted to show that enhancement was not affected by the gain (Figure 4.17).

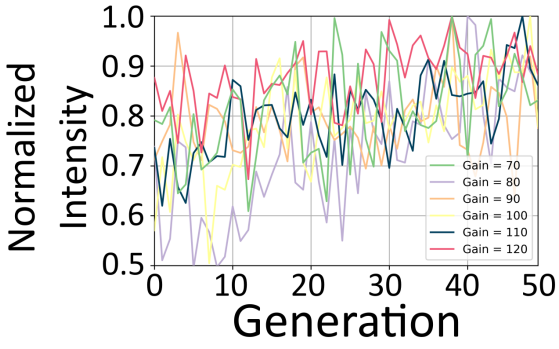

Figure 4.17: Normalized intensity increase shows that increases in PMT gain do not play a significant role in the scatter correction.

Implementation of this method into the existing LabVIEW code required a separate application where voltage from the DAQ attached to the output of the trans-impedance amplifier is input to the GA as the primary evaluation metric. Otherwise, the methods are similar, and an optimized pattern from the

GA is applied to the DMD while point-scanned imaging is conducted. Within an ex vivo murine skull, a region with the bone at a depth of approximately 120μm was identified and after correction, the scanned image shows increased intensity and SHG (Figure 4.18a), where an uncorrected pattern is applied, the intensity is low and the GFP labeled cell is dimly visible (Figure 4.18b), but after correction, the cell is clear (Figure 4.18c) and the peak intensity is increased by 1.5 (Figure 4.18d), while the spatial frequency is improved by 48.4% (Figure 4.18e). While collagen is visible when the uncorrected DMD pattern is applied (Figure 4.18f), the intensity is increased and more contrast is visible when the optimized pattern is applied (Figure 4.18g). At the indicated line, the cross section reveals an increased intensity of $1.5\times$ (Figure 4.18h) and an improvement of 41.9% (Figure 4.18i).

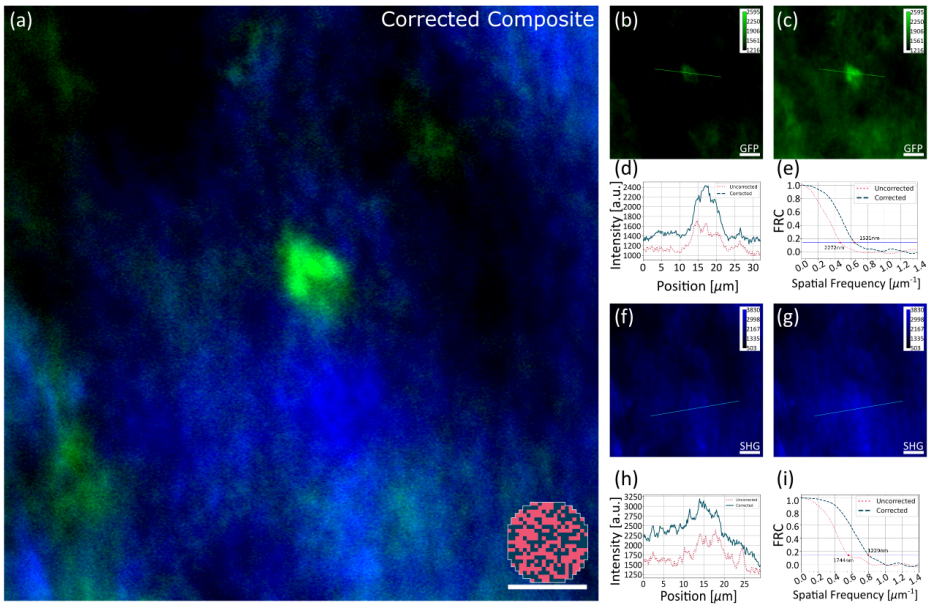

Figure 4.18: At a depth of approximately 120μm the scanned composite image reveals a GFP labeled cell, with the corrected pattern inset (a). The scanned image of GFP without correction shows fewer visible punctate mitochondria (b) but after correction the intensity is improved (c) by a factor of 1.5 at the indicated cross section (d) and spatial frequency is improved by 48.4% (e). Application of an uncorrected DMD pattern results in an SHG image where little SHG is visible (f), but the intensity is increased after correction (g) by a factor of 1.5 (h) and spatial frequency by 41.9% (i). Exposure time was set to 10ms per individual for a total exposure time of 90 seconds. Scale bar is 10μm.

While the overall intensity increased when using the single-pixel camera, the improvement is lower than the increase when using the sCMOS camera, but another difference is visible. The optimized pattern when using the sCMOS camera appears to have a larger continuous area, while the resulting pattern when using a PMT appears to bear more resemblance to a random pattern generated during the initial generations of the correction. As a result of this observation, other aspects of the pattern were investigated to understand the effect of pattern sparsity among other pattern characteristics on effective correction.

What appears to be an apparent difference in the optimized patterns between the two methods is the nature of the patterns. Beginning from an uncorrected pattern (Figure 4.19a), which appears to be random, the resulting optimized pattern when using the PMT as collection device (Figure 4.19b) appears to be as random as the initial pattern but the optimized output from the CMOS camera correction appears more structured (Figure 4.19c). With the restriction on patterns to not exceed $\sim$50% on segments, we can see that the PMT-based pattern is pushing against this restriction, while the other patterns did not trigger the restriction (if triggered, the restriction will reduce the total number of on segments to exactly 195 of 373.) This could indicate that during the optimization, the PMT-based solution seeks to switch more segments on, as if to open an aperture, while also incorporating more segments that increase intensity that others. This may not be the case for the CMOS-based optimized solution which appears to aggregate on segments in a region of the pattern, but does not exceed $\sim$50% on segments. Variation in patterns can measured by the Hamming distance, which indicates the minimum number of changes required to turn one binary pattern into another [146, 161]. The distance between the two optimized solutions is 178, which is less than the distance between the uncorrected pattern and either solution but is so large as to indicate that they are not related (Figure 4.19d).

To verify that the genetic algorithm aggregates DMD segments more when using the CMOS camera than it does when using the PMT as collection component, we analyzed the connectedness of the patterns. Connected-component labeling is a technique applicable to binary digital images and creates a labeled image in which the positions associated with connected components of the binary image have a unique label [162]. The labeling can be done according to 4-connected or 8-connected neighborhoods. In the 8-connected paradigm, pixels that are connected at 45° or adjacent (sharing a side) are considered connected, whereas the 4-connected paradigm only considers pixels directly adjacent as connected. Using the 4-connected neighborhood convention, we analyzed the uncorrected, PMT-based at 10 and 100ms, and CMOS-based at 10ms and 100ms

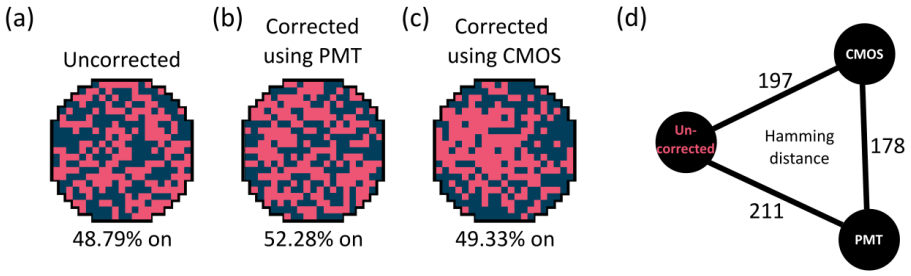

Figure 4.19: Beginning from an uncorrected pattern (a) comprised of 373 total segment, set to $\sim 50\%$ on, the PMT-based scatter correction results in a seemingly random pattern (b) with 52.3% segments on. The CMOS-based corrected DMD pattern appears more structured (c), with 49.33% segments on. Measuring the Hamming distance between these patterns shows that the vectorized patterns are very different (d).

corrected patterns (Table 4.2). We found that when the integration time of the collection is extended, more aggregation occurs. When the integration time was set to 10ms, the PMT-based correction generated a pattern with 38 connected components, but when integrating over 100ms, the total number of connected components reduced to 21. Similarly, the CMOS-based generated patterns reduced from 30 (10ms integration time) to 25 (100ms integration time). This reduction indicates that larger connected regions results in more significant improvement of the evaluation metric used during optimization. The mean number of connected components measures the average number of segments in connected components and shows separation between the PMT- and CMOS-based corrections at 100ms. Here the CMOS-based correction grouped an average of 6.233 segments, which is 2.957 lower than the PMT-based mean of 9.19. More tellingly, the median number of connected components, 2 for the CMOS-based correction, and 1 for the PMT-based corrections, reveals that more one-segment regions appear in the PMT-based correction. A median value of 1 shows how more small connected regions are generated. A standard deviation of 26.005 (CMOS-based; 10ms) indicates that many small regions are generated, but that one large region exists, as opposed to a standard deviation of 9.009 (PMT-based;10ms) which shows that the number of segments in connected regions is more consistent in number. Further confirmation of segment aggregation can be found in the size of the largest connected label by segment count as percentage of the total number of on segments. The largest connected region in the uncorrected pattern is 14.57% of the total segments

Table 4.2: Connected components labeling of DMD patterns

	Uncorrected	PMT (10ms)	PMT (100ms)	CMOS (10ms)	CMOS (100ms)
Total label count	28	30	25	38	21
Mean	6.357	6.066	6.233	4.912	9.19
Median	2.5	2	2	1	1
Mode	1	1	1	1	1
Standard Deviation	10.59	26.005	19.68	9.009	19.301
Largest region as %	14.47%	17.26%	29.76%	11.8%	18.3%

(55 of 373) within the active region of the DMD, which is smaller than that of the 19.3%(72 of 373) within the PMT-based optimized pattern, and 29.76% (111 of 373) of the CMOS-based optimized pattern. This statistical measurement confirms that the CMOS-based optimized patterns aggregate regions of segments.

4.8 Segment Sparsity

While optimized patterns identified by the GA thus far have been limited to a maximum of 52.5% segments *on*[57], based on the outcomes of the GA which often returned patterns with fewer than 50% *on* pixels, we investigated the effect of reducing the maximum number of *on* pixels further, to 20%, 30%, and 40% to compare against the 50% that had been used thus far. Reducing the number of *on* segments reduces the degrees of freedom, which runs counter to the transmission results where we found that more degrees of freedom result in improved enhancement, but results in the epi-detection configuration revealed that lower segment counts gave the highest enhancement.

[57] A maximum of 196/373, 754/1436, and 3037/5785 for the three segment counts used throughout.

Genetic Algorithm parameters from the prior experiments were maintained, with exact generations, population size, mutation rates, and crossovers constant across all experiments. The difference was only introduced by changing the initial populations to the specified percentage of *on* segments and limiting subsequent generations to a matching percentage of *on* segments.

We found that when reducing the maximum number of segments and implementing a scatter correction on the same spot at a depth of 100μm, the measured enhancement was best when 20% of the segments were used ($\eta = 1.525$), while when 30% were used, the enhancement was slightly lower ($\eta = 1.51$), but still better than the enhancement when 40% and 50% were used ($\eta = 1.465$) (Figure 4.20). This result confirms that in the epi-detection, with fewer degrees of freedom, the enhancement outperforms cases in which more degrees of freedom are available.

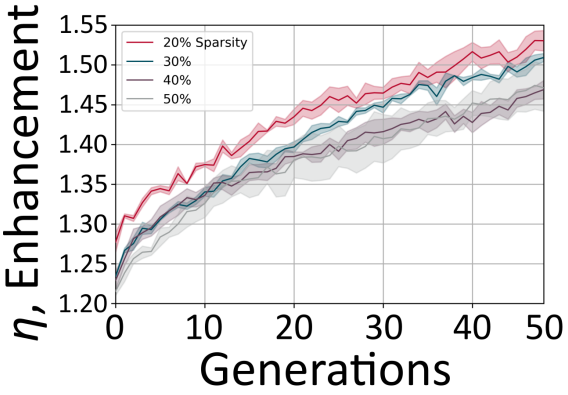

Figure 4.20: A comparison of the effect of sparsity of the DMD pattern on the enhancement, showing that the enhancement when limiting the number of on segments to 20% percent results in the highest enhancement while 40% and 50% yield the lowest enhancement.

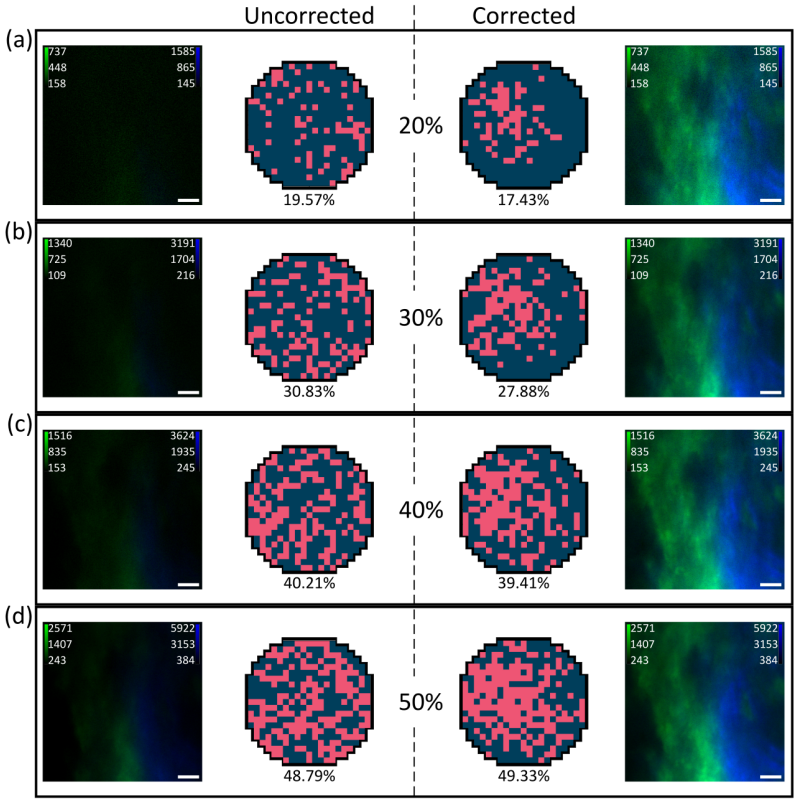

Figure 4.21: At a depth of approximately 120μm within an excised murine skull, the improvement in both fluorescence and SHG is measured when a maximum of 20% (a), 30% (b), 40% (c), and 50% (d) of the segments are allowed on. Note the different calibration bars indicating different intensities due to lower excitation power when fewer segments are switch on. Scale bar is 10μm.

When the resulting optimized DMD pattern is projected onto the DMD during point scanned imaging, lower sparsities reduce the imaging power (to the sparsity of the pattern, e.g. 20% sparsity reduces the power to $0.2\times$input power), so that the images when an uncorrected pattern is applied are extremely dim, such as in the case of 20% (Figure 4.21a). We found that when a limit was set, for the cases of $20-40\%$ sparsities 4.21a-c), the genetic algorithm identified that utilization of fewer segments further maximized the evaluation metric (intensity). In the case of 30% sparsity, the initial pattern was 19.57% (73 of 373 segments) and after optimization only 17.43% (65 of 373) remained, which is a reduction of 2.95 percentage points. This indicates that the algorithm identified that reducing the number of segments is potentially an effective approach to improved scatter correction.

The degree of improvement in the GFP intensity is highest when limiting the optimization to 30% of the segments *on*, resulting in a 3-fold increase, whereas in the SHG, a nearly 12-fold increase in intensity was found when the sparsity was set to 20% (Figure 4.22a). When considering the spatial frequency improvements, both GFP are maximized at a sparsity of 20% (Figure 4.22b). Current work in the literature shows maximum measured intensity when the sparsity is 40% [160], which is not a directly comparable metric, but confirms that reducing the sparsity can lead to improved scatter correction.

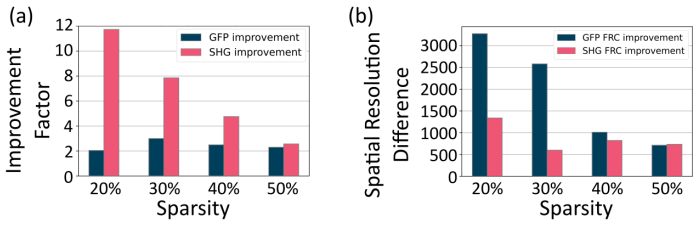

Figure 4.22: Improvement in intensity across various sparsity of segments shows that the GFP enhancement is maximized at a sparsity of 30%, but at 20% in SHG (a). The difference in spatial frequency when comparing the uncorrected to the corrected DMD pattern shows a maximum difference when the sparsity is 20% in both GFP and SHG (b).

We see that reducing the sparsity of *on* segments leads to better scatter corrections, the excitation power losses are not insignificant. Within our setup, the 3W at the output of the light source is quickly reduced along the optical path (especially by the compensatory diffraction grating and the DMD) and ultimately only 10% of that power is available at the sample. Reducing the sparsity further reduces this power and makes imaging very difficult. In the case of surplus power available, the principle of reducing the segment sparsity can

Table 4.3: Optimized pattern characteristics

Sparsity	Connected Components		Ratio	Largest component as %
	Uncorrected	Corrected		
20%	46	25	0.54	18.67
30%	54	31	0.57	47.3
40%	43	31	0.72	55.7
50%	30	28	0.93	66.3

be useful in imaging of thick tissues and living samples, but in our case power losses become debilitating.

Observations of the optimized patterns and comparing them to the initial uncorrected patterns indicates once again that the optimized patterns form large continuous groups of *on* pixels. To measure the degree of connectedness [162] of the binary pattern, image analysis is performed, counting the number of isolated or continuous regions on the DMD surface for each of the patterns presented in Figure 4.21a-d (Figure D.3).

Grouping of segments becomes more apparent when lower sparsity is used, with the ratio of connected components after the correction to before the correction measuring 0.54 with 20% sparsity, reducing the number of isolated segments (Table 4.3). The ratio for the 50% sparsity shows little change between uncorrected and corrected, with a ratio of 0.93. We can see that there is a large continuous region in the optimized DMD pattern when the sparsity is 50%, so with more degrees of freedom, the ratio metric is no longer useful to illustrate the continuity present in the patterns. An alternative is to measure the percentage of the DMD that the largest continuous region occupies relative to the maximum allowed in the specific sparsity. In doing so, we see that the lower sparsity 20% (18.67% of maximum segments) continuous region is actually less pronounced than that of the 50% sparsity (66.3% of maximum segments). This can be explained by the size of the search space and how the likelihood of isolated segments increases when more negative space remains (for example in the 20% sparsity) as the mutation rate decreases. In the case of the 50% sparsity, this likelihood is lower, and more segments end up being connected.

4.9 Aberration and Scatter Correction Combined

The benefits of adaptive optics are applicable in several types of light microscopy and have been widely reported in modalities such as confocal microscopy[163], 2-photon microscopy [123, 164–166], SHG imaging [167] and SIM [77]. These reported methods target low order aberrations, limited by the electro-optical component employed to compensate for the distorted wavefront. Higher order aberrations require electro-optical devices capable of high spatial frequency manipulation such as the DMD that has been employed in our scatter correction. Combining the low and high order aberration correction techniques will maximize the recovered signal at depth within tissue [168].

By executing a low order aberration correction of the sample at depth, a more effective scatter correction will be enabled. To this end, we combined the DM and DMD into custom setup (Figure 4.6), projecting the system correction onto the DMD and finding an SHG spot as deep as possible within the bone of an excised murine skull. Provided enough photons are collected, a sample correction can be executed using a maximum intensity metric, sweeping the lower 15 Zernike modes from -2V to $+2$V. Projecting the resulting compensatory phase map onto the DM will sharpen the PSF measured at this depth. A scatter correction at a slightly deeper position is enabled by this AO sample correction.

Low order aberrations such as astigmatism or defocus, originating from the optical components can be corrected by measuring the wavefront propagating into the back aperture of the objective lens and applying a compensatory phase onto a low order electro-optical component such as a deformable mirror (DM) [123]. This system correction ensures that subsequent aberrations impacting the image quality are caused by the sample. In less thick tissue samples in the order of tens of microns, contributions of low order aberrations are minimal, but as tissue is extended, low order aberrations and the scattering of emitted photons combine to degrade the resulting PSF significantly. Beyond a single scattering length ($\sim 45\mu$m in bone) the emitted SHG PSF intensity declines sharply so that imaging through whole skull without correction at wavelengths in the visible range is not feasible. To correct both low order aberrations and losses associated with scattering tissue, we combine our previously established low order aberration correction [123], with our binary modulation scatter correction using a DMD pattern optimized by a genetic algorithm. We expect that the combination of corrective approaches will correct the large amplitude low order and low amplitude high order aberrations that restrict the depth of imaging in highly scattering tissues [168]. The base scatter correction applied

utilized $\sim$50% of the segments, and the aberration correction was limited to 15 Zernike modes, without considering the first three modes (piston, tip, and tilt). To establish the most effective aberration correction within bone tissue, we examined an excised murine skull sample, conducting low order aberration correction at a depth of $\sim 65\mu$m with an uncorrected pattern projected onto the DMD. Here we found that the aberration correction failed (Figure 4.23a), characterized by the high phase values (limited to -π to π) measured by the correction algorithm which indicates that no significant peak was found during the sweep. When applying an corrected pattern to the DMD, we found that the aberration correction yielded a phase map recovering the PSF (Figure 4.23b). A cross section through the resulting images shows a 1.7-fold mean intensity increase where no peak is visible in the image resulting from the uncorrected pattern, but a sharp peak exists in the image resulting from the corrected DMD pattern (Figure 4.23c). The two peaks visible in the cross section (Figure 4.23b,c) 1.4 times above the mean intensity, and 1.8 times above the minimum intensity. As the focal plane is withdrawn through the sample in steps of 5μm, the corrected DMD pattern enables aberration correction while the uncorrected pattern does not yield useful correction. The deepest point in the sample at which an uncorrected DMD pattern aids in a sample aberration correction is 50μm, where a PSF is recovered, but the necessary phases projected onto the DM have outlier high values (Figure 4.23d). An aberration correction using the corrected DMD pattern yields a much sharper and brighter PSF (Figure 4.23e). A cross section through the resulting images shows a 1.7-fold peak intensity increase and generation of a peak (FWHM of 1.56μm) of the PSF, where no distinct peak was present in the uncorrected image (Figure 4.23f). These results confirm that scatter correction enables an improved sample aberration correction.

We then investigated the degree to which this combination of aberration and scatter correction affects scanned imaging. Here we found that imaging at a depth of $\sim 110\mu$m in an excised murine skull sample, without either aberration or scatter correction, that the resulting image is lacks contrast and is dim (Figure 4.24a). When only aberration correction is applied, the intensity increases marginally by a factor of 1.4 (Figure 4.24b). After a corrected DMD pattern was projected onto the DMD, but no aberration correction applied to the DM, a significant increase in intensity in evident (Figure 4.24c) and some subcellular features are visible. Finally, when the aberration correction was added to the scatter correction, the intensity was maximized and subcellular features became visible (Figure 4.24d). Cross sections of the GFP (green line in a) and SHG (blue line in b) across each of the configurations showed that without scatter

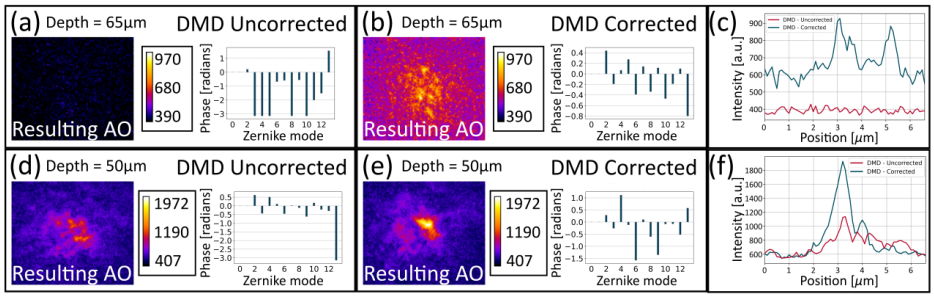

Figure 4.23: A comparison of low order aberration corrections at two depths. At 65μm deep the aberration correction fails when an uncorrected pattern is projected onto the DMD (a), but when the corrected pattern was used, the correction succeeded (b). A cross section across the center pf (a) and (b) shows a 1.7-fold increase in the mean intensity of the SHG PSF (c). At a depth of 50μm the uncorrected DMD pattern resulted in a successful aberration correction (d) and the aberration correction using the corrected DMD pattern resulted in a smaller, brighter SHG PSF (e). A cross section of (d) and (e) shows that the point improved by a factor of 1.7 and narrowed (f).

correction the intensity of both GFP and SHG was low, but increased more than 2-fold when the scatter correction was applied (Figure 4.24e,f). Aberration correction improved the intensity in both cases with or without scatter correction by a factor of approximately 1.2 and contributed to the visibility of more features and separate peaks in both GFP and SHG intensity profiles.

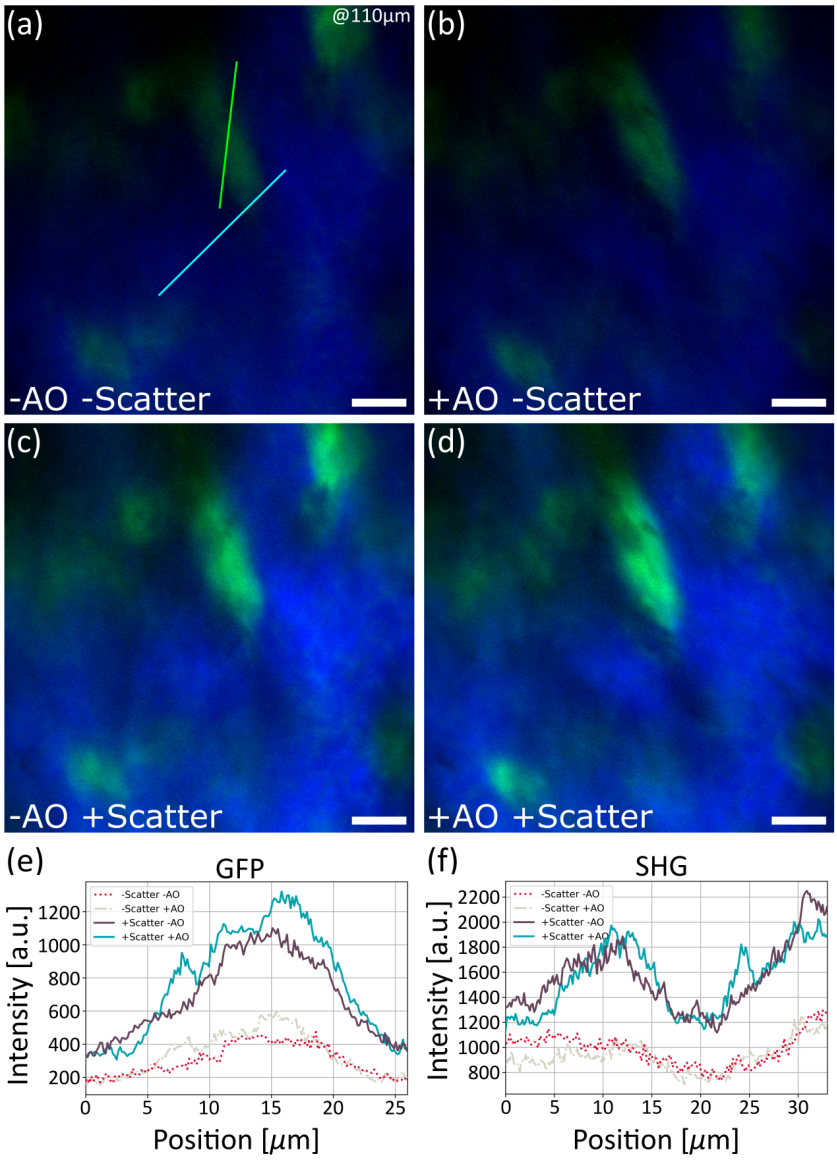

Figure 4.24: Without scatter or aberration correction the scanned image of an excised murine skull at a depth of $\sim$110μm presents dim GFP and SHG (a). Conducting a sample aberration correction step improves the intensity with new features visible within the cell of interest (b). After applying a scatter correction mask to the DMD, but without aberration correction, we see significant improvement in both GFP and SHG intensity (c). With both aberration and scatter correction applied, we see maximized intensity and finer features within the scanned image (d). A cross section of the GFP in each of the images confirms that the intensity is maximized when both corrections are applied (e) and the same is reflected in the SHG channel (f). Scale bar is 10μm.

4.10 Discussion

Highly scattering tissue such as bone negatively affects imaging quality by inducing low order aberrations and scattering the wavefront so that imaging at depths well beyond the scattering length of bone becomes challenging. We implemented a rapid scatter correction technique collecting the SHG PSF using a single-pixel component and reducing the integration time to 10ms to correct the scattering wavefront by binary modulation. This short exposure time enables rapid completion of the optimization of a DMD pattern within 90 seconds, and subsequent scanned imaging is improved by a factor of 2 in the GFP channel and by a factor of approximately 2 in the SHG channel. These improvements are less pronounced than when the CMOS camera is used with longer exposure times and a more focused region of the SHG PSF used as the evaluation metric for the optimization. We show that the CMOS-based optimization pattern contains a more continuous region of segments on the DMD because of a more consistent measurement of each individual due to longer exposure time and more consistent gain.

The sparsity of the DMD segments used in each correction is considered, and we find that reducing the sparsity of the segments to 20% results in the most significant scatter correction improvement. Set at 20% sparsity, the corrected pattern further reduces the number of on segments to 17.43% and scanned images using the pattern results in a nearly 12-fold increase in SHG intensity, and a spatial frequency improvement of 1.6 in SHG, while improving the spatial frequency of the GFP by more the 2.5 times. This improvement further confirms that binary modulation relies on removing elements that negatively interfere in degrading the PSF quality as opposed to increasing positive interference [84, 91]. Examining low order aberration and scatter correction methods we found that when an uncorrected DMD pattern is projected onto the DMD, at 50μm inside a murine skull sample a meager aberration correction is possible, while a corrected pattern results in an excellent low order aberration correction. However, at depths exceeding 50μm, the corrected DMD pattern is necessary to achieve any low order aberration correction as the uncorrected pattern fails to achieve any useful corrections. Finally, when combining the low order aberration and scatter corrections for scanned imaging, we saw that the aberration correction played a small role in improving the contrast of subcellular features 110μm below the surface of the skull. Here the scatter correction increased the intensity more than 2-fold in GFP and nearly 2-fold in SHG, but subcellular features were most distinct and brightest when both aberration and scatter correction were applied. Where surplus excitation power is available, the implementation

of low sparsity DMD-based binary scatter correction, combined with low order sample aberration correction can enable imaging of bone cell dynamics in the marrow and allow investigation of osteogenic processes in living bone tissue.

Chapter 5

3-Photon & Image Scanning Microscopy

super- *(prefix)*: larger, more effective, more powerful, or more successful than usual; very or more than usually

— Cambridge Dictionary

5.1 Introduction to ISM

Work described thus far has been conducted by collecting the epi-detected light by means of photon multiplier tubes (PMT), which are single pixel devices with high gain capability and relatively high quantum efficiency. The primary advantage of PMTs is the fast response and high photon sensitivity. Once these advantages have been leveraged to maximize point scanned imaging at high speed and improved by implementations of adaptive optics and scatter correction, concepts of super-resolution must be considered to further improve the spatial resolution and intensity. Stimulated emission depletion (STED) microscopy creates super resolution images by selectively deactivating fluorophores thereby enhancing the resolution of the system [169]. STED operates by shaping the PSF, but the image is created by collecting photons on a PMT or avalanche photodiode (APD). As opposed to conventional photodiodes (PIN) which operate in the linear mode with low output current and limited gain, APDs operate in reverse bias taking advantage of the avalanche breakdown to amplify very weak signals. By cleverly optimizing the structure of the APD junction, higher gains in the order of 1000s can be achieved with higher quantum effi-

ciency than PMTs. But even with the improved sensitivity provided by APDs, STED requires complex instrumentation to operate effectively [170].

Another microscopy technique that has been briefly discussed is confocal laser scanning microscopy (CLSM) which is a scanning technique that uses PMTs or APDs to collect photons and generate images[58]. CLSM operates similarly to conventional point scanning configurations, but introduces two pinholes, a first at the excitation source reducing the focal volume thereby reducing the the region within the sample that generated fluorescent signal. Another pinhole is positioned in front of the single pixel detector conjugate to the sample plane (confocal) which rejects significant amounts of fluorescence emitted by the sample that is not conjugate to the pinhole aperture. Only light that is perfectly delivered through the aperture of the pinhole is used to form the final image which is free of background noise. CLSM produces thin optical sections through fluorescent samples that enables imaging of living and fixed samples with vastly improved Z-stack capability when compared against physical sectioning of other methods of microscopy.

[58] The first records of confocal microscopes extend as far back as 1940 by Goldman, before Minsky filed the patent for the method [171] and lasers were first introduced into the confocal configuration in 1969 [172].

The first theoretical analysis of the method was published in 1977[59] [2] and shows how the resolution improvement expected from CLSM is a factor of two. Image improvement by using CLSM is dependent on using a pinhole significantly smaller than the airy disk [173]. With the integration of such a small pinhole into the system, much of the undesired out-of-focus light is rejected, but so too is much of the desired emitted light. The result is that in practice, biological samples with low fluorescent signal force microscopists to use larger pinholes, ultimately reducing the effective gain of CLSM to approximately $\sqrt{2}$. At its core, CLSM reduces the illumination focal volume to reduce fluorescence in planes outside the sample plane, and rejecting out-of-focus emission light to improve PSF quality, and not extending information acquired, and as such is not a true super resolution technique.

[59] This was also the first time the term confocal was used.

However, CLSM is the underlying principle of image scanning microscopy (ISM) which is based on the idea of overlapping the excitation and emission PSFs of a confocal microscope [57], but it can also be described in terms similar to SIM [58]. In a scanning microscope, a diffraction limited spot is raster scanned across the sample, exciting the sample, meaning that the Fourier transform of this spot contains each of the frequencies collected by the objective lens. Spatial frequency components of the sample are mixed with the excitation and high spatial frequencies are moved into the range of the detection OTF (optical transfer function). What this means is that the maximum spatial frequency moved into the supported region of the detection OTF is doubled [174]. By adding the pinholes to reduce the focal volume and reject out-of-

focus light some of this information is recovered, but as mentioned, reduces the signal-to-noise (SNR) so much as to require opening the pinhole and losing this information. ISM works to recover this loss of frequency information. The optical setup necessary to implement ISM must formulate a configuration to capture emission from the scanned spot through the pinhole on an array of collection devices. By replacing a single-pixel detector by a multi-pixel camera such as a CCD or CMOS, the scanned image can be scanned across the sample and a super-resolution image construction by pixel reassignment [175] (instead of a single pixel acquired for each scan position, an image is acquired - thus the name). For each scanned position, the captured image is reshaped according to several factors, and the reconstructed image is formed according to summation of these reassigned pixels. The reassignment configuration can be implemented by using an all optical setup with PMTs, but the complexity is prohibitive [176]. Alternatively a pixel reassignment using a spinning disk approach which speeds up the process can be used [177].

While use of a CCD in this configuration proved successful, light gathered by the camera is spread over the imaging surface and each pixel collected fewer photons, so that ultimately longer exposure or dwell times are needed. By using multiple excitation spots, this time can again be reduced [59]. Improvements such as this, PSF engineering [178], or improved reconstruction algorithms [179] have been the focus of improving ISM over the past decade. Many of these implementations are referred to as SIM techniques, as they use structured illumination[60], but in an approximation, these methods (SIM and ISM) can be considered as being cut from the same cloth, as SIM uses structured illumination and ISM structured detection. Where structured illumination suffers at depth, ISM based on point scanning architecture is more suited to thicker samples.

[60] Using spots as opposed to stripes.

Recently, the biggest opportunity for development in ISM came from the development of the APD and how manufacturers began to package them into arrays of single-photon avalanche diodes (SPAD). Where the pinhole in CLSM rejects out-of-focus light, it can be replaced by a SPAD where each pixel acts as a pinhole with all of the light reaching the plane of the camera collected. As the point is scanned across the sample, setup captures a single image for each pixel in the array (or scanned images) and the final image is reconstructed by combining the information contained in the two-dimensional dataset of the captured images [65]. Because the size of the focal volume is diffraction limited, it is typically in the range of a few hundred nanometers in diameter, a detector with few elements and no frame rate is required. SPAD cameras in the range of

5×5 or 7×7 with picosecond timing ability are ideally suited to overcome many issues that exist with ISM.

2-photon implementations of ISM using SPAD have begun to see implementation [180] increasing the resolution by a factor of two [181], and while there have been few implementations of ISM using SHG [182] and 3-photon [183], the opportunity to implement THG and 3-photon in ISM remains important in biologically relevant imaging.

To image osteogenic dynamics deep within bone, the long wavelengths that enable 3-photon and THG will provide deeper penetration than 2-photon imaging, and when combined with the power of ISM to increase the resolution[61] and scatter correction, we envisage an imaging system that will aid investigators in elucidating the mechanisms of osteogenesis and how osteopathies impact healthy bone development.

[61] Note that the longer wavelength reduces the resolution.

5.2 Wavelength Requirements

Multi-photon imaging of biological tissue is limited by the specific fluorophore in question, generally excited in the range 400 - 700nm. Excitation sources for this 2-photon imaging have traditionally been based on Titanium-Sapphire lasers that are tunable in the range of 640-1040nm [24, 184]. As previously discussed, the small focal volume is advantageous as the requirement for two photons to be absorbed for a molecule to emit fluorescence means that outside of this volume, no absorption takes place, and so the out-of-focus light is greatly reduced. Additionally, longer wavelengths are of lower energy and cause less photo-damage outside of the focus, but also experience much less scattering.

The scattering length of biological tissues increases monotonically with the wavelength, and using excitation at 920nm shows significantly longer effective scattering (μ_s [mm^{-1}]) [185, 186]. The absorption coefficient (μ_a[mm^{-1}]) of brain tissue at 920nm is almost negligible when compared to the scattering coefficient, but increasing the wavelength in pursuit of improved penetration, the absorption also increases so that the effective attenuation length (EAL) is given by [187]:

$$\frac{1}{\ell_e} = \frac{1}{\ell_a} + \frac{1}{\ell_s} \tag{5.1}$$

As the excitation wavelength is increased to 1320nm, the light experiences stronger water absorption and weaker scattering than at 920nm, but the EAL is twice as long (150μm at 920nm and 300μm at 1320nm) in the cortex subregion of murine brain tissue [186]. By further increasing the excitation wavelength to 1500nm we see the negative effect of water absorption of the excitation (EAL of

246μm in the murine neocortex) but again there is some improvement by using 1700nm (EAL of 375 in the murine neocortex) [25]. These measurements in the literature confirm the so-called "biological window" which is most useful for imaging biological tissue.

In the configuration of the SPAD implementation necessary for ISM, the emission light must be descanned along the same path as the excitation, so that the emission PSF is always located in the same position on the SPAD detector. THG and 3-photon excitation within the biological window (1300 - 1500nm) results in emission at wavelengths in the range of 433nm to 750nm[62], meaning that optical components in the descanned path would have to be compatible with wavelength ranging from 400nm to 1500nm. While 2-photon imaging requires a much narrower spectral band of antireflective (AR) coatings (400nm-1000nm for emission and excitation) compatible with current commercially available coatings (Figure 5.1) [63] there are currently no commercially available glass lenses necessary for the wide range of wavelengths necessary for 3-photon ISM. Many optical component manufacturers provide a wavelength range such as the "C" range (Figure 5.1), which would be suitable for the excitation, but incompatible with the emission. As such, an alternative scan engine for directing the excitation and emission is necessary.

[62] 433nm is the THG emission at 1300nm, and in a mixed mode system, SHG (while out of range of conventional SHG imaging) would result in 750nm when excited by 1500nm.

[63] Thorlabs options are presented in Figure 5.1, but other manufacturers have very similar options.

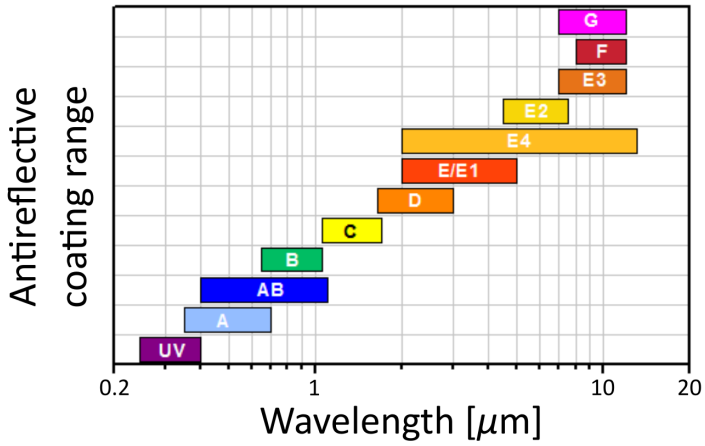

Figure 5.1: As per the Thorlabs listing of available antireflective coatings the AB coating is suited to 1- and 2-photon in both excitation and emission paths.

5.3 Achromatic Scan Engine

Conventional scan systems implemented in multi-photon imaging all have a similar configuration, where an excitation beam is raster scanned over the back aperture of an objective lens. This scanning is achieved by using either two galvanometer scanners, or a single galvanometer and a single resonant scanner, depending on the speed of the required scan. Generally, broadband AR coatings are applied to these mirrors compatible with wavelengths in a range from 500nm - 2000nm. While placement and alignment of these components is critical, scanning of the beam will contribute to aberrations within the imaging system as the beam is scanned across spherical glass lenses. Scan and tube lenses are specifically designed to compensate for these scan aberrations, but the AR coatings available for these components pull from the same stock as those previously specified (Figure 5.1), even as 3-photon imaging becomes more popular. Without options for broad spectra AR coatings in glass optical components, but with the knowledge that mirrors do have the option of silver or gold coatings with broad spectrum reflectance, an alternative for the scan and tube lenses can be found in off-axis parabolic (OAP) mirrors.

An OAP is a small section cut from a parent parabola which focuses a collimated beam, or collimates a divergent source, and the off-axis design separates the focal point from the rest of the beam path[64]. These characteristics allow OAPs to form optical relays with magnification and make them relatively easy to build into custom optical setups, the difference being based on a reflective paradigm as opposed to transmissive mindset. Importantly, the reflectivity of the OAP surfaces with silver coating provide $> 97\%$ between 450nm and 2000nm, which is ideally suited to the wavelengths necessary for excitation and emission in our proposed ISM.

[64] The off-axis angle can be selected from 15°-60° in steps of 15°, and 90°, to suit the construction angles on optical tables or other environments.

As near to an ideal scanning system would consist of a single scanning mirror, scanning the beam in both the x- and y-axes, and while such mirrors are approaching commercial and functional viability, the realistic solution is the implementation of two separate scanners. Simulations comparing the reference (single scan mirror) and parabolic scan engines reveal that the parabolic scan engine results in a field scan that closely matches results of the ideal (single mirror) configuration (Figure 5.2a) [188–190].

These simulations measure the deviation of the beam spot as it is scanned across a raster pattern (Figure 5.2b), where a slight coma aberration is introduced in both the reference and parabolic scan engines (Figure 5.2c-d).

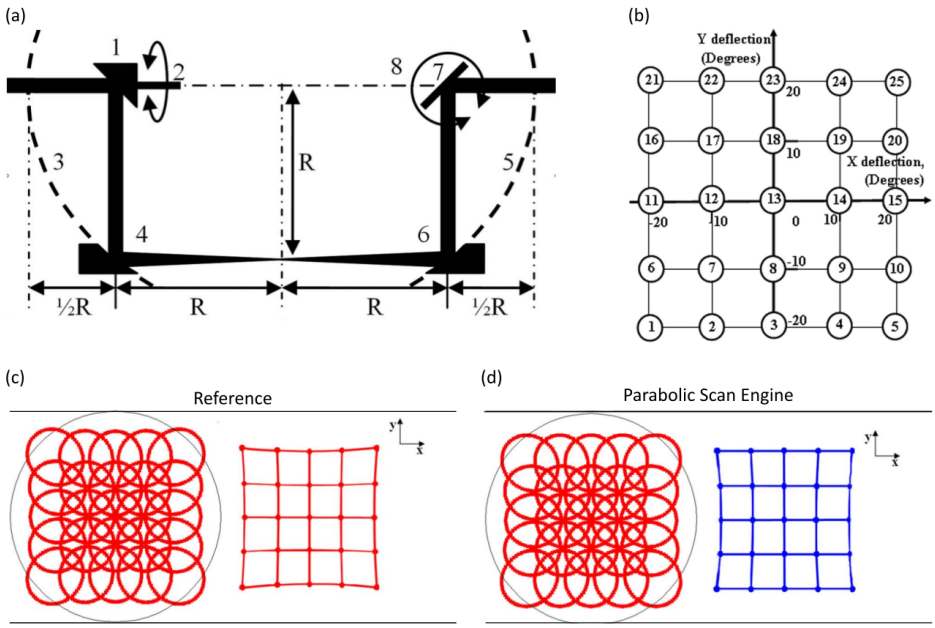

Figure 5.2: A parabolic scan engine incorporates a symmetrical configuration with four OAPs and two galvanometer scanners (a). Twenty-five scan field points (b) simulated shows aberrations introduced by the reference system (c) and parabolic mirrors (d) [188].

Based on the success of other works using OAPs to construct achromatic scan engines, our approach was to simulate our specific implementation using Zemax software which can accurately model optical components and their interactions. Importantly, the spot size required for ISM must be carefully tuned according to the airy disk size, or AU (airy unit). To optimize the configuration, the ideal magnification of the system needs to be identified so that photon collection is maximized without compromising the out-of-focus background rejection [191]. Directly comparing existing ISM configurations against our intended setup, we computed the PSF spot size, magnification and AU measure and compared it to our setup. The existing work [181] implements ISM in 2-photon by leveraging excitation to elicit emission in the range of 650nm, which then results in an AU of 1.494, which is ideally sized for ISM (calculations in appendix Figure E.1).

By overlaying the emission spot over the SPAD detector surface, we can see how PSFs imaged by each SPAD array element (or pixel) provide different information of the PSF. We see that in a SPAD configuration of 25 elements,

the emission spot can be imaged thoroughly by each of the 25 elements (5.3a) in existing successful implementations. With a magnification of 55.55, the resulting spot size is approximately 41.95μm which is far too small across the 50μm SPAD element, resulting in an AU metric of 5.96, which results in no improvement in resolution as the signal is almost negligible in the outer elements (Figure 5.3b). Tuning the magnification appropriately to 280 results in a emission spot size of 211.47μm and 1.182AUs for a spot emitted at 650nm, and 1.708AUs at a wavelength of 450nm (Figure 5.3c).

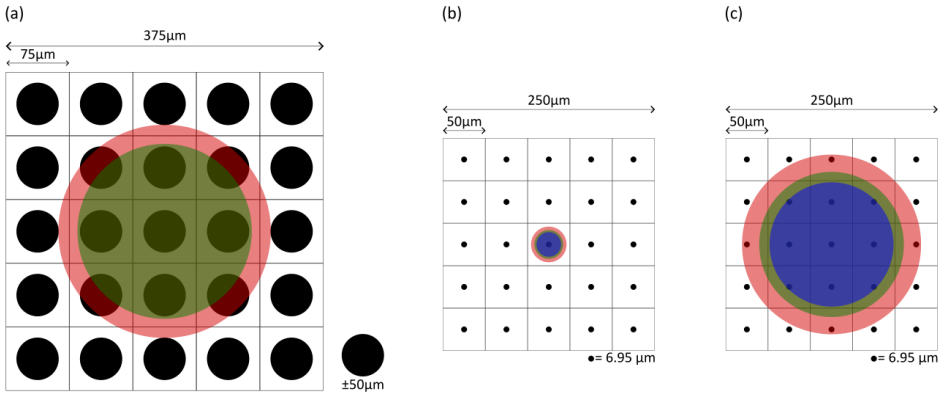

Figure 5.3: The ideal overlay of the spot (650nm & 425nm) across 25 SPAD array elements from existing literature [181] shows a well tuned AU metric (a). With poor magnification settings, the AU values overlay the emission spot on a single SPAD element (b), but with appropriate magnification, the AU metric is well tuned (c), similar to successful work (a).

By examining the emission spot overlaid in the model (Figure 5.3a,c), we see that two significant differences in the SPAD arrays exist. Firstly, the size of the elements in the array is 75μm in the existing work, while the element size in the SPAD device that we purchased (PF32-1M, Photon Force) is 50μm, and this has a direct impact on the necessary magnification to achieve a suitable AU. But the more significant difference is that of the effective element size (or fill factor), which in our configuration is much smaller ($\pm 50\mu$m vs. 6.95μm or 66.67% vs. 13.94%) which greatly limits the effectiveness in collecting photons[65]. While this fill factor is problematic in legacy SPAD devices (such as this), more modern devices have begun to deal with this problem, increasing the fill factor to over 80%. Older devices do require some degree of correction if the low photon collection is significant. Microlens arrays can be used to focus incoming light onto the 6.95μm region that is sensitive to photons. For the purposes of this implementation, we decided that the sensitivity of alignment required to

[65] This is without considering the quantum efficiency of the individual APDs, which will further reduce photon collection.

configure such a corrective action would be cumbersome and continuing with the low fill factor makes 3-photon imaging impractically difficult.

5.4 Simulations

With the optimal magnification of the beam calculated, the optical components required to achieve this magnification using OAPs could be modeled in Zemax. To emulate the simulations from prior literature, the polarity of OAPs must be identified. As previously mentioned, OAPs collimate divergent light and focus a collimated beam dependent on the propagation direction of the light. We simulated the flat galvo mirror to the collimated side of the OAP being focused by the OAP as "forward" (Figure 5.4a), and divergent light from a flat galvanometer to the focus side of the OAP as "reverse" (Figure 5.4b). Previous investigations and simulations [188] have shown that in the reverse configuration (Figure 5.2a) a perfect spot after scanning is the result. In our simulation, we found that when scanning in the x-direction across both the forward (Figure 5.4c) and reverse (Figure 5.4d) configurations resulted in little change in the wavefront, but when considering scans in the y-direction, there were significant aberrations (Figure 5.4e,f).

To quantify the wavefront aberrations the metric used was the root means square (RMS) error which is an important measure in optical systems. This metric provides a numerical representation of how closely the simulated (or measured[66]) wavefront aligns with a perfect wavefront. Calculation of the measure involves a comparison of the simulated (or real) wavefront against an ideal reference encapsulating the statistical average of squared deviations. A low error corresponds to an higher quality image produced by the system, with a value of zero matching the ideal wavefront completely [192]. Zemax does not propagate light through the simulated system but calculates the RMS error by analyzing the geometric relationship between ray errors and wavefront errors. The assumption of perfect components is also made, which cannot be expected in reality, so RMS error in simulation is the best-case scenario as manufacturing variations will impact RMS error. RMS error can also be described in terms of the Zernike modes which describe specific aberrations, such as coma, astigmatism, and defocus.

[66] The wavefront can be measured using Shack-Hartmann sensors as discussed in section 1.6. The wavefront can also be measured by interferometric and other means.

Another useful metric for image quality is the Strehl ratio[67], which also quantifies the aberrations that contribute to image quality loss. The Strehl ratio is the ratio of the peak aberrated image intensity from a point source compared to the maximum attainable intensity using an ideal optical system limited only by diffraction of a system's aperture [193], given by:

[67] Named for Karl Strehl who proposed the metric in 1895.

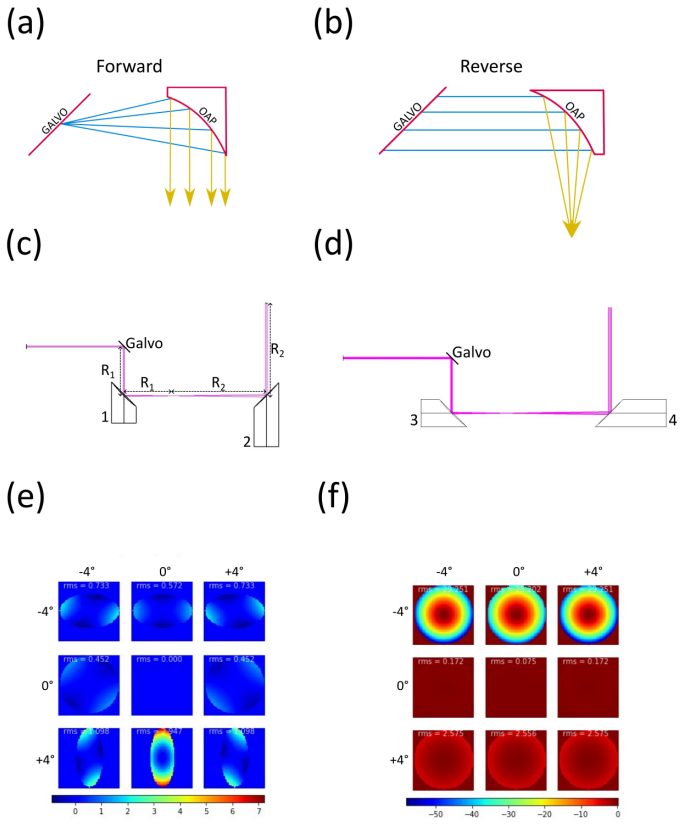

Figure 5.4: Forward (a) and reverse (b) configurations of the OAP relative to the direction of light. Emulating the existing literature, we implemented the scan engine in both forward (c) and reverse (d) configurations to evaluate the spot quality. Wavefront analysis in extreme scan positions in both the x- and y-directions (e-f).

$$S = \exp\left(-\left(\frac{2\pi\sigma}{\lambda}\right)^2\right) \tag{5.2}$$

where σ is the RMS error and λ is the wavelength of light in the system. The Strehl ratio can also be estimated by considering only the RMS error, simply [193]:

$$S \approx e^{-\sigma^2} \tag{5.3}$$

The Strehl ratio is widely used in astronomical seeing[68] and to assess the quality of images generated by adaptive optics microscopy systems [194]. A

[68] Astronomical seeing is the degradation of the image of astronomical objects as a result of the atmosphere of Earth.

value of 1 indicates that a perfect recreation of the object is present in the imaging system and gives the optical designer a summary value to describe the system. Generally one would decide whether a system is operating satisfactorily with a Strehl ratio of 0.8 or should there be an effort to maximize the Strehl ratio. In our case, the maximum Strehl ratio is desired, and because the RMS error can be described in terms of Zernike modes, we could also measure the effect of specific Zernike modes on the system Strehl ratio.

In the unscanned head-on beam position across the OAP scan engine, the RMS error should ideally approach 0, and the Strehl ratio 1, but at the extreme scan positions, we expect the maximum RMS error and minimum Strehl ratio. For both configurations we found low RMS error ($\sigma = 0.247$), but were interested in the impact of low order Zernike modes, as they could potentially be computationally corrected. As such for the reverse configuration, the overall Strehl ratio in the unscanned position was 0.496, which is extremely low, but the Strehl ratio for Zernike modes four and above, was 0.982, which means that the majority of the aberrations are due to Z_1 (Piston), Z_2 (Tilt X), and Z_3 (Tilt Y) (Figures E.4 & E.6). In the forward configuration the RMS error is much lower, measuring at 0.000, with the Strehl ratio on the edges of the scan returning the lowest Strehl ratio of 0.883, which is satisfactory in our setup. Again, we saw that the Strehl ratio for Zernike modes four and above was very high, so the majority of aberrations were caused by low order modes tip and tilt.

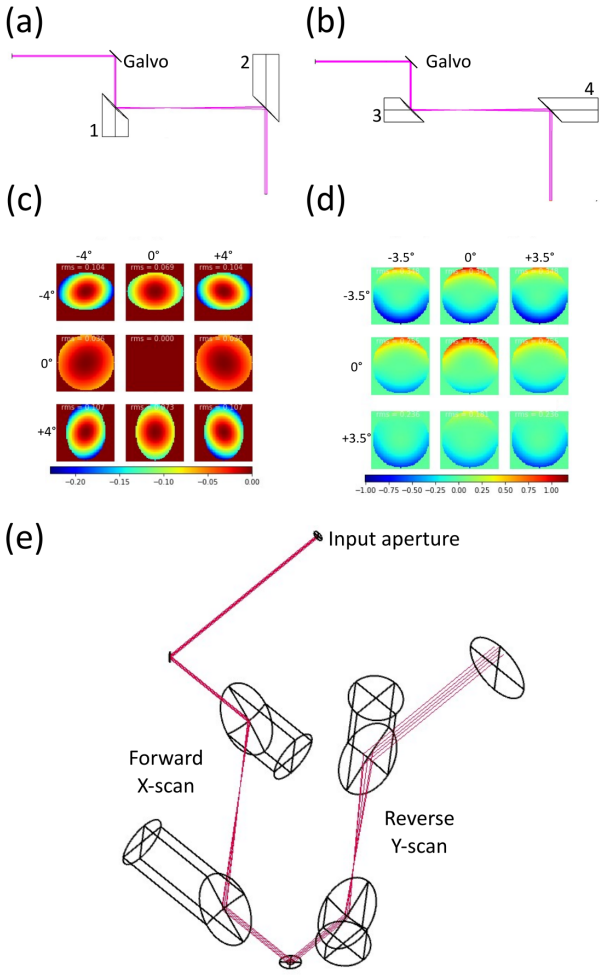

Figure 5.5: Based on results of prior simulations, the forward (a) and reverse (b) configurations of the OAP were simulated. In the forward configuration, the resulting wavefronts change more in the y-scan (c), but in the reverse configuration the wavefronts are consistent in both scan directions, but have more aberrations (d). This led to the final configuration where the x-scan was implemented using the forward configuration, as y-scan the reverse (e).

During analysis of the simulation results, we found that when positioning the OAPs with light propagating into the scan engine and designing the orientation to keep the light on the same side of the OAPs (Figure 5.4c,d) more significant aberrations were visible than in the case where the OAPs were not propagating light in the same direction (Figure 5.5a,b) (Full simulation results in Figure E.3, E.4, E.5, and E.6). We found that when scanning in the x-direction in either configuration, again almost no aberrations were revealed, but when scanning in the y-direction in the forward configuration fewer aberrations are measured (Figure 5.5a,c). When scanning in y-direction in the reverse configuration, even fewer aberrations are measured (Figure 5.5b,d). As such, the four OAP configuration to scan across both x- and y-directions can be implemented with four OAPs forming two relays, the first scanning in the y-direction in the reverse configuration and the second scanning the x-direction in the forward configuration (Figure 5.5e).

The limited number of commercially available OAPs and the requirement for specific magnification to size the emission spot perfectly according to the AU means that some compromise must be made so ultimately, we decided to use this configuration and correct aberrations computationally.

5.4.1 Final ISM achromatic scan engine layout

A 10W laser (Pharos, Light Conversion) outputs 1030nm into a non-collinear optical parametric amplifier (NOPA) (Orpheus, Light Conversion) which generates light in two ranges, a signal output in the range 650-940nm, and an idler output in the range 1160-2000nm[69]. Output power from the pump laser is controllable by means of a pulse pick off, which reduces the effective repetition rate of the pump, but does not change the pulse power, so that a more robust power control method is necessary. Power in the signal and idler paths is controlled separately by means of PBS cubes appropriate for the wavelengths in question (PBSH-450-2000-050, PBSH-450-1200-100, CVI Laser Optics), and half-wave plates (46-561, 39-049, Edmund Optics) that can be rotated easily to adjust the power. Light is then combined and propagated through a pinhole to ensure a Gaussian profile as the light is input to the OAP scan engine where two galvanometer mirrors (GVS001, GVS011, Thorlabs) scan the beam across the OAPs and ultimately into the back aperture of the 25× objective lens (XLPLN25XWMP2, Olympus). Olympus objective lenses have a focal length of 180mm, but the OAP with the nearest focal distance is 177.8mm which is very close. Light emitted by the sample is then collected by the objective lens and a removable dichroic mirror (FF705-Di01-25x36-T3, Semrock) can pick-off the emitted light which is then focused through an appropriate filter

[69] These outputs are two separate physical apertures, and the beams are put onto the same path as per figure E.7

onto the PMT (H7422-50, Hamamatsu) for a conventional implementation that can be controlled by means of scanimage software [119] after the electrical signal from the PMT passes through a trans-impedance amplifier (DHCPA-100, Femto) and acquired by a digital acquisition card (PXIe-6341, National Instruments). The descanned emission (when DiM_2 is removed) is propagated across the OAPs and focused onto the SPAD camera (PF32-1M, Photon Force) (Figure5.6).

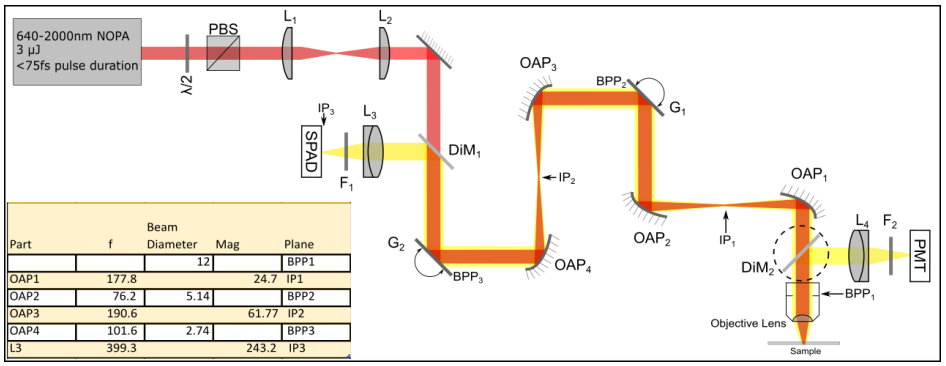

Part	f	Beam Diameter	Mag	Plane
		12		BPP1
OAP1	177.8		24.7	IP1
OAP2	76.2	5.14		BPP2
OAP3	190.6		61.77	IP2
OAP4	101.6	2.74		BPP3
L3	399.3		243.2	IP3

Figure 5.6: Schematic diagram of the optical components used to construct the custom achromatic microscope.

5.5 SPAD Characterization

One of the primary appeals of SPAD cameras is the high-speed transfer of frames, but there are a few disadvantages to using SPAD cameras. As the technology was in its infancy, the fill factor of the elements was very low (the PF32-1M device fill factor is approximately 13.9%), the quantum efficiency is lower than many PMTs, uncooled cameras are highly susceptible to noise, and the nature of the individual elements is fixed once the manufacturing is complete. This means that a map of the camera can be recorded, and so-called hot pixels will always return much higher values than those operating with low a noise floor. Characterization of our 32×32 SPAD was necessary to identify positions on the array that contain the fewest hot pixels, and many such regions exist after mapping our specific device (5.7a,b). Further, manufacturing standards specify that a dark count test conducted over one minute must return counts of fewer than 100 photons by more than 80% of the pixels[70]. Our results confirm that the SPAD camera meets this standard (Figure 5.7c).

To emulate the SPAD configuration that is commonly used [180, 183], the 32×32 elements must to be reduced to a specific 5×5 region where fewest hot pixels are present according to the pixel map. To do this, 27 rows and columns

[70] The dark count test is conducted by sealing the input aperture to the camera and ensuring that no ambient lighting is on.

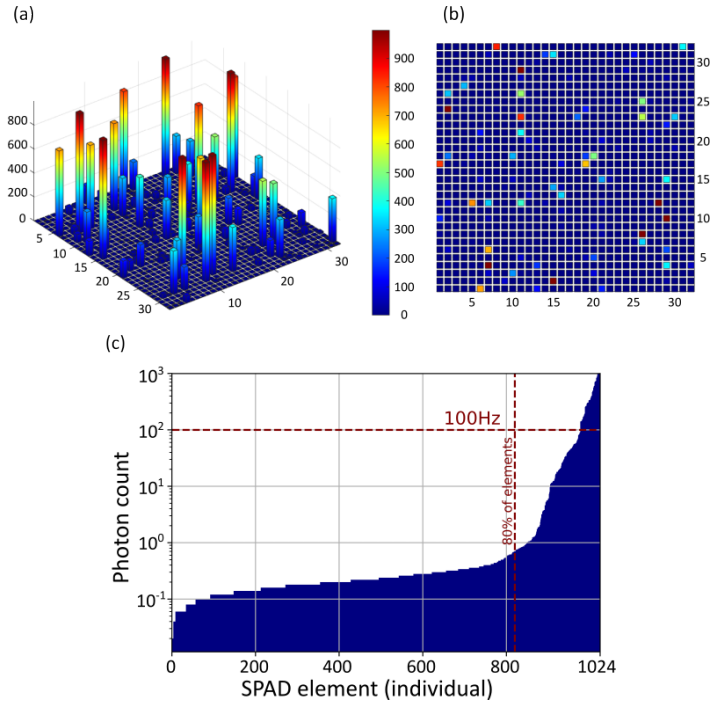

Figure 5.7: (a) A 3D bar representation of the measured hot pixel map of the SPAD (a). A top view of the 3D bar plot, showing where a 5×5 region can be found (b). Plot of the dark count rate (c). For all plots, the maximum hot pixel value is capped at 999 so that the lower dark counts become visible.

need to be switched off. While the firmware in our camera allows this, a limitation remains. Regardless of how many columns are switched on, each row that has any columns to be read, will have the full 32 columns read out, so that a 5×5 region of interest (ROI) will transmit 160 bytes (each pixel value is represented by 8 bits)[71]. This reduced ROI ensures improved frame transfer rates so that the data transfer impacts the timing to a smaller degree (Figure 5.8)[72]. With improved frame rates with smaller ROIs, the data transfer rate does not impact the raster scan image time necessary to generate an image. The primary consideration for the timing of each image will become the necessary pixel dwell time to capture enough signal.

[71] That is $32 \times 5 = 160$.

[72] The manufacturer only specifies that 150kfps is the maximum limit for 32×32, and no transfer rate is specified for other ROI configurations.

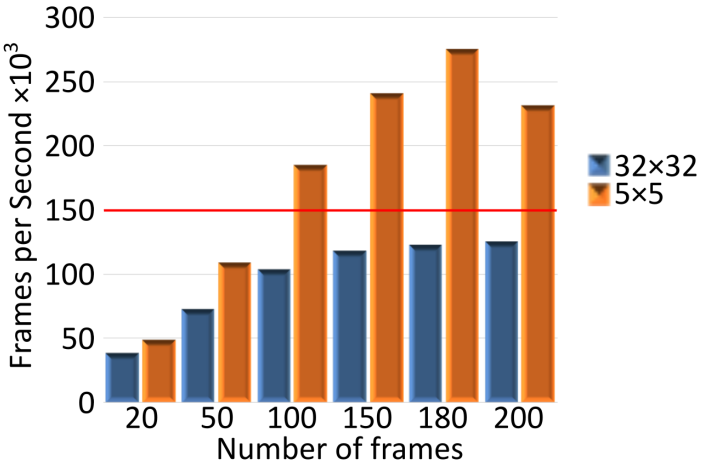

Figure 5.8: As more frames are included in the transfer, the speed of the USB3 increases to approximately 125kfps when the frames size is 32×32 pixels. The rate increases even further when the frame size is 5×5 pixels, to transfer rates above the SPAD specified transfer maximum speed indicated by the red line(150kfps).

5.6 Image Construction

Synchronization of galvanometer scanners with the camera is critical to the reconstruction of the ISM image. While the SPAD camera can be setup to acquire an image per external trigger, an alternative method of acquisition exists where an entire row is captured with specified dwell time per number of positions in the row. Operating in this manner means fewer synchronization pulses are required which in the LabVIEW environment can become unwieldy. In LabVIEW, a number of analog and digital outputs can be synchronized to either a hardware or software trigger. For the purposes of our scan setup three signals need to start simultaneously to control two scanners (analog triangle wave[73]) and the SPAD burst trigger (line trigger; digital) (The wiring configuration of the optoelectronic components can be found in Figure E.8). If each waveform (digital values for the full output) is completed as per the imaging parameters (dwell time, scan range, total number of pixels) they can all be loaded into memory and triggered by a software trigger (potentially a button) and repeated until imaging is no longer required (Figure 5.9) (GUI presented in Appendix E.5). It's important to note that the best wavefront to control the X-and-Y-scanners

[73] This is limited by the electronic filter used on the galvanometer control module, specified as a triangle wave for maximum speed up to 1kHz, depending on the movement distance.

is an analog sine wave (or for the fastest, a triangle wave) from a digital output on the DAQ device. An electrical filter on the scanner controller changes these discrete values to a more representative analog signal that controls the scanner in a smooth manner so that the scanner is always moving, and dwell times are not discrete.

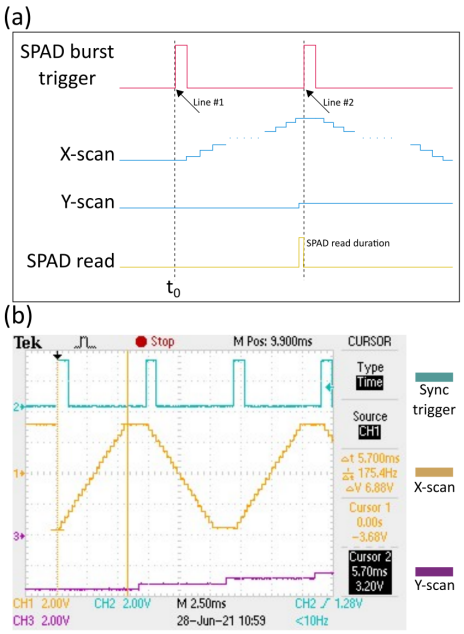

Figure 5.9: Designed synchronization of the X and Y scanners show how the line starts up and is synchronized to the analog (digitized in these plots) waveform controlling the scanners (a). The measured output controlling the scanners triggered by the "Sync trigger" which is a software-controlled output.

As each image acquired in the line scan is a 5×5 'imagelet' that is scanned across the field of view, the reconstructed image of the field of view requires knowledge of where the scanners were during the exposure of the 'imagelet'. Because all three components are synchronized, we know that the top left position is the first 'imagelet', and we can follow the line until the number of pixels for each row has been placed appropriately. Where the line is scanned in what is known as traditional snake scan, a sine wave is used to drive the line scan galvanometer mirror (as is configured in Figure 5.9). In this scan configuration, not flyback is necessary, so that faster scanning can be conducted, but flipping the data from the SPAD burst readout must be done. An added level of complexity is the meta data that is included by the SPAD burst readout for each frame, which indicates the frame count that can be used to confirm that no data has been lost (Figure 5.10a).

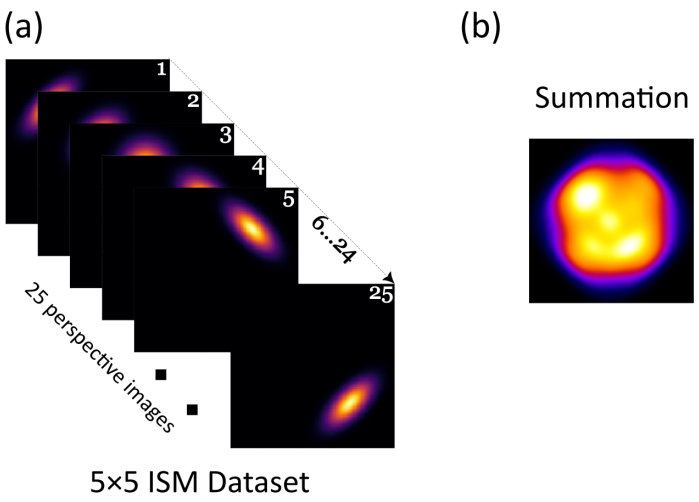

Figure 5.10: The dataset is comprised of scanned images from each of the individual pixel elements, so in a 5×5 configuration, there are 25 images (a). The simplest method of reconstruction is to compute the average projection of each of the images (b).

The simplest reconstruction of the ISM dataset into the final image is summation. For each imagelet, the photon count values of all 25 pixels (Figure 5.10a) can be summed and the single value placed into the image according to the scan position. This reconstruction can be considered a conventional imaging with a low-resolution detector, or an open pinhole image (Figure 5.10b).

While LabVIEW has libraries for saving acquired data to *.tiff* files, dividing the recorded information into pages of *.tiff* files is computationally costly and ultimately leads to numerous RAM issues. HDF5 (Hierarchical Data Format) files are similar to *.tiff* files as they record the raw, uncompressed data, but they are specifically designed for multidimensional arrays, which are well suited to record the ISM image dataset. Third party HDF5 libraries exist as the format is available under a BSD-like license[74] for general use. By incorporating HDF5 libraries to save the full ISM dataset without data writing or RAM issues, the raw outputs from the ISM capture can later be manipulated to reconstruct the ISM image according to commonly used techniques such as static or adaptive pixel reassignment.

[74] BSD licenses are a family of permissive free software licenses.

5.6.1 Pixel Reassignment

As the emission PSF is projected onto the central pixel of the 5×5 region, we can use it as a reference, with a shift vector ($s_i = (x, y)$) associated with the detector pixel based on the geometric layout of the SPAD pixels [175, 181]. Firstly, for a specific pixel i, the line connecting it to the central pixel and secondly the length of this line is proportional to α (the reassignment factor), the magnification of the imaging system M, and the distance between the pixel and the reference pixel d_i, ultimately $s_i = d_i \times \frac{\alpha}{M}$, and third, assuming the excitation and emission are of equal wavelengths so that $\alpha = 0.5$ [181]. As these values are constant for the device and imaging setup, this method is called static pixel reassignment (SPR) and is the simplest way to leverage the resolution improvement enabled by ISM.

Adaptive methods (adaptive pixel reassignment; APR) that first coregister the images recorded by each pixel to the central pixel and then form the final image can significantly improve the resolution of an ISM dataset[75]. Estimation of the shift required for the image recorded by each pixel has previously been shown to work by means of phase-correlation [60, 195] and iterative computation [181]. Iterative methods move the images of each off-center pixel until some prior selected metric is optimized. The final image is constructed by summing the coregistered pixel images and being placed into image space according to the scan position. For well-structured emission spots, a simple autocorrelation can be used to shift each of the off-center pixel images appropriately[76]. Then, by comparing the reconstructed images of a simulated ISM dataset we see that the summation image is not sharp (Figure 5.11a). The SPR (Figure 5.11b) and APR (Figure 5.11c) images are of much higher resolution, where the full-width half maximum (FWHM) of the summation image is below 0.01, the FWHM of the SPR and APR is 0.03 (Figure 5.11d).

[75] Note that the dataset is recorded once and either static or adaptive techniques applied to reconstruct the final image.

[76] Autocorrelation functions in Python can be computationally costly, and as such implementation of this adaptive pixel reassignment is not well suited to the live imaging.

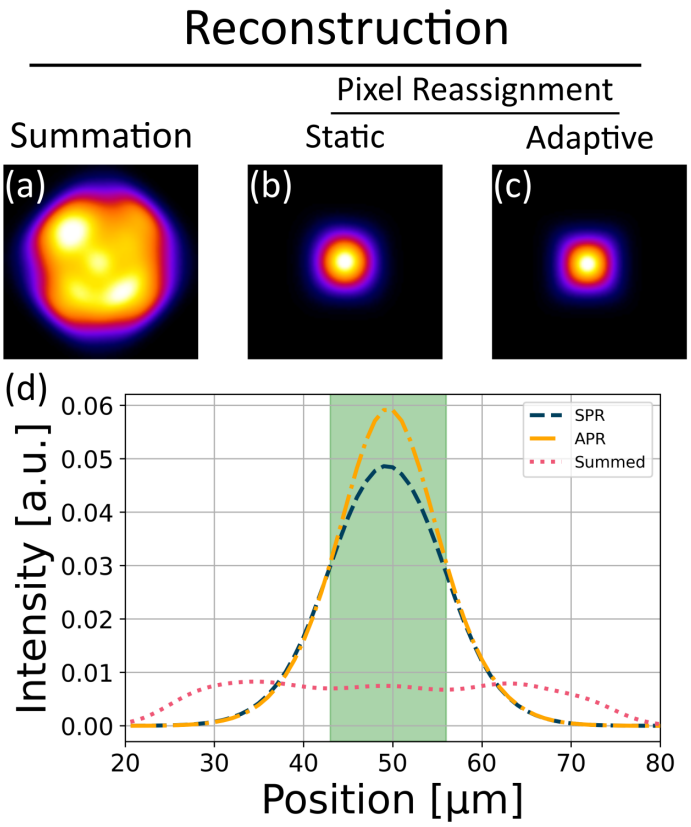

Figure 5.11: Reconstruction images of simulated PSFs showing the summation image (a), static pixel reassignment (b), and adaptive pixel reassignment (c). The full-width half maximum (FWHM) of the summation image is much lower than that of the SPR and APR, but the intensity of the APR is higher than that of the SPR(d).

Additional resolution improvement can be gained by deconvolution or frequency domain filtering [54, 196]. A "blind" Fourier Ring Correlation (FRC) method can also be used, where no measurement of the ideal PSF is necessary, but is estimated by the resulting APR image. By combining the adaptive pixel reassignment with a blind deconvolution, an overall resolution improvement near to a factor of 2 can be achieved [181].

5.7 ISM Results

Using the ISM techniques described, we imaged an autofluorescent plate using an excitation wavelength of 800nm which has been shown to emit strong 575nm signal. We found a central spot of the scanned image with an exposure time of 1ms across an image of 250×250 pixels (Figure 5.12) and compared it against images with various exposure times. With enough time for the fast line scanner to image the full field of view, no flyback blanking time is required. As the exposure time is reduced, the flyback time of the line scanner begins to generate a very narrow repeat image on the left-hand side of the image (500μs to 67.5μs) and this effect becomes more pronounced as the exposure time is decreased further. Eventually, at 8μs the flyback image on the left-hand side of the image is equal in size to the appropriately scanned section of the image. This indicates that in cases with bright signal, a flyback blanking period is required to image the field of view appropriately.

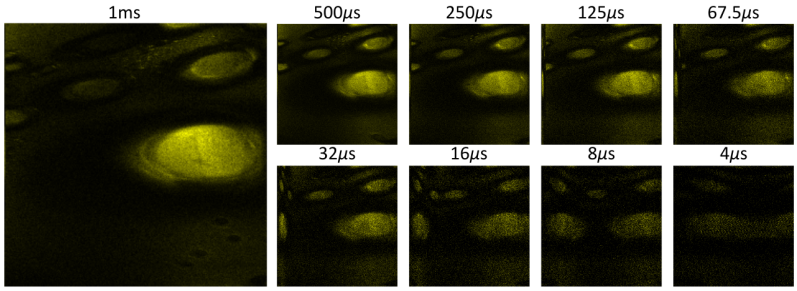

Figure 5.12: At 1ms exposure time no flyback image is visible, as enough time is available for the scanner to return to the beginning of the line. As the exposure time is reduced, this flyback image is more pronounced.

To remove statistical outliers, an evaluation of each 'imagelet' was conducted. If the total image intensity from a single SPAD element returned a value exceeding a single standard deviation, that image was removed from the pixel reassignment. This ensured that when a 5×5 region was selected that contains any hot-pixel elements, a computational correction can reduce the noise and recover suitable imaging.

The shape of these spots imaged in the autofluorescent plat is altered by the aberrations from the OAPs and numerous spots are visible where none are expected. At this point in the work, it is not clear if this is tenable for imaging, as less bright samples emitting fewer photons were not able to be imaged in the configuration.

5.8 Widefield Illumination

To overcome the difficulties associated with the aberrations caused by the OAPs, we implemented a solution where the excitation source is transmitted directly into the back aperture of the objective lens. As the beam is approximately 3mm in diameter, the effective NA is well below the 1.05 specified. This results in a larger excitation PSF which can loosely be considered a "widefield" illumination strategy. In this configuration, there are no scanning elements, and to generate images, the object is scanned using the electronic stage (X-LSM025A, Zaber).

To confirm that this illumination would provide sufficient photons to elicit 3-photon and THG emission, a basic confirmation of the cubed law when exciting a thin fluorescein sample was conducted. Additionally, the power required to achieve 3-photon imaging would be maximized in this configuration, as fewer optical elements are in the optical path, but excitation power is still significantly reduced as it propagates through the system, as approximately 90% of the power output from the NOPA is lost across the optical path (Figure E.16a).

Based on existing literature, the 3-photon response of fluorescein is maximized at approximately 1150nm [197] (based on the NOPA output, as there is a dead region from 950nm to 1150nm), but as we are interested in the penetration benefit of 1300nm we implemented an experiment to confirm 3-photon emission when using this lower effective NA illumination (and thus larger PSF) using 1300nm excitation. Using the PMT for emission collection and a half-wave plate to control the power, we increased excitation power from 40mW to 130mW and found that the emitted light closely followed the cubed nonlinearity (Figure 5.13) (Emission filter: 509/22).

5.8.1 3PE Imaging of Nanoparticles

Evaluating the $C_sPbBr_3@SiO_2$ nanoparticles (previously imaged in 2-photon in section 3.3.3) to evaluate the 3-photon response, a longer wavelength excitation source was used. A higher concentration of the nanoparticles was placed in a toluene solution (100μL) and placed into a small silicon well. When excited at 1160nm[77], the fluorescence intensity scaled according to an equation of $y = 3.0326 \times 10^3 \cdot x^{2.3354}$ (Figure 5.14a), where lower power excitation more closely follows the cubed power law, but as the power is increased, PMT readings fall off, but remain above the squared power law. Variation of 3-photon emission when excited by wavelengths in the range from 1160nm to 1400nm shows that maximum intensity was achieved when the samples were excited by 1190nm, and a minimum at 1360nm, but it appears as if another peak is possible beyond 1400nm (Figure 5.14b).

[77] Our Orpheus NOPA cannot output the "ideal" 1110nm as per the 370nm × 3, but can generate from 650-940nm and then from 1160nm and longer.

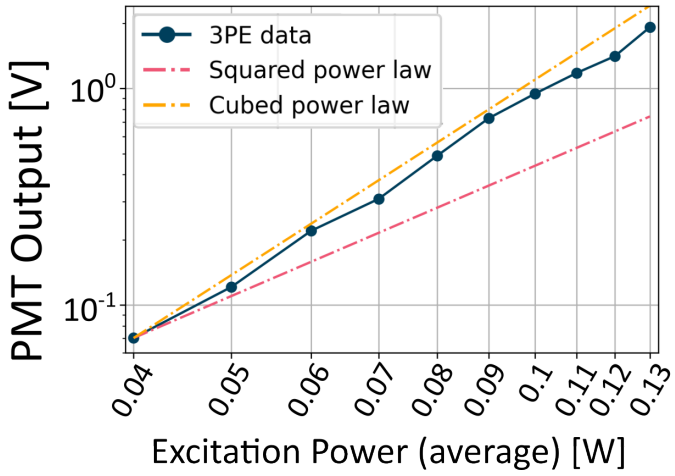

Figure 5.13: A 960μM concentration of fluorescein shows almost ideal 3-photon emission as the power is doubled, the emitted light is cubed.

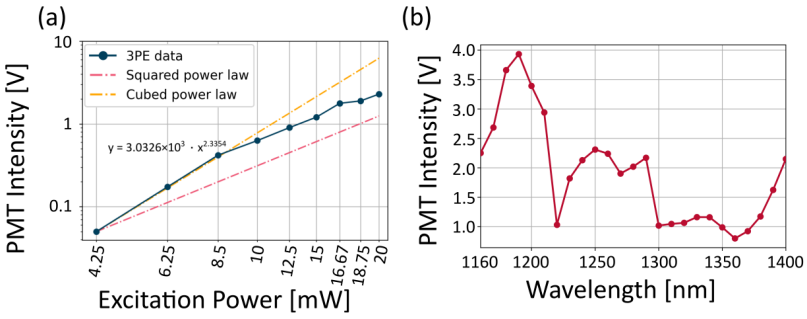

Figure 5.14: Fluorescence intensity measured by PMT when the nanoparticles are excited at 1160nm, showing 3-photon emission (a). The 3-photon response varies when excited across 1160nm to 1400nm (b).

5.8.2 Imaging MSCs in a monolayer

Mesenchymal Stromal Cells cultured in osteogenic media over a period of 14 days are expected to have begun mineral deposition by day 12 [198, 199]. Investigating this mineral deposition most often requires staining by dyes such as Alizarin red, so label-free quantification of mineral deposited is desirable. We envision using the THG contrast provided by the interface between mismatched refractive indices can be used to quantify the mineralization as the

refractive index will change across a sample where mineral has been put down. Once the cells are fixed, the monolayer of MSCs in a Petri dish was imaged and while it was very thin (15-25μm thick), we were able to identify single cells using SHG illuminated by 1280nm (Figure 5.15a; notion of nucleus labeled "1"). Viewing the THG channel where correlation between the channels is clear (the membrane labeled "2" in (a) fits into the gap in (b)), a layer of punctate mineral deposits is visible (Figure 5.15b). Using these THG images of MSCs over a period of 28 days can be used to quantify mineral deposition by MSCs in osteogenic differentiation. By combining this specificity with super resolution provided by an implementation of ISM, extracellular vesicles (EVs) could also be quantified in future experiments [200].

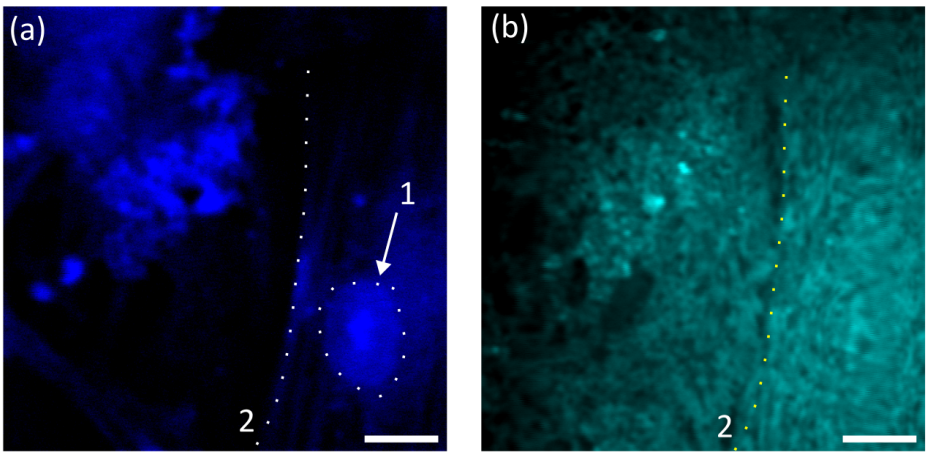

Figure 5.15: An image of cells using 1280nm excitation where the cell membrane and nucleus are visible in the SHG image (a). The THG image contains many punctate spots of deposited mineral as the MSCs were differentiated to bone (b). Scale bar is 10μm.

We have confirmed that narrowing the excitation beam into the back aperture of the objective lens creates a focal volume that elicits 3-photon and THG signal in nanoparticles and a monolayer of cells. By leveraging the long wavelengths associated with lower scattering, we anticipate that this setup can be used to image SHG and THG inside living tissue such as the PhAM floxed murine sample that expresses GFP in their mitochondria, exceeding depth of penetration that was achieved using scatter correction in 2-photon imaging.

Chapter 6

Conclusion

As numerous microscopy techniques become more available to researchers, selection of the appropriate modality is of paramount importance. Appropriate modalities are selected by criteria (1) is the sample thin, transparent, or thick and scattering? (2) How small are the features to be measured, and (3) are the samples going to be biologically representative if fluorescent dyes are used, or should label-free techniques be used? In this work we present options suitable for almost any biological sample and in some cases methods to improve the imaging modality.

Differential Phase Contrast (DPC) is well suited to thin, transparent samples and provides quantitative phase images that can be input to computational tools such as neural networks [201]. We show how implementation of this technique with low-cost components into a robust, user-friendly human-machine interface, enables investigators without specific knowledge of the technique to use it. Further improvements to the DPC images by reducing illumination and halo artifacts which distort the edges of larger features were made, resulting in halo-free images more closely representing the ground truth. Using this microscope setup allowed us to image MSCs where we could match the morphology of mesenchymal stromal cells (MSCs) to their chemical composition using MALDI-MSI. In other work, DPC acquired images were used to quantify mineral deposition of MSCs as they differentiated into bone cells by calculating the gray-level co-occurrence matrices (GLCM) and comparing them at weekly intervals. Longer term (beyond 24-hours) imaging of live MSCs also revealed how MSCs interact with T-cells. This DPC implementation installed into an existing upright microscope was combined with a single-photon fluorescence microscope that enabled multi-modal imaging with four channels of fluorescence alongside DPC. By combining these options and enabling long

term imaging, a multitude of imaging options are available to investigators in a robust configuration.

Multi-photon imaging, suited to thicker and scattering samples, improves the intensity of imaging by reducing the focal volume and limiting the generation of out-of-focus fluorescence, is a widely used technique in biological imaging. Using our custom-built 2-photon setup we were able to measure the 2-photon characteristics of perovskite nanoparticles and use them to observe MSCs that had been injected subdermally in a living mouse ear. In muscle tissue samples prepared and mounted onto microscope slides, we were able to image 2-photon emission and second harmonic generation (SHG) simultaneously. Using the intrinsic SHG from within type I collagen [8] we were able to quantify the collagen content within muscle tissue and differentiate injured samples from uninjured samples according to collagen quantification.

While we can use our 2-photon microscope for numerous sample types such as cell monolayers, fixed tissue, or living animal samples, each of these samples presents aberrations that degrade the image quality. Low order aberration correction by means of a low spatial frequency electro-optical component such as a deformable mirror recovers some intensity, but beyond the scattering length constant of bone, we found that high-order aberration of the sample overwhelms the PSF. Our approach to correct this scattering was to combine a high spatial frequency digital micromirror device (DMD) to manipulate the wavefront and restore high intensity and high spatial frequency imaging using a genetic algorithm to optimize the DMD pattern. Importantly, we used the SHG signal generated within the bone to evaluate the quality of the PSF during the optimization. In doing so, we achieved an 8-fold intensity increase in the green fluorescent protein (GFP) channel, enabling tracking of cells approximately 120μm below the surface of the skull in living bone marrow. Current state of the art scatter correction techniques such as IMPACT [94] and F-SHARP [71] have been shown to correct scattering within a few seconds using SLMs. These techniques decouple the slow wavefront correction device from the high-speed measurement device. F-SHARP in particular has been applied in 3-photon imaging at 1300nm and achieved an 8-fold increase in GFP 600μm inside the brain through a craniotomy in a living mouse [202]. While it has proven difficult to find consistency in the literature regarding the scattering length of brain tissue, we found that a useful value for the scattering length constant of brain tissue is approximately 150μm [159]. A direct comparison of our scatter correction implemented in bone tissue is not available, particularly in the case of binary wavefront modulation, which until this work has not seen implementation inside a living mammal. By relating our work in terms of scattering lengths

to other works in brain, we find that scatter correction using our system worked well up to three or four scattering lengths, where other state of the art methods achieve consistent recovery in up to four scattering lengths.

We then investigated strategies to improve intensity increase and reduce the scatter correction time. By replacing the multi-pixel CMOS camera with a single-pixel photon collection device, a PMT, we were able to complete the scatter correction more rapidly, but at the cost of lower intensity enhancement. Use of a PMT effectively reduced the evaluation metric within the genetic algorithm to an averaged intensity across a larger region of the PSF. As such, improvements in the evaluation metric by individuals within the population had less impact than in the multi-pixel configuration. This effect, compounded with the stochastic nature of PMT gain, lead to that lower intensity increase. Other work in the field has shown that using a PMT is effective in reducing the correction time, so in future iterations of this implementation, a cooled PMT could replace the uncooled PMT to stabilize the gain. Spatial filtering of the optical signal into the PMT and electrical low-pass filters on the PMT output can improve the performance of the single-pixel based method. A more stable and even faster device such as a SPAD camera could be integrated into the system to replace either the PMT or multi-pixel camera, provided the fill factor can enable imaging well above the noise floor.

Where surplus excitation power is available in a 2-photon system, a reduction of segments used in the DMD pattern was shown to increase the overall intensity enhancement. By reducing the segment sparsity from $\sim 50\%$ to $\sim 20\%$, we increased the intensity enhancement $1.5\times$ in GFP, but by nearly $6\times$ in SHG. Surplus power is necessary in the case of imaging bone, as $780nm$ has a scattering length of approximately 45μm, and for effective imaging, we needed the average illumination power to approach 150mW.

To bolster the improvement that we measured using our scatter correction, we included low order aberration correction, which had previously been implemented in our custom microscope [123]. Implementing this low order correction beyond one scattering length of bone reduced the SHG signal so that it became difficult to achieve a successful sample aberration correction when an uncorrected pattern was projected onto the DMD. Where an optimized DMD pattern was projected, the sample aberration correction was able to yield an improvement in the PSF intensity and shape. When this combination was used to image at 110μm inside excised bone, subcellular features that had not previously been visible became clear. In a living sample the punctate mitochondria became more visible, and a 2.5-fold increase in intensity was realized when the low order aberration correction was applied alongside scatter correction. Low

order aberration correction is a widely applied technique useful in enhancing intensity and resolution but is most commonly used in thin or transparent tissue [203]. A combination of these correction approaches is not widely applied in the literature and can combine the benefits of both to increase resolution at depth.

Ultimately, this aberration and scatter correction improves the excitation PSF, but the wavelengths useful in 2-photon imaging do not penetrate biological tissue as deeply as wavelengths in the "biological window". Three-photon imaging at 1300nm provides improved penetration, while reducing the optical resolution (according to the diffraction limit calculation), but scattering that does occur can be corrected by our binary wavefront modulation technique (provided the wavelength is compatible with the surface of the DMD).

To implement the first aspect of a longer wavelength 3-photon microscope, we simulated an achromatic scan engine. In our configuration, long excitation wavelengths as well as the shorter emission wavelengths must travel along the same optical path to be descanned and collected. This necessitates an achromatic path that is not feasible with current anti reflective coating in glass lenses so that they must be replaced by off-axis parabolic mirrors which are capable of broadband reflection. We found that while simulations of this OAP configuration showed aberrations in higher Zernike orders, meaning that computational correction could be implemented in the lower orders, the low photon count across the scan engine resulted in untenable imaging conditions when combined with the low order aberrations. This low photon count is exacerbated by the low fill factor of each SPAD element specified as 13.94% in our device. To recover a useful fill factor, a microlens array could be used to focus light onto the effective 6.95μm region of the SPAD. Alternatively, a more suitable SPAD camera can be acquired that has previously been shown to enable ISM in 2-photon implementations [60]. To date, no 3-photon SPAD-based implementation of ISM has been shown inside scattering biological tissue, but it has been presented in cleared, stained tissues [183]. Further, while SHG enhancement has been shown via ISM [63], this has not been illustrated in thick living samples, nor in using third harmonic generation (THG).

When reducing the system to a "widefield" excitation, we confirmed 3-photon imaging in Fluorescein, as well as SHG and THG imaging of excised bone. Additionally, this system was used to confirm the 3-photon response of the perovskite nanoparticles, and to image SHG and THG emission from MSCs cultured in osteogenic media. This more primitive implementation enables deep tissue imaging by leveraging the long wavelengths in the "biological

window" and label free SHG and THG imaging due to high pulse power and short pulse durations necessary for high contrast THG imaging [46].

In the ultimate vision for this imaging system, a combination of aberration and scatter correction when using long wavelengths will enable deeper penetration that is necessary for examining osteogenic processes deep within living bone. Implementation of ISM in this configuration can potentially increase the resolution of the system by a factor of two, which would restore resolution in the range of 250nm that is desirable in imaging of the lacunar-canalicular network [204].

Appendix A

DPC Microscope setup

The inter communications document (ICD) for communications between the LED Matrix controller Arduino and LabVIEW, the DPC reconstruction code, the

A.1 Communications between LED array, Arduino, and LabVIEW

These tables describe the messages sent from the Arduino to the LabVIEW PC over USB. Specifically this is the Arduino that controls the LED array. Note that the LabVIEW and Arduino themselves play no role in the decisions made in this document, this is simply a communication message protocol.

This first table simply illustrates usage of the ICD

Table A.1: LED array communications message structure

Byte Number	Byte Description	Byte Expected	Byte Representation
1	Sync byte	`0x7C` (|)	UINT8
2	Message header	`0x0*`	UINT8
3	Message length	Number of bytes in the message (excluding sync byte and message header, message length, but including checksum	UINT8
4 . . . n-1	Message payload	Number of bytes	UINT8
n	Checksum	XOR of each of the bytes in the message (incl. sync byte, message header and message length)	UINT8

Message 1 - Set Circle Upon receiving message 1, the LED array controlling Arduino sets a circle on the LED array.

Table A.2: LabVIEW to LED array Arduino - Message 1

Byte Number	Byte Description	Byte Expected	Byte Representation
1	Sync byte	`0x7C` (|)	UINT8
2	Message header	`0x01`	UINT8
3	Message length	`0x08`	UINT8
4	Filled or Outline	`0`: Outline `1`: Filled	UINT8
5	Matrix 'X' position	`0 - 15`	UINT8
6	Matrix 'Y' position	`0 - 15`	UINT8
7	Circle radius	`0 - 15`	UINT8
8	Red intensity	`0 - 15`	UINT8
9	Green intensity	`0 - 15`	UINT8
10	Blue intensity	`0 - 15`	UINT8
11	Checksum	XOR of each of the bytes in the message (incl. sync byte, message header and message length)	UINT8

Table A.3: LED array Arduino response to LabVIEW - Message 1

Byte Number	Byte Description	Byte Expected	Byte Representation
1	Sync byte	`0x7C` (|)	UINT8
2	Message header	`0xA1`	UINT8
3	Message length	`0x09`	UINT8
4	Matrix 'X' position	`0 - 15`	UINT8
5	Matrix 'Y' position	`0 - 15`	UINT8
6	Circle radius	`0 - 15`	UINT8
7	Red intensity	`0 - 15`	UINT8
8	Green intensity	`0 - 15`	UINT8
9	Blue intensity	`0 - 15`	UINT8
10	Checksum	XOR of each of the bytes in the message (incl. sync byte, message header and message length)	UINT8

Message 2 - Set Specific LED Upon receiving message 2, the LED array controlling Arduino sets the RGB value on a specific LED.

Table A.4: LabVIEW to LED array Arduino - Message 2

Byte Number	Byte Description	Byte Expected	Byte Representation
1	Sync byte	0x7C (|)	UINT8
2	Message header	0x02	UINT8
3	Message length	0x06	UINT8
4	LED 'X' position	0 - 31	UINT8
5	LED 'Y' position	0 - 31	UINT8
6	R Value	0 - 15	UINT8
7	G Value	0 - 15	UINT8
8	B Value	0 - 15	UINT8
9	Checksum	XOR of each of the bytes in the message (incl. sync byte, message header and message length)	UINT8

Table A.5: LED array Arduino response to LabVIEW - Message 2

Byte Number	Byte Description	Byte Expected	Byte Representation
1	Sync byte	0x7C (|)	UINT8
2	Message header	0x02	UINT8
3	Message length	0x06	UINT8
4	LED 'X' position	0 - 31	UINT8
5	LED 'Y' position	0 - 31	UINT8
6	R Value	0 - 15	UINT8
7	G Value	0 - 15	UINT8
8	B Value	0 - 15	UINT8
9	Checksum	XOR of each of the bytes in the message (incl. sync byte, message header and message length)	UINT8

Message 3 - Set Rectangle Upon receiving message 3, the LED array controlling Arduino sets the RGB value on a rectangle of LEDs.

Table A.6: LabVIEW to LED array Arduino - Message 3

Byte Number	Byte Description	Byte Expected	Byte Representation
1	Sync byte	`0x7C` (|)	UINT8
2	Message header	`0x03`	UINT8
3	Message length	`0x09`	UINT8
4	Filled or Outline	`0`: Outline `1`: Filled	UINT8
5	Top left 'X' position	`0 - 31`	UINT8
6	Top left 'Y' position	`0 - 31`	UINT8
7	Width in pixels	`0 - 31`	UINT8
8	Height in pixels	`0 - 31`	UINT8
9	R Value	`0 - 15`	UINT8
10	G Value	`0 - 15`	UINT8
11	B Value	`0 - 15`	UINT8
12	Checksum	XOR of each of the bytes in the message (incl. sync byte, message header and message length)	UINT8

Table A.7: LED array Arduino response to LabVIEW - Message 3

Byte Number	Byte Description	Byte Expected	Byte Representation
1	Sync byte	0x7C (|)	UINT8
2	Message header	0x03	UINT8
3	Message length	0x09	UINT8
4	Rectangle filled?	0: Outline 1: Filled	UINT8
5	Top left 'X' position	0 - 31	UINT8
6	Top left 'Y' position	0 - 31	UINT8
7	Width in pixels	0 - 31	UINT8
8	Height in pixels	0 - 31	UINT8
9	R Value	0 - 15	UINT8
10	G Value	0 - 15	UINT8
11	B Value	0 - 15	UINT8
12	Checksum	XOR of each of the bytes in the message (incl. sync byte, message header and message length)	UINT8

Messages 4 and 5 are not used in this configuration controlling the LED array. There is no code in the Arduino listening for or responding to these messages.

Message 6 - Set Half Circle Upon receiving message 6, the LED array controlling Arduino sets the RGB value on a Half Circle.

Table A.8: LabVIEW to LED array Arduino - Message 6

Byte Number	Byte Description	Byte Expected	Byte Representation
1	Sync byte	0x7C (|)	UINT8
2	Message header	0x06	UINT8
3	Message length	0x06	UINT8
4	Half Circle Orientation	1: Top 2: Left 3: Bottom 4: Right	UINT8
5	LED 'Y' position	-Don't care-	UINT8
6	R Value	0 - 15	UINT8
7	G Value	0 - 15	UINT8
8	B Value	0 - 15	UINT8
9	Checksum	XOR of each of the bytes in the message (incl. sync byte, message header and message length)	UINT8

Table A.9: LED array Arduino response to LabVIEW- Message 6

Byte Number	Byte Description	Byte Expected	Byte Representation
1	Sync byte	0x7C (|)	UINT8
2	Message header	0xA6	UINT8
3	Message length	0x06	UINT8
4	Half Circle Orientation	1: Top 2: Left 3: Bottom 4: Right	UINT8
5	LED 'Y' position	-Don't care-	UINT8
6	R Value	0 - 15	UINT8
7	G Value	0 - 15	UINT8
8	B Value	0 - 15	UINT8
9	Checksum	XOR of each of the bytes in the message (incl. sync byte, message header and message length)	UINT8

A.2 DPC Arduino source code

```
1 #include <RGBmatrixPanel.h>
2
3 #define CLK  8   // USE THIS ON ARDUINO UNO,
    ADAFRUIT METRO M0, etc.
4 //#define CLK A4 // USE THIS ON METRO M4 (not M0
    )
5 //#define CLK 11 // USE THIS ON ARDUINO MEGA
6 #define OE   9
7 #define LAT 10
8 #define A   A0
9 #define B   A1
10 #define C   A2
11 #define D   A3
12
13 #define startMarker 0x7C
14 #define maxMessage 16
15
16 byte bytesRecvd = 0;
17 byte dataRecvCount = 0;
18
19 byte dataRecvd[maxMessage];
20 byte tempBuffer[maxMessage];
21
22 boolean inProgress = false;
23 boolean allReceived = false;
24 boolean msgHeaderknown = false;
25 boolean msgLengthknown = false;
26
27 boolean bRunLines = false;
28 byte bPrescaler = 0;
29 byte bOffset = 0;
30 byte bRunRed;
31 byte bRunGreen;
32 byte bRunBlue;
33 int nFPCount = 0;
34 int nTotalLines = 0;
35 byte bCurrentX = 0;
```

```
36 byte bCurrentY = 0;
37
38 byte bMessageBytes[maxMessage];
39 byte bChecksum = 0;
40 unsigned int msgLength = 0;
41 unsigned int msgRecLength = 0;
42 unsigned long previousMillis = 0;
43 int ledState = LOW;
44
45 RGBmatrixPanel matrix(A, B, C, D, CLK, LAT, OE,
     false);
46
47 void setup()
48 {
49   pinMode(13, OUTPUT); // the onboard LED
50   pinMode(12, INPUT); // Camera trigger pin
51
52   Serial.begin(115200);
53
54   matrix.begin();
55 }
56
57 void loop()
58 {
59   unsigned long currentMillis = millis();
60 /* seems to not work when using this heartbeat
     code
61   if (currentMillis - previousMillis >= 1000)
62   {
63     // save the last time you blinked the LED
64     previousMillis = currentMillis;
65     // if the LED is off turn it on and vice-
        versa:
66     if (ledState == LOW)
67     {
68       ledState = HIGH;
69     //  matrix.drawPixel(0, 2, matrix.Color333
        (7, 7, 7));
70     }
```

```
71      else
72      {
73        ledState = LOW;
74     //   matrix.drawPixel(0, 2, matrix.Color444
          (0, 0, 0));
75      }
76      // set the LED with the ledState of the
           variable:
77      digitalWrite(13, ledState);
78    }
79  */
80    // Check if serial communications required
81    getSerialData();
82
83    // Once a full message has been received,
         process the instruction
84    if(allReceived)
85    {
86      allReceived = false;
87      processData();
88    }
89
90    // if the received message instructed to begin
          sequence, enter here
91    if(bRunLines)
92    {
93      // ledState = HIGH;
94      // poll IO12
95      // Wait until the input goes high
96      while(digitalRead(12) == LOW)
97      {
98        // do nothing (wait for pin to go high)
99      }
100
101     // Do what needs to be done when the pin is
           high (turn on correct LED, as per
           prsecaler & offset; determine nTotalLines)
```

```
102     matrix.drawPixel(bCurrentX, bCurrentY,
          matrix.Color444(bRunRed, bRunGreen,
          bRunBlue));
103     switch(bPrescaler)
104     {
105       case 1:
106         nTotalLines = 1023;
107         if(bCurrentX+1 >= 32)
108         {
109           bCurrentY += 1;
110           bCurrentX = bCurrentX - 31;
111         }
112         else
113         {
114           bCurrentX += 1;
115         }
116
117         break;
118       case 2:
119         nTotalLines = 255;
120         if(bCurrentX+2 >= 32)
121         {
122           bCurrentY += 2;
123           bCurrentX = bCurrentX - 30;
124         }
125         else
126         {
127           bCurrentX += 2;
128         }
129         break;
130       case 3:
131         nTotalLines = 63;
132         if(bCurrentX+4 >= 32)
133         {
134           bCurrentY += 4;
135           bCurrentX = bCurrentX - 28;
136         }
137         else
138         {
```

```
139           bCurrentX += 4;
140         }
141         break;
142       case 4:
143         nTotalLines = 15;
144         if(bCurrentX+8 >= 32)
145         {
146           bCurrentY += 8;
147           bCurrentX = bCurrentX - 24;
148         }
149         else
150         {
151           bCurrentX += 8;
152         }
153         break;
154       default:
155         break;
156     }
157
158     while(digitalRead(12) == HIGH)
159     {
160       // do nothing (wait for pin to go low)
161     }
162
163     // Do what needs to be done when the pin is
          low (turn off panel)
164     matrix.fillScreen(matrix.Color333(0, 0, 0));
165
166     // If the whole array has been done, stop
          polling
167     if(nFPCount++ >= nTotalLines)
168     {
169       bRunLines = false;
170     }
171   }
172 }
173
174 void getSerialData()
175 {
```

```
176       // Receives data into tempBuffer[]
177       //   saves the number of bytes that the PC
              said it sent - which will be in
              tempBuffer[1]
178       //   uses decodeHighBytes() to copy data
              from tempBuffer to dataRecvd[]
179
180       // the Arduino program will use the data it
              finds in dataRecvd[]
181   bChecksum = 0;
182   if(Serial.available() > 0)
183   {
184     byte x = Serial.read();
185     if ((x == 0x7C) && (!msgHeaderknown))
186     {
187       bytesRecvd = 0;
188       inProgress = true;
189       // blinkLED(2);
190       // Serial.write("start received\n");
191     }
192
193     if(inProgress)
194     {
195       tempBuffer[bytesRecvd] = x;
196       bytesRecvd ++;
197     }
198
199     if(!msgHeaderknown)
200     {
201       // Regardless of message header, we need
              to read 1 more byte to get message
              length, so keep receiving
202       // tempBuffer[1] is the message header
203       msgHeaderknown = true;
204     }
205     if(!msgLengthknown)
206     {
207       switch (tempBuffer[2])
208       {
```

```
209         case 0x01:
210           msgLength = tempBuffer[2];
211           msgLengthknown = true;
212           break;
213         case 0x02:
214           msgLength = tempBuffer[2];
215           msgLengthknown = true;
216           break;
217         case 0x03:
218           msgLength = tempBuffer[2];
219           msgLengthknown = true;
220           break;
221         case 0x04:
222           msgLength = tempBuffer[2];
223           msgLengthknown = true;
224           break;
225         case 0x05:
226           msgLength = tempBuffer[2];
227           msgLengthknown = true;
228           break;
229         case 0x06:
230           msgLength = tempBuffer[2];
231           msgLengthknown = true;
232           break;
233         case 0x07:
234           msgLength = tempBuffer[2];
235           msgLengthknown = true;
236           break;
237         case 0x08:
238           msgLength = tempBuffer[2];
239           msgLengthknown = true;
240           break;
241         case 0x09:
242           msgLength = tempBuffer[2];
243           msgLengthknown = true;
244           break;
245         default:
246         break;
247       }
```

```
248     }
249
250     if(msgLengthknown)
251     {
252       msgRecLength += 1;
253       if(msgRecLength == msgLength+1)
254       {
255         inProgress = false;
256         allReceived = true;
257         msgLengthknown = false;
258         msgHeaderknown = false;
259         dataRecvd[0] = tempBuffer[0];
260         dataRecvd[1] = tempBuffer[1];
261         dataRecvd[2] = tempBuffer[2];
262         dataRecvd[3] = tempBuffer[3];
263         dataRecvd[4] = tempBuffer[4];
264         dataRecvd[5] = tempBuffer[5];
265         dataRecvd[6] = tempBuffer[6];
266         dataRecvd[7] = tempBuffer[7];
267         dataRecvd[8] = tempBuffer[8];
268         dataRecvd[9] = tempBuffer[9];
269         dataRecvd[10] = tempBuffer[10];
270         dataRecvd[11] = tempBuffer[11];
271         tempBuffer[0] = 0;
272         tempBuffer[1] = 0;
273         tempBuffer[2] = 0;
274         msgRecLength = 0;
275         allReceived = true;
276         //Serial.write("got all\n");
277         //Serial.write(dataRecvd, bytesRecvd);
278       }
279     }
280   }
281 }
282
283 //Adrian message decoders
284 void Message1()
285 {
```

```
286  /*
       ============================================================

287    * Message 1 responds with the intensity
         values of the ADC's as a percentage from
         0-100%
288    * analogRead returns an integer (16 bits) and
          is maxed out at 1024
289    * multiplying by .09765625, normalizes 1024
         to 100% (as required)
290    * casting the resulting integer to a byte
         results in a single byte intensity
291    */
292  matrix.fillScreen(matrix.Color333(0, 0, 0));
293
294  if(dataRecvd[3])
295  {
296    matrix.fillCircle(dataRecvd[4], dataRecvd
         [5], dataRecvd[6], matrix.Color444(
         dataRecvd[7], dataRecvd[8], dataRecvd[9]))
         ;
297  }
298  else
299  {
300    matrix.drawCircle(dataRecvd[4], dataRecvd
         [5], dataRecvd[6], matrix.Color444(
         dataRecvd[7], dataRecvd[8], dataRecvd[9]))
         ;
301  }
302
303  bChecksum = 0;
304  bMessageBytes[0] = 0x7C;
305  bChecksum = bChecksum ^ bMessageBytes[0];
306  bMessageBytes[1] = 0xA1;
307  bChecksum = bChecksum ^ bMessageBytes[1];
308  bMessageBytes[2] = 0x08;
309  bChecksum = bChecksum ^ bMessageBytes[2];
310  bMessageBytes[3] = dataRecvd[3];
311  bChecksum = bChecksum ^ bMessageBytes[3];
```

```
312   bMessageBytes[4] = dataRecvd[4];
313   bChecksum = bChecksum ^ bMessageBytes[4];
314   bMessageBytes[5] = dataRecvd[5];
315   bChecksum = bChecksum ^ bMessageBytes[5];
316   bMessageBytes[6] = dataRecvd[6];
317   bChecksum = bChecksum ^ bMessageBytes[6];
318   bMessageBytes[7] = dataRecvd[7];
319   bChecksum = bChecksum ^ bMessageBytes[7];
320   bMessageBytes[8] = dataRecvd[8];
321   bChecksum = bChecksum ^ bMessageBytes[8];
322   bMessageBytes[9] = dataRecvd[9];
323   bChecksum = bChecksum ^ bMessageBytes[9];
324   bMessageBytes[10] = bChecksum;
325   Serial.write(bMessageBytes, 11);
326   return;
327 }
328
329 void Message2()
330 {
331   /*
        ==========================================================================

332    * Message 2 responds with the intensity
         settings that the DAC has recorded for each
          channel
333    * and sets the DAC's to the specified values
334    */
335
336   matrix.fillScreen(matrix.Color333(0, 0, 0));
337   matrix.drawPixel(dataRecvd[3], dataRecvd[4],
        matrix.Color444(dataRecvd[5], dataRecvd[6],
        dataRecvd[7]));
338
339   bChecksum = 0;
340   bMessageBytes[0] = 0x7C;
341   bChecksum = bChecksum ^ bMessageBytes[0];
342   bMessageBytes[1] = 0xA2;
343   bChecksum = bChecksum ^ bMessageBytes[1];
344   bMessageBytes[2] = 0x06;
```

```
345   bChecksum = bChecksum ^ bMessageBytes[2];
346   bMessageBytes[3] = dataRecvd[3];
347   bChecksum = bChecksum ^ bMessageBytes[3];
348   bMessageBytes[4] = dataRecvd[4];
349   bChecksum = bChecksum ^ bMessageBytes[4];
350   bMessageBytes[5] = dataRecvd[5];
351   bChecksum = bChecksum ^ bMessageBytes[5];
352   bMessageBytes[6] = dataRecvd[6];
353   bChecksum = bChecksum ^ bMessageBytes[6];
354   bMessageBytes[7] = dataRecvd[7];
355   bChecksum = bChecksum ^ bMessageBytes[7];
356   bMessageBytes[8] = bChecksum;
357   Serial.write(bMessageBytes, 9);
358   return;
359 }
360
361 void Message3()
362 {
363   /*
        ============================================================

364    * Message 3 responds with the LED's that are
         turned on/off as per GUI instruction
365    * as well as the exposure and dead times as
         per the GUI
366    * These values are stored so that a pulse
         train can be setup appropriately
367    */
368
369   matrix.fillScreen(matrix.Color444(0, 0, 0));
370
371   if(dataRecvd[3])
372   {
373     matrix.fillScreen(matrix.Color444(dataRecvd
          [8], dataRecvd[9], dataRecvd[10]));
374   }
375   else
376   {
```

```
377     matrix.drawRect(dataRecvd[4], dataRecvd[5],
          dataRecvd[6], dataRecvd[7], matrix.
          Color444(dataRecvd[8], dataRecvd[9],
          dataRecvd[10]));
378   }
379
380   bChecksum = 0;
381   bMessageBytes[0] = 0x7C;
382   bChecksum = bChecksum ^ bMessageBytes[0];
383   bMessageBytes[1] = 0xA3;
384   bChecksum = bChecksum ^ bMessageBytes[1];
385   bMessageBytes[2] = 0x09;
386   bChecksum = bChecksum ^ bMessageBytes[2];
387   //bMessageBytes[3] is populated ^^
388   bChecksum = bChecksum ^ bMessageBytes[3];
389   bMessageBytes[4] = dataRecvd[4];
390   bChecksum = bChecksum ^ bMessageBytes[4];
391   bMessageBytes[5] = dataRecvd[5];
392   bChecksum = bChecksum ^ bMessageBytes[5];
393   bMessageBytes[6] = dataRecvd[6];
394   bChecksum = bChecksum ^ bMessageBytes[6];
395   bMessageBytes[7] = dataRecvd[7];
396   bChecksum = bChecksum ^ bMessageBytes[7];
397   bMessageBytes[8] = dataRecvd[8];
398   bChecksum = bChecksum ^ bMessageBytes[8];
399   bMessageBytes[9] = dataRecvd[9];
400   bChecksum = bChecksum ^ bMessageBytes[9];
401   bMessageBytes[10] = dataRecvd[10];
402   bChecksum = bChecksum ^ bMessageBytes[10];
403   bMessageBytes[11] = bChecksum;
404   Serial.write(bMessageBytes, 12);
405   return;
406 }
407
408 void Message4()
409 {
410   /*
        ================================================================
```

```
411     * Message 4 responds by executing the pulse
          train or checking the status of the pulse
          train
412     * depending on the request from the GUI
413     */
414   bRunLines = (boolean)dataRecvd[3];
415   bPrescaler = dataRecvd[4];
416   bOffset = dataRecvd[5];
417   bRunRed = dataRecvd[6];
418   bRunGreen = dataRecvd[7];
419   bRunBlue = dataRecvd[8];
420
421   bCurrentX = bOffset;
422   bCurrentY = bOffset;
423   nFPCount = 0;
424
425   bChecksum = 0;
426   bMessageBytes[0] = 0x7C;
427   bChecksum = bChecksum ^ bMessageBytes[0];
428   bMessageBytes[1] = 0xA4;
429   bChecksum = bChecksum ^ bMessageBytes[1];
430   bMessageBytes[2] = 0x02;
431   bChecksum = bChecksum ^ bMessageBytes[2];
432   bMessageBytes[3] = (byte)bRunLines;
433   bChecksum = bChecksum ^ bMessageBytes[3];
434   bMessageBytes[4] = bPrescaler;
435   bChecksum = bChecksum ^ bMessageBytes[4];
436   bMessageBytes[5] = bOffset;
437   bChecksum = bChecksum ^ bMessageBytes[5];
438   bMessageBytes[6] = bChecksum;
439   Serial.write(bMessageBytes, 7);
440   return;
441 }
442
443 //============================
444
445 void processData()
446 {
447   switch (dataRecvd[1])
```

```
448   {
449     case 0x01:
450       Message1();
451       break;
452     case 0x02:
453       Message2();
454       break;
455     case 0x03:
456       Message3();
457       break;
458     case 0x04:
459       Message4();
460       break;
461     case 0x05:
462     default:
463     break;
464   }
465 }
```

A.3 DPC Microscope user interfaces

Devices attached are attached to the PC via USB (Table A.10). The custom LAbVIEW GUI connects to these devices through USB COM ports which are setup in the initialization file (.ini) which is embedded in the LabVIEW project.

Table A.10: DPC USB Components

Component/Device	**Part number**	**Manufacturer**
CMOS camera	Zyla 4.2	Andor
Fluorescence LED controller	Uno	Arduino
LED Array controller	Uno	Arduino
Electronic Stage	Part number MS2000	ASI Imaging

The Custom LabVIEW GUI is based on a producer/consumer template which uses two while loops running concurrently. The first while loop contains an event structure which responds to events on the GUI and places the corresponding actions onto a queue. As the queue is filled, the second loop contains a case structure to deal with the queued actions appropriately.

When running the GUI, the user can change the exposure time and binning of the camera to find a good image in the "Live Mode" tab (Figure A.1). LED

settings can be adjusted on the right-hand-side of the GUI where intensity and use during automatic can be configured. Based on the image displayed in the "Live Mode" tab, the user can set parameters for a Z-stack using the "Z-Stack" tab. In this tab, x and y positions are confirmed and the Z-step size set (Figure A.2). "Mosaic" mode is the mode in which the electronic stage can be set to move in x or y directions in specified steps and across a specified range. A progress bar shows how far along in the mosaic the process is (Figure A.3). A time lapse image of a fixed region can be captured in the "Time Lapse" tab, where an interval between captures and total number of captures can be configured. A progress bar indicates how far into the time lapse the process is. (Figure A.4).

For debugging and advanced purposes a "Camera Settings" tab was created. Here the specific camera settings can be adjusted, but this mode is not thoroughly tested and if followed by automated imaging modes, it may cause problems (Figure A.5).

Individual control of the LED array (perhaps for illumination of the sample in a dark room) can be configured in the "FP LED Array" tab. Here the user can configure circles or squares of on LEDs onto the array, with options for colour and fill available. Single LEDs can also be switched on independently, and the whole panel can be switched off (Figure A.6).

The most used mode in this setup is the "DPC" tab. Here the user can choose to image a select a single field of view for DPC capture, or a mosaic with the starting point being the current live image. Additionally, the user can specify an interval at which the DPC mosaic is captured (Figure A.7). Remember that the larger the mosaic region, the longer it takes to capture, and could perhaps push up against the interval. The resulting images are stored in separate folders (each containing the 4 angle illumination images) and must be reconstructed according to the code in appendix A.4.

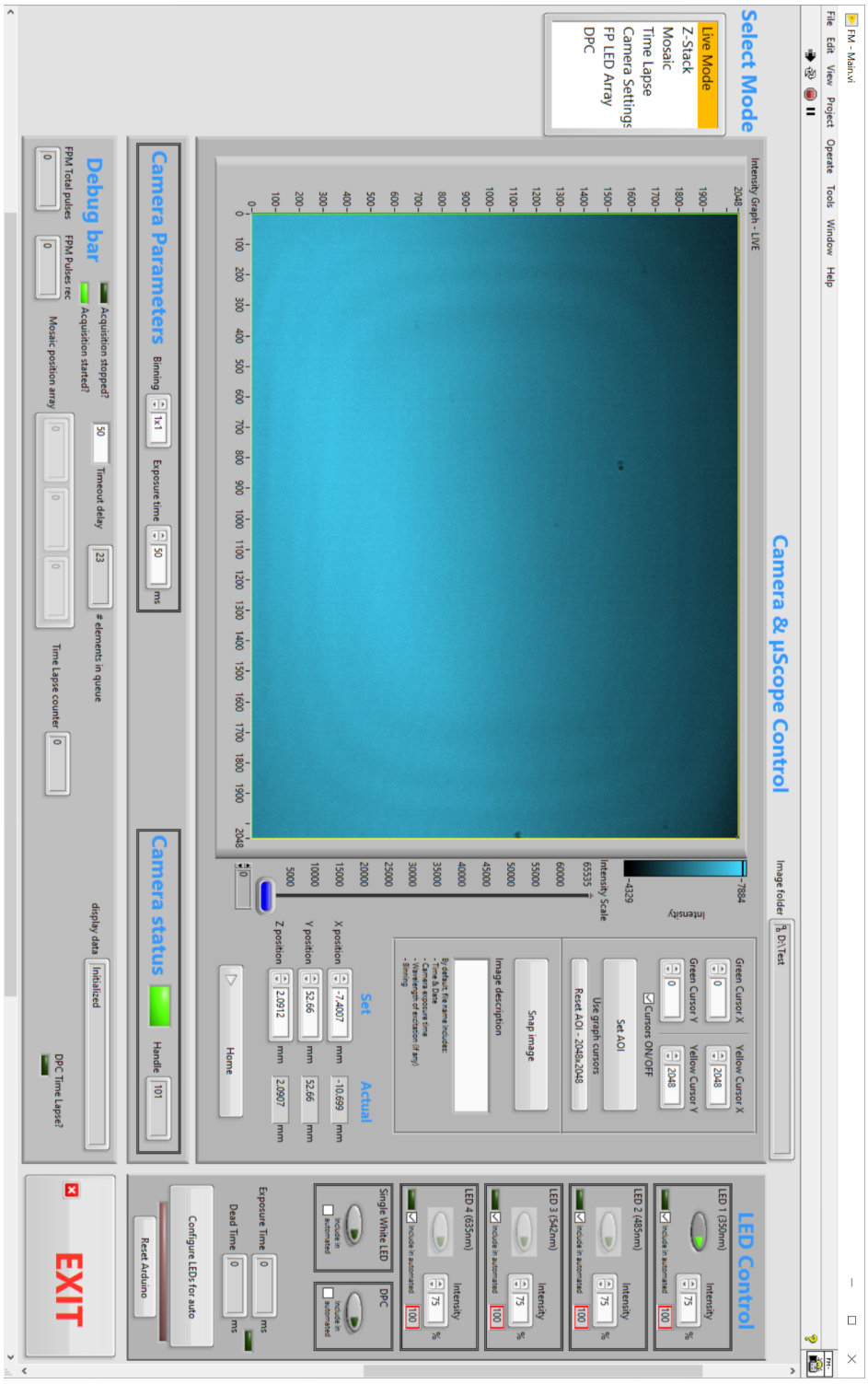

Figure A.1: The custom LabVIEW GUI allows for live imaging of the brightfield image. When a specific LED is used to illuminate the sample, the corresponding pseudocolour is applied to the current view. Each of four LEDs can be used to illuminate the sample independently, or setup for mosaic, Z-stack, or time lapse.

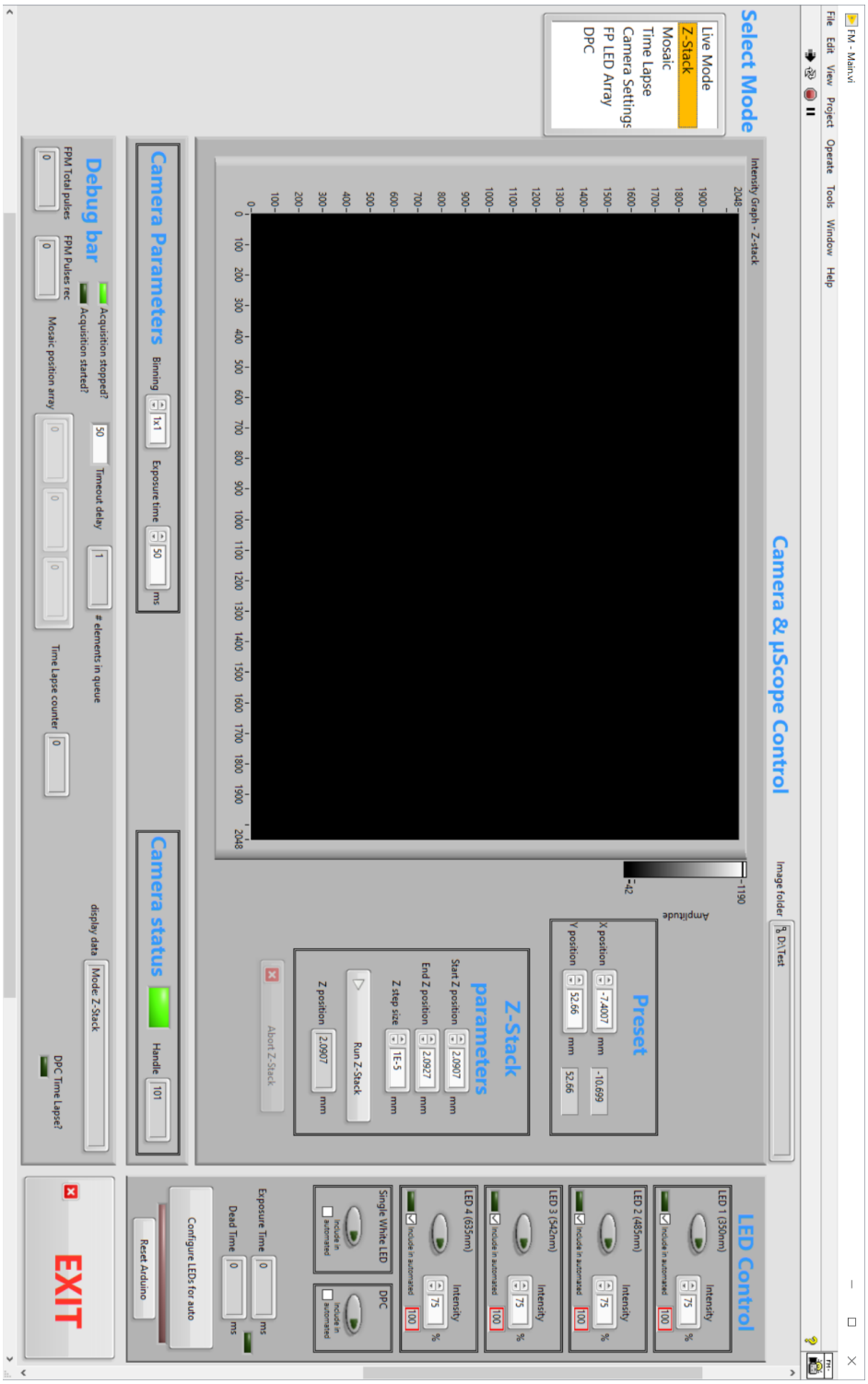

Figure A.2: In order to execute a Z-stack, the x and y positions should be set and then the Z-steps specified. Once these settings are confirmed, run the Z-stack and the resulting single file Z-stack will be saved in the default folder (as set in the .ini file).

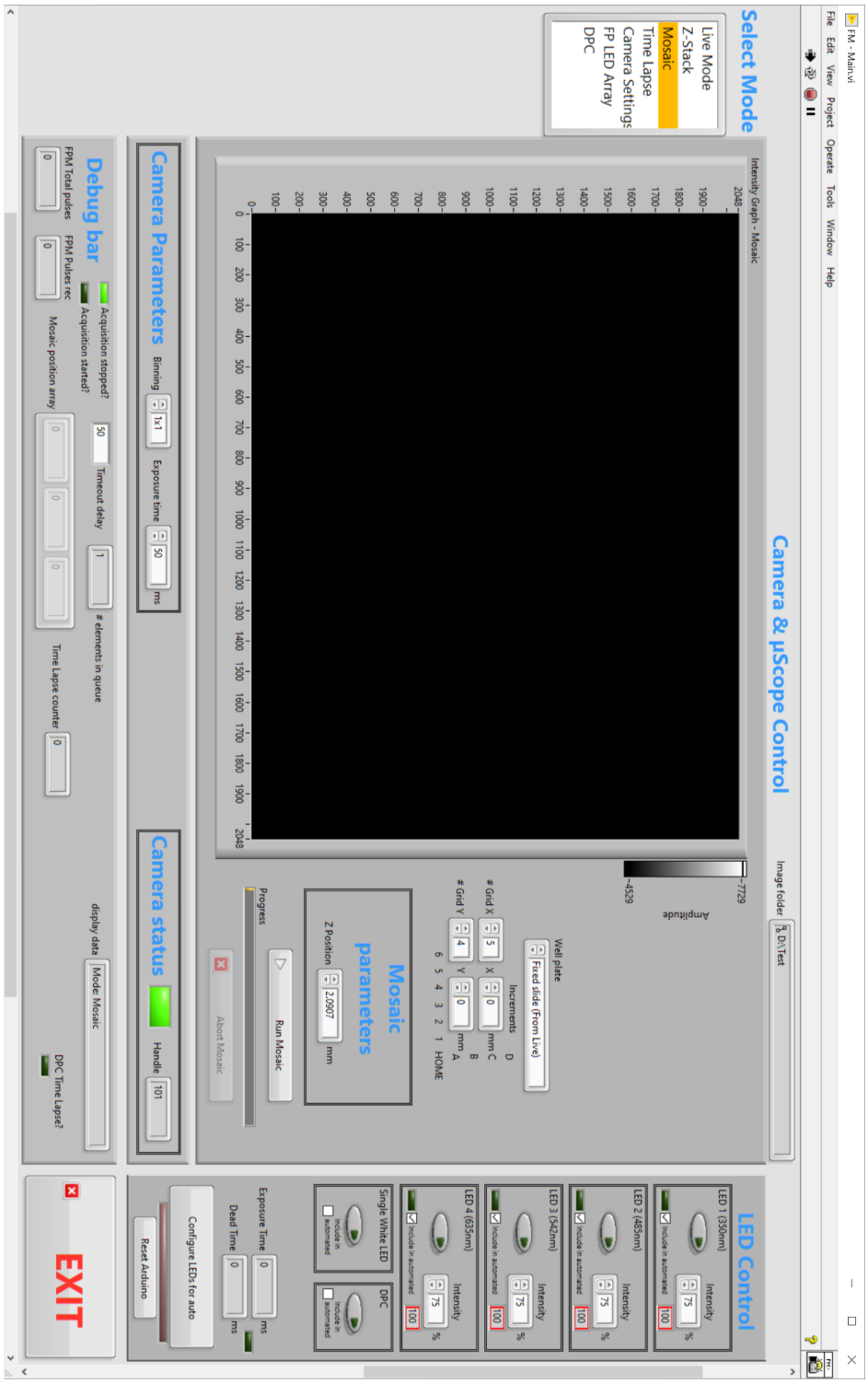

Figure A.3: The mosaic tab enables automatic movement of the stage in x- and y-increments. Illumination sources can be switched on or off automatically during the mosaic capture, and DPC can be included in the mosaic capture.

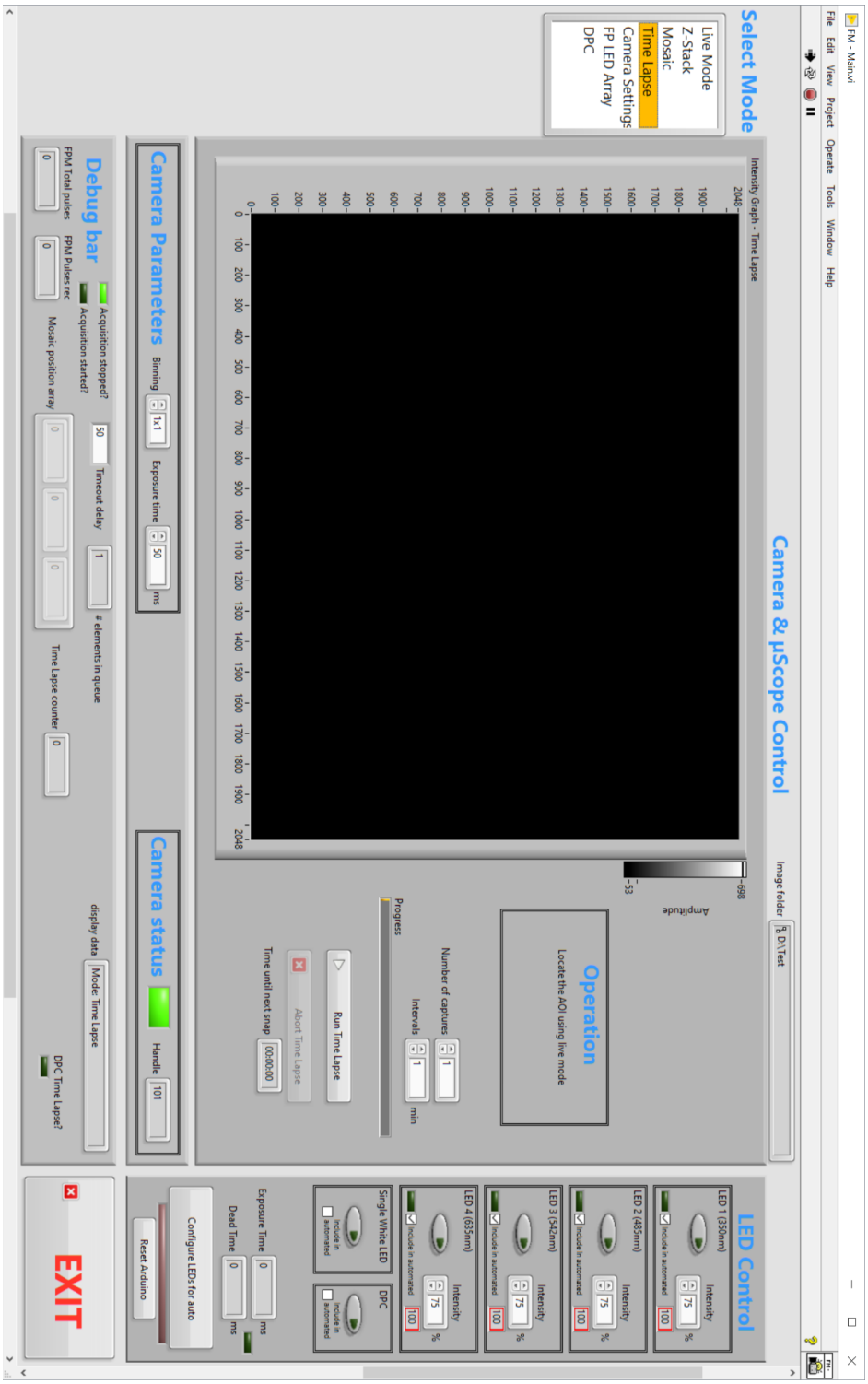

Figure A.4: A time lapse will run a capture of the single frame with any automated illumination sources. Once the specified time has elapsed, a dialog will pop up to inform the user that the capture is complete.

Figure A.5: As an advanced debug tool, the user can adjust any of the camera settings.

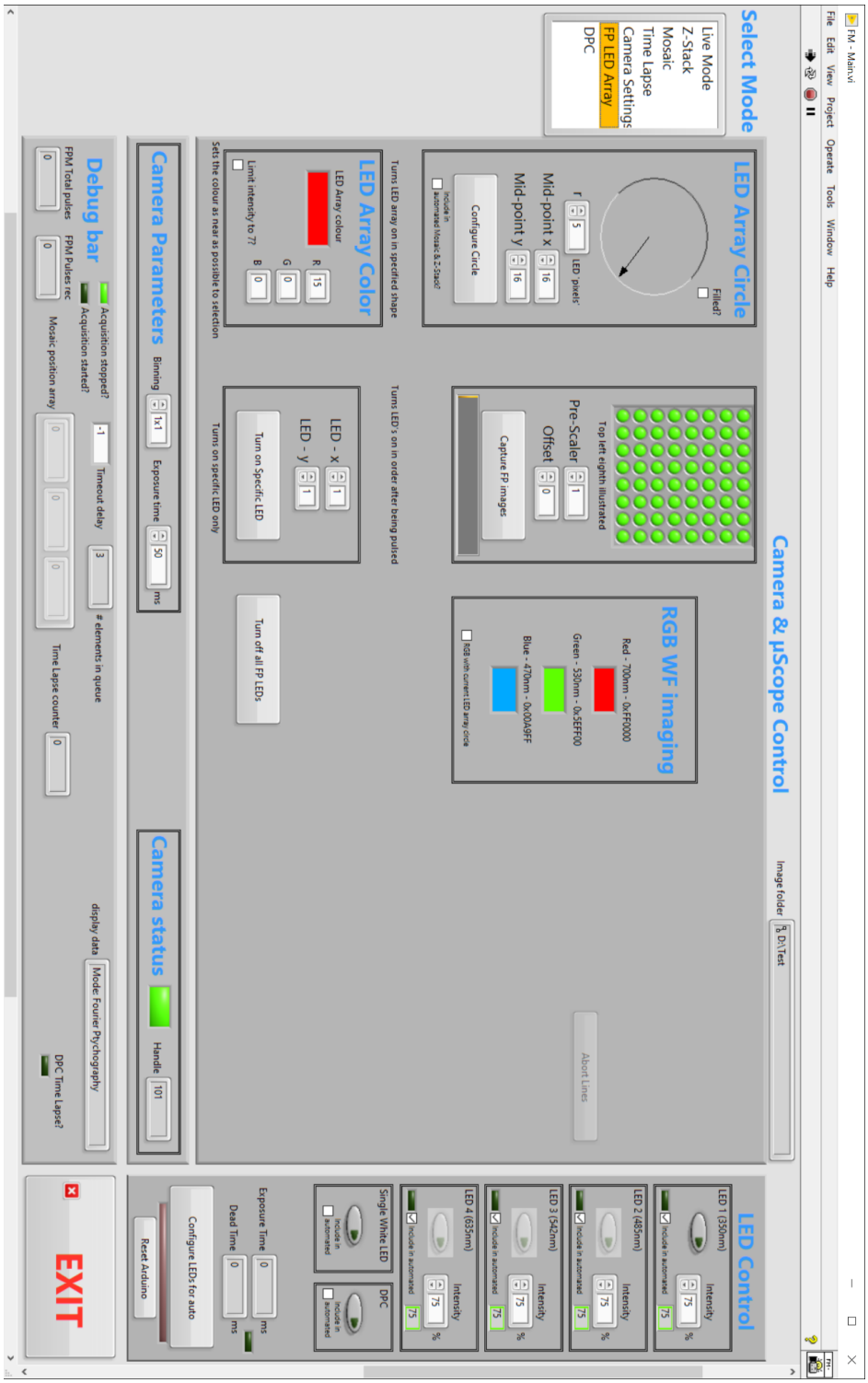

Figure A.6: The GUI is connected to the Adafruit LED array through and Arduino. Settings of the LED array, such as LED colour and specific shapes of LEDs can be adjusted using the GUI.

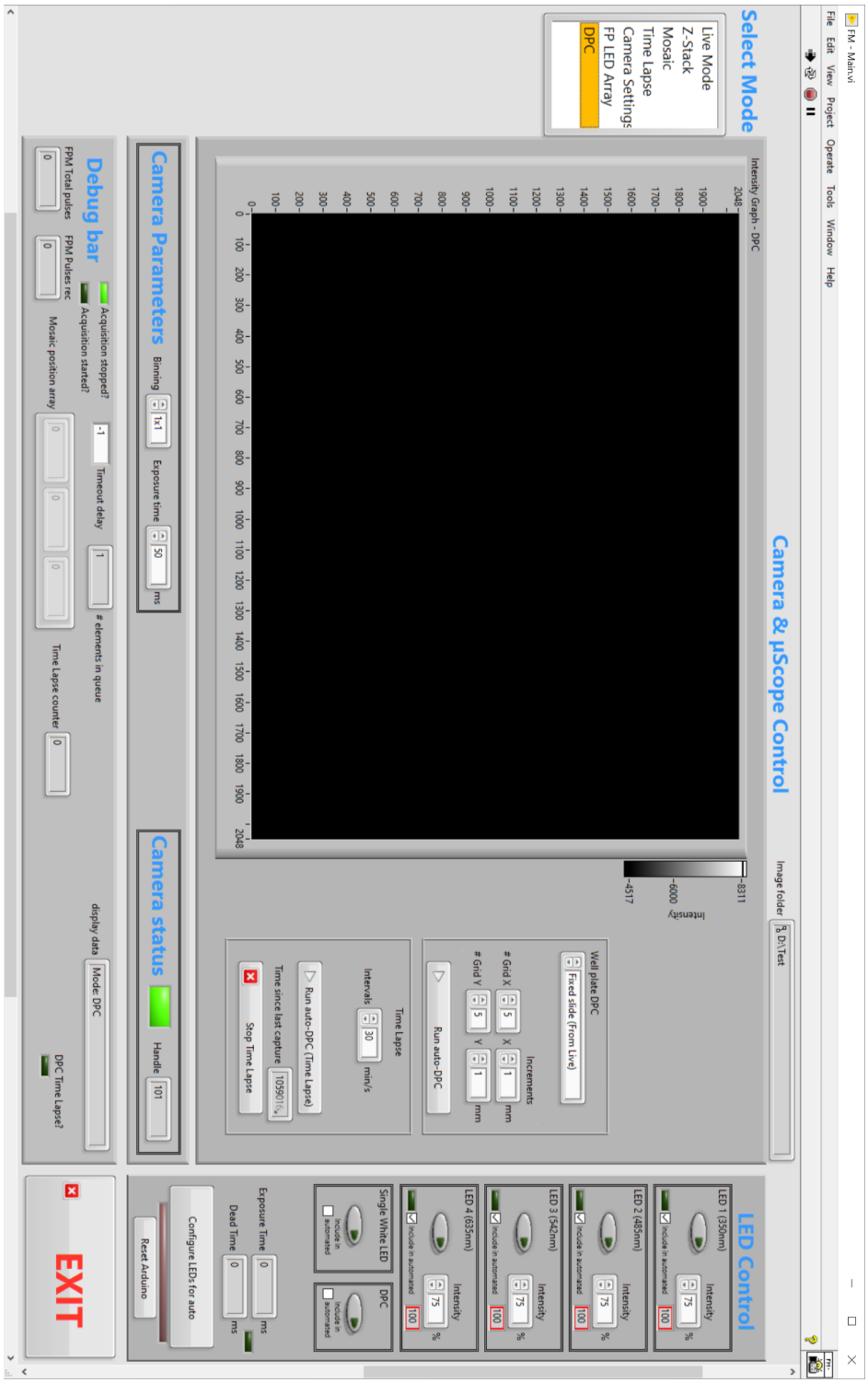

Figure A.7: DPC capture can be setup to run on a single spot, but more often, members of our lab use the mosaic feature along with the DPC imaging. This mosaic can also be used to capture a full mosaic of DPC images at a fixed interval.

A.4 Matlab DPC image reconstruction

The only edit required to execute this script is to input the folder path of the original amplitude images. The folder should contain 4 subimages, and an example folder would be: `"D:\Test\Mosaic\7_17_2024_6_59_41PM_MSC+CFSE\"`. The code recorded here is edited to fit fully within the margins of this document and will not run if copied without correcting some syntax errors that would result.

A big adaptation from the original Waller provided code and this code is the change of saving the resulting phase image as a *tiff* file. Matlab does not have a simple way of saving *tiff* files, so I had to do it in a manner that feels very manual.

```
%%%%%%%%%%%%%%%%%%%%%%%%%%%%%%%%%%%%%%%%%%%%%%%%%%%%%%%%%%
% main_dpc_aberration_estimation -
%
% Main file for DPC amplitude and phase recovery with aberrati
%
%
% Copyright (C) 2018 Michael Chen and Zack Phillips
%
%
%
% This program is free software: you can redistribute it and/
%
% it under the terms of the GNU General Public License as pub
%
% the Free Software Foundation, either version 3 of the Licens
%
% (at your option) any later version.
%
%
%
% This program is distributed in the hope that it will be usef
%
% but WITHOUT ANY WARRANTY; without even the implied warranty
%
% MERCHANTABILITY or FITNESS FOR A PARTICULAR PURPOSE.
See the          %
```

```
% GNU General Public License for more details.
%
%
%
% You should have received a copy of the GNU General Public License
%
% along with this program.  If not, see <http://www.gnu.org/licenses/>.
%
%%%%%%%%%%%%%%%%%%%%%%%%%%%%%%%%%%%%%%%%%%%%%%%%%%%%%%%%%%%%%%%%%%%%%%%%
clear; close all;
set(0, 'DefaultFigureWindowStyle', 'docked');
global zernike_poly pupil dim source fIDPC pupilphase f_amplitude f_phase
use_gpu
addpath('.\dpc_functions');
F           = @(x) fft2(x);
IF          = @(x) ifft2(x);

%% load data
aberration_correction = false;
save_amplitude_output = false;

clc
% HIGH LEVEL FOLDER LOCATION (With a large number of "DPC"
folders within it":
High_Folder ='D:\Test\Mosaic\7_17_2024_6_59_41 PM_MSC+CFSE\';

% CALIBRATION SCALING FACTOR
Scale = 3.775;

%Need to make a correction for if there is already a folder
Reconstruction_Folder = append(High_Folder,'Reconstructions\');
    if ~isfolder(Reconstruction_Folder)
        mkdir(Reconstruction_Folder);
    end

Folder_List = ls(High_Folder);
Num_Folders = size(Folder_List);
if Folder_List(1) == '.'
    Foldercount = Num_Folders(1) - 3;
```

```
else
    Foldercount = 1;
end

list_of_folders(Num_Folders(1,1)-3) = 0;
list_of_folders = list_of_folders';
for c = 1:Num_Folders(1)-3
    list_of_folders(c,1) = str2num(Folder_List(c+2,:));
end

sorted_list = sort(list_of_folders);


tStart = tic;
for Folder_Iterations = 1:Foldercount
    clc
    Text_to_Display = append('Begin reconstruction ',
                num2str(Folder_Iterations),' of ',num2str(Fold
    disp(Text_to_Display)
    tic

    Im_folder = append(High_Folder,
                num2str(sorted_list(Folder_Iterations)),'\');

    File_List = ls(Im_folder);

    File1 = append(Im_folder,File_List(3,:));
    File2 = append(Im_folder,File_List(4,:));
    File3 = append(Im_folder,File_List(5,:));
    File4 = append(Im_folder,File_List(6,:));
    IDPC(:,:,1) = imread(File1, 'tiff');
    IDPC(:,:,2) = imread(File2, 'tiff');
    IDPC(:,:,3) = imread(File3, 'tiff');
    IDPC(:,:,4) = imread(File4, 'tiff');

    if aberration_correction
        %this example dataset for DPC with aberrations
                                already remove the DC term
        %and normalized by the total energy (DC term)
```

```
    %load('..\sample_data\dataset_DPC_with_aberration.mat');
    IDPC = double(IDPC)/65535;

else
%     load('..\sample_data\dataset_DPC_MCF10A.mat');
%     IDPC = permute(double(IDPC), [2, 3, 1]);

    IDPC = double(IDPC)/65535;
    % image normalization
      for image_index = 1:size(IDPC, 3)
          image_load                = IDPC(:, :, image_index);
          IDPC(:, :, image_index) = image_load/mean2(image_load)-1;
      end
end
disp('.')
%% system parameters
            % image size
dim           = [size(IDPC, 1), size(IDPC, 2)];
% partial coherence factor
            sigma         = 1.0;
            % numerical aperture of the imaging system
na            = 0.30;
            % numerical aperture of the illumination
na_illum      = sigma*na;
            % magnification of the imaging system
magnification = 5*2;
% wavelength in micron
            lambda        = 0.510;
      % pixel size in micron
ps            = 6.5/magnification;
% wave number
            wavenumber    = 2*pi/lambda;
if aberration_correction
            % orientation of the illumination
    illu_rotation = [0, 180, 90];
else
    %illu_rotation = [0, 180, 90, 270];
    illu_rotation = [270, 180, 90, 0];
end
```

```
            % number of illumination used in DPC
num_rotation  = numel(illu_rotation);
            % if annular illumination is used, set the NA
            corresponds to the inner radius
na_inner      = [0, 0, 0, 0];
            % highest order of Zernike coefficients used
            for pupil estimation
num_Zernike   = 21;
setCoordinate();
disp('.')
%% show measurements
if aberration_correction
    num_images = num_rotation+1;
else
    num_images = num_rotation;
end
disp('.')
% figure('Name', 'normalized, background substracted DPC i
% for source_index = 1:num_images
%     subplot(2, 2, source_index);
%     imagesc(IDPC(:, :, source_index)); axis image; axis o
%     title(['DPC ', num2str(source_index)], 'FontSize', 2
% end
% drawnow;

%% generate illumination sources
source              = zeros(dim(1), dim(2), num_images);
disp('.')
for source_index = 1:num_images
  if source_index <= num_rotation
     source(:, :, source_index) =
            genSource(illu_rotation(source_index),
                      na_illum, na_inner(source_inde
  else
      if aberration_correction
          % additional coherent illumination
          source_temp                 = zeros(dim(1), dim(2
          source_temp(Fx==0 & Fy==0) = 1;
          source(:, :, source_index) = source_temp;
```

```
        end
    end
end
disp('.')
% figure('Name', 'Illumination and Phase Optical Transfer Functions',
% fig_rows     = floor(sqrt(num_images));
% fig_cols     = floor(num_images/fig_rows);
% for fig_index = 1:num_images
%     ax = subplot(fig_rows, fig_cols, fig_index);
%     imagesc(fftshift(fx), fftshift(fy), fftshift(source(:, :, fig_i
%     title(['Source ', num2str(fig_index)]);
%     colormap(ax, 'gray'); caxis([0, 1]);
% end
% drawnow;
disp('.')
%% generate Zernike polynomials
pupil          = (Fx.^2+Fy.^2<=(na/lambda)^2);
zernike_poly   = genZernikePoly(Fx, Fy, na, lambda, num_Zernike);

% figure('Name', 'generated Zernike polynomials (Defocus and Astigmat
% subplot(131)
% imagesc(fftshift(fx), fftshift(fy), fftshift(reshape(zernike_poly(:
% title('aberration, Z_3', 'fontsize', 24);
% subplot(132)
% imagesc(fftshift(fx), fftshift(fy), fftshift(reshape(zernike_poly(:
% title('aberration, Z_4', 'fontsize', 24);
% subplot(133)
% imagesc(fftshift(fx), fftshift(fy), fftshift(reshape(zernike_poly(:
% title('aberration, Z_5', 'fontsize', 24);
% drawnow;

%% joint estimation pupil function, amplitude and phase
disp('.')
% calculate frequency spectrum of the measurements
fIDPC                = F(IDPC);

% parameters for amplitude and phase reconstruction
% initalization of Zernike coefficients for pupil estimation,
            ignoring the first three orders
```

```
            zernike_coeff_k      = 0*randn(num_Zernike-3,
if aberration_correction
                    % maximum number of iteration of algor
    max_iter_algorithm  = 25;
else
                    % only need 1 iteration if pupil estim
    max_iter_algorithm  = 1;
end
            % parameters for L2 regurlarization [amplitude
            (can set to a very small value in noiseless ca
reg_L2              = 1.0*[1e-1, 5e-3];
            % true: use TV regularization, false: use L2
use_tv              = false;
            % parameters for total variation [amplitude, p
            (can set to a very small value in noiseless ca
tau                 = [1e-5, 5e-3];
            % true: show loss value and elapsed time at ea
verbose             = true;
            % true: show amplitude, phase and aberration
show_result         = false;
            % true: use GPU, false: use CPU
use_gpu             = false;
disp('.')
% parameters of L-BFGS algorithm for pupil estimation
            (default values should work)
%addpath(genpath('..\minFunc\'));
            % add the path where you install the minFunc p
addpath('.\minFunc');
addpath('.\imwrite2TIF');
options.Method      = 'lbfgs';
options.maxIter     = 10;
options.PROGTOL     = 1e-30;
options.optTol      = 1e-30;
options.MAXFUNEVALS = 500;
options.corr        = 50;
options.usemex      = 0;
options.display     = false;

if use_gpu
```

```
        % place measurements and variables into GPU memory
        source = gpuArray(source);
        pupil  = gpuArray(pupil);
        fIDPC  = gpuArray(fIDPC);
    end

    t_start              = tic();
    loss                 = zeros(max_iter_algorithm, 1);
    %fig_results          = figure('Name', 'Reconstruction Process', 'Num
    disp('.')
    for iter = 1:max_iter_algorithm

        if ~use_tv
            % Least-Squares with L2 regularization
            [amplitude_k, phase_k]       =
DPC_L2(zernike_coeff_k, reg_L2);
        else
            %ADMM algorithm with total variation regularization
            global padsize Dx Dy;
            padsize                      = 0;
            temp                         = zeros(dim);
            temp(1, 1)                   = 1;
            temp(1, end)                 = -1;
            Dx                           = F(temp);
            temp                         = zeros(dim);
            temp(1, 1)                   = 1;
            temp(end, 1)                 = -1;
            Dy                           = F(temp);
            rho                          = 1;
            D_x                          = zeros(dim(1), dim(2), 4);
            u_k                          = zeros(dim(1), dim(2), 4);
            z_k                          = zeros(dim(1), dim(2), 4);
            if use_gpu
               Dx = gpuArray(Dx);
               Dy = gpuArray(Dy);
               D_x= gpuArray(D_x);
               u_k= gpuArray(u_k);
               z_k= gpuArray(z_k);
            end
```

```
    for iter_ADMM = 1:20
        [amplitude_k, phase_k] =
DPC_TV(zernike_coeff_k, rho, z_k, u_k, reg_L2);
        if iter_ADMM < 20
            D_x(:, :, 1)   = amplitude_k - circshift(a
            D_x(:, :, 2)   = amplitude_k - circshift(a
            D_x(:, :, 3)   = phase_k - circshift(phase
            D_x(:, :, 4)   = phase_k - circshift(phase
            z_k            = D_x + u_k;
            z_k(:, :, 1:2) = max(z_k(:, :, 1:2) - tau
                             max(-z_k(:, :, 1:2) - tau
            z_k(:, :, 3:4) = max(z_k(:, :, 3:4) - tau
                             max(-z_k(:, :, 3:4) - tau
            u_k            = u_k + (D_x-z_k);
        end
    end
        clear u_k z_k D_x;
end


if aberration_correction
    f_amplitude = F(amplitude_k);
    f_phase     = F(phase_k);

    % pupil estimation
    [zernike_coeff_k, loss(iter)] = minFunc(@gradientL
    pupilphase                    = aberrationGenerati

    % print cost function value and computation time a
    if verbose
        fprintf('iteration: %04d, loss: %5.5e, elapsed
    end
end

% plot recovered amplitude, phase and aberration at ea
if show_result
    figure(fig_results);
    ax1 = subplot(2, 2, 1);
```

```
            imagesc(x, y, amplitude_k); axis image; axis off;
            colormap(ax1, 'gray'); caxis([-.15, 0.02]);
            title('recovered \alpha','FontSize', 24);
            ax2 = subplot(2, 2, 2);
            imagesc(x, y, phase_k); axis image; axis off;
            colormap(ax2, 'gray');
            colorbar
            title('recovered \phi', 'FontSize', 24);
            if aberration_correction
                ax3 = subplot(2, 2, 3);
                imagesc(fftshift(fx), fftshift(fy), fftshift(pupilphase))
                colormap(ax3, 'jet'); caxis([-1.0, 1.0]);
                title('recovered aberration', 'FontSize', 24);
                subplot(2, 2, 4);
                plot(1:iter, log10(loss(1:iter)), 'bo'); axis square;
                xlabel('iteration', 'FontSize', 20);
                ylabel('log_1_0(loss)', 'FontSize', 20)
                title('loss', 'FontSize', 24);
                linkaxes([ax1, ax2]);
            end
            drawnow;
        end
    end

    % extract results and variables from GPU memory if using GPU computat
    amplitude  = gather(amplitude_k); % optimized amplitude
    phase      = gather(phase_k);     % optimized phase
    pupilphase = gather(pupilphase); % optimized aberration function
    pupil      = gather(pupil);
    source     = gather(source);
    fIDPC      = gather(fIDPC);


    %save phase image
    phase = phase*Scale;
    phase = single(phase);
    Phasetarget = append(Reconstruction_Folder, num2str(Folder_Iterations
    t = Tiff(Phasetarget, 'w');
    tagstruct.ImageLength = size(phase, 1);
```

```
        tagstruct.ImageWidth = size(phase, 2);
        tagstruct.Compression = Tiff.Compression.None;
        tagstruct.SampleFormat = 3;
        tagstruct.Photometric = Tiff.Photometric.MinIsBlack;
        tagstruct.BitsPerSample = 32;
        tagstruct.SamplesPerPixel = 1;
        tagstruct.PlanarConfiguration = Tiff.PlanarConfiguration.C
        t.setTag(tagstruct);
        t.write(phase);
        t.close();

        %Example using imwrite2tif
    %    tag1 = imfinfo(Phasetarget);
    %    tag1.BitsPerSample = 64;
    %    amplitude = single(amplitude);
    %    imwrite2tif(amplitude, tag1, 'C:\Users\heiro\Desktop\pha

        if(save_amplitude_output)
            %save amplitude image
            amplitude = single(amplitude);
            Amplitudetarget = append(Im_folder, '\out_amplitude.ti
            t = Tiff(Amplitudetarget, 'w');
            tagstruct.ImageLength = size(amplitude, 1);
            tagstruct.ImageWidth = size(amplitude, 2);
            tagstruct.Compression = Tiff.Compression.None;
            tagstruct.SampleFormat = Tiff.SampleFormat.IEEEFP;
            tagstruct.Photometric = Tiff.Photometric.MinIsBlack;
            tagstruct.BitsPerSample = 32;
            tagstruct.SamplesPerPixel = 1;
            tagstruct.PlanarConfiguration = Tiff.PlanarConfigurati
            t.setTag(tagstruct);
            t.write(amplitude);
            t.close();
        end

        disp('Reconstruction complete')
        toc
    end
    tEnd = toc(tStart)
```

A.5 Python halo removal script

The only edit required to execute this script is to input the folder path of the reconstruction result from Matlab. It should be something resembling: `"D:/Workbigdata/DPC/1-phasetarget/4_26_2024_4_27_20PM-USAF1/Reconstructions/0.tiff"`, it will be a single image corrected at a time. Stored with this code on the desktop PC is a very similar script that executes the correction on an entire folder of images.

```
# -*- coding: utf-8 -*-
"""
Created on Thu May 23 10:55:28 2024

@author: arl01586

This filtering is based on:
    https://opg.optica.org/boe/fulltext.cfm?uri=boe-9-2-623&id=380814
    Real-time halo correction in phase contrast imaging
    Mikhail E. Kandel, Michael Fanous, Catherine Best-Popescu,
                and Gabriel Popescu 2018

    It requires an input folder, the Reconstructions folder of
                a whole folder of DPC reconstructions output from the MA
                reconstructions

    Where to make changes:
        1 - Import the input folder
"""

import numpy as np
from PIL import Image
import os
from progress.bar import Bar
import time

# ============================================================================
# Import the input image - EDIT APPROPRIATELY
# ============================================================================

Directory_Name = "_/Reconstructions"
```

```
# ============================================================
# DO NOT CHANGE ANYTHING FURTHER
# ============================================================

# ============================================================
# Generate the FILTERS
# ============================================================
t = time.time()
# Create first level of filter; Must be applied to 2048x2048
# image
x = np.ones([1,2048])

# Shoulder of the filter is 1/Lc
# In their (Popescu) example they set Lc = 2um. 1/0.002 = 500
#, so 500 pixels
# According to them, you set this once for an objective lens
# But each pixel is 0.65um, so is it then multiplied by 0.65,
# 500*0.65 = 325
Lc = 0.002 #um

Shoulder = int((1/Lc) * 0.65) # Pixels per micron

# Coordinate position of middle position and the gradients
Midpoint = 1024
Left_Shoulder = Midpoint - Shoulder
Right_Shoulder = Midpoint + Shoulder

# Generate the linespace according to the shoulder of the
# filter and the midpoint
Line_Up = np.linspace(1, Midpoint-Left_Shoulder,
Midpoint-Left_Shoulder)
Line_Up = np.reshape(Line_Up, [1,Midpoint-Left_Shoulder])
Gradient = 1/(Midpoint-Left_Shoulder)
Line_Up = Gradient*Line_Up
Line_Down = np.flip(Line_Up, axis=None)

# Multiply these values in to the flatspace appropriately
```

```
# Single row
x[0,Left_Shoulder:Midpoint] = Line_Down[:,:]
x[0,Midpoint] = 0
x[0,Midpoint+1:Right_Shoulder+1] = Line_Up[:,:]

# Multiply the single row into a 2D space
Filter_90 = np.ones([2048, 2048])
for i in range(2048):
    Filter_90[i,:] = x[:,:]

im_F90 = Image.fromarray(Filter_90)
im_F90.save("./Filter_90.tiff")

# Make a 0 degree filter (based on the 90 degree filter that we made)
Filter_0 = np.rot90(Filter_90)
im_F0 = Image.fromarray(Filter_0)
im_F0.save("./Filter_0.tiff")

# Make a 45 degree filter (based on the 90 degree filter that we made)
Filter_45 = np.ones([2048,2048])
for i in range(2048):
    x2 = np.roll(x, 1023-i)
    Filter_45[i,:] = x2[:,:]

# Fill in the top left and bottom right with ones
fill = np.ones([300,300])
Filter_45[0:300,0:300] = fill[:,:]
Filter_45[2048-300:2048, 2048-300:2048] = fill[:,:]
im_F45 = Image.fromarray(Filter_45)
im_F45.save("./Filter_45.tiff")

# ================================================================
# Sort out the outside loop for each image within the
# reconstructions folder
# ================================================================

'''
    For the given path, get the List of all files in
            the directory tree
```

```
'''
def getListOfFiles(dirName):
    # create a list of file and sub directories
    # names in the given directory
    listOfFile = os.listdir(dirName)
    allFiles = list()
    # Iterate over all the entries
    for entry in listOfFile:
        # Create full path
        fullPath = os.path.join(dirName, entry)
        # If entry is a directory then get the list of files
                                # in this directory
        if os.path.isdir(fullPath):
            allFiles = allFiles + getListOfFiles(fullPath)
        else:
            allFiles.append(fullPath)

    return allFiles

# List all of the images in the folder
ListOfFiles = getListOfFiles(Directory_Name)
# Create a new folder for output of the filtered images
path = os.path.join(Directory_Name, "Halo Removed")
# Check if the folder exists, if it does, do nothing,
# else create it
isdir = os.path.isdir(path)
if isdir == False:
    os.mkdir(path)

# ============================================================
# Filter each image in the reconstructions folder
# ============================================================
print("Begin Filtering")
# Start progress bar
bar = Bar('Processing', max = len(ListOfFiles))
for elem in ListOfFiles:
    imo = np.array(Image.open(elem))
    #imo = imread(elem)
    fft_image = np.fft.fftshift(np.fft.fft2(imo))
```

```
# ========================================================================
# FILTER The input image
# ========================================================================
# Multiply the magnitude with the filters
FFT_od = fft_image * Filter_o
FFT_45d = fft_image * Filter_45
FFT_90d = fft_image * Filter_90

# ========================================================================
# Inverse FFT of each image
# ========================================================================
# Original image
IFT = np.fft.ifftshift(fft_image)
IFT = np.fft.ifft2(IFT)
IFT_real = np.real(IFT)
# Normalize the reconstructed image to match the original image scale
IFT_real = IFT_real * (np.max(np.abs(imo)) / np.max(np.abs(IFT_real))

# 0 degree filtered image
IFT_od = np.fft.ifftshift(FFT_od)
IFT_od = np.fft.ifft2(IFT_od)
IFT_od_real = np.real(IFT_od)
# Normalize the reconstructed image to match the original image scale
# IFT_real = IFT_real * (np.max(np.abs(imo)) /
            np.max(np.abs(IFT_od_real)))

# 45 degree filtered image
IFT_45d = np.fft.ifftshift(FFT_45d)
IFT_45d = np.fft.ifft2(IFT_45d)
IFT_45d_real = np.real(IFT_45d)

# 90 degree filtered image
IFT_90d = np.fft.ifftshift(FFT_90d)
IFT_90d = np.fft.ifft2(IFT_90d)
IFT_90d_real = np.real(IFT_90d)

# ========================================================================
# Find the Maximum values of the 4 images:
```

```
        #    1: 0 degree filtered
        #    2: 45 degree filtered
        #    3: 90 degree filtered
        #    4: original image
        # ========================================================
        # Compare the 0d & 45d filtered images.
                    # Keep the maximum values between the two
        max1 = np.maximum(IFT_0d_real, IFT_45d_real)
        # Compare the max of the previous comparison (0d v 45d)
                    # to the 90d filtered image
        max2 = np.maximum(max1, IFT_90d_real)
        # Compare the max of the previous comparison,
                    # which would result in the maximum
        # value among all the filtered images to the
                    # original phase image
        max3 = np.maximum(max2, imo)

        # ========================================================
        # Result
        # ========================================================
        # Save filtered images
        # Rename the file
        # Split into path and filename
        head_tail = os.path.split(elem)
        # Split filename into file name and extension
        split_tup = os.path.splitext(head_tail[1])
        File_Name_Only = split_tup[0] + ".tiff"
        Final_file_Name = os.path.join(path, File_Name_Only)
        im_Maxed = Image.fromarray(max3)
        im_Maxed.save(Final_file_Name)
        bar.next()
bar.finish()
print("\n")
elapsed = time.time() - t
print("Elapsed time: ", round(elapsed,2), " seconds\n")
```

Appendix B

Single photon microscope

These appendices are related to the fluorescence extension applied to the upright microscope that accomodates the DPC microscope referenced above.

B.1 Fluorescence microscope block diagram

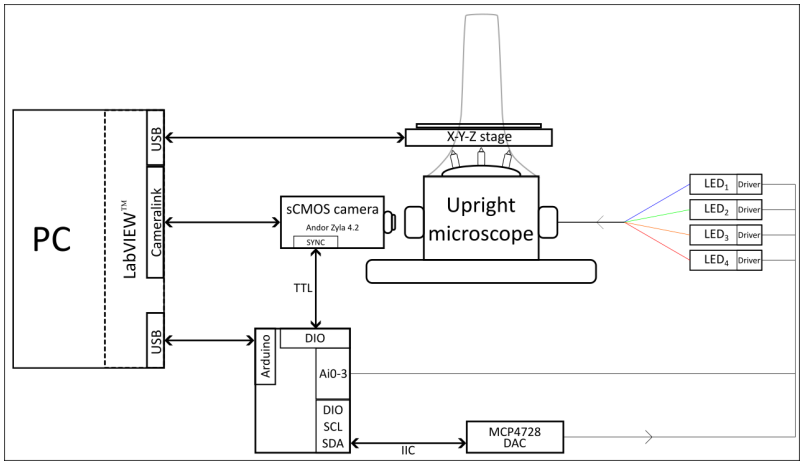

Figure B.1: Schematic diagram of the electronic components used to construct the single-photon microscope including four high intensity LEDs and digital to analog converters.

B.2 Communications between iPE LEDs controlled by the Arduino and LabVIEW

These tables describe the messages sent from the Arduino to the LabVIEW PC over USB. Specifically this is the Arduino that controls the fluorescence LEDs.

Note that the LabVIEW and Arduino themselves play no role in the decisions made in this document, this is simply a communication message protocol.

This first table simply illustrates usage of the ICD.

Table B.1: LED intensity communications message structure

Byte Number	Byte Description	Byte Expected	Byte Representation
1	Sync byte	0x3C (<)	UINT8
2	Message header	0x0*	UINT8
3	Message length	Number of bytes in the message (excluding sync byte and message header, message length, but including checksum	UINT8
4 ... n-1	Message payload	Number of bytes	UINT8
n	Checksum	XOR of each of the bytes in the message (incl. sync byte, message header and message length)	UINT8

Message 1 - Get voltage. Upon receiving message 1, the LED controlling Arduino responds with voltage measurements of each DAC output.

Table B.2: LabVIEW to LED intensity control Arduino - Message 1

Byte Number	Byte Description	Byte Expected	Byte Representation
1	Sync byte	0x3C (<)	UINT8
2	Message header	0x01	UINT8
3	Message length	0x02	UINT8
4	Message payload	0x52	UINT8
5	Checksum	XOR of each of the bytes in the message (incl. sync byte, message header and message length)	UINT8

Table B.3: LED intensity control Arduino to LabVIEW response - Message 1

Byte Number	Byte Description	Byte Expected	Byte Representation
1	Sync byte	`0x3C` (<)	UINT8
2	Message header	`0xA1`	UINT8
3	Message length	`0x05`	UINT8
4	LED1 Intensity	0 - 100 as a percentage	UINT8
5	LED2 Intensity	0 - 100 as a percentage	UINT8
6	LED3 Intensity	0 - 100 as a percentage	UINT8
7	LED4 Intensity	0 - 100 as a percentage	UINT8
8	Checksum	XOR of each of the bytes in the message (incl. sync byte, message header and message length)	UINT8

Message 2 - Set voltage. Upon receiving message 2, the LED controlling Arduino configures the DAC with voltage outputs according to this message.

Table B.4: LabVIEW to LED intensity control Arduino - Message 2

Byte Number	Byte Description	Byte Expected	Byte Representation
1	Sync byte	`0x3C` (<)	UINT8
2	Message header	`0x02`	UINT8
3	Message length	`0x05`	UINT8
4	LED1 Intensity	`0 - 100` as a percentage	UINT8
5	LED2 Intensity	`0 - 100` as a percentage	UINT8
6	LED3 Intensity	`0 - 100` as a percentage	UINT8
7	LED4 Intensity	`0 - 100` as a percentage	UINT8
8	Checksum	XOR of each of the bytes in the message (incl. sync byte, message header and message length)	UINT8

Table B.5: LED intensity control Arduino to LabVIEW response - Message 2

Byte Number	Byte Description	Byte Expected	Byte Representation
1	Sync byte	`0x3C` (<)	UINT8
2	Message header	`0xA2`	UINT8
3	Message length	`0x05`	UINT8
4	LED1 Intensity	0 - 100 as a percentage	UINT8
5	LED2 Intensity	0 - 100 as a percentage	UINT8
6	LED3 Intensity	0 - 100 as a percentage	UINT8
7	LED4 Intensity	0 - 100 as a percentage	UINT8
8	Checksum	XOR of each of the bytes in the message (incl. sync byte, message header and message length)	UINT8

Message 3 - Set LED. Upon receiving message 3, the LED controlling Arduino configures the output details such as exposure time, etc.

Table B.6: LabVIEW to LED intensity control Arduino - Message 3

Byte Number	Byte Description	Byte Expected	Byte Representation
1	Sync byte	`0x3C` (<)	UINT8
2	Message header	`0x03`	UINT8
3	Message length	`0x06`	UINT8
4	LED used?	`bit0`: LED1 `bit1`: LED2 `bit2`: LED3 `bit3`: LED4 on(1)/off(0)	UINT8
5..6	Exposure time	20ms - 1000ms	UINT16
7..8	Dead time	20ms - 1000ms	UINT16
9	Checksum	XOR of each of the bytes in the message (incl. sync byte, message header and message length)	UINT8

Table B.7: LED intensity control Arduino to LabVIEW response - Message 3

Byte Number	Byte Description	Byte Expected	Byte Representation
1	Sync byte	`0x3C` (<)	UINT8
2	Message header	`0x03`	UINT8
3	Message length	`0x06`	UINT8
4	LED used?	`bit0`: LED_1 `bit1`: LED_2 `bit2`: LED_3 on(1)/off(0) `bit3`: LED_4	UINT8
5..6	Exposure time	20ms - 1000ms	UINT16
7..8	Dead time	20ms - 1000ms	UINT16
9	Checksum	XOR of each of the bytes in the message (incl. sync byte, message header and message length)	UINT8

Message 4 - Set LED. Upon receiving message 4, the LED controlling Arduino configures the output details such as exposure time, etc.

Table B.8: LabVIEW to LED intensity control Arduino - Message 4

Byte Number	Byte Description	Byte Expected	Byte Representation
1	Sync byte	`0x3C` (<)	UINT8
2	Message header	`0x04`	UINT8
3	Message length	`0x02`	UINT8
4	Run command	`0x00`: No action `0x01`: Run	UINT8
5	Checksum	XOR of each of the bytes in the message (incl. sync byte, message header and message length)	UINT8

Table B.9: LED intensity control Arduino to LabVIEW response - Message 4

Byte Number	Byte Description	Byte Expected	Byte Representation
1	Sync byte	`0x3C` (<)	UINT8
2	Message header	`0xA4`	UINT8
3	Message length	`0x02`	UINT8
4	Message payload	`0x00`: None `0x01`: Running	UINT8
5	Checksum	XOR of each of the bytes in the message (incl. sync byte, message header and message length)	UINT8

Message 5 is not used in the Arduino code, but the idea is for it to be used to calibrate the Fourier Ptychography system.

Message 6 - Set LED. Upon receiving message 6, the LED controlling Arduino turns specific LEDs on or off according to the GUI.

Table B.10: LabVIEW to LED intensity control Arduino - Message 6

Byte Number	Byte Description	Byte Expected	Byte Representation
1	Sync byte	`0x3C` (<)	UINT8
2	Message header	`0x06`	UINT8
3	Message length	`0x02`	UINT8
4	LED on?	`bit0`: LED1 `bit1`: LED2 `bit2`: LED3 `bit3`: LED4 on(1)/off(0)	UINT8
5	Checksum	XOR of each of the bytes in the message (incl. sync byte, message header and message length)	UINT8

Table B.11: LED intensity control Arduino to LabVIEW response - Message 6

Byte Number	Byte Description	Byte Expected	Byte Representation
1	Sync byte	`0x3C` (<)	UINT8
2	Message header	`0x06`	UINT8
3	Message length	`0x02`	UINT8
4	LED on?	`bit0`: LED_1 `bit1`: LED_2 `bit2`: LED_3 on(1)/off(0) `bit3`: LED_4	UINT8
5	Checksum	XOR of each of the bytes in the message (incl. sync byte, message header and message length)	UINT8

B.3 Fluorescence microscope Arduino code

```
1
2 // 11 Sep 2019
3 // This program receives the messages from
    LabVIEW and sets up:
4 // LED intensity
5 // Exposure time
6 // Dead time
7 // Protocol document is available
8 // Sync byte = 0x32. There is no end marker byte
    , the message contains message length
9 // and so the receive is complete after the
    appropriate number of bytes have been received
10
11
12 //================
13 #include <Wire.h>
14 #include "MCP4728.h"
15
16 MCP4728 dac;
17 #define startMarker 0x3C
18 #define maxMessage 16
```

```
19
20 // the program could be rewritten to use local
       variables instead of some of these globals
21 //  however globals make the code simpler
22 //  and simplify memory management
23
24 byte bytesRecvd = 0;
25 byte dataRecvCount = 0;
26
27 byte dataRecvd[maxMessage];
28 byte tempBuffer[maxMessage];
29
30 boolean inProgress = false;
31 boolean allReceived = false;
32 boolean msgHeaderknown = false;
33 boolean msgLengthknown = false;
34
35 byte bMessageBytes[maxMessage];
36 byte bChecksum=0;
37 unsigned int msgLength = 0;
38 unsigned int msgRecLength = 0;
39 unsigned long previousMillis = 0;
40 int ledState = LOW;
41
42 byte DACch1Intensity = 0;
43 byte DACch2Intensity = 0;
44 byte DACch3Intensity = 0;
45 byte DACch4Intensity = 0;
46
47 byte bLED1 = 0;
48 byte bLED2 = 0;
49 byte bLED3 = 0;
50 byte bLED4 = 0;
51 unsigned int nExposureTime = 10000;
52 unsigned int nDeadTime = 10000;
53
54
55 //================
56
```

```
57 void setup()
58 {
59   pinMode(13, OUTPUT); // the onboard LED &
       output to LAC arduino
60   pinMode(12, OUTPUT); // Camera trigger pin
61
62   Serial.begin(115200);
63
64   Wire.begin();
65
66   dac.attatch(Wire, 14);
67   dac.readRegisters();
68
69   dac.selectVref(MCP4728::VREF::VDD, MCP4728::
       VREF::VDD, MCP4728::VREF::VDD, MCP4728::VREF
       ::VDD);
70   //dac.selectPowerDown(MCP4728::PWR_DOWN::
       GND_500KOHM, MCP4728::PWR_DOWN::GND_500KOHM,
        MCP4728::PWR_DOWN::GND_500KOHM, MCP4728::
       PWR_DOWN::GND_500KOHM);
71   dac.selectGain(MCP4728::GAIN::X1, MCP4728::
       GAIN::X1, MCP4728::GAIN::X1, MCP4728::GAIN::
       X1);
72   dac.analogWrite(MCP4728::DAC_CH::A, 444);
73   dac.analogWrite(MCP4728::DAC_CH::B, 444);
74   dac.analogWrite(MCP4728::DAC_CH::C, 444);
75   dac.analogWrite(MCP4728::DAC_CH::D, 444);
76
77   dac.enable(true);
78
79   dac.selectPowerDown(MCP4728::PWR_DOWN::
       GND_500KOHM, MCP4728::PWR_DOWN::GND_500KOHM,
        MCP4728::PWR_DOWN::GND_500KOHM, MCP4728::
       PWR_DOWN::GND_500KOHM);
80 }
81
82 //================
83
84 void loop()
```

```
85 {
86   unsigned long currentMillis = millis();
87
88   /*if (currentMillis - previousMillis >= 1000)
89   {
90     // save the last time you blinked the LED
91     previousMillis = currentMillis;
92     // if the LED is off turn it on and vice-
          versa:
93     if (ledState == LOW)
94       ledState = HIGH;
95     else
96       ledState = LOW;
97     // set the LED with the ledState of the
          variable:
98     digitalWrite(13, ledState);
99   }*/
100
101  // Check if serial communications required
102  getSerialData();
103
104  // Once a full message has been received,
       process the instruction
105  if(allReceived)
106  {
107    allReceived = false;
108    processData();
109  }
110 }
111
112 //================
113
114 void getSerialData()
115 {
116      // Receives data into tempBuffer[]
117      //   saves the number of bytes that the PC
           said it sent - which will be in
           tempBuffer[1]
```

```
118       //   uses decodeHighBytes() to copy data
              from tempBuffer to dataRecvd[]
119
120       // the Arduino program will use the data it
              finds in dataRecvd[]
121   bChecksum = 0;
122   if(Serial.available() > 0)
123   {
124     byte x = Serial.read();
125     if ((x == 0x3C) && (!msgHeaderknown))
126     {
127       bytesRecvd = 0;
128       inProgress = true;
129       // blinkLED(2);
130       // Serial.write("start received\n");
131     }
132
133     if(inProgress)
134     {
135       tempBuffer[bytesRecvd] = x;
136       bytesRecvd ++;
137     }
138
139     if(!msgHeaderknown)
140     {
141       // Regardless of message header, we need
              to read 1 more byte to get message
              length, so keep receiving
142       // tempBuffer[1] is the message header
143       msgHeaderknown = true;
144     }
145     if(!msgLengthknown)
146     {
147       switch (tempBuffer[2])
148       {
149         case 0x01:
150           msgLength = tempBuffer[2];
151           msgLengthknown = true;
152           break;
```

```
153         case 0x02:
154           msgLength = tempBuffer[2];
155           msgLengthknown = true;
156           break;
157         case 0x03:
158           msgLength = tempBuffer[2];
159           msgLengthknown = true;
160         case 0x04:
161           msgLength = tempBuffer[2];
162           msgLengthknown = true;
163         case 0x05:
164           msgLength = tempBuffer[2];
165           msgLengthknown = true;
166         case 0x06:
167           msgLength = tempBuffer[2];
168           msgLengthknown = true;
169         default:
170         break;
171       }
172     }
173
174     if(msgLengthknown)
175     {
176       msgRecLength += 1;
177       if(msgRecLength == msgLength+1)
178       {
179         inProgress = false;
180         allReceived = true;
181         msgLengthknown = false;
182         msgHeaderknown = false;
183         dataRecvd[0] = tempBuffer[0];
184         dataRecvd[1] = tempBuffer[1];
185         dataRecvd[2] = tempBuffer[2];
186         dataRecvd[3] = tempBuffer[3];
187         dataRecvd[4] = tempBuffer[4];
188         dataRecvd[5] = tempBuffer[5];
189         dataRecvd[6] = tempBuffer[6];
190         dataRecvd[7] = tempBuffer[7];
191         dataRecvd[8] = tempBuffer[8];
```

```
192         tempBuffer[0] = 0;
193         tempBuffer[1] = 0;
194         tempBuffer[2] = 0;
195         msgRecLength = 0;
196         allReceived = true;
197         //Serial.write("got all\n");
198         //Serial.write(dataRecvd, bytesRecvd);
199       }
200     }
201   }
202 }
203
204 //Adrian message decoders
205 void Message1()
206 {
207   /*
      ==========================================================================

208    * Message 1 responds with the intensity
       values of the ADC's as a percentage from
       0-100%
209    * analogRead returns an integer (16 bits) and
        is maxed out at 1024
210    * multiplying by .09765625, normalizes 1024
       to 100% (as required)
211    * casting the resulting integer to a byte
       results in a single byte intensity
212    */
213   int analogA1 = A1;
214   int analogA2 = A2;
215   int analogA3 = A3;
216   int analogA4 = A4;
217   int val = 0;
218   int intensity1 = 0, intensity2 = 0, intensity3
       = 0, intensity4 = 0;
219
220   val = analogRead(analogA1);
221   intensity1 = val*.09765625;
222   bMessageBytes[0] = (byte)intensity1;
```

```
223
224   val = analogRead(analogA2);
225   intensity2 = val*.09765625;
226   bMessageBytes[1] = (byte)intensity2;
227
228   val = analogRead(analogA3);
229   intensity3 = val*.09765625;
230   bMessageBytes[2] = (byte)intensity3;
231
232   val = analogRead(analogA4);
233   intensity4 = val*.09765625;
234   bMessageBytes[3] = (byte)intensity4;
235
236   bChecksum = 0;
237   bMessageBytes[0] = 0x3C;
238   bChecksum = bChecksum ^ bMessageBytes[0];
239   bMessageBytes[1] = 0xA1;
240   bChecksum = bChecksum ^ bMessageBytes[1];
241   bMessageBytes[2] = 0x05;
242   bChecksum = bChecksum ^ bMessageBytes[2];
243   bMessageBytes[3] = (byte)intensity1;
244   bChecksum = bChecksum ^ bMessageBytes[3];
245   bMessageBytes[4] = (byte)intensity2;
246   bChecksum = bChecksum ^ bMessageBytes[4];
247   bMessageBytes[5] = (byte)intensity3;
248   bChecksum = bChecksum ^ bMessageBytes[5];
249   bMessageBytes[6] = (byte)intensity4;
250   bChecksum = bChecksum ^ bMessageBytes[6];
251   bMessageBytes[7] = bChecksum;
252   Serial.write(bMessageBytes, 8);
253   return;
254 }
255
256 void Message2()
257 {
258   /*
      ============================================================
```

```
259     * Message 2 responds with the intensity
            settings that the DAC has recorded for each
             channel
260     * and sets the DAC's to the specified values
261     */
262   DACch1Intensity = dataRecvd[3];
263   DACch2Intensity = dataRecvd[4];
264   DACch3Intensity = dataRecvd[5];
265   DACch4Intensity = dataRecvd[6];
266   unsigned int DAC1 = 0, DAC2 = 0, DAC3 = 0,
          DAC4 = 0;
267
268   // prevent any inputs over 100%
269   if(DACch1Intensity > 100)
270     DACch1Intensity = 100;
271   if(DACch2Intensity > 100)
272     DACch1Intensity = 100;
273   if(DACch3Intensity > 100)
274     DACch1Intensity = 100;
275   if(DACch4Intensity > 100)
276     DACch1Intensity = 100;
277
278   // Set the DAC's here via I2C
279   // Total is 4096, need to scale a 100 to 4095
          (factor of 40.95)
280   DAC1 = DACch1Intensity * 40.95;
281   DAC2 = DACch2Intensity * 40.95;
282   DAC3 = DACch3Intensity * 40.95;
283   DAC4 = DACch4Intensity * 40.95;
284 // This line causes the LED's to all switch on
285   dac.analogWrite(DAC1, DAC2, DAC3, DAC4);
286   delay(10);
287   dac.readRegisters();
288
289   // Read back the values from the DAC
290   DAC1 = round(dac.getDACData(0)/40.95);
291   DAC2 = round(dac.getDACData(1)/40.95);
292   DAC3 = round(dac.getDACData(2)/40.95);
293   DAC4 = round(dac.getDACData(3)/40.95);
```

```
294   bMessageBytes[3] = byte(DAC1);
295   bMessageBytes[4] = byte(DAC2);
296   bMessageBytes[5] = byte(DAC3);
297   bMessageBytes[6] = byte(DAC4);
298
299   bChecksum = 0;
300   bMessageBytes[0] = 0x3C;
301   bChecksum = bChecksum ^ bMessageBytes[0];
302   bMessageBytes[1] = 0xA2;
303   bChecksum = bChecksum ^ bMessageBytes[1];
304   bMessageBytes[2] = 0x05;
305   bChecksum = bChecksum ^ bMessageBytes[2];
306   //bMessageBytes[3] is populated ^^
307   bChecksum = bChecksum ^ bMessageBytes[3];
308   //bMessageBytes[4] is populated ^^
309   bChecksum = bChecksum ^ bMessageBytes[4];
310   //bMessageBytes[5] is populated ^^
311   bChecksum = bChecksum ^ bMessageBytes[5];
312   //bMessageBytes[6] is populated ^^
313   bChecksum = bChecksum ^ bMessageBytes[6];
314   bMessageBytes[7] = bChecksum;
315   Serial.write(bMessageBytes, 8);
316   // Power down all of the outputs
317   dac.selectPowerDown(MCP4728::PWR_DOWN::
         GND_500KOHM, MCP4728::PWR_DOWN::GND_500KOHM,
          MCP4728::PWR_DOWN::GND_500KOHM, MCP4728::
         PWR_DOWN::GND_500KOHM);
318   dac.readRegisters();
319   return;
320 }
321
322 void Message3()
323 {
324   /*
         ============================================================

325     * Message 3 responds with the LED's that are
          turned on/off as per GUI instruction
```

```
326     * as well as the exposure and dead times as
          per the GUI
327     * These values are stored so that a pulse
          train can be setup appropriately
328     */
329   byte LEDsOnOff = dataRecvd[3];
330   byte hExpT, lExpT, hDeadT, lDeadT;
331
332   bLED1 = LEDsOnOff & 0b00000001;
333   bLED2 = LEDsOnOff & 0b00000010;
334   bLED3 = LEDsOnOff & 0b00000100;
335   bLED4 = LEDsOnOff & 0b00001000;
336   bMessageBytes[3] = 0;
337
338   if(bLED1 > 0)
339     bMessageBytes[3] |= 0b00000001;
340   else
341     bMessageBytes[3] &= 0b11111110;
342   if(bLED2 > 0)
343     bMessageBytes[3] |= 0b00000010;
344   else
345     bMessageBytes[3] &= 0b11111101;
346   if(bLED3 > 0)
347     bMessageBytes[3] |= 0b00000100;
348   else
349     bMessageBytes[3] &= 0b11111011;
350   if(bLED4 > 0)
351     bMessageBytes[3] |= 0b00001000;
352   else
353     bMessageBytes[3] &= 0b11110111;
354
355   nExposureTime = dataRecvd[4]*256 + dataRecvd
        [5];
356   nDeadTime = dataRecvd[6]*256 + dataRecvd[7];
357
358   hExpT = highByte(nExposureTime);
359   lExpT = lowByte(nExposureTime);
360   hDeadT = highByte(nDeadTime);
361   lDeadT = lowByte(nDeadTime);
```

```
362
363
364   bChecksum = 0;
365   bMessageBytes[0] = 0x3C;
366   bChecksum = bChecksum ^ bMessageBytes[0];
367   bMessageBytes[1] = 0xA3;
368   bChecksum = bChecksum ^ bMessageBytes[1];
369   bMessageBytes[2] = 0x06;
370   bChecksum = bChecksum ^ bMessageBytes[2];
371   //bMessageBytes[3] is populated ^^
372   bChecksum = bChecksum ^ bMessageBytes[3];
373   bMessageBytes[4] = dataRecvd[4];
374   bChecksum = bChecksum ^ bMessageBytes[4];
375   bMessageBytes[5] = dataRecvd[5];
376   bChecksum = bChecksum ^ bMessageBytes[5];
377   bMessageBytes[6] = dataRecvd[6];
378   bChecksum = bChecksum ^ bMessageBytes[6];
379   bMessageBytes[7] = dataRecvd[7];
380   bChecksum = bChecksum ^ bMessageBytes[7];
381   bMessageBytes[8] = bChecksum;
382   Serial.write(bMessageBytes, 9);
383   return;
384 }
385
386 void Message4()
387 {
388   /*
        ============================================================

389    * Message 4 responds by executing the pulse
          train or checking the status of the pulse
          train
390    * depending on the request from the GUI
391    */
392
393   switch(dataRecvd[3])
394   {
395     case 1:
396       bMessageBytes[3] = CheckPulseStatus(true);
```

```
397     break;
398     default:
399       bMessageBytes[3] = CheckPulseStatus(false)
          ;
400     break;
401   }
402
403   bChecksum = 0;
404   bMessageBytes[0] = 0x3C;
405   bChecksum = bChecksum ^ bMessageBytes[0];
406   bMessageBytes[1] = 0xA4;
407   bChecksum = bChecksum ^ bMessageBytes[1];
408   bMessageBytes[2] = 0x02;
409   bChecksum = bChecksum ^ bMessageBytes[2];
410   //bMessageBytes[3] is populated ^^
411   bChecksum = bChecksum ^ bMessageBytes[3];
412   bMessageBytes[4] = bChecksum;
413   Serial.write(bMessageBytes, 5);
414   return;
415 }
416
417 void Message6()
418 {
419   /*
        ============================================================================

420     * Message 6 responds by turning on the
          appropriate channel (and others off)
421     * depending on the request from the GUI
422     */
423
424     byte LEDsOnOff = dataRecvd[3];
425
426     bLED1 = LEDsOnOff & 0b00000001;
427     bLED2 = LEDsOnOff & 0b00000010;
428     bLED3 = LEDsOnOff & 0b00000100;
429     bLED4 = LEDsOnOff & 0b00001000;
430     bMessageBytes[3] = 0;
431
```

```
432   if(!LEDsOnOff)
433   {
434      //Serial.write("All off");
435      bMessageBytes[3] |= 0b00000000;
436      dac.selectPowerDown(MCP4728::PWR_DOWN::
            GND_500KOHM, MCP4728::PWR_DOWN::
            GND_500KOHM, MCP4728::PWR_DOWN::
            GND_500KOHM, MCP4728::PWR_DOWN::
            GND_500KOHM);
437   }
438   else
439   {
440     if(bLED1 > 0)
441     {
442       bMessageBytes[3] |= 0b00000001;
443       dac.selectPowerDown(MCP4728::PWR_DOWN::
             NORMAL, MCP4728::PWR_DOWN::GND_500KOHM,
              MCP4728::PWR_DOWN::GND_500KOHM,
             MCP4728::PWR_DOWN::GND_500KOHM);
444     }
445     else
446     {
447       bMessageBytes[3] &= 0b11111110;
448     }
449     if(bLED2 > 0)
450     {
451       bMessageBytes[3] |= 0b00000010;
452       dac.selectPowerDown(MCP4728::PWR_DOWN::
             GND_500KOHM, MCP4728::PWR_DOWN::NORMAL,
              MCP4728::PWR_DOWN::GND_500KOHM,
             MCP4728::PWR_DOWN::GND_500KOHM);
453     }
454     else
455     {
456       bMessageBytes[3] &= 0b11111101;
457     }
458     if(bLED3 > 0)
459     {
460       bMessageBytes[3] |= 0b00000100;
```

```
461         dac.selectPowerDown(MCP4728::PWR_DOWN::
               GND_500KOHM, MCP4728::PWR_DOWN::
               GND_500KOHM, MCP4728::PWR_DOWN::NORMAL,
                MCP4728::PWR_DOWN::GND_500KOHM);
462       }
463       else
464       {
465         bMessageBytes[3] &= 0b11111011;
466       }
467       if(bLED4 > 0)
468       {
469         bMessageBytes[3] |= 0b00001000;
470         dac.selectPowerDown(MCP4728::PWR_DOWN::
               GND_500KOHM, MCP4728::PWR_DOWN::
               GND_500KOHM, MCP4728::PWR_DOWN::
               GND_500KOHM, MCP4728::PWR_DOWN::NORMAL)
               ;
471       }
472       else
473       {
474         bMessageBytes[3] &= 0b11110111;
475       }
476     }
477
478     bChecksum = 0;
479     bMessageBytes[0] = 0x3C;
480     bChecksum = bChecksum ^ bMessageBytes[0];
481     bMessageBytes[1] = 0xA6;
482     bChecksum = bChecksum ^ bMessageBytes[1];
483     bMessageBytes[2] = 0x02;
484     bChecksum = bChecksum ^ bMessageBytes[2];
485     //bMessageBytes[3] is populated ^^
486     bChecksum = bChecksum ^ bMessageBytes[3];
487     bMessageBytes[4] = bChecksum;
488     Serial.write(bMessageBytes, 5);
489     return;
490 }
491
492
```

```
493 void Message7()
494 {
495   /*
        ============================================================

496    * Message 7 responds by turning on the IOs 12
         & 13 (camera & FP arduino)
497    */
498
499   byte OnOff = dataRecvd[3];
500   byte hExpT, lExpT, hcount, lcount;
501   int nCount_pulses = 0;
502   int nIterations = 0;
503   int nExposure_div2 = 0;
504   int nExposure_div2_less = 0;
505
506   nExposureTime = dataRecvd[6]*256 + dataRecvd
        [7];
507   nCount_pulses = dataRecvd[4]*256 + dataRecvd
        [5];
508   nExposure_div2 = nExposureTime/2;
509   nExposure_div2_less = nExposure_div2 - 2;
510
511   hExpT = highByte(nExposureTime);
512   lExpT = lowByte(nExposureTime);
513   hcount = highByte(nCount_pulses);
514   lcount = lowByte(nCount_pulses);
515
516
517
518   bChecksum = 0;
519   bMessageBytes[0] = 0x3C;
520   bChecksum = bChecksum ^ bMessageBytes[0];
521   bMessageBytes[1] = 0xA6;
522   bChecksum = bChecksum ^ bMessageBytes[1];
523   bMessageBytes[2] = 0x02;
524   bChecksum = bChecksum ^ bMessageBytes[2];
525   bMessageBytes[3] = OnOff;
526   bChecksum = bChecksum ^ bMessageBytes[3];
```

```
527   bMessageBytes[4] = hcount;
528   bChecksum = bChecksum ^ bMessageBytes[4];
529   bMessageBytes[5] = lcount;
530   bChecksum = bChecksum ^ bMessageBytes[5];
531   bMessageBytes[6] = hExpT;
532   bChecksum = bChecksum ^ bMessageBytes[6];
533   bMessageBytes[7] = hExpT;
534   bChecksum = bChecksum ^ bMessageBytes[7];
535   bMessageBytes[8] = bChecksum;
536   Serial.write(bMessageBytes, 9);
537
538   digitalWrite(12,HIGH);
539   delay(nExposureTime);
540   digitalWrite(12,LOW);
541
542   // IO12 is the camera trigger
543   // IO13 is the onboard LED & LAC control pulse
544   for(nIterations = 0; nIterations <
          nCount_pulses; nIterations++)
545   {
546     if(OnOff)
547     {
548       digitalWrite(12, HIGH);
549       digitalWrite(13, HIGH);
550
551       //delay(nExposure_div2);
552       //digitalWrite(12, LOW);
553
554       delay(nExposureTime);
555       digitalWrite(12, LOW);
556       digitalWrite(13, LOW);
557       // 2ms dead time delay
558       delay(15);
559     }
560   }
561   return;
562 }
563
564
```

```
565 byte CheckPulseStatus(boolean Start)
566 {
567   byte bStatus=0;
568   if(Start)
569   {
570     // Build a pulse train according to info
        that we have
571     delay(nDeadTime);
572     // If LED1 is set 'ON', use it's set voltage
         as part of the pulse wave using the
        exposure and dead times
573     if (bLED1 > 0)
574     {
575       digitalWrite(12, HIGH);
576       digitalWrite(13, HIGH);
577       dac.selectPowerDown(MCP4728::PWR_DOWN::
          NORMAL, MCP4728::PWR_DOWN::GND_500KOHM,
          MCP4728::PWR_DOWN::GND_500KOHM, MCP4728
          ::PWR_DOWN::GND_500KOHM);
578       delay(nExposureTime);
579       digitalWrite(12, LOW);
580       digitalWrite(13, LOW);
581       dac.selectPowerDown(MCP4728::PWR_DOWN::
          GND_500KOHM, MCP4728::PWR_DOWN::
          GND_500KOHM, MCP4728::PWR_DOWN::
          GND_500KOHM, MCP4728::PWR_DOWN::
          GND_500KOHM);
582       delay(nDeadTime);
583     }
584
585     // If LED2 is set 'ON', use it's set voltage
         as part of the pulse wave using the
        exposure and dead times
586     if(bLED2 > 0)
587     {
588       digitalWrite(12, HIGH);
589       digitalWrite(13, HIGH);
590       dac.selectPowerDown(MCP4728::PWR_DOWN::
          GND_500KOHM, MCP4728::PWR_DOWN::NORMAL,
```

```
            MCP4728::PWR_DOWN::GND_500KOHM, MCP4728
            ::PWR_DOWN::GND_500KOHM);
591       delay(nExposureTime);
592       digitalWrite(12, LOW);
593       digitalWrite(13, LOW);
594       dac.selectPowerDown(MCP4728::PWR_DOWN::
            GND_500KOHM, MCP4728::PWR_DOWN::
            GND_500KOHM, MCP4728::PWR_DOWN::
            GND_500KOHM, MCP4728::PWR_DOWN::
            GND_500KOHM);
595       delay(nDeadTime);
596     }
597
598     // If LED3 is set 'ON', use it's set voltage
          as part of the pulse wave using the
         exposure and dead times
599     if(bLED3 > 0)
600     {
601       digitalWrite(12, HIGH);
602       digitalWrite(13, HIGH);
603       dac.selectPowerDown(MCP4728::PWR_DOWN::
            GND_500KOHM, MCP4728::PWR_DOWN::
            GND_500KOHM, MCP4728::PWR_DOWN::NORMAL,
            MCP4728::PWR_DOWN::GND_500KOHM);
604       delay(nExposureTime);
605       digitalWrite(12, LOW);
606       digitalWrite(13, LOW);
607       dac.selectPowerDown(MCP4728::PWR_DOWN::
            GND_500KOHM, MCP4728::PWR_DOWN::
            GND_500KOHM, MCP4728::PWR_DOWN::
            GND_500KOHM, MCP4728::PWR_DOWN::
            GND_500KOHM);
608       delay(nDeadTime);
609     }
610
611     // If LED4 is set 'ON', use it's set voltage
          as part of the pulse wave using the
         exposure and dead times
612     if(bLED4 > 0)
```

```
613     {
614       digitalWrite(12, HIGH);
615       digitalWrite(13, HIGH);
616       dac.selectPowerDown(MCP4728::PWR_DOWN::
             GND_500KOHM, MCP4728::PWR_DOWN::
             GND_500KOHM, MCP4728::PWR_DOWN::
             GND_500KOHM, MCP4728::PWR_DOWN::NORMAL);
617       delay(nExposureTime);
618       digitalWrite(12, LOW);
619       digitalWrite(13, LOW);
620       dac.selectPowerDown(MCP4728::PWR_DOWN::
             GND_500KOHM, MCP4728::PWR_DOWN::
             GND_500KOHM, MCP4728::PWR_DOWN::
             GND_500KOHM, MCP4728::PWR_DOWN::
             GND_500KOHM);
621       delay(nDeadTime);
622     }
623     bStatus = 0x55;
624   }
625   else
626     bStatus = 0x00;
627   return bStatus;
628 }
629
630
631
632 //============================
633
634 void processData()
635 {
636   switch (dataRecvd[1])
637   {
638     case 0x01:
639       Message1();
640       break;
641     case 0x02:
642       Message2();
643       break;
644     case 0x03:
```

```
645       Message3();
646       break;
647     case 0x04:
648       Message4();
649       break;
650     case 0x05:
651       break;
652     case 0x06:
653       Message6();
654       break;
655     case 0x07:
656       Message7();
657       break;
658     default:
659     break;
660   }
661 }
```

Appendix C

2-Photon microscope

C.1 2-Photon microscope component part numbers

Table C.1: 2-Photon home built microscope components

Component/Device	Part number	Manufacturer
DiM	FF01-705 25x36	Semrock
PMT	H10770B-40	Hamamatsu
Objective lens	LUMFLN60XW	Olympus
Galvo/Resonant scanner	MDR-R	Sutter Instruments
Laser	Chameleon Ultra	Coherent
TIA	DHPCA-100	Femto
NI PXI	PXIe-1073	National Instruments
DAQ	PXIe-6341	National Instruments
DAQ - FPGA	NI-5734	National Instruments
FPGA adaptor	PXIe-7975R	National Instruments
Deformable Mirror	DM97-15	Alpao
Scan lens	SL50-2P2	Thorlabs
Tube lens	TTL200MP	Thorlabs

C.2 2-Photon imaging parameters

Imaging the VML tissue samples that were previously stained with DAPI (nuclear stain), AF405 for Macrophages, and AF488 for FAPs made use of filters as per table C.2 in accordance with Spectraviewer in figure C.1.

Table C.2: VML 2PE imaging parameters

Excitation wavelength	780nm	5 – 20mW average
DiM_A	FF01-705 25x36	Semrock
DiM_A	FF01-409 25x36	Semrock
DiM_B	FF01-552 25x36	Semrock
F_1	650SP	Semrock
F_2	390/18	Semrock
F_3	457/50	Semrock
F_4	542/27	Semrock

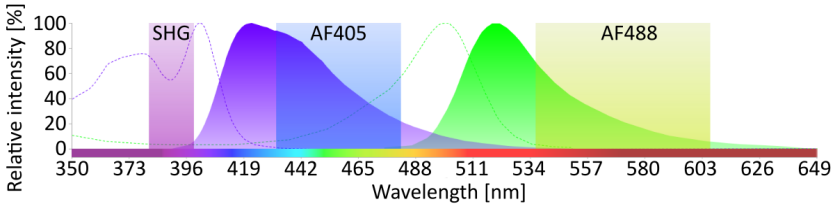

Figure C.1: Rectangular colouration indicates the filters that were used to image the dyes specified.

Table C.3: Nanoparticle 2PE imaging parameters

Excitation wavelength	780nm	5 – 50mW average
DiM_A	FF01-705 25x36	Semrock
DiM_A	FF01-409 25x36	Semrock
DiM_B	FF01-552 25x36	Semrock
F_1	650SP	Semrock
F_2	NA	Semrock
F_3	509/22	Semrock
F_4	571/72	Semrock

Table C.4: Organoid 2PE imaging parameters

Excitation wavelength	780, 1040nm	25 – 150mW average
DiM_A	FF01-705 25x36	Semrock
DiM_A	FF01-409 25x36	Semrock
DiM_B	FF01-552 25x36	Semrock
F_1	650SP	Semrock
F_2	390/18	Semrock
F_3	509/22; 457/50	Semrock
F_4	571/72; 570/47	Semrock

Appendix D

Scatter Correction

D.1 Transmission geometry setup

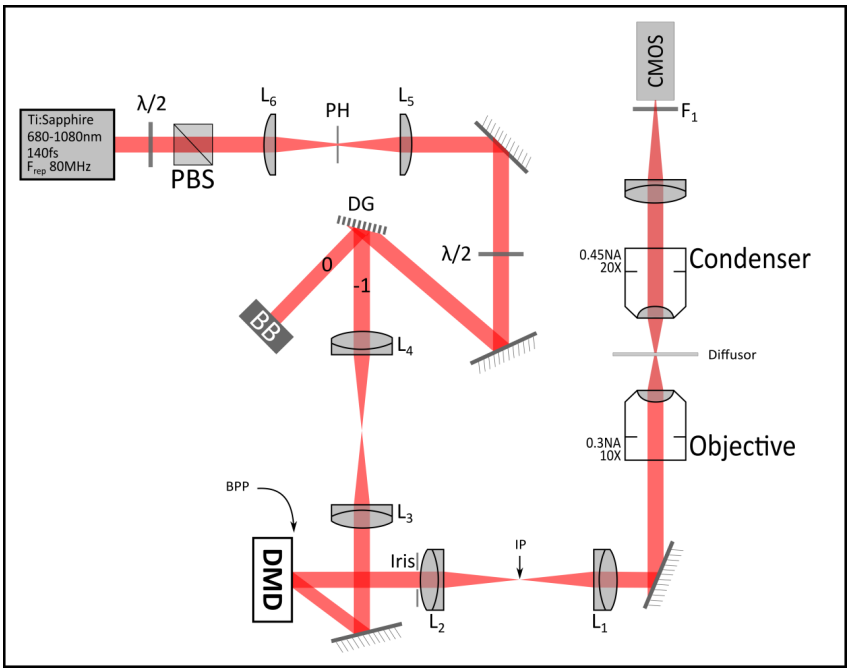

Figure D.1: Transmission geometry setup with DMD conjugated to the back pupil plane, and the light collected after passing through an objective lens and condenser lens.

D.2 In vivo mouse imaging with head-bar

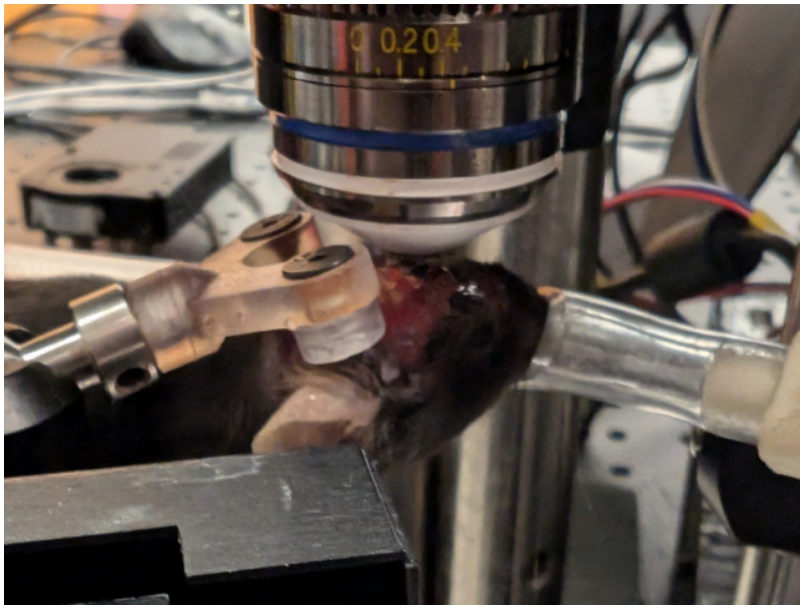

Figure D.2: A photograph of a mouse with a surgically implanted head-bar mounted to the stage along with the animal housing to enable movement of the sample without changing the position of the animal relative to the housing.

D.3 Connected components count

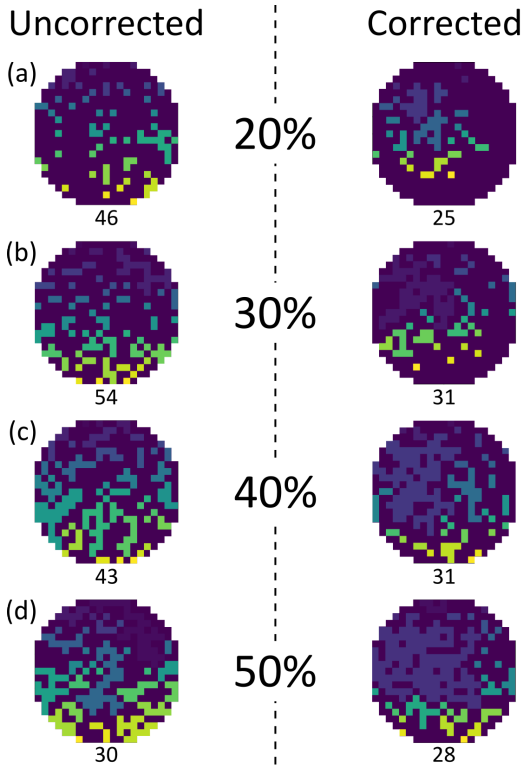

Figure D.3: An illustration of how connected components identifies the continuous regions within the optimized pattern.

D.4 Hadamard search

An alternative method to the genetic algorithm implementation is included in the code and GUI for the correction. It is a simple method that employs the equations setup below.

$$I_{j,sum} = \sum_{n=1}^{P} I_{j,n} \tag{D.1}$$

Here, $I_{j,n}$ represents the mean intensity measured by the camera for the pattern n and j the range of segments individually controlled by the DMD, $0 : seg$, where *seg* is the number of segments on the DMD capable of being individually controlled by the program. P is the number of Hadamard patterns projected onto the DMD and evaluated (e.g. 4096 [64×64]).

$$I_{j,onseg} = \sum_{n}^{P} \begin{cases} I_{j,n} & s_{j,n} = ON \\ 0 & s_{j,n} = OFF \end{cases} \tag{D.2}$$

In this case, $s_{j,n}$ is the segment within the individual population for each Hadamard pattern. $I_{j,onseg}$ represents the summed value of mean intensity (or some other evaluated metric)[78], when the j^{th} segment was turned on. Similarly $I_{j,offseg}$ represents the same when the j^{th} segment was turned off.

[78] For the implementation within the GUI, this metric is set to intensity

Within a binary setup used when the mirrors can only be set to on, or off, we know that:

$$I_{j,offseg} = I_{j,sum} - I_{j,onseg} \tag{D.3}$$

and we can then extrapolate that:

$$seg_{j,on} = \sum_{n}^{P} \begin{cases} 1 & s_{j,n} = ON \\ 0 & s_{j,n} = OFF \end{cases} \tag{D.4}$$

$seg_{j,on}$ counts the number of times that a segment is on through each of the Hadamard patterns. Similarly, $seg_{j,off}$ counts the number of times that a segment is turned off through each of the Hadamard patterns:

$$seg_{j,off} = \sum_{n}^{P} \begin{cases} 0 & s_{j,n} = ON \\ 1 & s_{j,n} = OFF \end{cases} \tag{D.5}$$

By counting both of these conditions, we can calculate the average number of times that the specific segment was on:

$$I_{j,aveon} = \frac{I_{j,onseg}}{seg_{j,on}} \tag{D.6}$$

where $I_{j,aveon}$ is the average intensity of the measured signal when the j^{th} pixel was turned on, and $I_{j,aveoff}$ when the j^{th} segment was turned off.

$$I_{j,aveoff} = \frac{I_{j,offseg}}{seg_{j,off}} \tag{D.7}$$

Finally, we can determine which pixels should be turned on, so that the computed pattern, *CP*, can be projected onto the DMD:

$$CP_j = \begin{cases} 1 & I_{aveon} > I_{aveoff} \\ 0 & I_{aveon} \leq I_{aveoff} \end{cases} \tag{D.8}$$

Appendix E

Image Scanning Microscope

E.1 AU calculations

Calculations of PSF size from [181] (E.1a) based on emission wavelength of 650nm and 525nm resulting in 1.494 and 1.82AUs respectively. Calculations for our ISM setup tuned poorly with low magnification (E.1b) and appropriately (E.1c).

These calculations are based on Rayleigh's emission spot size equation:

$$S_{dia} = 1.22 \times \frac{\lambda_{em}}{NA} \tag{E.1}$$

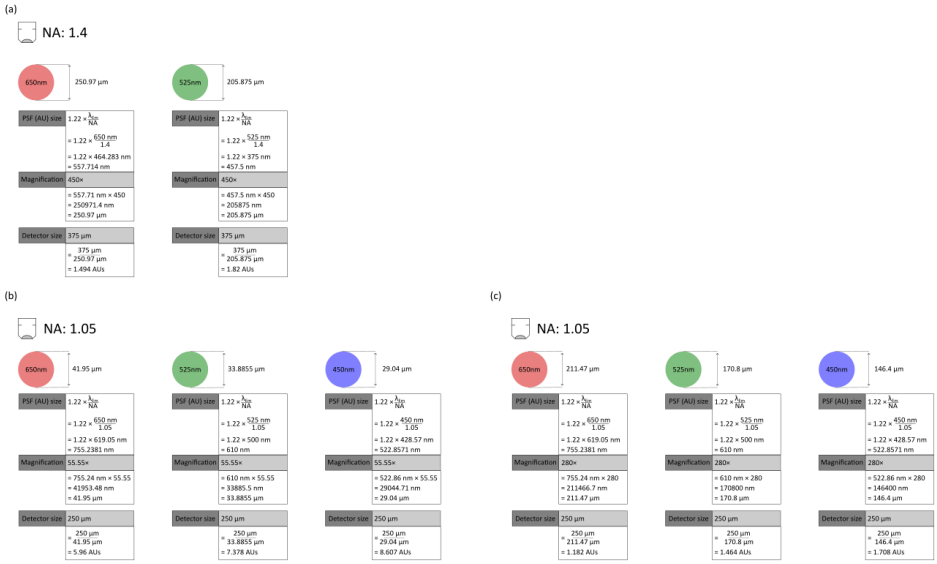

Figure E.1: According to the existing ISM literature, the PSF spot size and AU metric from [181] are well tuned (a). For our configuration, a small magnification opens the excitation to a widefield implementation, but results in a poorly tuned AU (b), whereas with appropriate magnification across three wavelengths results in well tuned AU sizing (c).

E.2 Zemax simulations

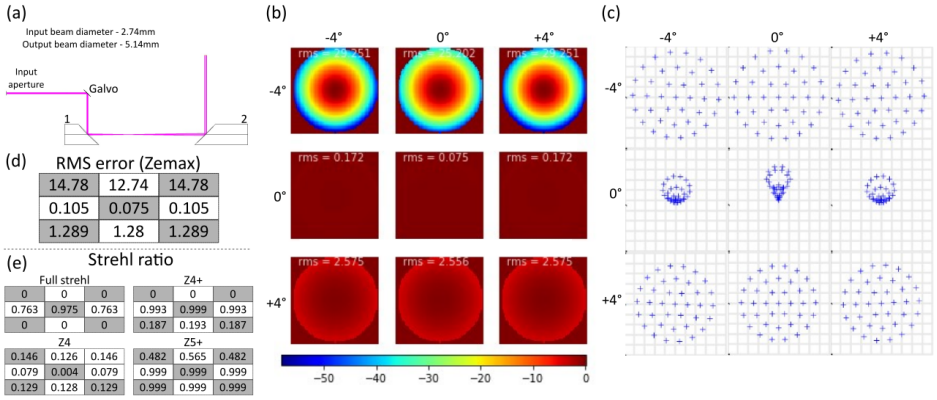

Figure E.2: Schematic of the OAPs and galvo (a). RMS error calculations at scan positions (b). Spot simulations of each scan position (c). RMS error as per Zemax (d). Strehl ratios (0-1) for the full Zernike modes, modes 4 and above, Zernike mode 4 only and finally Zernike modes 5 and above (e).

Figure E.3: Schematic of the OAPs and galvo (a). RMS error calculations at scan positions (b). Spot simulations of each scan position (c). RMS error as per Zemax (d). Strehl ratios (0-1) for the full Zernike modes, modes 4 and above, Zernike mode 4 only and finally Zernike modes 5 and above (e).

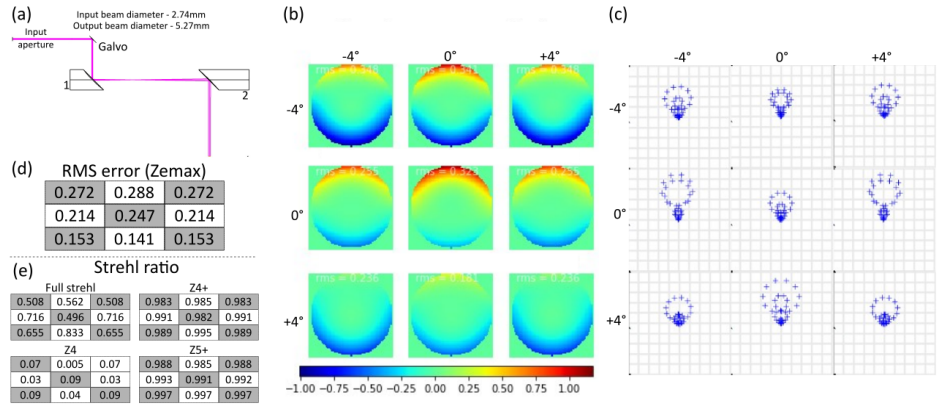

Figure E.4: Schematic of the OAPs and galvo (a). RMS error calculations at scan positions (b). Spot simulations of each scan position (c). RMS error as per Zemax (d). Strehl ratios (0-1) for the full Zernike modes, modes 4 and above, Zernike mode 4 only and finally Zernike modes 5 and above (e).

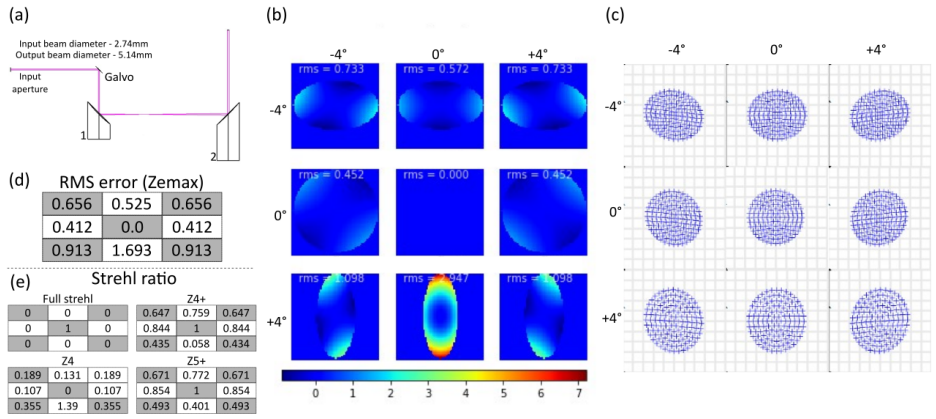

Figure E.5: Schematic of the OAPs and galvo (a). RMS error calculations at scan positions (b). Spot simulations of each scan position (c). RMS error as per Zemax (d). Strehl ratios (0-1) for the full Zernike modes, modes 4 and above, Zernike mode 4 only and finally Zernike modes 5 and above (e).

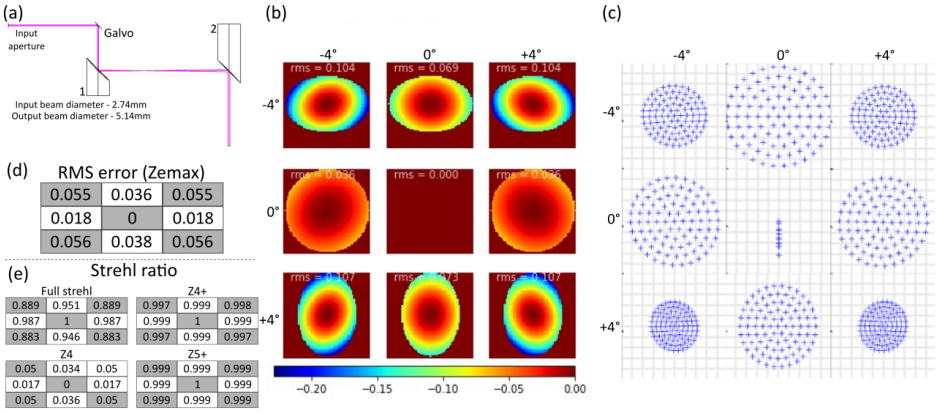

Figure E.6: Schematic of the OAPs and galvo (a). RMS error calculations at scan positions (b). Spot simulations of each scan position (c). RMS error as per Zemax (d). Strehl ratios (0-1) for the full Zernike modes, modes 4 and above, Zernike mode 4 only and finally Zernike modes 5 and above (e).

E.3 Excitation configuration

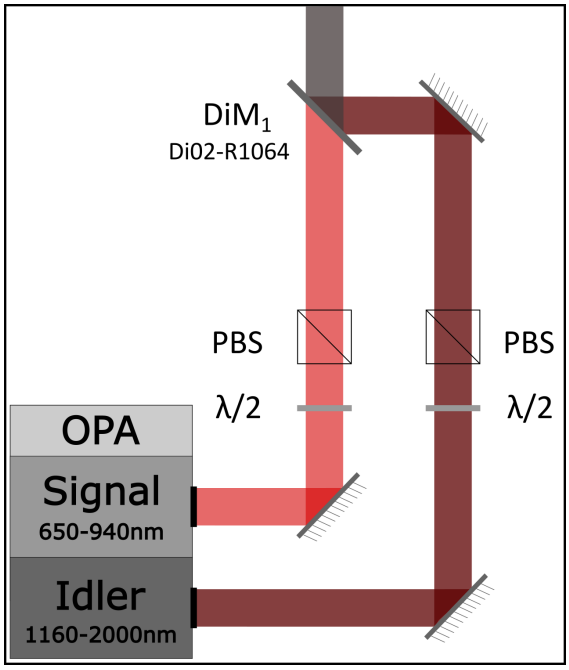

Figure E.7: Schematic of the Orpheus outputs, signal and idler, which are separate outputs, must be restricted to only one on at a time, but must be joined into the same path input to the scan engine.

E.4 Wiring diagram - ISM setup

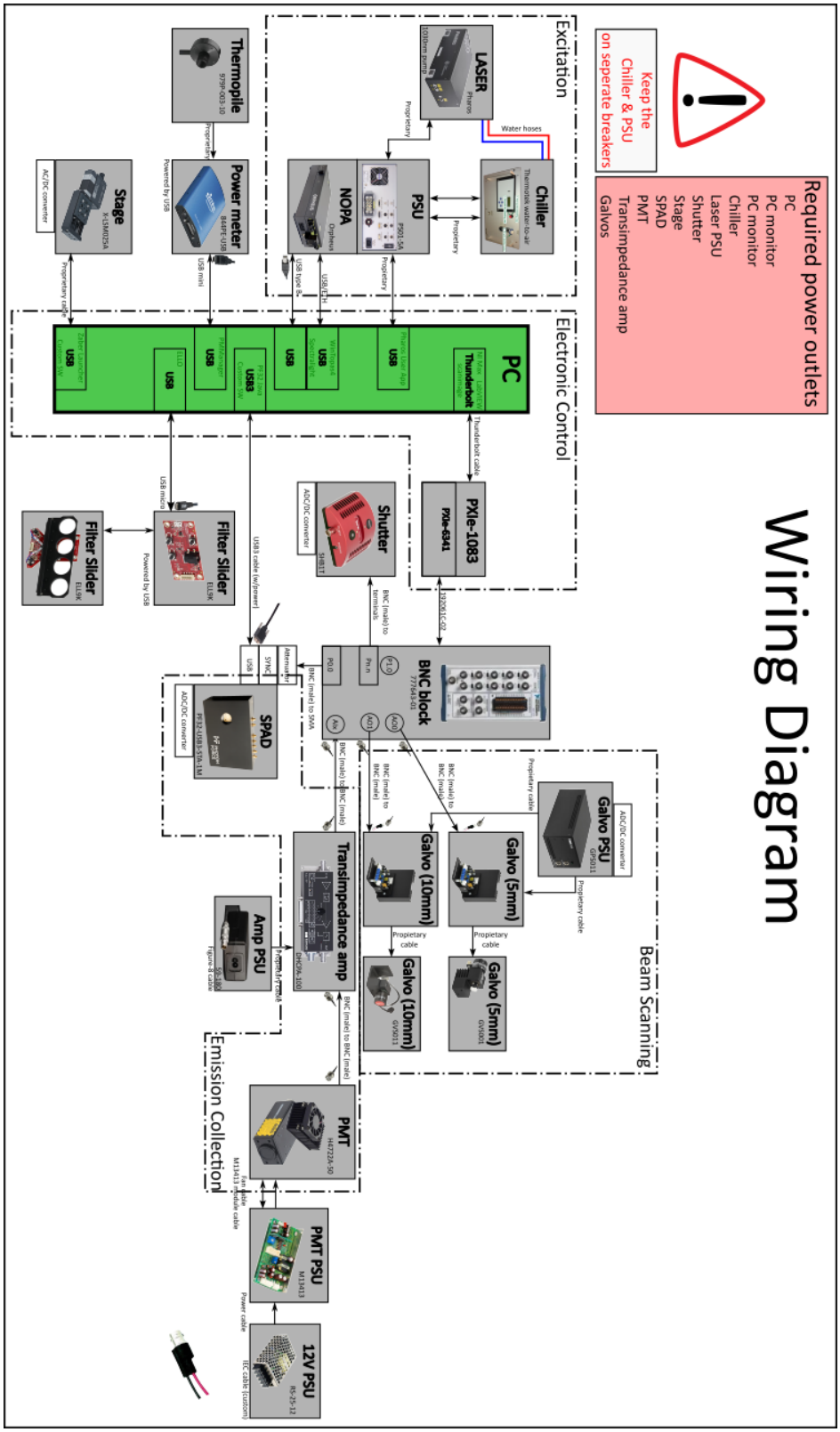

Figure E.8: A full wiring diagram of all components necessary to run the ISM setup.

E.5 ISM graphic user interface

Screenshots of the GUIs used to drive the ISM hardware components show how the user interacts with separate components (Figure E.9). The test pattern is a rolling image that shifts values from 0 to 1024 with meta data, which shifts the values across the 32×32 image array (Figure E.10). DCR tests average the pixel values over either 1 of 50 seconds. There should be no ambient light and the input aperture should be closed (Figure E.11). SPAD elements can be switched on or off using the ROI dialog (Figure E.12). The SPAD DAC voltages can be adjusted, but this should only be done when the manufacturers have suggested it (Figure E.13). Before capturing ISM image datasets, the destination folder must be set (Figure E.14). Once an image is presented on the GUI, it can be inspected at a granular level, with a number of statistical analyses and a histogram displayed (Figure E.15).

The underlying LabVIEW code leverages the producer/consumer style of coding as suggested by National Instruments. This method uses two while loops running simultaneously where one loop contains an event structure executing commands for each button and adds elements to a queue. As the queue is input to the second while loop, which contains a case structure and runs the appropriate code. This disconnects the GUI display from the effective control, but care must be taken to ensure that the GUI is not overwhelmed and hangs. This is how the current status of the program can accurately be displayed on the GUI.

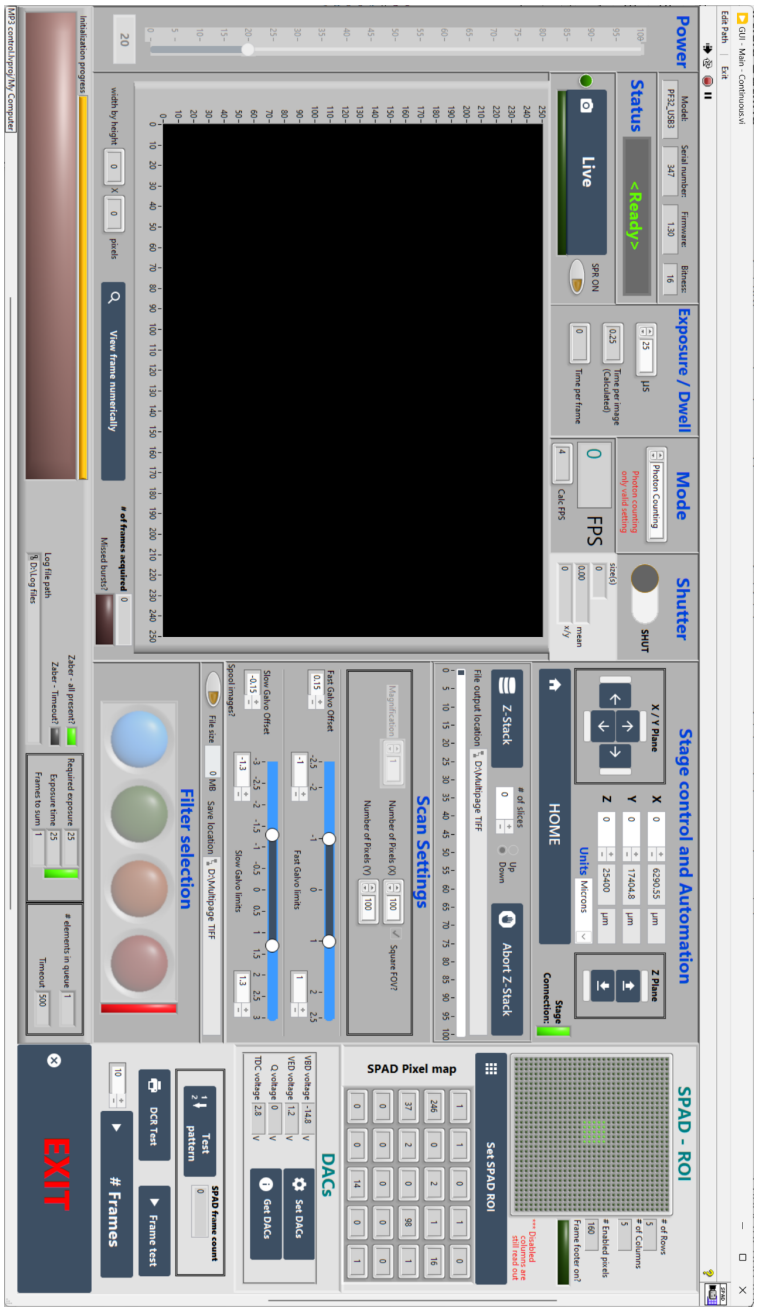

Figure E.9: The front panel of the ISM GUI starts by presenting the specifics of the connected SPAD camera. A specific ROI of the SPAD elements can be selected and the pixel map of that ROI is written out on the GUI (to allow users to identify regions with few hot pixels). Scan, DAC, and filter settings can be adjusted, while a test pattern and DCR tests can be executed to ensure that output for the camera is as expected.

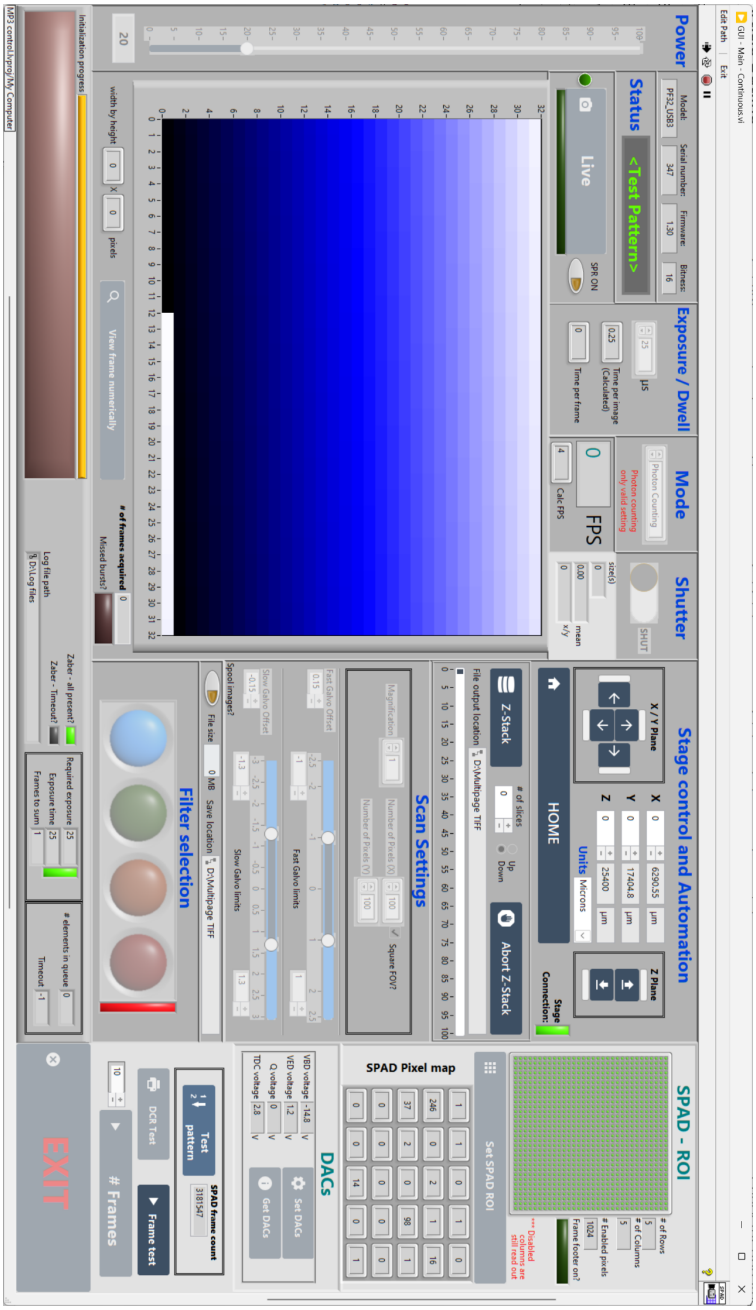

Figure E.10: The SPAD can output a test pattern that counts from 0 to 1024, as well as the meta data, which means that across the 32×32 output it shifts by a byte after each read.

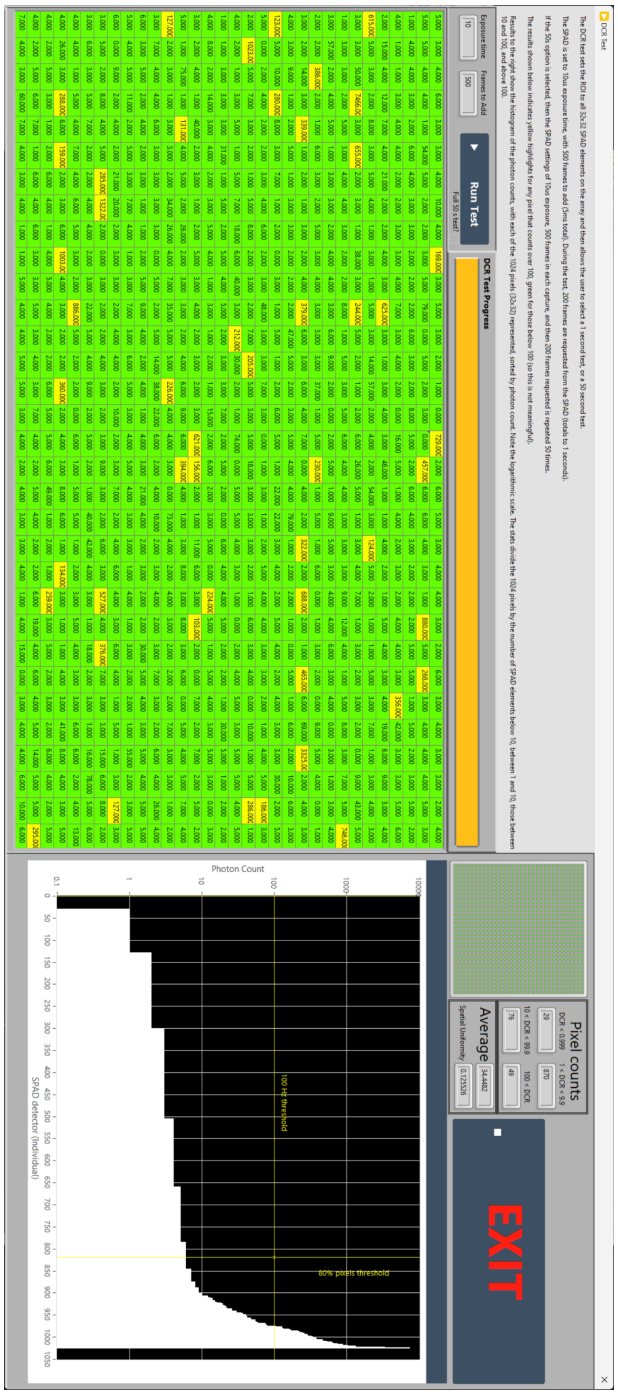

Figure E.11: Two options for DCR are available in the GUI. The first allows for a one second test, but the full 50 second test is more thorough. Resulting DCR should show that 80% of the pixels measure below 100Hz.

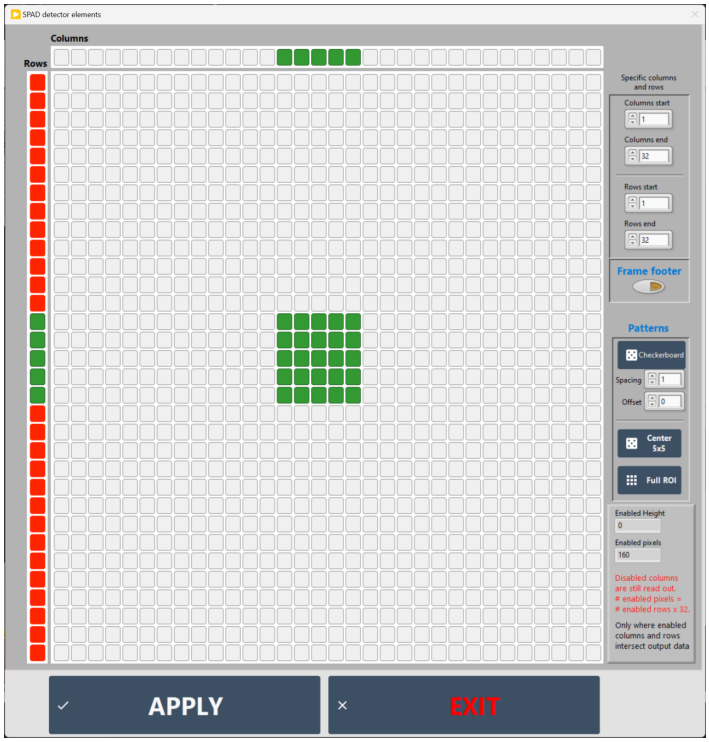

Figure E.12: Setting the SPAD ROI is used to identify the spot on which the PSF is projected.

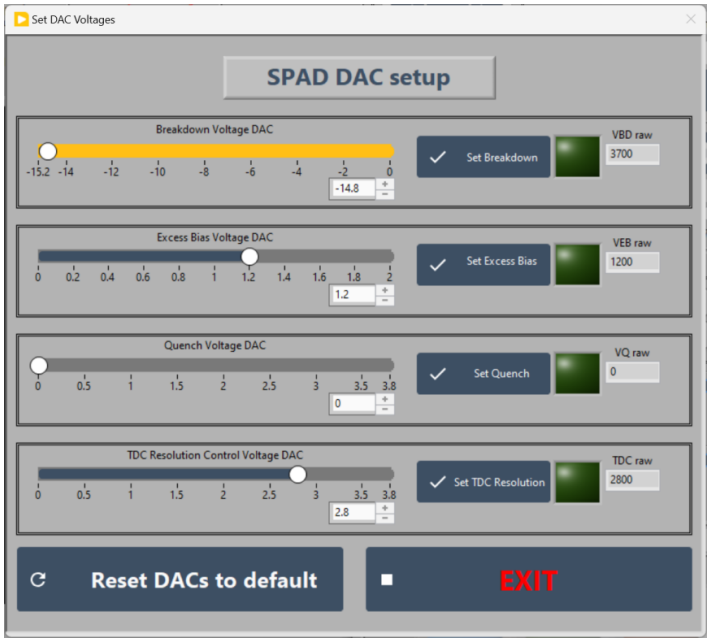

Figure E.13: Setting the SPAD DACs is an advanced feature that should only be conducted when the manufacturers have been consulted.

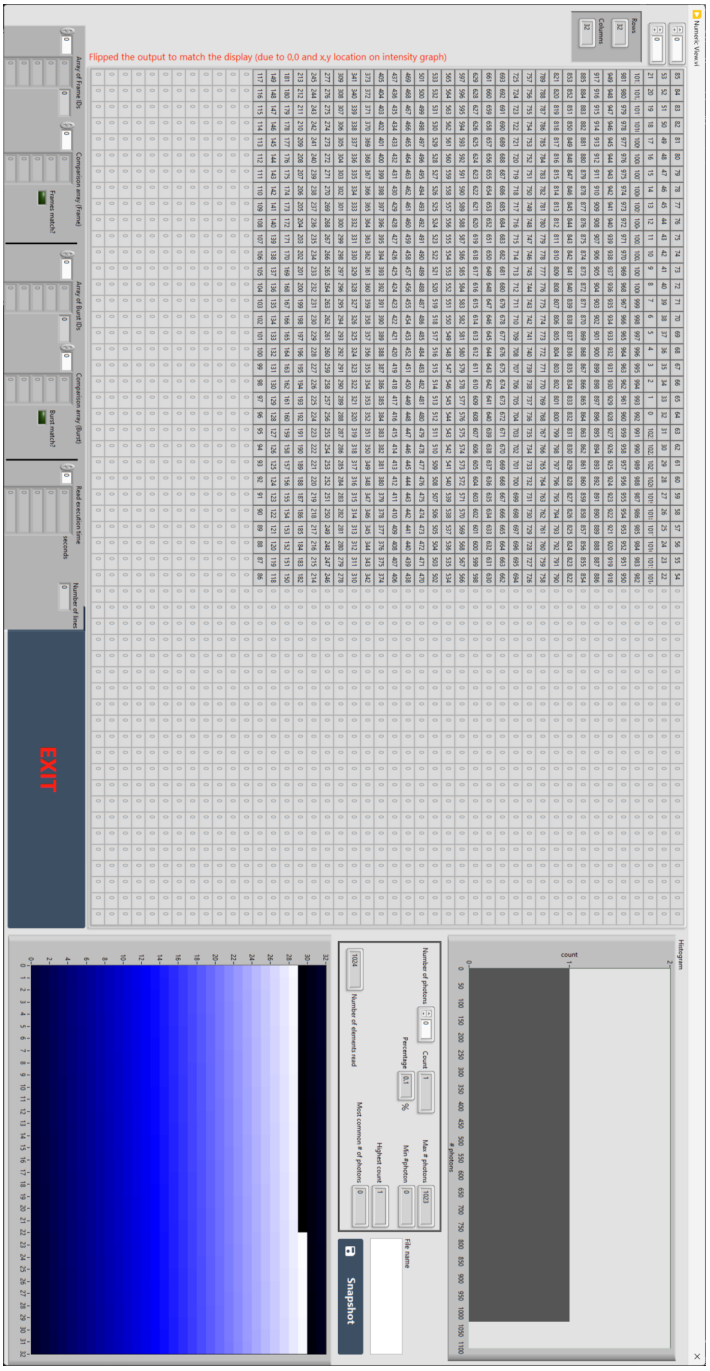

Figure E.14: Before capturing images, the location of save HDF5 files can be specified.

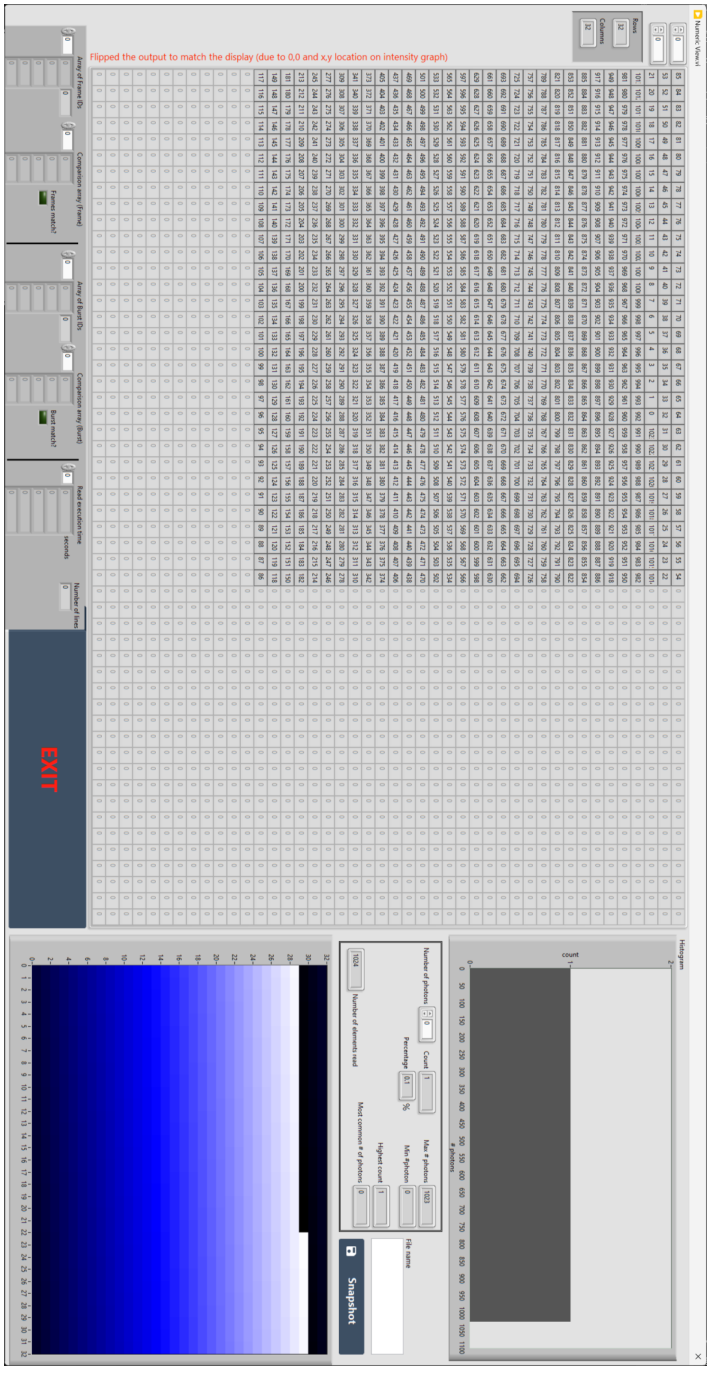

Figure E.15: As an extra debug feature the current frame can be inspected at a granular level.

E.6 Excitation source losses

The stability of NOPA power output varies over time, as the humidity and temperature changes slowly shift the optical components away from the perfect alignment. Measurements taken for Figure E.16 were acquired before a realignment so the maximum power at 820nm was slightly below 500mW, but after the realignment, maximum power was restored at 820nm to over 780mW. This percentage increase is then extrapolated across the full spectrum of the NOPA, and as a result power exceeding 115mW at the wavelengths used in Figure 5.13 are possible.

(a)

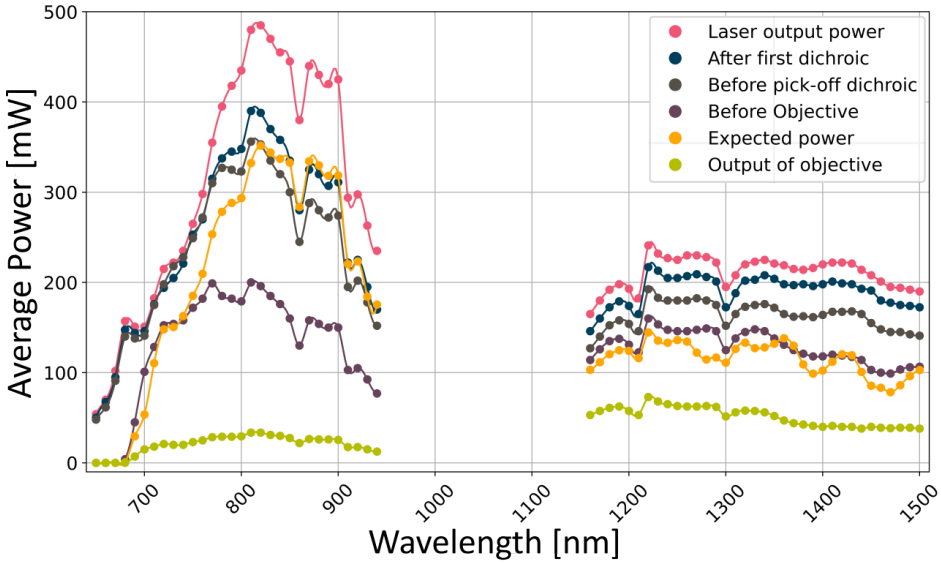

(b)

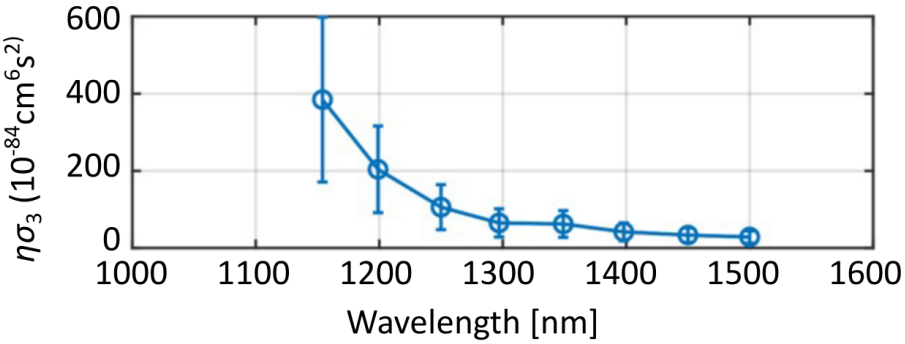

Figure E.16: Power measurement through various components of the system across a wide spectrum shows a loss of approximately 90% of the NOPA output propagated therough the objective lens (a). 3-photon response of fluorescein when excited by 1150nm to 1500nm directly from the manuscript [197] (b).

E.7 PMT gain control GUI

Connecting to the H4722A-50 PMT (Hamamatsu) using an Arduino to control the voltages and in turn the gain of the PMT, and the Arduino is controlled by a LabVIEW GUI (Figure E.17). The LabVIEW code implements a simple while loop containing and event structure to execute commands as the buttons and switches are clicked.

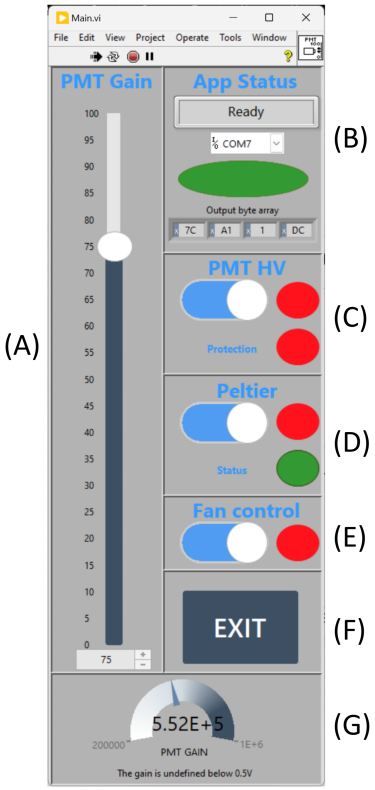

Figure E.17: The PMT GUI allows users to control the gain of the PMT, effectively gain below 40% is not changing anything on the PMT, but gain above 40% is effective (A). Status of the app and current instructions are displayed, with the current hex values and COM port (B). Status of the high voltage control (HV) of the PMT can be set using a switch (C). The peltier (D) and fan (E) can be controlled by GUI switches. An exit button closes the COM port and exits the program (F). The current gain as per the voltage is displayed (G).

Bibliography

[1] Luis Cardoso, Susannah P. Fritton, Gaffar Gailani, Mohammed Benalla, and Stephen C. Cowin. Advances in assessment of bone porosity, permeability and interstitial fluid flow. *Journal of Biomechanics*, 46(2):253–265, 2013. ISSN 0021-9290. doi: https://doi.org/10.1016/j.jbiomech.2012.10.025. URL https://www.sciencedirect.com/science/article/pii/S002192901200632X.

[2] C. J. R. Sheppard and A. Choudhury. Image formation in the scanning microscope. *Optica Acta: International Journal of Optics*, 24(10):1051–1073, 1977. ISSN 0030-3909. doi: 10.1080/713819421. URL https://doi.org/10.1080/713819421. doi: 10.1080/713819421.

[3] Colin Sheppard and David Shotton. *Confocal laser scanning microscopy*. Royal Microscopical Society microscopy handbooks. BIOS Scientific, 1997. ISBN 0387915141. URL https://cir.nii.ac.jp/crid/1130282273352291456.

[4] Margarita Arango-Lievano, Yann Dromard, Pierre Fontanaud, Chrystel Lafont, Patrice Mollard, and Freddy Jeanneteau. Regeneration of the neurogliovascular unit visualized in vivo by transcranial live-cell imaging. *Journal of Neuroscience Methods*, 343:108808, 2020. ISSN 0165-0270. doi: https://doi.org/10.1016/j.jneumeth.2020.108808. URL https://www.sciencedirect.com/science/article/pii/S0165027020302314.

[5] Lize Engelbrecht, Tracey Ollewagen, and Dalene de Swardt. Advances in fluorescence microscopy can reveal important new aspects of tissue regeneration. *Biochimie*, 196:194–202, 2022. ISSN 0300-9084. doi: https://doi.org/10.1016/j.biochi.2022.02.001. URL https://www.sciencedirect.com/science/article/pii/S030090842200030X.

[6] Gabriella T. Heller, Francesco A. Aprile, Thomas C. T. Michaels, Ryan Limbocker, Michele Perni, Francesco Simone Ruggeri, Benedetta Mannini, Thomas Löhr, Massimiliano Bonomi, Carlo Camilloni, Alfonso De Simone, Isabella C. Felli, Roberta Pierattelli, Tuomas P. J. Knowles, Christopher M. Dobson, and Michele Vendruscolo. Small-molecule sequestration of amyloid-beta as a drug discovery strategy for alzheimer's disease. *Science Advances*, 6(45):eabb5924, 2020. doi: doi: 10.1126/sciadv.abb5924. URL https://www.science.org/doi/abs/10.1126/sciadv.abb5924.

[7] P. J. Campagnola, A. C. Millard, M. Terasaki, P. E. Hoppe, C. J. Malone, and W. A. Mohler. Three-dimensional high-resolution second-harmonic generation imaging of endogenous structural proteins in biological tissues. *Biophys J*, 82(1 Pt 1):493–508, 2002. ISSN 0006-3495 (Print) 0006-3495. doi: 10.1016/s0006-3495(02)75414-3. 1542-0086 Campagnola, Paul J Millard, Andrew C Terasaki, Mark Hoppe, Pamela E Malone, Christian J Mohler, William A R01-GM35063/GM/NIGMS NIH HHS/United States R01-GM60389/GM/NIGMS NIH HHS/United States Journal Article Research Support, Non-U.S. Gov't Research Support, U.S. Gov't, Non-P.H.S. Research Support, U.S. Gov't, P.H.S. United States 2001/12/26 Biophys J. 2002 Jan;82(1 Pt 1):493-508. doi: 10.1016/S0006-3495(02)75414-3.

[8] Paul Campagnola. Second harmonic generation imaging microscopy: Applications to diseases diagnostics. *Analytical Chemistry*, 83(9):3224–3231, 2011. ISSN 0003-2700. doi: 10.1021/ac1032325. URL https://doi.org/10.1021/ac1032325. doi: 10.1021/ac1032325.

[9] A. Aghigh, S. Bancelin, M. Rivard, M. Pinsard, H. Ibrahim, and F. Légaré. Second harmonic generation microscopy: a powerful tool for bio-imaging. *Biophys Rev*, 15(1):43–70, 2023. ISSN 1867-2450 (Print) 1867-2450. doi: 10.1007/s12551-022-01041-6. 1867-2469 Aghigh, Arash Orcid: 0000-0001-6205-4707 Bancelin, Stéphane Rivard, Maxime Pinsard, Maxime Ibrahim, Heide Légaré, François Journal Article Review Germany 2023/03/14 Biophys Rev. 2023 Jan 19;15(1):43-70. doi: 10.1007/s12551-022-01041-6. eCollection 2023 Feb.

[10] Bettina Weigelin, Gert-Jan Bakker, and Peter Friedl. Third harmonic generation microscopy of cells and tissue organization. *Journal of Cell Science*, 129(2):245–255, 2016. ISSN 0021-9533. doi: 10.1242/jcs.152272. URL https://doi.org/10.1242/jcs.152272.

[11] Najva Akbari, Rose L. Tatarsky, Kristine E. Kolkman, Joseph R. Fetcho, Chris Xu, and Andrew H. Bass. Label-free, whole-brain in vivo mapping in an adult vertebrate with third harmonic generation microscopy. *Journal of Comparative Neurology*, 532(4): e25614, 2024. ISSN 0021-9967. doi: https://doi.org/10.1002/cne.25614. URL https://onlinelibrary.wiley.com/doi/abs/10.1002/cne.25614.

[12] Sung Ji Ahn, Nancy E. Ruiz-Uribe, Baoqiang Li, Jason Porter, Sava Sakadzic, and Chris B. Schaffer. Label-free assessment of hemodynamics in individual cortical brain vessels using third harmonic generation microscopy. *Biomedical Optics Express*, 11(5):2665–2678, 2020. doi: 10.1364/BOE.385848. URL https://opg.optica.org/boe/abstract.cfm?URI=boe-11-5-2665.

[13] Hongji Liu, Xinlin Chen, Xiangquan Deng, Ziwei Zhuang, Shen Tong, Weixin Xie, Jia Li, Ping Qiu, and Ke Wang. In vivo deep-brain blood flow speed measurement through third-harmonic generation imaging excited at the 1700-nm window. *Biomedical Optics Express*, 11(5):2738–2744, 2020. doi: 10.1364/BOE.389662. URL https://opg.optica.org/boe/abstract.cfm?URI=boe-11-5-2738.

[14] C. A. Combs. Fluorescence microscopy: a concise guide to current imaging methods. *Curr Protoc Neurosci*, Chapter 2:Unit2.1, 2010. ISSN 1934-8584 (Print) 1934-8576. doi: 10.1002/0471142301.ns0201s50. 1934-8576 Combs, Christian A Z99 HL999999/ImNIH/Intramural NIH HHS/United States Journal Article Research Support, N.I.H., Intramural United States 2010/01/13 Curr Protoc Neurosci. 2010 Jan;Chapter 2:Unit2.1. doi: 10.1002/0471142301.ns0201s50.

[15] Yuliang Wang, Zaicheng Zhang, Huimin Wang, and Shusheng Bi. Segmentation of the clustered cells with optimized boundary detection in negative phase contrast images. *PLOS ONE*, 10(6):e0130178, 2015. doi: 10.1371/journal.pone.0130178. URL https://doi.org/10.1371/journal.pone.0130178.

[16] George Gabriel Stokes. Xxx. on the change of refrangibility of light. *Philosophical Transactions of the Royal Society of London*, 142:463–562, 1852. doi: doi:10.1098/rstl.1852.0022. URL https://royalsocietypublishing.org/doi/abs/10.1098/rstl.1852.0022.

[17] Jeff W. Lichtman and José-Angel Conchello. Fluorescence microscopy. *Nature Methods*, 2(12):910–919, 2005. ISSN 1548-7105. doi: 10.1038/nmeth817. URL https://doi.org/10.1038/nmeth817.

[18] W. Gray Jerome. *The Theory of Fluorescence*, pages 21–36. Springer International Publishing, Cham, 2018. ISBN 978-3-319-97454-5. doi: 10.1007/978-3-319-97454-5_2. URL https://doi.org/10.1007/978-3-319-97454-5_2. (Jay).

[19] W. Hell Stefan, Bahlmann Karsten, Schrader Martin, Soini Aleksi, M. Malak Henryk, Gryczynski Ignacy, and R. Lakowicz Joseph. Three-photon excitation in fluorescence microscopy. *Journal of Biomedical Optics*, 1(1):71–74, 1996. doi: 10.1117/12.229062. URL https://doi.org/10.1117/12.229062.

[20] A. Ustione and D. W. Piston. A simple introduction to multiphoton microscopy. *Journal of Microscopy*, 243(3):221–226, 2011. ISSN 0022-2720. doi: https://doi.org/10.1111/j.1365-2818.2011.03532.x. URL https://doi.org/10.1111/j.1365-2818.2011.03532.x.

[21] Manuel Nieto-Vesperinas. *2 - Fundamentals of Mie scattering*, pages 39–72. Woodhead Publishing, 2020. ISBN 978-0-08-102403-4. doi: https://doi.org/10.1016/B978-0-08-102403-4.00007-4. URL https://www.sciencedirect.com/science/article/pii/B9780081024034000074.

[22] Winfried Denk, James H. Strickler, and Watt W. Webb. Two-photon laser scanning fluorescence microscopy. *Science*, 248(4951):73–76, 1990. doi: 10.1126/science.2321027. URL https://doi.org/10.1126/science.2321027. doi: 10.1126/science.2321027.

[23] W. Denk, K. R. Delaney, A. Gelperin, D. Kleinfeld, B. W. Strowbridge, D. W. Tank, and R. Yuste. Anatomical and functional imaging of neurons using 2-photon laser scanning microscopy. *Journal of Neuroscience Methods*, 54(2):151–162, 1994. ISSN 0165-0270. doi: https://doi.org/10.1016/0165-0270(94)90189-9. URL https://www.sciencedirect.com/science/article/pii/0165027094901899.

[24] Patrick Theer, Bernd Kuhn, Dorine Keusters, and Winfried Denk. Two-photon microscopy and imaging. *Neurobiology*, 77:5.2, 2005.

[25] M. Wang, C. Wu, D. Sinefeld, B. Li, F. Xia, and C. Xu. Comparing the effective attenuation lengths for long wavelength in vivo imaging of the mouse brain. *Biomed Opt Express*, 9(8):3534–3543, 2018. ISSN 2156-7085 (Print) 2156-7085. doi: 10.1364/boe.9.003534. 2156-7085 Wang, Mengran Wu, Chunyan Sinefeld, David Li, Bo Xia, Fei Xu, Chris Journal Article United States 2018/10/20 Biomed Opt Express. 2018 Jul 5;9(8):3534-3543. doi: 10.1364/BOE.9.003534. eCollection 2018 Aug 1.

[26] H. Andersson, T. Baechi, M. Hoechl, and C. Richter. Autofluorescence of living cells. *J Microsc*, 191(Pt 1):1–7, 1998. ISSN 0022-2720 (Print) 0022-2720. doi: 10.1046/j.1365-2818.1998.00347.x. Andersson, H Baechi, T Hoechl, M Richter, C Journal Article Research Support, Non-U.S. Gov't England 1998/09/02 J Microsc. 1998 Jul;191(Pt 1):1-7. doi: 10.1046/j.1365-2818.1998.00347.x.

[27] Tiffany M. Heaster, Alexa R. Heaton, Paul M. Sondel, and Melissa C. Skala. Intravital metabolic autofluorescence imaging captures macrophage heterogeneity across normal and cancerous tissue. *Frontiers in Bioengineering and Biotechnology*, 9, 2021. ISSN 2296-4185. URL https://www.frontiersin.org/journals/bioengineering-and-biotechnology/articles/10.3389/fbioe.2021.644648.

[28] Xiyi Chen, Oleg Nadiarynkh, Sergey Plotnikov, and Paul J. Campagnola. Second harmonic generation microscopy for quantitative analysis of collagen fibrillar structure. *Nature Protocols*, 7(4):654–669, 2012. ISSN 1750-2799. doi: 10.1038/nprot.2012.009. URL https://doi.org/10.1038/nprot.2012.009.

[29] Alex C. Kwan, Daniel A. Dombeck, and Watt W. Webb. Polarized microtubule arrays in apical dendrites and axons. *Proceedings of the National Academy of Sciences*, 105(32):11370–11375, 2008. doi: doi:10.1073/pnas.0805199105. URL https://www.pnas.org/doi/abs/10.1073/pnas.0805199105.

[30] V. Nucciotti, C. Stringari, L. Sacconi, F. Vanzi, L. Fusi, M. Linari, G. Piazzesi, V. Lombardi, and F. S. Pavone. Probing myosin structural conformation in vivo by second-harmonic generation microscopy. *Proceedings of the National Academy of Sciences*, 107(17):7763–7768, 2010. doi: doi:10.1073/pnas.0914782107. URL https://www.pnas.org/doi/abs/10.1073/pnas.0914782107.

[31] Paul J. Campagnola, Mei-de Wei, Aaron Lewis, and Leslie M. Loew. High-resolution nonlinear optical imaging of live cells by second harmonic generation. *Biophysical Journal*, 77(6):3341–3349, 1999. ISSN 0006-3495. doi: https://doi.org/10.1016/S0006-3495(99)77165-1. URL https://www.sciencedirect.com/science/article/pii/S0006349599771651.

[32] R. M. Williams, W. R. Zipfel, and W. W. Webb. Interpreting second-harmonic generation images of collagen i fibrils. *Biophys J*, 88 (2):1377–86, 2005. ISSN 0006-3495 (Print) 0006-3495. doi: 10.1529/biophysj.104.047308. 1542-0086 Williams, Rebecca M Zipfel, Warren R Webb, Watt W P41 EB001976/EB/NIBIB NIH HHS/United States R33 CA094311/CA/NCI NIH HHS/United States 9 P41 EB001976-16/EB/NIBIB NIH HHS/United States Evaluation Study Journal Article Research Support, N.I.H., Extramural Research Support, U.S. Gov't, P.H.S. United States 2004/11/10 Biophys J. 2005 Feb;88(2):1377-86. doi: 10.1529/biophysj.104.047308. Epub 2004 Nov 8.

[33] F. Légaré, C. Pfeffer, and B. R. Olsen. The role of backscattering in shg tissue imaging. *Biophys J*, 93(4):1312–20, 2007. ISSN 0006-3495 (Print) 0006-3495. doi: 10.1529/biophysj.106.100586. 1542-0086 Légaré, François Pfeffer, Christian Olsen, Bjorn R R01 AR036819/AR/NIAMS NIH HHS/United States R21 AR053143/AR/NIAMS NIH HHS/United States R01 AR 36819/AR/NIAMS NIH HHS/United States Journal Article Research Support, N.I.H., Extramural Research Support, Non-U.S. Gov't United States 2007/04/24 Biophys J. 2007 Aug 15;93(4):1312-20. doi: 10.1529/biophysj.106.100586. Epub 2007 Apr 20.

[34] R. Lacomb, O. Nadiarnykh, S. S. Townsend, and P. J. Campagnola. Phase matching considerations in second harmonic generation from tissues: Effects on emission directionality, conversion efficiency and observed morphology. *Opt Commun*, 281(7):1823–1832, 2008. ISSN 0030-4018 (Print) 0030-4018. doi: 10.1016/j.optcom.2007.10.040. Lacomb, Ronald Nadiarnykh, Oleg Townsend, Sallie S Campagnola, Paul J R01 EB001842/EB/NIBIB NIH HHS/United States R01 EB001842-04/EB/NIBIB NIH HHS/United States Journal Article Netherlands 2009/04/04 Opt Commun. 2008 Apr 1;281(7):1823-1832. doi: 10.1016/j.optcom.2007.10.040.

[35] Danielle E. Desa, Robert L. Strawderman, Wencheng Wu, Robert L. Hill, Marcel Smid, J. W. M. Martens, Bradley M. Turner, and Ed-

ward B. Brown. Intratumoral heterogeneity of second-harmonic generation scattering from tumor collagen and its effects on metastatic risk prediction. *BMC Cancer*, 20(1):1217, 2020. ISSN 1471-2407. doi: 10.1186/s12885-020-07713-4. URL https://doi.org/10.1186/s12885-020-07713-4.

[36] E. Hase, T. Minamikawa, K. Sato, D. Yonekura, M. Takahashi, and T. Yasui. Quantitative evaluation of both histological and mechanical recovery in injured tendons using fourier-transform second-harmonic-generation microscopy. *IEEE Journal of Selected Topics in Quantum Electronics*, 27(4):1–8, 2021. ISSN 1558-4542. doi: 10.1109/JSTQE.2021.3063535.

[37] Shi-Wei Chu, Shih-Peng Tai, Tzu-Ming Liu, Chi-Kuang Sun, and Chi-Hung Lin. Selective imaging in second-harmonic-generation microscopy with anisotropic radiation. *Journal of Biomedical Optics*, 14(1):010504, 2009. doi: 10.1117/1.3080722. URL https://doi.org/10.1117/1.3080722.

[38] Leila B. Mostaço-Guidolin, Alex C. T. Ko, Fei Wang, Bo Xiang, Mark Hewko, Ganghong Tian, Arkady Major, Masashi Shiomi, and Michael G. Sowa. Collagen morphology and texture analysis: from statistics to classification. *Scientific Reports*, 3(1):2190, 2013. ISSN 2045-2322. doi: 10.1038/srep02190. URL https://doi.org/10.1038/srep02190.

[39] G.M. Georgiou and K. Voigt. Stochastic computation of moments, mean, variance, skewness and kurtosis. *Electronics Letters*, 51(9):673–674, 2015. ISSN 0013-5194. doi: https://doi.org/10.1049/el.2015.0066. URL https://ietresearch.onlinelibrary.wiley.com/doi/abs/10.1049/el.2015.0066.

[40] R. M. Haralick, K. Shanmugam, and I. Dinstein. Textural features for image classification. *IEEE Transactions on Systems, Man, and Cybernetics*, SMC-3(6):610–621, 1973. ISSN 2168-2909. doi: 10.1109/TSMC.1973.4309314.

[41] Calvin C. Gotlieb and Herbert E. Kreyszig. Texture descriptors based on co-occurrence matrices. *Computer Vision, Graphics, and Image Processing*, 51(1):70–86, 1990. ISSN 0734-189X. doi: https://doi.org/10.1016/S0734-189X(05)80063-5.

URL https://www.sciencedirect.com/science/article/pii/S0734189X05800635.

[42] Z. Wang, A. C. Bovik, and L. Lu. Why is image quality assessment so difficult? In *2002 IEEE International Conference on Acoustics, Speech, and Signal Processing*, volume 4, pages IV–3313–IV–3316, 2002. ISBN 1520-6149. doi: 10.1109/ICASSP.2002.5745362.

[43] Jeff A. Squier, Michiel Müller, G. J. Brakenhoff, and Kent R. Wilson. Third harmonic generation microscopy. *Optics Express*, 3(9):315–324, 1998. doi: 10.1364/OE.3.000315. URL https://opg.optica.org/oe/abstract.cfm?URI=oe-3-9-315.

[44] Robert W. Boyd. *Nonlinear Optics, Third Edition*. Academic Press, Inc., 2008. ISBN 0123694701.

[45] Thomas Y. F. Tsang. Optical third-harmonic generation at interfaces. *Physical Review A*, 52(5):4116–4125, 1995. doi: 10.1103/PhysRevA.52.4116. URL https://link.aps.org/doi/10.1103/PhysRevA.52.4116. PRA.

[46] Jeffrey B. Guild, Chris Xu, and Watt W. Webb. Measurement of group delay dispersion of high numerical aperture objective lenses using two-photon excited fluorescence. *Applied Optics*, 36(1):397–401, 1997. doi: 10.1364/AO.36.000397. URL https://opg.optica.org/ao/abstract.cfm?URI=ao-36-1-397.

[47] Alejandro De la Cadena, Jaena Park, Kayvan F. Tehrani, Carlos A. Renteria, Guillermo L. Monroy, and Stephen A. Boppart. Simultaneous label-free autofluorescence multi-harmonic microscopy driven by the supercontinuum generated from a bulk nonlinear crystal. *Biomedical Optics Express*, 15(2):491–505, 2024. doi: 10.1364/BOE.504832. URL https://opg.optica.org/boe/abstract.cfm?URI=boe-15-2-491.

[48] Peter Fratzl, Klaus Misof, Ivo Zizak, Gert Rapp, Heinz Amenitsch, and Sigrid Bernstorff. Fibrillar structure and mechanical properties of collagen. *Journal of Structural Biology*, 122(1):119–122, 1998. ISSN 1047-8477. doi: https://doi.org/10.1006/jsbi.1998.3966. URL https://www.sciencedirect.com/science/article/pii/S1047847798939661.

[49] Bernhard Hesse, Peter Varga, Max Langer, Alexandra Pacureanu, Susanne Schrof, Nils Männicke, Heikki Suhonen, Peter Maurer, Peter Cloetens, Francoise Peyrin, and Kay Raum. Canalicular network morphology is the major determinant of the spatial distribution of mass density in human bone tissue: Evidence by means of synchrotron radiation phase-contrast nano-ct. *Journal of Bone and Mineral Research*, 30 (2):346–356, 2014. ISSN 0884-0431. doi: 10.1002/jbmr.2324. URL https://doi.org/10.1002/jbmr.2324.

[50] Li-Dan You, Sheldon Weinbaum, Stephen C. Cowin, and Mitchell B. Schaffler. Ultrastructure of the osteocyte process and its pericellular matrix. *The Anatomical Record Part A: Discoveries in Molecular, Cellular, and Evolutionary Biology*, 278A(2):505–513, 2004. ISSN 1552-4884. doi: https://doi.org/10.1002/ar.a.20050. URL https://anatomypubs.onlinelibrary.wiley.com/doi/abs/10.1002/ar.a.20050.

[51] S. M. Johnson, A. Banyard, C. Smith, A. Mironov, and M. G. McCabe. Large extracellular vesicles can be characterised by multiplex labelling using imaging flow cytometry. *Int J Mol Sci*, 21(22), 2020. ISSN 1422-0067. doi: 10.3390/ijms21228723.

[52] Zeev Zalevsky and David Mendlovic. *Optical Superresolution*. Springer, 2004.

[53] John M. Guerra. Super-resolution through illumination by diffraction-born evanescent waves. *Applied Physics Letters*, 66(26):3555–3557, 1995. ISSN 0003-6951. doi: 10.1063/1.113814. URL https://doi.org/10.1063/1.113814.

[54] M. G. L. Gustafsson. Surpassing the lateral resolution limit by a factor of two using structured illumination microscopy. *Journal of Microscopy*, 198(2):82–87, 2000. ISSN 0022-2720. doi: https://doi.org/10.1046/j.1365-2818.2000.00710.x. URL https://doi.org/10.1046/j.1365-2818.2000.00710.x.

[55] E. Hesper Rego and Lin Shao. *Practical Structured Illumination Microscopy*. Advanced Fluorescence Microscopy: Methods and Protocols. Springer New York, New York, NY, 2015. ISBN 978-1-4939-2080-8. doi: 10.1007/978-1-4939-2080-8_10. URL https://doi.org/10.1007/978-1-4939-2080-8_10.

[56] Ingo Gregor and Jörg Enderlein. Image scanning microscopy. *Current Opinion in Chemical Biology*, 51:74–83, 2019. ISSN 1367-5931. doi: https://doi.org/10.1016/j.cbpa.2019.05.011. URL https://www.sciencedirect.com/science/article/pii/S1367593119300456.

[57] Colin Sheppard. Super-resolution in confocal imaging. *Optik - International Journal for Light and Electron Optics*, 80:53, 1988.

[58] Claus B. Müller and Jörg Enderlein. Image scanning microscopy. *Physical Review Letters*, 104(19):198101, 2010. doi: 10.1103/PhysRevLett.104.198101. URL https://link.aps.org/doi/10.1103/PhysRevLett.104.198101. PRL.

[59] Andrew G. York, Sapun H. Parekh, Damian Dalle Nogare, Robert S. Fischer, Kelsey Temprine, Marina Mione, Ajay B. Chitnis, Christian A. Combs, and Hari Shroff. Resolution doubling in live, multicellular organisms via multifocal structured illumination microscopy. *Nature Methods*, 9(7):749–754, 2012. ISSN 1548-7105. doi: 10.1038/nmeth.2025. URL https://doi.org/10.1038/nmeth.2025.

[60] Marco Castello, Giorgio Tortarolo, Mauro Buttafava, Takahiro Deguchi, Federica Villa, Sami Koho, Luca Pesce, Michele Oneto, Simone Pelicci, Luca Lanzanó, Paolo Bianchini, Colin J. R. Sheppard, Alberto Diaspro, Alberto Tosi, and Giuseppe Vicidomini. A robust and versatile platform for image scanning microscopy enabling super-resolution flim. *Nature Methods*, 16(2):175–178, 2019. ISSN 1548-7105. doi: 10.1038/s41592-018-0291-9. URL https://doi.org/10.1038/s41592-018-0291-9.

[61] Maria Ingaramo, Andrew G. York, Peter Wawrzusin, Oleg Milberg, Amy Hong, Roberto Weigert, Hari Shroff, and George H. Patterson. Two-photon excitation improves multifocal structured illumination microscopy in thick scattering tissue. *Proceedings of the National Academy of Sciences*, 111(14):5254–5259, 2014. doi: doi:10.1073/pnas.1314447111. URL https://www.pnas.org/doi/abs/10.1073/pnas.1314447111.

[62] C. J. R. Sheppard, M. Castello, G. Tortarolo, G. Vicidomini, and A. Diaspro. Image formation in image scanning microscopy, including the case of two-photon excitation. *J Opt Soc Am A Opt Image Sci Vis*, 34(8):1339–1350, 2017. ISSN 1084-7529. doi: 10.1364/josaa.34.001339. 1520-8532

Sheppard, Colin J R Castello, Marco Tortarolo, Giorgio Vicidomini, Giuseppe Diaspro, Alberto Journal Article United States 2017/10/17 J Opt Soc Am A Opt Image Sci Vis. 2017 Aug 1;34(8):1339-1350. doi: 10.1364/JOSAA.34.001339.

[63] Ingo Gregor, Martin Spiecker, Roman Petrovsky, Jörg Großhans, Robert Ros, and Jörg Enderlein. Rapid nonlinear image scanning microscopy. *Nature Methods*, 14(11):1087–1089, 2017. ISSN 1548-7105. doi: 10.1038/nmeth.4467. URL https://doi.org/10.1038/nmeth.4467.

[64] Baokai Wang, Limin Zou, Su Zhang, and Jiubin Tan. Super-resolution confocal microscopy with structured detection. *Optics Communications*, 381:277–281, 2016. ISSN 0030-4018. doi: https://doi.org/10.1016/j.optcom.2016.07.005. URL https://www.sciencedirect.com/science/article/pii/S0030401816305922.

[65] Marco Castello, Colin J. R. Sheppard, Alberto Diaspro, and Giuseppe Vicidomini. Image scanning microscopy with a quadrant detector. *Optics Letters*, 40(22):5355–5358, 2015. doi: 10.1364/OL.40.005355. URL https://opg.optica.org/ol/abstract.cfm?URI=ol-40-22-5355.

[66] Youhua Chen, Dazhao Zhu, Yue Fang, Cuifang Kuang, and Xu Liu. A novel method for enhancing the lateral resolution and image snr in confocal microscopy. *Optics Communications*, 404:184–188, 2017. ISSN 0030-4018. doi: https://doi.org/10.1016/j.optcom.2017.04.073. URL https://www.sciencedirect.com/science/article/pii/S0030401817303681.

[67] Joseph Huff. The airyscan detector from zeiss: confocal imaging with improved signal-to-noise ratio and super-resolution. *Nature Methods*, 12(12):i–ii, 2015. ISSN 1548-7105. doi: 10.1038/nmeth.f.388. URL https://doi.org/10.1038/nmeth.f.388.

[68] G. M. De Luca, R. M. Breedijk, R. A. Brandt, C. H. Zeelenberg, B. E. de Jong, W. Timmermans, L. N. Azar, R. A. Hoebe, S. Stallinga, and E. M. Manders. Re-scan confocal microscopy: scanning twice for better resolution. *Biomed Opt Express*, 4(11):2644–56, 2013. ISSN 2156-7085 (Print) 2156-7085. doi: 10.1364/boe.4.002644. 2156-7085 De Luca, Giulia M R Breedijk, Ronald M P Brandt, Rick A J Zeelenberg, Christiaan H C de Jong, Babette E Timmermans, Wendy Azar, Leila Nahidi Hoebe,

Ron A Stallinga, Sjoerd Manders, Erik M M Journal Article United States 2013/12/04 Biomed Opt Express. 2013 Oct 25;4(11):2644-56. doi: 10.1364/BOE.4.002644. eCollection 2013.

[69] Shinichi Hayashi. Resolution doubling using confocal microscopy via analogy with structured illumination microscopy. *Japanese Journal of Applied Physics*, 55(8):082501, 2016. ISSN 1347-4065 0021-4922. doi: 10.7567/JJAP.55.082501. URL https://dx.doi.org/10.7567/JJAP.55.082501.

[70] Martin J. Booth. Adaptive optical microscopy: the ongoing quest for a perfect image. *Light: Science & Applications*, 3(4):e165–e165, 2014. ISSN 2047-7538. doi: 10.1038/lsa.2014.46. URL https://doi.org/10.1038/lsa.2014.46.

[71] Ioannis N. Papadopoulos, Jean-Sébastien Jouhanneau, James F. A. Poulet, and Benjamin Judkewitz. Scattering compensation by focus scanning holographic aberration probing (f-sharp). *Nature Photonics*, 11(2):116–123, 2017. ISSN 1749-4893. doi: 10.1038/nphoton.2016.252. URL https://doi.org/10.1038/nphoton.2016.252.

[72] M. Schwertner, M. Booth, and T. Wilson. Characterizing specimen induced aberrations for high na adaptive optical microscopy. *Opt Express*, 12(26):6540–52, 2004. ISSN 1094-4087. doi: 10.1364/opex.12.006540. 1094-4087 Schwertner, M Booth, M Wilson, T Journal Article United States 2004/12/27 Opt Express. 2004 Dec 27;12(26):6540-52. doi: 10.1364/opex.12.006540.

[73] M Girkin, John and N Marsh, Paul. Use of adaptive optics for improved multiphoton imaging. In *Proc.SPIE*, volume 5323, pages 260–266, 2004. doi: 10.1117/12.525659. URL https://doi.org/10.1117/12.525659.

[74] Martin J Booth. Adaptive optics in microscopy. *Philosophical Transactions of the Royal Society A: Mathematical, Physical and Engineering Sciences*, 365(1861):2829–2843, 2007. doi: doi:10.1098/rsta.2007.0013. URL https://royalsocietypublishing.org/doi/abs/10.1098/rsta.2007.0013.

[75] Maximilian Sohmen, Molly A. May, Nicolas Barré, Monika Ritsch-Marte, and Alexander Jesacher. Sensorless wavefront correction in two-photon microscopy across different turbidity scales. *Frontiers in Physics*, 10, 2022. ISSN 2296-424X.

URL https://www.frontiersin.org/journals/physics/articles/10.3389/fphy.2022.884053.

[76] Dong Li, Lin Shao, Bi-Chang Chen, Xi Zhang, Mingshu Zhang, Brian Moses, Daniel E. Milkie, Jordan R. Beach, John A. Hammer, Mithun Pasham, Tomas Kirchhausen, Michelle A. Baird, Michael W. Davidson, Pingyong Xu, and Eric Betzig. Extended-resolution structured illumination imaging of endocytic and cytoskeletal dynamics. *Science*, 349(6251):aab3500, 2015. doi: doi:10.1126/science.aab3500. URL https://www.science.org/doi/abs/10.1126/science.aab3500.

[77] Ruizhe Lin, Edward T. Kipreos, Jie Zhu, Chang Hyun Khang, and Peter Kner. Subcellular three-dimensional imaging deep through multicellular thick samples by structured illumination microscopy and adaptive optics. *Nature Communications*, 12(1):3148, 2021. ISSN 2041-1723. doi: 10.1038/s41467-021-23449-6. URL https://doi.org/10.1038/s41467-021-23449-6.

[78] W. Zheng, Y. Wu, P. Winter, R. Fischer, D. D. Nogare, A. Hong, C. McCormick, R. Christensen, W. P. Dempsey, D. B. Arnold, J. Zimmerberg, A. Chitnis, J. Sellers, C. Waterman, and H. Shroff. Adaptive optics improves multiphoton super-resolution imaging. *Nat Methods*, 14(9):869–872, 2017. ISSN 1548-7091 (Print) 1548-7091. doi: 10.1038/nmeth.4337. 1548-7105 Zheng, Wei Orcid: 0000-0001-6107-7261 Wu, Yicong Winter, Peter Fischer, Robert Nogare, Damian Dalle Hong, Amy McCormick, Chad Christensen, Ryan Dempsey, William P Arnold, Don B Zimmerberg, Joshua Orcid: 0000-0002-1707-3789 Chitnis, Ajay Sellers, James Waterman, Clare Shroff, Hari R01 MH107238/MH/NIMH NIH HHS/United States ZIA EB000074/Intramural NIH HHS/United States Journal Article Video-Audio Media United States 2017/06/20 Nat Methods. 2017 Sep;14(9):869-872. doi: 10.1038/nmeth.4337. Epub 2017 Jun 19.

[79] Francesco Fersini, Alessandro Zunino, Pietro Morerio, Alessio Del Bue, Martin Booth, and Giuseppe Vicidomini. *Direct access to optical aberration information in fluorescence laser scanning microscopy using detector arrays*, volume 12851 of *SPIE BiOS*. SPIE, 2024. URL https://doi.org/10.1117/12.3000914.

[80] Ivo Micha Vellekoop and Allard Mosk. Phase control algorithms for focusing light through turbid media. *Optics communications*, 281(11):

3071–3080, 2008. ISSN 0030-4018. doi: 10.1016/j.optcom.2008.02.022. 10.1016/j.optcom.2008.02.022.

[81] Jongchan Park, Jung-Hoon Park, Hyeonseung Yu, and YongKeun Park. Focusing through turbid media by polarization modulation. *Optics Letters*, 40(8):1667–1670, 2015. doi: 10.1364/OL.40.001667. URL https://opg.optica.org/ol/abstract.cfm?URI=ol-40-8-1667.

[82] Xiaolong Zhang and Peter Kner. Binary wavefront optimization using a genetic algorithm. *Journal of Optics*, 16:125704, 2014. ISSN 0150-536X. doi: 10.1088/2040-8978/16/12/125704. URL https://ui.adsabs.harvard.edu/abs/2014JOpt...16l5704Z.

[83] Longjie Fang, Haoyi Zuo, Zuogang Yang, Xicheng Zhang, Jinglei Du, and Lin Pang. Binary wavefront optimization using particle swarm algorithm. *Laser Physics*, 28:076204, 2018. ISSN 1054-660X. doi: 10.1088/1555-6611/aab7d9. URL https://ui.adsabs.harvard.edu/abs/2018LaPhy..28g6204F.

[84] I. M. Vellekoop and A. P. Mosk. Focusing coherent light through opaque strongly scattering media. *Optics Letters*, 32(16):2309–2311, 2007. doi: 10.1364/OL.32.002309. URL https://opg.optica.org/ol/abstract.cfm?URI=ol-32-16-2309.

[85] Roarke Horstmeyer, Haowen Ruan, and Changhuei Yang. Guidestar-assisted wavefront-shaping methods for focusing light into biological tissue. *Nature Photonics*, 9(9):563–571, 2015. ISSN 1749-4893. doi: 10.1038/nphoton.2015.140. URL https://doi.org/10.1038/nphoton.2015.140.

[86] Wai-Hon Lee. Binary synthetic holograms. *Applied Optics*, 13(7):1677–1682, 1974. doi: 10.1364/AO.13.001677. URL https://opg.optica.org/ao/abstract.cfm?URI=ao-13-7-1677.

[87] Donald B. Conkey, Albert N. Brown, Antonio M. Caravaca-Aguirre, and Rafael Piestun. Genetic algorithm optimization for focusing through turbid media in noisy environments. *Optics Express*, 20(5):4840–4849, 2012. doi: 10.1364/OE.20.004840. URL https://opg.optica.org/oe/abstract.cfm?URI=oe-20-5-4840.

[88] Sebastianus A. Goorden, Jacopo Bertolotti, and Allard P. Mosk. Superpixel-based spatial amplitude and phase modulation using a digital micromirror device. *Optics Express*, 22(15):17999–18009, 2014. doi: 10.1364/OE.22.017999. URL https://opg.optica.org/oe/abstract.cfm?URI=oe-22-15-17999.

[89] Wai-Hon Lee. *III Computer-Generated Holograms: Techniques and Applications*, volume 16, pages 119–232. Elsevier, 1978. ISBN 0079-6638. doi: https://doi.org/10.1016/S0079-6638(08)70072-6. URL https://www.sciencedirect.com/science/article/pii/S0079663808700726.

[90] R Gutiérrez-Cuevas and S.M. Popoff. Binary holograms for shaping light with digital micromirror devices. *arXiv*, (physics.optics), 2023. URL https://arxiv.org/abs/2311.16685.

[91] D. Akbulut, T. J. Huisman, E. G. van Putten, W. L. Vos, and A. P. Mosk. Focusing light through random photonic media by binary amplitude modulation. *Optics Express*, 19(5):4017–4029, 2011. doi: 10.1364/OE.19.004017. URL https://opg.optica.org/oe/abstract.cfm?URI=oe-19-5-4017.

[92] Meng Cui. Parallel wavefront optimization method for focusing light through random scattering media. *Optics Letters*, 36(6):870–872, 2011. doi: 10.1364/OL.36.000870. URL https://opg.optica.org/ol/abstract.cfm?URI=ol-36-6-870.

[93] M. Cui, E. J. McDowell, and C. Yang. An in vivo study of turbidity suppression by optical phase conjugation (tsopc) on rabbit ear. *Opt Express*, 18(1):25–30, 2010. ISSN 1094-4087. doi: 10.1364/oe.18.000025. 1094-4087 Cui, Meng McDowell, Emily J Yang, Changhuei R21 EB008866/EB/NIBIB NIH HHS/United States R21EB008866-02/EB/NIBIB NIH HHS/United States Journal Article Research Support, N.I.H., Extramural United States 2010/02/23 Opt Express. 2010 Jan 4;18(1):25-30. doi: 10.1364/OE.18.000025.

[94] J. Tang, R. N. Germain, and M. Cui. Superpenetration optical microscopy by iterative multiphoton adaptive compensation technique. *Proc Natl Acad Sci U S A*, 109(22):8434–9, 2012. ISSN 0027-8424 (Print) 0027-8424. doi: 10.1073/pnas.1119590109. 1091-6490 Tang, Jianyong Germain, Ronald N Cui, Meng Howard Hughes Medical Institute/United States Intramural NIH HHS/United States Journal Article Research

Support, N.I.H., Intramural Research Support, Non-U.S. Gov't United States 2012/05/16 Proc Natl Acad Sci U S A. 2012 May 29;109(22):8434-9. doi: 10.1073/pnas.1119590109. Epub 2012 May 14.

[95] Y. Liu, P. Lai, C. Ma, X. Xu, A. A. Grabar, and L. V. Wang. Optical focusing deep inside dynamic scattering media with near-infrared time-reversed ultrasonically encoded (true) light. *Nat Commun*, 6: 5904, 2015. ISSN 2041-1723. doi: 10.1038/ncomms6904. 2041-1723 Liu, Yan Lai, Puxiang Ma, Cheng Xu, Xiao Grabar, Alexander A Wang, Lihong V DP1 EB016986/EB/NIBIB NIH HHS/United States R01 CA186567/CA/NCI NIH HHS/United States DP1 EB016986/DP/NCCDPHP CDC HHS/United States Journal Article Research Support, N.I.H., Extramural England 2015/01/06 Nat Commun. 2015 Jan 5;6:5904. doi: 10.1038/ncomms6904.

[96] Lihong Ma, Gannavarpu Rajshekhar, Ru Wang, Basanta Bhaduri, Shamira Sridharan, Mustafa Mir, Arindam Chakraborty, Rajashekar Iyer, Supriya Prasanth, Larry Millet, Martha U. Gillette, and Gabriel Popescu. Phase correlation imaging of unlabeled cell dynamics. *Scientific Reports*, 6(1):32702, 2016. ISSN 2045-2322. doi: 10.1038/srep32702. URL https://doi.org/10.1038/srep32702.

[97] T. L. Nguyen, S. Pradeep, R. L. Judson-Torres, J. Reed, M. A. Teitell, and T. A. Zangle. Quantitative phase imaging: Recent advances and expanding potential in biomedicine. *ACS Nano*, 16(8):11516–11544, 2022. ISSN 1936-0851 (Print) 1936-0851. doi: 10.1021/acsnano.1c11507. 1936-086x Nguyen, Thang L Orcid: 0000-0002-9809-3836 Pradeep, Soorya Judson-Torres, Robert L Reed, Jason Orcid: 0000-0002-3314-8699 Teitell, Michael A Orcid: 0000-0002-4495-8750 Zangle, Thomas A Orcid: 0000-0001-5899-3517 R01 GM127985/GM/NIGMS NIH HHS/United States R01 CA185189/CA/NCI NIH HHS/United States P30 CA016042/CA/NCI NIH HHS/United States R21 CA227480/CA/NCI NIH HHS/United States P30 CA016059/CA/NCI NIH HHS/United States R01 CA246182/CA/NCI NIH HHS/United States R01 GM114188/GM/NIGMS NIH HHS/United States Journal Article Research Support, N.I.H., Extramural Research Support, U.S. Gov't, Non-P.H.S. Review United States 2022/08/03 ACS Nano. 2022 Aug 23;16(8):11516-11544. doi: 10.1021/acsnano.1c11507. Epub 2022 Aug 2.

[98] S. W. Hur, M. Kwon, R. Manoharaan, M. H. Mohammadi, A. Z. Samuel, M. P. Mulligan, P. J. Hergenrother, and R. Bhargava. Capturing cell morphology dynamics with high temporal resolution using single-shot quantitative phase gradient imaging. *J Biomed Opt*, 29 (Suppl 2):S22712, 2024. ISSN 1083-3668 (Print) 1083-3668. doi: 10.1117/1.Jbo.29.S2.S22712. 1560-2281 Hur, Sun Woong Orcid: 0000-0002-6886-0619 Kwon, Minsung Manoharaan, Revathi Orcid: 0009-0003-8780-5783 Mohammadi, Melika Haji Samuel, Ashok Zachariah Orcid: 0000-0002-6901-6348 Mulligan, Michael P Hergenrother, Paul J Bhargava, Rohit Orcid: 0000-0001-7360-994x Journal Article United States 2024/07/17 J Biomed Opt. 2024 Jun;29(Suppl 2):S22712. doi: 10.1117/1.JBO.29.S2.S22712. Epub 2024 Jul 16.

[99] A. Keating. Mesenchymal stromal cells. *Curr Opin Hematol*, 13(6): 419–25, 2006. ISSN 1065-6251 (Print) 1065-6251. doi: 10.1097/01.moh.0000245697.54887.6f. 1531-7048 Keating, Armand R01 HL077643-02/HL/NHLBI NIH HHS/United States Journal Article Review United States 2006/10/21 Curr Opin Hematol. 2006 Nov;13(6):419-25. doi: 10.1097/01.moh.0000245697.54887.6f.

[100] Oren Levy, Rui Kuai, Erika M. J. Siren, Deepak Bhere, Yuka Milton, Nabeel Nissar, Michael De Biasio, Martina Heinelt, Brock Reeve, Reza Abdi, Meshael Alturki, Mohanad Fallatah, Abdulaziz Almalik, Ali H. Alhasan, Khalid Shah, and Jeffrey M. Karp. Shattering barriers toward clinically meaningful msc therapies. *Science Advances*, 6(30):eaba6884, 2020. doi: doi:10.1126/sciadv.aba6884. URL https://www.science.org/doi/abs/10.1126/sciadv.aba6884.

[101] Mnfb Hassan, M. D. Yazid, M. H. M. Yunus, S. R. Chowdhury, Y. Lokanathan, R. B. H. Idrus, A. M. H. Ng, and J. X. Law. Large-scale expansion of human mesenchymal stem cells. *Stem Cells Int*, 2020:9529465, 2020. ISSN 1687-966X (Print). doi: 10.1155/2020/9529465. 1687-9678 Hassan, Muhammad Najib Fathi Bin Yazid, Muhammad Dain Yunus, Mohd Heikal Mohd Chowdhury, Shiplu Roy Lokanathan, Yogeswaran Idrus, Ruszymah Bt Hj Ng, Angela Min Hwei Law, Jia Xian Orcid: 0000-0001-9045-5145 Journal Article Review United States 2020/08/01 Stem Cells Int. 2020 Jul 15;2020:9529465. doi: 10.1155/2020/9529465. eCollection 2020.

[102] Yo Mabuchi, Chikako Okawara, Simón Méndez-Ferrer, and Chihiro Akazawa. Cellular heterogeneity of mesenchymal stem/stromal cells in

the bone marrow. *Frontiers in cell and developmental biology*, 9:689366, 2021. ISSN 2296-634X.

[103] Y. Lin, R. Trouillon, G. Safina, and A. G. Ewing. Chemical analysis of single cells. *Anal Chem*, 83(12):4369–92, 2011. ISSN 0003-2700 (Print) 0003-2700. doi: 10.1021/ac2009838. 1520-6882 Lin, Yuqing Trouillon, Raphaël Safina, Gulnara Ewing, Andrew G R01 EB002016/EB/NIBIB NIH HHS/United States R01 EB002016-19/EB/NIBIB NIH HHS/United States Journal Article Research Support, N.I.H., Extramural Research Support, Non-U.S. Gov't Review United States 2011/04/20 Anal Chem. 2011 Jun 15;83(12):4369-92. doi: 10.1021/ac2009838. Epub 2011 Apr 28.

[104] K. Hu, T. D. K. Nguyen, S. Rabasco, P. E. Oomen, and A. G. Ewing. Chemical analysis of single cells and organelles. *Anal Chem*, 93(1):41–71, 2021. ISSN 0003-2700 (Print) 0003-2700. doi: 10.1021/acs.analchem.0c04361. 1520-6882 Hu, Keke Nguyen, Tho D K Rabasco, Stefania Oomen, Pieter E Ewing, Andrew G Orcid: 0000-0002-2084-0133 Journal Article Research Support, N.I.H., Extramural Research Support, Non-U.S. Gov't Review United States 2020/12/08 Anal Chem. 2021 Jan 12;93(1):41-71. doi: 10.1021/acs.analchem.0c04361. Epub 2020 Dec 7.

[105] Gabriel Popescu. *Quantitative Phase Imaging of Cells and Tissues*. McGraw-Hill Education, New York, 1st edition edition, 2011. ISBN 9780071663427. URL https://www.accessengineeringlibrary.com/content/book/9780071663427.

[106] Lei Tian and Laura Waller. Quantitative differential phase contrast imaging in an led array microscope. *Optics Express*, 23(9):11394–11403, 2015. doi: 10.1364/OE.23.011394. URL https://opg.optica.org/oe/abstract.cfm?URI=oe-23-9-11394.

[107] Lei Tian, Jingyan Wang, and Laura Waller. 3d differential phase-contrast microscopy with computational illumination using an led array. *Optics Letters*, 39(5):1326–1329, 2014. doi: 10.1364/OL.39.001326. URL https://opg.optica.org/ol/abstract.cfm?URI=ol-39-5-1326.

[108] C. Platt Ben and Roland Shack. History and principles of shack-hartmann wavefront sensing. *Journal of Refractive Surgery*, 17(5):S573–S577, 2001. doi: 10.3928/1081-597X-20010901-13. URL https:

//doi.org/10.3928/1081-597X-20010901-13. doi: 10.3928/1081-597X-20010901-13.

[109] I. Ersoy, F. Bunyak, M. A. Mackey, and K. Palaniappan. Cell segmentation using hessian-based detection and contour evolution with directional derivatives. In *2008 15th IEEE International Conference on Image Processing*, pages 1804–1807, 2008. ISBN 2381-8549. doi: 10.1109/ICIP.2008.4712127.

[110] M.E. Ambühl, C. Brepsant, J.-J. Meister, A.B. Verkhovsky, and I.F. Sbalzarini. High-resolution cell outline segmentation and tracking from phase-contrast microscopy images. *Journal of Microscopy*, 245(2):161–170, 2012. ISSN 0022-2720. doi: https://doi.org/10.1111/j.1365-2818.2011.03558.x. URL https://onlinelibrary.wiley.com/doi/abs/10.1111/j.1365-2818.2011.03558.x.

[111] Mikhail E. Kandel, Michael Fanous, Catherine Best-Popescu, and Gabriel Popescu. Real-time halo correction in phase contrast imaging. *Biomedical Optics Express*, 9(2):623–635, 2018. doi: 10.1364/BOE.9.000623. URL https://opg.optica.org/boe/abstract.cfm?URI=boe-9-2-623.

[112] Bjarke Follin, Morten Juhl, Smadar Cohen, Anders Elm Pedersen, Jens Kastrup, and Annette Ekblond. Increased paracrine immunomodulatory potential of mesenchymal stromal cells in three-dimensional culture. *Tissue Engineering Part B: Reviews*, 22(4):322–329, 2016. doi: 10.1089/ten.teb.2015.0532. URL https://www.liebertpub.com/doi/abs/10.1089/ten.teb.2015.0532.

[113] Matthew W. Klinker, Ross A. Marklein, Jessica L. Lo Surdo, Cheng-Hong Wei, and Steven R. Bauer. Morphological features of ifn-gamma–stimulated mesenchymal stromal cells predict overall immunosuppressive capacity. *Proceedings of the National Academy of Sciences*, 114(13):E2598–E2607, 2017. doi: doi:10.1073/pnas.1617933114. URL https://www.pnas.org/doi/abs/10.1073/pnas.1617933114.

[114] Priyanka Priyadarshani, Alexandria Van Grouw, Adrian Ross Liversage, Kejie Rui, Arina Nikitina, Kayvan Forouhesh Tehrani, Bhavay Aggarwal, Steven L. Stice, Saurabh Sinha, Melissa L. Kemp, Facundo M. Fernández, and Luke J. Mortensen. Investigation of msc potency metrics via integration of imaging modalities with lipidomic characteriza-

tion. *Cell Reports*, 43(8), 2024. ISSN 2211-1247. doi: 10.1016/j.celrep.2024.114579. URL https://doi.org/10.1016/j.celrep.2024.114579. doi: 10.1016/j.celrep.2024.114579.

[115] Joseph R. Lakowicz. *Principles of Fluorescence Spectroscopy*. Springer, Baltimore, MD, third edition, 2006.

[116] R. Datta, T. M. Heaster, J. T. Sharick, A. A. Gillette, and M. C. Skala. Fluorescence lifetime imaging microscopy: fundamentals and advances in instrumentation, analysis, and applications. *J Biomed Opt*, 25(7):1–43, 2020. ISSN 1083-3668 (Print) 1083-3668. doi: 10.1117/1.Jbo.25.7.071203. 1560-2281 Datta, Rupsa Heaster, Tiffany M Sharick, Joe T Gillette, Amani A Skala, Melissa C R01 CA205101/CA/NCI NIH HHS/United States U01 TR002383/TR/NCATS NIH HHS/United States P30 CA014520/CA/NCI NIH HHS/United States R01 CA185747/CA/NCI NIH HHS/United States R01 CA211082/CA/NCI NIH HHS/United States R21 CA224280/CA/NCI NIH HHS/United States R37 CA226526/CA/NCI NIH HHS/United States Journal Article Research Support, N.I.H., Extramural Research Support, Non-U.S. Gov't Research Support, U.S. Gov't, Non-P.H.S. Review United States 2020/05/15 J Biomed Opt. 2020 May;25(7):1-43. doi: 10.1117/1.JBO.25.7.071203.

[117] A. Netaev, N. Schierbaum, and K. Seidl. Advantages and limitations of fluorescence lifetime measurements using single-photon avalanche diode (spad) array detector: A comprehensive theoretical and experimental study. *Sensors (Basel)*, 22(10), 2022. ISSN 1424-8220. doi: 10.3390/s22103822. 1424-8220 Netaev, Alexander Orcid: 0000-0002-6957-5270 Schierbaum, Nicolas Orcid: 0000-0001-8977-5176 Seidl, Karsten Orcid: 0000-0001-6197-5037 Journal Article Switzerland 2022/05/29 Sensors (Basel). 2022 May 18;22(10):3822. doi: 10.3390/s22103822.

[118] Warren R. Zipfel, Rebecca M. Williams, and Watt W. Webb. Nonlinear magic: multiphoton microscopy in the biosciences. *Nature Biotechnology*, 21(11):1369–1377, 2003. ISSN 1546-1696. doi: 10.1038/nbt899. URL https://doi.org/10.1038/nbt899.

[119] Thomas A. Pologruto, Bernardo L. Sabatini, and Karel Svoboda. Scanimage: Flexible software for operating laser scanning microscopes. *BioMedical Engineering OnLine*, 2(1):13, 2003. ISSN 1475-925X. doi:

10.1186/1475-925X-2-13. URL https://doi.org/10.1186/1475-925X-2-13.

[120] William M. Southern, Anna S. Nichenko, Kayvan F. Tehrani, Melissa J. McGranahan, Laxminarayanan Krishnan, Anita E. Qualls, Nathan T. Jenkins, Luke J. Mortensen, Hang Yin, Amelia Yin, Robert E. Guldberg, Sarah M. Greising, and Jarrod A. Call. Pgc-1alpha overexpression partially rescues impaired oxidative and contractile pathophysiology following volumetric muscle loss injury, 2019/03// 2019. URL http://europepmc.org/abstract/MED/30858541https://www.nature.com/articles/s41598-019-40606-6.pdfhttps://doi.org/10.1038/s41598-019-40606-6https://europepmc.org/articles/PMC6411870https://europepmc.org/articles/PMC6411870?pdf=render.

[121] Lauren A. Hymel, Shannon E. Anderson, Thomas C. Turner, William Y. York, Hongmanlin Zhang, Adrian R. Liversage, Hong Seo Lim, Peng Qiu, Luke J. Mortensen, Young C. Jang, Nick J. Willett, and Edward A. Botchwey. Identifying dysregulated immune cell subsets following volumetric muscle loss with pseudo-time trajectories. *Communications Biology*, 6(1):749, 2023. ISSN 2399-3642. doi: 10.1038/s42003-023-04790-6. URL https://doi.org/10.1038/s42003-023-04790-6.

[122] Shannon E. Anderson, Woojin M. Han, Vunya Srinivasa, Mahir Mohiuddin, Marissa A. Ruehle, June Young Moon, Eunjung Shin, Cheryl L. San Emeterio, Molly E. Ogle, Edward A. Botchwey, Nick J. Willett, and Young C. Jang. Determination of a critical size threshold for volumetric muscle loss in the mouse quadriceps. *Tissue Engineering Part C: Methods*, 25(2):59–70, 2019. doi: 10.1089/ten.tec.2018.0324. URL https://www.liebertpub.com/doi/abs/10.1089/ten.tec.2018.0324.

[123] Tianyi Zheng, Adrian R. Liversage, Kayvan F. Tehrani, Jarrod A. Call, Peter A. Kner, and Luke J. Mortensen. Imaging mitochondria through bone in live mice using two-photon fluorescence microscopy with adaptive optics. *Frontiers in Neuroimaging*, 2, 2023. ISSN 2813-1193. doi: 10.3389/fnimg.2023.959601. URL https://www.frontiersin.org/journals/neuroimaging/articles/10.3389/fnimg.2023.959601.

[124] Maureen A. Walling, Jennifer A. Novak, and Jason R. E. Shepard. Quantum dots for live cell and in vivo imaging. *International Journal of Molecular Sciences*, 10(2):441–491, 2009. ISSN 1422-0067. URL https://www.mdpi.com/1422-0067/10/2/441.

[125] Hélio M. Gil, Thomas W. Price, Kanik Chelani, Jean-Sebastien G. Bouillard, Simon D. J. Calaminus, and Graeme J. Stasiuk. Nir-quantum dots in biomedical imaging and their future. *iScience*, 24(3), 2021. ISSN 2589-0042. doi: 10.1016/j.isci.2021.102189. URL https://doi.org/10.1016/j.isci.2021.102189. doi: 10.1016/j.isci.2021.102189.

[126] Peuli Nath, Adrian Ross Liversage, Luke J. Mortensen, and Aniruddha Ray. Perovskites as multiphoton fluorescence contrast agents for in vivo imaging. *ACS Applied Materials and Interfaces*, 16(35):46035–46043, 2024. ISSN 1944-8244. doi: 10.1021/acsami.4c08672. URL https://doi.org/10.1021/acsami.4c08672. doi: 10.1021/acsami.4c08672.

[127] Pradip Shahi Thakuri, Chun Liu, Gary D. Luker, and Hossein Tavana. Biomaterials-based approaches to tumor spheroid and organoid modeling. *Advanced Healthcare Materials*, 7(6):1700980, 2018. ISSN 2192-2640. doi: https://doi.org/10.1002/adhm.201700980. URL https://onlinelibrary.wiley.com/doi/abs/10.1002/adhm.201700980.

[128] Plansky Hoang and Zhen Ma. Biomaterial-guided stem cell organoid engineering for modeling development and diseases. *Acta Biomaterialia*, 132:23–36, 2021. ISSN 1742-7061. doi: https://doi.org/10.1016/j.actbio.2021.01.026. URL https://www.sciencedirect.com/science/article/pii/S1742706121000544.

[129] Lisa Hutchinson and Rebecca Kirk. High drug attrition rates—where are we going wrong? *Nature Reviews Clinical Oncology*, 8(4):189–190, 2011. ISSN 1759-4782. doi: 10.1038/nrclinonc.2011.34. URL https://doi.org/10.1038/nrclinonc.2011.34.

[130] Meghan M. Capeling, Michael Czerwinski, Sha Huang, Yu-Hwai Tsai, Angeline Wu, Melinda S. Nagy, Benjamin Juliar, Nambirajan Sundaram, Yang Song, Woojin M. Han, Shuichi Takayama, Eben Alsberg, Andres J. Garcia, Michael Helmrath, Andrew J. Putnam, and Jason R. Spence. Nonadhesive alginate hydrogels support growth of

pluripotent stem cell-derived intestinal organoids. *Stem Cell Reports*, 12(2):381–394, 2019. ISSN 2213-6711. doi: 10.1016/j.stemcr.2018.12.001. URL https://doi.org/10.1016/j.stemcr.2018.12.001. doi: 10.1016/j.stemcr.2018.12.001.

[131] Susanne Ramm, Robert Vary, Twishi Gulati, Jennii Luu, Karla J. Cowley, Michael S. Janes, Nicholas Radio, and Kaylene J. Simpson. High-throughput live and fixed cell imaging method to screen matrigel-embedded organoids. *Organoids*, 2(1):1–19, 2023. ISSN 2674-1172. URL https://www.mdpi.com/2674-1172/2/1/1.

[132] G. Hall, K. B. Tilbury, K. R. Campbell, K. W. Eliceiri, and P. J. Campagnola. Experimental and simulation study of the wavelength dependent second harmonic generation of collagen in scattering tissues. *Opt Lett*, 39(7):1897–900, 2014. ISSN 0146-9592 (Print) 0146-9592. doi: 10.1364/ol.39.001897. 1539-4794 Hall, Gunnsteinn Tilbury, Karissa B Campbell, Kirby R Eliceiri, Kevin W Campagnola, Paul J R01 CA136590/CA/NCI NIH HHS/United States T32 CA009206/CA/NCI NIH HHS/United States 5T32CA009206-34/CA/NCI NIH HHS/United States R01 CA136590-01A1/CA/NCI NIH HHS/United States Journal Article Research Support, N.I.H., Extramural Research Support, Non-U.S. Gov't Research Support, U.S. Gov't, Non-P.H.S. United States 2014/04/02 Opt Lett. 2014 Apr 1;39(7):1897-900. doi: 10.1364/OL.39.001897.

[133] Fritjof Helmchen and Winfried Denk. Deep tissue two-photon microscopy. *Nature Methods*, 2(12):932–940, 2005. ISSN 1548-7105. doi: 10.1038/nmeth818. URL https://doi.org/10.1038/nmeth818.

[134] D. Kobat, M. E. Durst, N. Nishimura, A. W. Wong, C. B. Schaffer, and C. Xu. Deep tissue multiphoton microscopy using longer wavelength excitation. *Opt Express*, 17(16):13354–64, 2009. ISSN 1094-4087. doi: 10.1364/oe.17.013354. 1094-4087 Kobat, Demirhan Durst, Michael E Nishimura, Nozomi Wong, Angela W Schaffer, Chris B Xu, Chris Evaluation Study Journal Article Research Support, Non-U.S. Gov't Research Support, U.S. Gov't, Non-P.H.S. United States 2009/08/06 Opt Express. 2009 Aug 3;17(16):13354-64. doi: 10.1364/oe.17.013354.

[135] Kayvan Forouhesh Tehrani, Charles V. Latchoumane, W. Michael Southern, Emily G. Pendleton, Ana Maslesa, Lohitash Karumbaiah, Jarrod A. Call, and Luke J. Mortensen. Five-dimensional two-photon

volumetric microscopy of in-vivo dynamic activities using liquid lens remote focusing. *Biomedical Optics Express*, 10(7):3591–3604, 2019. doi: 10.1364/BOE.10.003591. URL https://opg.optica.org/boe/abstract.cfm?URI=boe-10-7-3591.

[136] K. F. Tehrani, P. Kner, and L. J. Mortensen. Characterization of wavefront errors in mouse cranial bone using second-harmonic generation. *J Biomed Opt*, 22(3):36012, 2017. ISSN 1083-3668. doi: 10.1117/1.Jbo.22.3.036012. 1560-2281 Tehrani, Kayvan Forouhesh Kner, Peter Mortensen, Luke J Journal Article United States 2017/03/23 J Biomed Opt. 2017 Mar 1;22(3):36012. doi: 10.1117/1.JBO.22.3.036012.

[137] Kayvan F. Tehrani, Yiwen Zhang, Ping Shen, and Peter Kner. Adaptive optics stochastic optical reconstruction microscopy (ao-storm) by particle swarm optimization. *Biomedical Optics Express*, 8(11):5087–5097, 2017. doi: 10.1364/BOE.8.005087. URL https://opg.optica.org/boe/abstract.cfm?URI=boe-8-11-5087.

[138] Lina Streich, Juan Carlos Boffi, Ling Wang, Khaleel Alhalaseh, Matteo Barbieri, Ronja Rehm, Senthilkumar Deivasigamani, Cornelius T. Gross, Amit Agarwal, and Robert Prevedel. High-resolution structural and functional deep brain imaging using adaptive optics three-photon microscopy. *Nature Methods*, 18(10):1253–1258, 2021. ISSN 1548-7105. doi: 10.1038/s41592-021-01257-6. URL https://doi.org/10.1038/s41592-021-01257-6.

[139] Tomer Yeminy and Ori Katz. Guidestar-free image-guided wavefront shaping. *Science Advances*, 7(21):eabf5364, 2021. doi: doi:10.1126/sciadv.abf5364. URL https://www.science.org/doi/abs/10.1126/sciadv.abf5364.

[140] Oleksandr Danko, Volodymyr Danko, and Andrey Kovalenko. *Experimental study of light focusing through strongly scattering media using binary amplitude spatial light modulator*, volume 11369 of *Fourteenth International Conference on Correlation Optics*. SPIE, 2020. URL https://doi.org/10.1117/12.2553684.

[141] E. Durech, W. Newberry, J. Franke, and M. V. Sarunic. Wavefront sensor-less adaptive optics using deep reinforcement learning. *Biomed Opt Express*, 12(9):5423–5438, 2021. ISSN 2156-7085 (Print) 2156-7085. doi: 10.1364/boe.427970. 2156-7085 Durech, Eduard Orcid: 0000-0002-9186-073x Newberry, William Franke, Jonas Sarunic, Marinko V Jour-

nal Article United States 2021/10/26 Biomed Opt Express. 2021 Aug 6;12(9):5423-5438. doi: 10.1364/BOE.427970. eCollection 2021 Sep 1.

[142] John R. Koza and Riccardo Poli. *Genetic Programming*, pages 127–164. Springer US, Boston, MA, 2005. ISBN 978-0-387-28356-2. doi: 10.1007/0-387-28356-0_5. URL https://doi.org/10.1007/0-387-28356-0_5.

[143] Ahmad Hassanat, Khalid Almohammadi, Esra'a Alkafaween, Eman Abunawas, Awni Hammouri, and V. B. Surya Prasath. Choosing mutation and crossover ratios for genetic algorithms—a review with a new dynamic approach. *Information*, 10(12):390, 2019. ISSN 2078-2489. URL https://www.mdpi.com/2078-2489/10/12/390.

[144] Bin Zhang, Zhenfeng Zhang, Qi Feng, Zhipeng Liu, Chengyou Lin, and Yingchun Ding. Focusing light through strongly scattering media using genetic algorithm with sbr discriminant. *Journal of Optics*, 20:025601, 2018. ISSN 0150-536X. doi: 10.1088/2040-8986/aa9f91. URL https://ui.adsabs.harvard.edu/abs/2018JOpt...20b5601Z.

[145] Daixuan Wu, Jiawei Luo, Zhaohui Li, and Yuecheng Shen. A thorough study on genetic algorithms in feedback-based wavefront shaping. *Journal of Innovative Optical Health Sciences*, 12 (04):1942004, 2019. doi: 10.1142/s1793545819420045. URL https://www.worldscientific.com/doi/abs/10.1142/S1793545819420045.

[146] Jiamiao Yang, Qiaozhi He, Linxian Liu, Yuan Qu, Rongjun Shao, Bowen Song, and Yanyu Zhao. Anti-scattering light focusing by fast wavefront shaping based on multi-pixel encoded digital-micromirror device. *Light: Science & Applications*, 10(1):149, 2021. ISSN 2047-7538. doi: 10.1038/s41377-021-00591-w. URL https://doi.org/10.1038/s41377-021-00591-w.

[147] Xiaodong Tao, Dare Bodington, Marc Reinig, and Joel Kubby. High-speed scanning interferometric focusing by fast measurement of binary transmission matrix for channel demixing. *Optics Express*, 23(11):14168–14187, 2015. doi: 10.1364/OE.23.014168. URL https://opg.optica.org/oe/abstract.cfm?URI=oe-23-11-14168.

[148] A. G. Borovoi. Analytical description of snake photons. In *Advances in Optical Imaging and Photon Migration*, Technical Digest Series, page PMST69. Optica Publishing Group, 1996. doi: 10.1364/AOIPM.1996.PMST69. URL https://opg.optica.org/abstract.cfm?URI=AOIPM-1996-PMST69.

[149] Molly A. May, Nicolas Barré, Kai K. Kummer, Michaela Kress, Monika Ritsch-Marte, and Alexander Jesacher. Fast holographic scattering compensation for deep tissue biological imaging. *Nature Communications*, 12(1):4340, 2021. ISSN 2041-1723. doi: 10.1038/s41467-021-24666-9. URL https://doi.org/10.1038/s41467-021-24666-9.

[150] J. D. Briers and S. Webster. Quasi real-time digital version of single-exposure speckle photography for full-field monitoring of velocity or flow fields. *Optics Communications*, 116:36–42, 1995. ISSN 0030-4018. doi: 10.1016/0030-4018(95)00042-7. URL https://ui.adsabs.harvard.edu/abs/1995OptCo.116...36B.

[151] Baptiste Blochet, Kelly Joaquina, Lisa Blum, Laurent Bourdieu, and Sylvain Gigan. Enhanced stability of the focus obtained by wavefront optimization in dynamical scattering media. *Optica*, 6(12):1554–1561, 2019. doi: 10.1364/OPTICA.6.001554. URL https://opg.optica.org/optica/abstract.cfm?URI=optica-6-12-1554.

[152] C. A. Schneider, W. S. Rasband, and K. W. Eliceiri. Nih image to imagej: 25 years of image analysis. *Nat Methods*, 9(7):671–5, 2012. ISSN 1548-7091 (Print) 1548-7091. doi: 10.1038/nmeth.2089. 1548-7105 Schneider, Caroline A Rasband, Wayne S Eliceiri, Kevin W RC2 GM092519/GM/NIGMS NIH HHS/United States Historical Article Journal Article Research Support, N.I.H., Extramural United States 2012/08/30 Nat Methods. 2012 Jul;9(7):671-5. doi: 10.1038/nmeth.2089.

[153] Robert P. J. Nieuwenhuizen, Keith A. Lidke, Mark Bates, Daniela Leyton Puig, David Grünwald, Sjoerd Stallinga, and Bernd Rieger. Measuring image resolution in optical nanoscopy. *Nature Methods*, 10 (6):557–562, 2013. ISSN 1548-7105. doi: 10.1038/nmeth.2448. URL https://doi.org/10.1038/nmeth.2448.

[154] K. F. Tehrani, E. G. Pendleton, W. M. Southern, J. A. Call, and L. J. Mortensen. Two-photon deep-tissue spatially resolved mitochondrial imaging using membrane potential fluorescence fluctuations. *Biomed*

Opt Express, 9(1):254–259, 2018. ISSN 2156-7085 (Print) 2156-7085. doi: 10.1364/boe.9.000254. 2156-7085 Tehrani, Kayvan Forouhesh Pendleton, Emily G Southern, William M Call, Jarrod A Mortensen, Luke J Journal Article United States 2018/01/24 Biomed Opt Express. 2017 Dec 19;9(1):254-259. doi: 10.1364/BOE.9.000254. eCollection 2018 Jan 1.

[155] E. G. Pendleton, K. F. Tehrani, R. P. Barrow, and L. J. Mortensen. Second harmonic generation characterization of collagen in whole bone. *Biomed Opt Express*, 11(8):4379–4396, 2020. ISSN 2156-7085 (Print) 2156-7085. doi: 10.1364/boe.391866. 2156-7085 Pendleton, Emily G Orcid: 0000-0002-2487-1009 Tehrani, Kayvan F Orcid: 0000-0002-3766-616x Barrow, Ruth P Mortensen, Luke J Orcid: 0000-0002-4331-4099 R21 EB027802/EB/NIBIB NIH HHS/United States Journal Article United States 2020/09/15 Biomed Opt Express. 2020 Jul 17;11(8):4379-4396. doi: 10.1364/BOE.391866. eCollection 2020 Aug 1.

[156] David G. Lowe. Distinctive image features from scale-invariant keypoints. *International Journal of Computer Vision*, 60(2):91–110, 2004. ISSN 1573-1405. doi: 10.1023/B:VISI.0000029664.99615.94. URL https://doi.org/10.1023/B:VISI.0000029664.99615.94.

[157] Gerald Donnert, Christian Eggeling, and Stefan W. Hell. Major signal increase in fluorescence microscopy through dark-state relaxation. *Nature Methods*, 4(1):81–86, 2007. ISSN 1548-7105. doi: 10.1038/nmeth986. URL https://doi.org/10.1038/nmeth986.

[158] David J. L. Graham, Shu-Fen Tseng, Jer-Tsong Hsieh, David J. Chen, and George Alexandrakis. Dependence of two-photon egfp bleaching on femtosecond pulse spectral amplitude and phase. *Journal of Fluorescence*, 25(6):1775–1785, 2015. ISSN 1573-4994. doi: 10.1007/s10895-015-1667-1. URL https://doi.org/10.1007/s10895-015-1667-1.

[159] Sophia Imperato, Fabrice Harms, Antoine Hubert, Mathias Mercier, Laurent Bourdieu, and Alexandra Fragola. Single-shot quantitative aberration and scattering length measurements in mouse brain tissues using an extended-source shack-hartmann wavefront sensor. *Optics Express*, 30 (9):15250–15265, 2022. doi: 10.1364/OE.456651. URL https://opg.optica.org/oe/abstract.cfm?URI=oe-30-9-15250.

[160] Daniel Zepeda, Yucheng Li, and Yi Xue. Scattering compensation through fourier-domain open-channel coupling in two-photon microscopy. *arXiv preprint arXiv:2401.15192*, 2024.

[161] Abraham Bookstein, Vladimir A. Kulyukin, and Timo Raita. Generalized hamming distance. *Information Retrieval*, 5(4):353–375, 2002. ISSN 1573-7659. doi: 10.1023/A:1020499411651. URL https://doi.org/10.1023/A:1020499411651.

[162] Azriel Rosenfeld and John L. Pfaltz. Sequential operations in digital picture processing. *J. ACM*, 13(4):471–494, 1966. ISSN 0004-5411. doi: 10.1145/321356.321357. URL https://doi.org/10.1145/321356.321357.

[163] Martin J. Booth, Mark A. A. Neil, Rimas Juškaitis, and Tony Wilson. Adaptive aberration correction in a confocal microscope. *Proceedings of the National Academy of Sciences*, 99(9):5788–5792, 2002. doi: doi:10.1073/pnas.082544799. URL https://www.pnas.org/doi/abs/10.1073/pnas.082544799.

[164] P. N. Marsh, D. Burns, and J. M. Girkin. Practical implementation of adaptive optics in multiphoton microscopy. *Optics Express*, 11(10):1123–1130, 2003. doi: 10.1364/OE.11.001123. URL https://opg.optica.org/oe/abstract.cfm?URI=oe-11-10-1123.

[165] Markus Rueckel, Julia A. Mack-Bucher, and Winfried Denk. Adaptive wavefront correction in two-photon microscopy using coherence-gated wavefront sensing. *Proceedings of the National Academy of Sciences*, 103(46):17137–17142, 2006. doi: doi:10.1073/pnas.0604791103. URL https://www.pnas.org/doi/abs/10.1073/pnas.0604791103.

[166] Delphine Débarre, Edward J. Botcherby, Tomoko Watanabe, Shankar Srinivas, Martin J. Booth, and Tony Wilson. Image-based adaptive optics for two-photon microscopy. *Optics Letters*, 34(16):2495–2497, 2009. doi: 10.1364/OL.34.002495. URL https://opg.optica.org/ol/abstract.cfm?URI=ol-34-16-2495.

[167] Alexander Jesacher, Anisha Thayil, Kate Grieve, Delphine Débarre, Tomoko Watanabe, Tony Wilson, Shankar Srinivas, and Martin Booth. Adaptive harmonic generation microscopy of mammalian embryos. *Optics Letters*, 34(20):3154–3156, 2009. doi: 10.1364/OL.34.

003154. URL https://opg.optica.org/ol/abstract.cfm?URI=ol-34-20-3154.

[168] Qinggele Li, Marc Reinig, Daich Kamiyama, Bo Huang, Xiaodong Tao, Alex Bardales, and Joel Kubby. Woofer-tweeter adaptive optical structured illumination microscopy. *Photonics Research*, 5(4):329–334, 2017. doi: 10.1364/PRJ.5.000329. URL https://opg.optica.org/prj/abstract.cfm?URI=prj-5-4-329.

[169] Volker Westphal, Silvio O. Rizzoli, Marcel A. Lauterbach, Dirk Kamin, Reinhard Jahn, and Stefan W. Hell. Video-rate far-field optical nanoscopy dissects synaptic vesicle movement. *Science*, 320(5873):246–249, 2008. doi: doi:10.1126/science.1154228. URL https://www.science.org/doi/abs/10.1126/science.1154228.

[170] Lothar Schermelleh, Rainer Heintzmann, and Heinrich Leonhardt. A guide to super-resolution fluorescence microscopy. *Journal of Cell Biology*, 190(2):165–175, 2010. ISSN 0021-9525. doi: 10.1083/jcb.201002018. URL https://doi.org/10.1083/jcb.201002018.

[171] M Minsky. Microscopy apparatus, 1961.

[172] Paul Davidovits and M. David Egger. Scanning laser microscope. *Nature*, 223(5208):831–831, 1969. ISSN 1476-4687. doi: 10.1038/22383110. URL https://doi.org/10.1038/223831a0.

[173] T. Wilson. *The Role of the Pinhole in Confocal Imaging System*, pages 167–182. Springer US, Boston, MA, 1995. ISBN 978-1-4757-5348-6. doi: 10.1007/978-1-4757-5348-6_11. URL https://doi.org/10.1007/978-1-4757-5348-6_11.

[174] E.N. Ward and R. Pal. Image scanning microscopy: an overview. *Journal of Microscopy*, 266(2):221–228, 2017. ISSN 0022-2720. doi: https://doi.org/10.1111/jmi.12534. URL https://onlinelibrary.wiley.com/doi/abs/10.1111/jmi.12534.

[175] Colin J. R. Sheppard, Shalin B. Mehta, and Rainer Heintzmann. Superresolution by image scanning microscopy using pixel reassignment. *Optics Letters*, 38(15):2889–2892, 2013. doi: 10.1364/OL.38.002889. URL https://opg.optica.org/ol/abstract.cfm?URI=ol-38-15-2889.

[176] Stephan Roth, Colin J. R. Sheppard, Kai Wicker, and Rainer Heintzmann. Optical photon reassignment microscopy (opra). *Optical Nanoscopy*, 2(1):5, 2013. ISSN 2192-2853. doi: 10.1186/2192-2853-2-5. URL https://doi.org/10.1186/2192-2853-2-5.

[177] Takuya Azuma and Takayuki Kei. Super-resolution spinning-disk confocal microscopy using optical photon reassignment. *Optics Express*, 23(11):15003–15011, 2015. doi: 10.1364/OE.23.015003. URL https://opg.optica.org/oe/abstract.cfm?URI=oe-23-11-15003.

[178] Yue Fang, Cuifang Kuang, Ye Ma, Yifan Wang, and Xu Liu. Resolution and contrast enhancements of optical microscope based on point spread function engineering. *Frontiers of Optoelectronics*, 8(2):152–162, 2015. ISSN 2095-2767. doi: 10.1007/s12200-015-0479-x. URL https://doi.org/10.1007/s12200-015-0479-x.

[179] Alessandro Zunino, Marco Castello, and Giuseppe Vicidomini. Reconstructing the image scanning microscopy dataset: an inverse problem. *Inverse Problems*, 39(6):064004, 2023. ISSN 0266-5611. doi: 10.1088/1361-6420/accdc5. URL https://dx.doi.org/10.1088/1361-6420/accdc5.

[180] Mauro Buttafava, Federica Villa, Marco Castello, Giorgio Tortarolo, Enrico Conca, Mirko Sanzaro, Simonluca Piazza, Paolo Bianchini, Alberto Diaspro, Franco Zappa, Giuseppe Vicidomini, and Alberto Tosi. Spad-based asynchronous-readout array detectors for image-scanning microscopy. *Optica*, 7(7):755–765, 2020. doi: 10.1364/OPTICA.391726. URL https://opg.optica.org/optica/abstract.cfm?URI=optica-7-7-755.

[181] Sami V. Koho, Eli Slenders, Giorgio Tortarolo, Marco Castello, Mauro Buttafava, Federica Villa, Elena Tcarenkova, Marcel Ameloot, Paolo Bianchini, Colin J. R. Sheppard, Alberto Diaspro, Alberto Tosi, and Giuseppe Vicidomini. Two-photon image-scanning microscopy with spad array and blind image reconstruction. *Biomedical Optics Express*, 11(6):2905–2924, 2020. doi: 10.1364/BOE.374398. URL https://opg.optica.org/boe/abstract.cfm?URI=boe-11-6-2905.

[182] Dekel Raanan, Man Suk Song, William A. Tisdale, and Dan Oron. Super-resolved second harmonic generation imaging by coherent image

scanning microscopy. *Applied Physics Letters*, 120(7):071111, 2022. ISSN 0003-6951. doi: 10.1063/5.0073161. URL https://doi.org/10.1063/5.0073161.

[183] Anton Classen, I. Michel Antolovic, Stanislav Vitha, Mia Pacheco, Dylan McCreedy, Alexei V. Sokolov, Girish S. Agarwal, Aart J. Verhoef, and Alma Fernández. Three photon excited image scanning microscopy for in-depth super-resolution studies of biological samples. *PRX Life*, 2(3): 033010, 2024. doi: 10.1103/PRXLife.2.033010. URL https://link.aps.org/doi/10.1103/PRXLife.2.033010. PRXLIFE.

[184] Chris Xu and Watt W. Webb. Measurement of two-photon excitation cross sections of molecular fluorophores with data from 690 to 1050 nm. *Journal of the Optical Society of America B*, 13(3):481–491, 1996. doi: 10.1364/JOSAB.13.000481. URL https://opg.optica.org/josab/abstract.cfm?URI=josab-13-3-481.

[185] A. J. Moy, B. V. Capulong, R. B. Saager, M. P. Wiersma, P. C. Lo, A. J. Durkin, and B. Choi. Optical properties of mouse brain tissue after optical clearing with focusclear™. *J Biomed Opt*, 20(9):95010, 2015. ISSN 1083-3668 (Print) 1083-3668. doi: 10.1117/1.Jbo.20.9.095010. 1560-2281 Moy, Austin J Capulong, Bernard V Saager, Rolf B Wiersma, Matthew P Lo, Patrick C Durkin, Anthony J Choi, Bernard P41 EB015890/EB/NIBIB NIH HHS/United States R01 HD065536/HD/NICHD NIH HHS/United States EB015890/EB/NIBIB NIH HHS/United States Journal Article Research Support, N.I.H., Extramural United States 2015/09/22 J Biomed Opt. 2015;20(9):95010. doi: 10.1117/1.JBO.20.9.095010.

[186] Tianyu Wang, Chunyan Wu, Dimitre G. Ouzounov, Wenchao Gu, Fei Xia, Minsu Kim, Xusan Yang, Melissa R. Warden, and Chris Xu. Quantitative analysis of 1300-nm three-photon calcium imaging in the mouse brain. *eLife*, 9:e53205, 2020. ISSN 2050-084X. doi: 10.7554/eLife.53205. URL https://doi.org/10.7554/eLife.53205.

[187] Nicholas G. Horton, Ke Wang, Demirhan Kobat, Catharine G. Clark, Frank W. Wise, Chris B. Schaffer, and Chris Xu. In vivo three-photon microscopy of subcortical structures within an intact mouse brain. *Nature Photonics*, 7(3):205–209, 2013. ISSN 1749-4893. doi: 10.1038/nphoton.2012.336. URL https://doi.org/10.1038/nphoton.2012.336.

[188] Galiya Sharafutdinova, John Holdsworth, and Dirk van Helden. Improved field scanner incorporating parabolic optics. part 1: Simulation. *Applied Optics*, 48(22):4389–4396, 2009. doi: 10.1364/AO.48.004389. URL https://opg.optica.org/ao/abstract.cfm?URI=ao-48-22-4389.

[189] John Holdsworth, Galiya Sharafutdinova, Michael Sanderson, and Dirk van Helden. *Off-axis parabolic optical relays: almost perfect imaging*, volume 8011 of *International Commission for Optics (ICO 22)*. SPIE, 2011. URL https://doi.org/10.1117/12.903430.

[190] Galiya Sharafutdinova, John Holdsworth, and Dirk van Helden. Improved field scanner incorporating parabolic optics. part 2: experimental verification and potential for volume scanning. *Applied Optics*, 49(29): 5517–5527, 2010. doi: 10.1364/AO.49.005517. URL https://opg.optica.org/ao/abstract.cfm?URI=ao-49-29-5517.

[191] Colin J. R. Sheppard, Marco Castello, Giorgio Tortarolo, Takahiro Deguchi, Sami V. Koho, Giuseppe Vicidomini, and Alberto Diaspro. Pixel reassignment in image scanning microscopy: a re-evaluation. *Journal of the Optical Society of America A*, 37(1):154–162, 2020. doi: 10.1364/JOSAA.37.000154. URL https://opg.optica.org/josaa/abstract.cfm?URI=josaa-37-1-154.

[192] Raymond A. Applegate, Charles Ballentine, Hillery Gross, Edwin J. Sarver, and Charlene A. Sarver. Visual acuity as a function of zernike mode and level of root mean square error. *Optometry and Vision Science*, 80(2), 2003. ISSN 1538-9235. URL https://journals.lww.com/optvissci/fulltext/2003/02000/visual_acuity_as_a_function_of_zernike_mode_and.5.aspx.

[193] Virendra N. Mahajan. Strehl ratio for primary aberrations in terms of their aberration variance. *Journal of the Optical Society of America*, 73(6): 860–861, 1983. doi: 10.1364/JOSA.73.000860. URL https://opg.optica.org/abstract.cfm?URI=josa-73-6-860.

[194] Maximilian Sohmen, Juan D. Muñoz-Bolaños, Pouya Rajaeipour, Monika Ritsch-Marte, Çağlar Ataman, and Alexander Jesacher. Optofluidic adaptive optics in multi-photon microscopy. *Biomedical Optics Express*, 14(4):1562–1578, 2023. doi: 10.1364/BOE.481453. URL

https://opg.optica.org/boe/abstract.cfm?URI=boe-14-4-1562.

[195] Clemens Roider, Monika Ritsch-Marte, and Alexander Jesacher. High-resolution confocal raman microscopy using pixel reassignment. *Optics Letters*, 41(16):3825–3828, 2016. doi: 10.1364/OL.41.003825. URL https://opg.optica.org/ol/abstract.cfm?URI=ol-41-16-3825.

[196] Andrew G. York, Panagiotis Chandris, Damian Dalle Nogare, Jeffrey Head, Peter Wawrzusin, Robert S. Fischer, Ajay Chitnis, and Hari Shroff. Instant super-resolution imaging in live cells and embryos via analog image processing. *Nature Methods*, 10(11):1122–1126, 2013. ISSN 1548-7105. doi: 10.1038/nmeth.2687. URL https://doi.org/10.1038/nmeth.2687.

[197] Aaron K. LaViolette, Dimitre G. Ouzounov, and Chris Xu. Measurement of three-photon excitation cross-sections of fluorescein from 1154nm to 1500nm. *Biomedical Optics Express*, 14(8):4369–4382, 2023. doi: 10.1364/BOE.498214. URL https://opg.optica.org/boe/abstract.cfm?URI=boe-14-8-4369.

[198] H. Li, H. A. Nawaz, F. F. Masieri, S. Vogel, U. Hempel, A. K. Bartella, R. Zimmerer, J. C. Simon, M. Schulz-Siegmund, M. Hacker, B. Lethaus, and V. Savković. Osteogenic potential of mesenchymal stem cells from adipose tissue, bone marrow and hair follicle outer root sheath in a 3d crosslinked gelatin-based hydrogel. *Int J Mol Sci*, 22(10), 2021. ISSN 1422-0067. doi: 10.3390/ijms22105404. 1422-0067 Li, Hanluo Orcid: 0000-0001-9109-2972 Nawaz, Hafiz Awais Masieri, Federica Francesca Vogel, Sarah Hempel, Ute Bartella, Alexander K Orcid: 0000-0002-3545-1341 Zimmerer, Rüdiger Simon, Jan-Christoph Schulz-Siegmund, Michaela Hacker, Michael Orcid: 0000-0002-4776-2294 Lethaus, Bernd Orcid: 0000-0002-9619-9362 Savković, Vuk Chair to BL/Department for Oral- and Maxillofacial Surgery, University Hospital Leipzig/ to SIKT/Saxon Ministry of Science and Fine Arts (SMWK)/ SFB TRR 67 B12/German Research Council (DFG)/ SFB TRR 67 B3/German Research Council (DFG)/ Journal Article Switzerland 2021/06/03 Int J Mol Sci. 2021 May 20;22(10):5404. doi: 10.3390/ijms22105404.

[199] V. S. R. Choppa, G. Liu, Y. H. Tompkins, and W. K. Kim. Altered osteogenic differentiation in mesenchymal stem cells isolated from compact bone of chicken treated with varying doses of lipopolysaccharides.

Biomolecules, 13(11), 2023. ISSN 2218-273x. doi: 10.3390/biom13111626. 2218-273x Choppa, Venkata Sesha Reddy Liu, Guanchen Tompkins, Yuguo Hou Kim, Woo Kyun Orcid: 0000-0002-0005-352x Journal Article Switzerland 2023/11/25 Biomolecules. 2023 Nov 7;13(11):1626. doi: 10.3390/biom13111626.

[200] E. E. Ural, V. Toomajian, E. Hoque Apu, M. Veletic, I. Balasingham, N. Ashammakhi, M. Kanada, and C. H. Contag. Visualizing extracellular vesicles and their function in 3d tumor microenvironment models. *Int J Mol Sci*, 22(9), 2021. ISSN 1422-0067. doi: 10.3390/ijms22094784. 1422-0067 Ural, Evran E Orcid: 0000-0002-8281-634x Toomajian, Victoria Hoque Apu, Ehsanul Orcid: 0000-0001-6840-3787 Veletic, Mladen Orcid: 0000-0003-1960-8019 Balasingham, Ilangko Ashammakhi, Nureddin Orcid: 0000-0003-0181-6055 Kanada, Masamitsu Orcid: 0000-0001-9025-9582 Contag, Christopher H Journal Article Review Switzerland 2021/05/06 Int J Mol Sci. 2021 Apr 30;22(9):4784. doi: 10.3390/ijms22094784.

[201] Baekcheon Seong, Ingyoung Kim, Taegyun Moon, Malith Ranathunga, Daesuk Kim, and Chulmin Joo. Untrained deep learning-based differential phase-contrast microscopy. *Optics Letters*, 48(13):3607–3610, 2023. doi: 10.1364/OL.493391. URL https://opg.optica.org/ol/abstract.cfm?URI=ol-48-13-3607.

[202] Caroline Berlage, Malinda L. S. Tantirigama, Mathias Babot, Diego Di Battista, Clarissa Whitmire, Ioannis N. Papadopoulos, James F. A. Poulet, Matthew Larkum, and Benjamin Judkewitz. Deep tissue scattering compensation with three-photon f-sharp. *Optica*, 8(12):1613–1619, 2021. doi: 10.1364/OPTICA.440279. URL https://opg.optica.org/optica/abstract.cfm?URI=optica-8-12-1613.

[203] Kayvan F. Tehrani, Jianquan Xu, Yiwen Zhang, Ping Shen, and Peter Kner. Adaptive optics stochastic optical reconstruction microscopy (ao-storm) using a genetic algorithm. *Optics Express*, 23(10):13677–13692, 2015. doi: 10.1364/OE.23.013677. URL https://opg.optica.org/oe/abstract.cfm?URI=oe-23-10-13677.

[204] D. Tokarz, R. Cisek, M. N. Wein, R. Turcotte, C. Haase, S. A. Yeh, S. Bharadwaj, A. P. Raphael, H. Paudel, C. Alt, T. M. Liu, H. M. Kronenberg, and C. P. Lin. Intravital imaging of

osteocytes in mouse calvaria using third harmonic generation microscopy. *PLoS One*, 12(10):e0186846, 2017. ISSN 1932-6203. doi: 10.1371/journal.pone.0186846. 1932-6203 Tokarz, Danielle Orcid: 0000-0001-8893-0293 Cisek, Richard Wein, Marc N Turcotte, Raphaël Haase, Christa Yeh, Shu-Chi A Bharadwaj, Srinidhi Raphael, Anthony P Paudel, Hari Alt, Clemens Liu, Tzu-Ming Kronenberg, Henry M Lin, Charles P K08 AR067285/AR/NIAMS NIH HHS/United States P01 DK011794/DK/NIDDK NIH HHS/United States P30 AR066261/AR/NIAMS NIH HHS/United States R01 EB017274/EB/NIBIB NIH HHS/United States Journal Article United States 2017/10/25 PLoS One. 2017 Oct 24;12(10):e0186846. doi: 10.1371/journal.pone.0186846. eCollection 2017.